Fock space localisation in the disordered transverse-field Ising Model



Isabel Creed

Thesis submitted for the degree of Doctor of Philosophy

St Edmund Hall, University of Oxford

Trinity 2023

I dedicate this thesis to my mum, brothers Jacob and Harry, nan and Emma, alongside my dogs Katie, Teddy and Milo. You have always been there for me, even on the toughest of days, and mean the world to me. Without you all this thesis would have never come to be.

Declaration of Authorship

The work presented in this thesis is my own, except where otherwise stated. No part of this thesis has been submitted for any other degree at this or any other university.

Isabel Creed

July 2023

Abstract

In recent years, there has been considerable interest both theoretically and experimentally in the field of many-body localisation (MBL). This thesis considers aspects of many-body localisation in Fock-space for the one-dimensional disordered transverse-field Ising model, focusing on the behaviour in the ergodic and the MBL phases.

In contrast to the ergodic phase, systems in the MBL phase fail to thermalize under their own dynamics, and memory of their initial state survives locally for arbitrarily long times. As such behaviour falls outside the paradigm of conventional statistical mechanics, the dynamics in the MBL phase is of fundamental interest. At the same time, even within the ergodic phase but at disorder strengths preceding the MBL transition, the dynamics is known to be anomalously slow. Clearly, understanding aspects of the time evolution in both phases is of interest.

One of the simplest questions one can ask is, given an initial state, how does it evolve in time on the associated Fock-space graph, in terms of the distribution of probabilities thereon? In chapters 3 and 4, we discuss our work on probability transport, where we find it exhibits a rich phenomenology, which is markedly different between the ergodic and many-body localized phases. The dynamics is, for example, found to be strongly inhomogeneous at intermediate times in both phases, but while it gives way to homogeneity at long times in the ergodic phase, the dynamics remain inhomogeneous and multifractal in nature for arbitrarily long times in the localized phase. We also show that an appropriately defined dynamical lengthscale on the Fock-space graph is directly related to the local spin autocorrelation, and as such sheds light on the (anomalous) decay of the autocorrelation in the ergodic phase,

and lack of it in the localized phase.

The MBL phase transition is an eigenstate phase transition, meaning the properties of the eigenstates differ in the ergodic and the MBL phases. One of the most fundamental questions one can ask is how are the amplitudes of the eigenstates distributed across the Fock-space graph? It is well known in the MBL literature that this can be understood by examining the generalised IPR. In chapter 5, we discuss our work on IPR distributions and our understanding of the origins of multifractality in MBL. Here, we find the distributions of the IPRs are different in the ergodic and the MBL phases, with a larger inhomogeneity in the distributions in the MBL phase than in the ergodic phase. We also discuss generally the origins of multifractality in MBL, and show that the multifractality arising in the interacting problem can be regarded as having its origins in the non-interacting but many-particle limit.

It has been well known since the early days of Anderson localisation that the extent to which nearest neighbour eigenstates overlap - or equivalently are found in the same region of space - differs significantly between localised and extended states. In chapter 6, we define new order parameters for the MBL transition, which probe this difference in overlap in Fock-space. A scaling theory is then constructed, which is closely connected to that for the inverse participation ratio and Fock-space correlations. It yields a volume-scale in the ergodic phase and a length-scale in the MBL phase. The critical properties are in agreement with previous work that the MBL transition is indeed Kosterlitz-Thouless-like. We also show using an appropriately defined probability distribution that the extent to which nearest neighbour in energy eigenstates overlap has little dependence in the ergodic and strong dependence in the MBL phase on the disorder realisation or the particular eigenstate considered. By comparing the interacting and non-interacting distributions, we shed some light on the inhomogeneity in the distributions seen in the MBL phase, alongside defining a rescaling of the distributions which collapse the results for different system sizes onto a common long-tailed curve.

Acknowledgements

Firstly, I would like to thank my supervisor David Logan for introducing me to localisation phenomena, and for all his support and guidance academically over the last 6 years. My thanks also goes to my collaborator Sthitadhi Roy for all his help on the numerical work done in this thesis. Additionally, I would like to thank the Theory and Modelling in the Chemical Sciences CDT for the training and support provided throughout my DPhil and my funders Clarendon and St Edmund Hall. I would also like to thank the other theory students particularly Ian, Sandra, Alex, Stash and Dilhan. I have throughly enjoyed our time spent together in the department over the years.

Additionally, I would like to thank Rob Penfold and David Manolopoulos, and the various colleges I have taught at, for the fantastic opportunities they have given me to teach throughout my time as a DPhil student. Teaching has been a highly rewarding and enriching experience, and has enabled me to meet some fantastic people. It has also increased my own confidence and ability to explain things which has helped in my life as a researcher. In addition, I would like to thank Saskia, Tristan and Joe. I have throughly enjoyed the time we spent together working on outreach projects and chatting, and have learnt so much from being involved in these projects.

I would also like to thank Oxford University Walking Club for allowing me to be your President for almost four years and helping/encouraging me to lead some amazing (if at times crazy) trips over my time as a DPhil student. Particular thanks goes to my friends from the club: Chris, Gordon, Henry, Clare, Arina, Sarah, Lis, Grace, Zach, Matthew, Ravi, Mohan, Parth, Alasdair, Corri, Paola, Tom, Andy, Alec, Kai,

Benoit, Milli, Kan, Endre, Akshay, Yue, Cayla, Danchen, Hameem, Adam, Maria, Jonathan, Sophia, Otto, Holly, Emily and Becca. Our trips together including the Camino, LDWA hundred, Pennine way and various weekends away have been welcome breaks to studying, researching and writing the thesis. I would also like to thank my other friends Esthy, Emily, Hannah and Andrew for their friendship and putting up with me moaning at points about either problems with my research or the thesis.

In addition, I would like to thank Ben for getting me involved in SfL during the pandemic, and to the friends I have made through the society: Adam, Daniel, Juna, Paul, Sanjush, Avesta, Alex, Connor, Joe, Martin, Kartik, Roisin, Judith, Alison and Emily. In particular, I like to thank the current executive for bearing with me as chair while I have written the thesis. My thanks also goes to my friends in Banbury and Bicester Labour Party, our discussions on politics in the evenings have been a very welcome break to writing the thesis.

Most importantly of all I would like to thank my family, and in particular my mum, my brothers Jacob and Harry, nan and Emma. Thank you for always having faith in me both academically and personally - even when I did not have faith in myself - and for supporting me in everything I do. Special thanks must go to my mum. All that I have achieved would not be possible without you. You are my biggest supporter and believer. Thank you Jacob and mum for looking after my dogs Teddy and Milo when I having been working on the DPhil in Oxford.

Abbreviations

ED	Exact Diagonalisation
ETH	Eigenstate Thermalisation Hypothesis
FS	Fock Space
IPR	Inverse Participation Ratio
KT	Kosterlitz-Thouless
LIOM	Local Integral of Motion
MBL	Many-body localised
TFI	Transverse-field Ising
GRV	Gaussian Random Eigenvector
PE	Participation Entropy
SD	Steepest Descents

Contents

Dedications i
Declaration of Authorship ii
Abstract iv
Acknowledgements vi
Abbreviations vii

1 Introduction **2**
1.1 Anderson localisation 3
1.2 MBL models 5
1.3 Ergodicity 9
1.4 Eigenstate thermalisation hypothesis 9
1.5 FS and real-space perspectives 10
1.6 Commonly studied order parameters 11
1.6.1 IPR 11
1.6.2 Spectral statistics 12
1.6.3 Self-energy expansion 13
1.6.4 Entanglement entropy 13
1.6.5 Magnetisation per site 14
1.7 Time dynamics 15
1.7.1 Return probability 15
1.7.2 Autocorrelation function 17
1.7.3 Entanglement entropy 17
1.8 Phenomenological approaches to MBL 18
1.8.1 Local Integrals of Motion 18
1.8.2 Griffith regions 19
1.9 Our work 19

2 Transverse-field Ising model **21**
2.1 Introducing the TFI model 21
2.2 Analytical handles 25
2.2.1 Gaussian Random Eigenvectors 25
2.2.2 Non-interacting problem 26
2.3 Time scales in the dynamics 27

2.4 Numerical methods . . . 28
2.5 Overview of this thesis . . . 29

3 Longitudinal probability transport 31
3.1 Introduction . . . 31
3.2 Longitudinal transport . . . 34
3.2.1 Diagnosing Longitudinal transport . . . 34
3.2.2 Connecting to the spin autocorrelation function . . . 36
3.2.3 Short-time universal behaviour . . . 39
3.2.4 Broad overview: $\overline{P}(r;t)$ . . . 44
3.2.5 Relevant bound for $\overline{C}(t)$ and $\overline{r}(t)$ . . . 47
3.2.6 Energy resolving $\overline{C}(t)$ and $\overline{r}(t)$ . . . 48
3.2.7 Ergodic phase: Band centre $\overline{C}^{[n]}(t)$ and $\overline{r}^{[n]}(t)$ . . . 54
3.2.8 MBL_0 exact results for $\overline{C}(t)$ and $\overline{r}(t)$ . . . 57
3.2.9 MBL phase: Band centre $\overline{C}^{[n]}(t)$ and $\overline{r}^{[n]}(t)$ . . . 60
3.2.10 Moving away from the band centre . . . 62
3.2.11 Full $\overline{C}(t)$ and $\overline{r}(t)$ . . . 65
3.2.12 Examining fluctuations . . . 69
3.2.13 Summary of Longitudinal transport . . . 71

4 Lateral probability transport and the emergence of multifractality 73
4.1 Lateral transport . . . 74
4.1.1 Diagnosing Lateral transport . . . 74
4.1.2 Short-time results . . . 77
4.1.3 Connecting to a row-resolved IPR . . . 78
4.1.4 Time evolution of $\langle R \rangle$ . . . 81
4.1.5 Examining $P_R(x)$ time dependence . . . 85
4.1.6 Further probing inhomogeneity in a row using $P_{\mathrm{rel}}(x)$ . . . 91
4.2 Time dependent IPR and participation entropy . . . 96
4.2.1 Introducing the relevant quantities . . . 96
4.2.2 Emergent multifractality . . . 99
4.2.3 Numerical results for $\tau_2(t)$ and $a_1(t)$ . . . 101
4.3 Examining 'self-averaging': $P_{m;rel}(x)$ . . . 104
4.4 Issues with the 'simple' spin flipping picture . . . 107
4.5 Overview of probability transport . . . 108

5 Multifractality and associated distributions 111
5.1 Introduction . . . 111
5.1.1 Defining relevant quantities . . . 113
5.1.2 Insight from one-body localisation . . . 115

5.2 Generalised IPR distributions . . . 118
5.2.1 Exact results for MBL_0 . . . 118
5.2.2 Results obtained using gaussian random eigenvectors . . . 123
5.2.3 Average fractal exponent, $\langle \tau_q \rangle$ . . . 126
5.2.4 $P_{\tau_2}(x)$ . . . 129
5.2.5 Examining $P_{u_2}(x)$ . . . 131
5.2.6 Results for $P_{L_2}(x)$ . . . 136
5.3 Understanding the origins of multifractality . . . 139
5.3.1 Non-interacting problem $J_z = 0$: TFI model . . . 139
5.3.2 Non-interacting problem $J_z = 0$: Spinless fermions . . . 142
5.3.3 Interacting problem . . . 145
5.4 Conclusion . . . 148

6 New order parameters **150**
6.1 Introduction . . . 150
6.1.1 Defining relevant quantities . . . 151
6.1.2 Gaussian Random Eigenvector results . . . 154
6.1.3 MBL_0 results . . . 157
6.2 L^{NN}_{avg}, L^{NN}_{typ}, S^{NN}_{avg} and S^{NN}_{typ} . . . 159
6.2.1 Numerical results . . . 159
6.2.2 Introducing the scaling theory . . . 162
6.2.3 Results from scaling theory . . . 166
6.3 Nearest neighbour distributions . . . 171
6.3.1 Numerical results $\mathcal{P}_{L^{NN}}(x)$ and $\mathcal{P}_{S^{NN}}(x)$ . . . 172
6.3.2 Rescaled distributions . . . 174
6.3.3 Comparing to the non-interacting problem . . . 177
6.4 Summary . . . 180

7 Conclusion and Future work **182**
7.1 Summary . . . 182
7.2 Possible directions for future work . . . 188

Bibliography **190**

A Numerical Methods **210**
A.0.1 Probability transport . . . 210
A.0.2 Multifractality . . . 212
A.0.3 New order parameter . . . 213

B Examining $\overline{P}^{[n]}(r;t)$ **214**
B.1 Behemoth operators . . . 215

C Analytical results for $\overline{C}(t)$ and $\overline{r}(t)$ MBL_0 **217**

D Further validating lateral transport results **223**
D.1 Validating the partial sum over FS sites 223
D.2 Results for other r values 224

E Fitting of $\overline{L}_2(t)$ and $\overline{S}_1(t)$ **228**

F $\tilde{P}_{m;rel}(x)$ results for other r values **230**

G Fluctuations in $C_j^{[n]}(t)$ **233**

H IPR distributions MBL_0 **236**

I IPR distributions GRV **240**

J IPR distributions for other q values **244**

K Scaling of $\langle L_2 \rangle$ and $\sigma^2_{L_2}$ with N_H **246**

L Scaling theory results S^{NN}_{avg} and L^{NN}_{avg} **247**

M Further details of the scaling analysis **249**
M.1 Procedure for scaling analysis 249
M.2 Scaling analysis 251

Chapter 1

Introduction

Since the publication of Anderson's seminal work [1] on one-body localisation in 1958, a considerable amount of theoretical and experimental research has been conducted to try to understand localisation phenomenon. Today localisation is known to occur in both single particle [2–5] and many-particle systems [6–10], and has been observed experimentally with sound [11, 12], light [13–15] and in ultra-cold atom experiments [16–19]. It is also known to occur in systems that are not truly disordered but have incommensurate potentials [20–24]. Due to the complexity of the localisation problem, many questions have however remain unanswered.

Throughout this thesis we shall discuss several different aspects of localisation phenomenon in one MBL model, the Transverse-Field Ising (TFI) model (introduced later in this chapter). In this chapter, we shall start by reminding the reader of some of the key features of one-body/Anderson localisation. We will then move on to consider what is known from previous work about many-body localisation (MBL), and elude to how the work discussed in this thesis provides further insight.

1.1 Anderson localisation

Within Anderson/one-body localisation, the usual Hamiltonian considered [2–5] for a system of N real-space sites $|i\rangle$,

$$\mathcal{H}_{1b} = \sum_{i=1}^{N} \epsilon_i \left|i\right\rangle \left\langle i\right| + \sum_{ij}{}' t_{ij} \left|i\right\rangle \left\langle j\right|, \tag{1.1}$$

with the $'$ in the second sum denoting $i \neq j$. The set of site energies, $\{\epsilon_i\}$, are normally taken to be uniformly distributed independent random variables with $\epsilon_i \in [-W, W]$. The hopping term ($\sum_{ij}' t_{ij} \left|i\right\rangle \left\langle j\right|$) is usually taken to be to nearest neighbour sites only.

Within this model, an eigenstate phase transition - where the properties of the eigenstates differ in the two phases - is known to occur [2–5] at a critical disorder strength, W_c, which depends on the dimensionality d of the problem [25–29] and on the region of the one-particle spectrum the eigenstates are taken from [28, 30–33]. In the absence of disorder, the eigenstates of $\mathcal{H}_{1b}$ are known to be Bloch states [34] or plane-waves which are delocalised, or equivalently extended across all real-space sites, $\{|i\rangle\}$. At a finite disorder strength W below the critical disorder strength, W_c, the one-body eigenstates are similarly delocalised across all real-space sites of the system [2–5]. By contrast, above W_c the eigenstates are exponentially localised on $\mathcal{O}(1)$ real-space sites $|i\rangle$.

The critical disorder strength W_c is known to depend strongly on the dimensionality of the problem [25–29]. In one and two dimensions, from the scaling theory of localisation we know that all eigenstates are localised for any finite disorder strength [26, 27], meaning the critical disorder strength $W_c \simeq 0^+$. This means the lower critical dimension above which an Anderson localisation phase transition occurs at a finite W is $d = 3$. By contrast, the upper critical dimension, above which all states

are delocalised for any disorder strength W is $d = \infty$ [25]. In Anderson localisation the critical disorder strength W_c is known to increase [25–28] as the dimensionality of the problem increases, or equivalently higher dimensional systems are 'harder' to localise.

The one-body spectrum, $D(\omega)$ is known [28, 30–33] to have mobility edges present below a certain disorder strength. States at different energies ω in the band have different propensities for localisation. It is well known [28, 30–33] that states in the edges of the spectrum i.e. those at very large or small ω values, are the first to localise. By contrast, the band centre ($\omega = 0$) states are the last to localise. The localisation of the band centre states therefore sets a critical disorder strength, W_c, above which all states in the band are localised. At $W < W_c$, there exists mobility edges in the one-body spectrum which separate regions of the band that are localised from those that are delocalised. The presence of these mobility edges has an impact on the dynamics in one-body localisation (discussed below).

One quantity which has been studied in Anderson localisation is the return probability [1–5],

$$P_{ii}(t) = |G_{ii}(t)|^2; \quad G_{ii}(t) = -i\theta(t) \langle i \,|\, \exp[-i\mathcal{H}t] \,|\, i \rangle \,, \tag{1.2}$$

with $G_{ii}(t)$ the diagonal retarded propagator [35]. The return probability measures the probability of finding a particle on real-space site $|i\rangle$ at time t given its initiation on $|i\rangle$ at $t = 0$. In Anderson localisation, the long-time behaviour of the return probability depends on the behaviour of all eigenstates in the spectrum. If all states - or more strictly all but a vanishing fraction of states - are delocalised then the return probability vanishes at long times. By contrast, if a finite fraction of states in the spectrum are localised, the return probability remains finite even at long times.

From the above discussion it is clear that the time dynamics depends on the properties of all eigenstates in the spectrum [2]. If we want to understand the properties of eigenstates within a certain region of the spectrum we need to either energy resolve time-dependent properties (we shall come back to this remark in chapter 3) or to consider properties of the eigenstates themselves.

Within Anderson localisation several quantities are known to distinguish between localised and extended states. These include the self-energy [5, 36–42], spectral statistics [43, 44] and IPR [2, 45–53]. We shall define these quantities and discuss their behaviour in both Anderson/one-body localisation and many-body localisation in section 1.6.

Within the field of Anderson localisation the question naturally arose as to what effect adding interactions had on the localisation phase transition. The earliest work considered the stability of the Anderson localisation transition to the addition of interactions [54], and the effect of the addition of interactions to the ground state problem [55–57]. In more recent years, several proofs have emerged [58, 59] which have shown that a localised phase can persist with finite interactions at a finite energy density above the ground state, i.e. in 'high temperature' states. Following the publication of these proofs, the rich field of many-body localisation has emerged.

1.2 MBL models

In many-body localisation there are several model Hamiltonians that are commonly used to examine the MBL phase transition; for example the TFI [60–64], spinless fermion [8, 65–69], XXZ [70–73] and p-spin [74–76] models. The spinless fermion and XXZ models are of course related by a Jordan Wigner transformation [77]. We shall now move onto briefly discuss these models.

The TFI model usually considered [60–64] is the one-dimensional spin-1/2 model

which describes a system consisting of L spins specified by the Hamiltonian

$$\mathcal{H}_{TFI} = \sum_{l=1}^{L} h_l \hat{\sigma}_l^z + \sum_{l=1}^{L-1} \mathcal{J}_l \hat{\sigma}_l^z \hat{\sigma}_{l+1}^z + \sum_{l=1}^{L} \Gamma \hat{\sigma}_l^x, \tag{1.3}$$

with $\hat{\sigma}_l^x = \hat{\sigma}_l^+ + \hat{\sigma}_l^-$, $\hat{\sigma}_l^\alpha = 2\hat{S}_l^\alpha$ with $\hat{S}_l^\alpha$ the usual $\alpha = x, y,$ or z spin-1/2 operators and $\hat{S}_l^\pm = \hat{\sigma}_l^\pm$. It follows that $(\hat{\sigma}_l^z)^2 = 1$ meaning its eigenvalues are ± 1 (rather than the usual $\pm 1/2$ for spin-1/2 operators). The commutation relations are then $[\sigma_l^\pm, \sigma_l^z] = \mp 2\hat{\sigma}_l^\pm$ and $[\hat{\sigma}_l^+, \hat{\sigma}_l^-] = \hat{\sigma}_l^z$. The set of fields $\{h_l\}$ are taken to be uniformly distributed independent random variables with $h_l \in [-W, W]$. The set of interaction strengths, $\{J_l\}$, are uniformly distributed independent random variables where $J_l \in [0.8, 1.2]$ and $\Gamma = 1$.

We shall consider the TFI model throughout this thesis, due to it having a much simpler Fock space structure (introduced in section 2.1) than the other models. Additionally, the non-interacting problem can be solved exactly, thereby providing an analytical handle for the MBL phase (discussed in section 2.2.2).

The standard spinless fermion model used in MBL is the one-dimensional problem which has a Hamiltonian of the form [8, 65–69]

$$\mathcal{H}_{sf} = \sum_{i=1}^{N} \epsilon_i \hat{n}_i + \sum_{\langle ij \rangle} t(\hat{c}_i^\dagger \hat{c}_j + \hat{c}_j^\dagger \hat{c}_i) + \sum_{\langle ij \rangle} V \hat{n}_i \hat{n}_j, \tag{1.4}$$

where $\{\epsilon_i\}$ are the site energies of the orbitals on real-space sites i, and are taken to be uniformly distributed independent random variables, $\epsilon_i \in [-W, W]$. The hopping (t) and the interactions (V) are taken to be nearest neighbour (NN), denoted in eq. 1.4 by $\langle ij \rangle$. As usual $\hat{n}_i = \hat{c}_i^\dagger \hat{c}_i$ is the number operator on real-space site i, which simply counts whether there is a fermion or not on this real-space site, and $\hat{c}_i^\dagger$ and $\hat{c}_i$ are respectively the creation and annhilation operators for a fermion on real-space site i. The chain has N real-space sites and N_e fermions. The filling fraction

$\nu = \frac{N_e}{N} \in [0,1]$, and in MBL we are generally interested in the thermodynamic limit $N \to \infty$ holding ν fixed and non-vanishing. We briefly consider this model in chapter 5.

Another commonly studied model which by a Jordan Wigner transformation [77] is equivalent to a spinless fermion model - included here for completeness - is the disordered XXZ model [70–73] in one dimension, with the Heisenberg model being a special case - which has a Hamiltonian

$$\mathcal{H}_{XXZ} = \sum_{l=1}^{L} h_l \hat{\sigma}_l^z + J_z \sum_{l=1}^{L-1} \hat{\sigma}_l^z \hat{\sigma}_{l+1}^z + J \sum_{l=1}^{L-1} \left(\hat{\sigma}_l^x \hat{\sigma}_{l+1}^x + \hat{\sigma}_l^y \hat{\sigma}_{l+1}^y \right). \tag{1.5}$$

The set of fields, $\{h_l\}$, are taken to be uniformly distributed independent random variables with $h_l \in [-W, W]$. The interaction constant J_z and 'hopping constant' J are usually both taken to be 1.

The final type of model we discuss which is known to have an MBL transition [74–76] are so called p-spin models. In this case, the Hamiltonian

$$\mathcal{H}^{p-spin} = \mathcal{H}_{diag}^{p-spin} + \mathcal{H}_1, \tag{1.6}$$

where

$$\mathcal{H}_{diag}^{p-spin} = \frac{1}{N^{\frac{p-1}{2}}} \sum_{l_1, l_2 ..... l_p} J_{l_1, l_2, ... l_p} \hat{\sigma}_{l_1}^z \hat{\sigma}_{l_2}^z ..... \hat{\sigma}_{l_p}^z \tag{1.7}$$

and $H_1 = \sum_l \Gamma \hat{\sigma}_l^x$. The $J_{l_1, l_2 ... l_p}$ are independent random variables drawn from a normal distribution with zero mean and standard deviation W_J.

In all of these one-dimensional models the MBL phase transition is known to occur [6–10, 74–76] at a critical disorder strength, $W_c(\omega)$, which depends on the region of the many-body spectrum the eigenstates are taken from [78–81]. For $W < W_c(\omega)$ the eigenstates in the energy window set by ω are ergodic, while for

$W > W_c(\omega)$ the eigenstates are many-body localised (MBL). Precisely what we mean by ergodic and MBL eigenstates will be discussed below.

States at different energies ω in the band have different propensities for localisation [78–81]. It is well known [78–81] that states in the tails of the band, i.e. those at very large or small ω values, are the first to localise. By contrast, the band centre ($\omega = 0$) states are the last to localise. The localisation of the band centre states therefore sets a critical disorder strength, W_c, above which *all* states in the band are MBL. At $W < W_c$, there exists mobility edges in the many-body spectrum which separate regions of the band that are MBL from those that are ergodic. For a given ω, there is a critical W, $W_c(\omega)$, above which states at that ω (and all states at larger $|\omega|$) are localised. In chapter 3, we shall discuss that the presence of these mobility edges has an impact on the dynamics of e.g. the autocorrelation function [82–87] (introduced in section 1.7).

At this point it is important to note that the addition of non-zero interactions has meant that for a given ω the localisation transition in one dimension occurs at a finite W, which is very different to the non-interacting problem where all eigenstates are localised for all non-vanishing W [26, 27].

Since the MBL phase transition is an eigenstate phase transition, the properties of individual eigenstates are different in the ergodic phase and the MBL phase. In section 1.6 we shall discuss previous work [41, 42, 61, 65–67, 71, 79, 84, 88–109] to define different order parameters based on these differences. Additionally, the time-evolution of systems composed of ergodic states is very different to those composed of MBL states. We shall discuss what is known from previous work [7, 70, 82–87, 110–118] on the time evolution in the different phases in section 1.7.

1.3 Ergodicity

Ergodicity is a basic postulate of statistical mechanics [119] and assumes that given sufficient time the system is able to explore all of its accessible phase space. As a concrete example, let us consider initialising a system of spins in a particular orientation, e.g. $|\uparrow\downarrow\uparrow\downarrow\downarrow\uparrow\downarrow\uparrow\rangle$. If the system is ergodic at long times each spin in the system is equally likely to point up or down. By contrast, in a non-ergodic system some memory of the initial state remains for all times, i.e. some spins are frozen.

Anderson localised states are a well known example of non-ergodic states [44, 120, 121]. Similarly, the time evolution of systems with MBL eigenstates is not ergodic [122–124], as some information on the initial state persists for all times. This is reflected in the time evolution of e.g. the autocorrelation function [82–87] discussed in section 1.7.

1.4 Eigenstate thermalisation hypothesis

The eigenstate thermalisation hypothesis (ETH) explains how thermalisation occurs in isolated non-integrable systems [6, 9, 125–130]. This hypothesis can be thought of as a generalisation of the well known [119] equivalence in the thermodynamic limit of the three ensembles the grand canonical, canonical and microcanonical ensembles to the extreme limit that the microcanonical ensemble window contains only a single eigenstate [125, 126].

In order for this to be true two criteria [125, 126] must be met for the matrix elements $A_{n,m} = \left\langle \Psi_n \middle| \hat{A} \middle| \Psi_m \right\rangle$ where $|\Psi_n\rangle$ / $|\Psi_m\rangle$ are the eigenstates of the Hamiltonian with eigenenergies E_n and E_m respectively. These criteria are:

- $A_{n,n}$ is a smooth function of energy, with the differences between the expectation value of the nearest neighbour in energy eigenstates when the eigenstates

are energy ordered, $|\Psi_{n+1}\rangle$ and $|\Psi_n\rangle$, $A_{n+1,n+1} - A_{n,n}$, decreasing exponentially with increasing system size L, and thus vanishing in the thermodynamic limit.

- The off-diagonal matrix elements $A_{n,m}$ are small and decrease exponentially with increasing system size L.

It is well known [6, 9, 128–130] that ergodic states obey the ETH, while, MBL states similarly to integrable systems [125, 126] violate the ETH.

1.5 FS and real-space perspectives

For the models introduced in section 1.2, the localisation problem can be examined from either the 'FS perspective' or the 'real-space perspective'.

Fock space (FS) provides a natural framework for studying many-body localisation [61, 63, 64, 66, 72, 74, 94, 97, 100, 101, 124, 131–143] in part because a generic many-body Hamiltonian maps exactly onto a tight-binding model on the associated FS graph (or 'lattice'), of the form

$$\mathcal{H} = \sum_J \mathcal{E}_J |J\rangle\langle J| \; + \; \sum_{J,K}{}' T_{JK} |J\rangle\langle K|, \tag{1.8}$$

with the $'$ denoting $K \neq J$.

As the disorder couples to the $\{\hat{\sigma}_l^z\}$ in both the TFI and XXZ models, the natural FS site basis $\{|I\rangle\}$ to consider the localisation problem on is the basis composed of product states of $\sigma_l^z = \pm 1$ [61, 63, 64, 124]. While in spinless fermion models the natural FS site basis to consider the problem on are the single slater determinant formed by an arbitrary set of N_e site-orbitals $\{|I\rangle\}$ being occupied [66, 131].

The properties of the eigenstates in FS are very different in the ergodic and the MBL phase [6–10]. In the ergodic phase the many-body eigenstates are essentially uniformly distributed across the entire FS lattice. By contrast, while in the MBL

phase the wavefunction is spread across a macroscopic number of FS sites, these sites occupy a vanishing fraction of the entire FS lattice. The IPR (introduced in section 1.6) is an example of a quantity used in the MBL literature [79, 88–103] to examine how the wavefunction is distributed in FS.

Additionally, the MBL problem can be examined from the 'real-space' perspective. Here, the time evolution or expectation values of properties on individual real-space sites are examined. For example, in the TFI model, the eigenstate expectation value and time-evolution of the expectation value of the $\hat{\sigma}_l^z$ operator on each real-space site l can be studied. This is probed by quantities which measure the magnetisation on each site [61, 84] (introduced in section 1.6) and by the autocorrelation function [82–87] (introduced in section 1.7) respectively.

In sections 1.6 and 1.7 we shall discuss what is already known about the MBL problem from both the real-space and FS perspectives. Not much work, however, has been done to connect between these two perspectives. In [61], a relationship was found between the long-time value of a relevant real-space and FS quantity. A key result of this thesis [144] (chapter 3) is the relationship we have found between the time evolution of an important real-space and FS quantity. This is a generalisation of the result in [61].

1.6 Commonly studied order parameters

We shall now move onto briefly introduce/remind the reader of the order parameters typically used [41, 42, 61, 65–67, 71, 79, 84, 88–109] to examine the MBL transition.

1.6.1 IPR

In MBL, the wavefunction $|\Psi_n\rangle$ can be written as a sum over all FS sites $\{|I\rangle\}$, i.e. $|\Psi_n\rangle = \sum_I A_{nI}\,|I\rangle$, with the amplitudes $A_{nI} = \langle I|\Psi_n\rangle$. The IPR [79, 88–103]

is defined as $L_q = \sum_I |A_{nI}|^{2q}$. Similarly in one-body/Anderson localisation, the wavefunction can be written as a sum over all real-spaces i, i.e. $|\psi_\alpha\rangle = \sum_i a_{\alpha i} |i\rangle$, with $a_{\alpha i} = \langle i|\psi_\alpha\rangle$. In this case, the IPR [2, 45–53] is given by $L_q = \sum_i a_{\alpha i}^{2q}$.

The system size dependence of the IPR is known [79, 88–103] within many-body localisation to distinguish between ergodic and MBL eigenstates. In the ergodic phase, $L_q \sim N_H^{-(q-1)}$, while in the MBL phase, $L_q \sim N_H^{-\tau_q}$ with $0 < \tau_q < q-1$ (for $q > 1$), and is a non-linear function of q, meaning the wavefunction is multifractal. Examining the system size dependence of L_q clearly allows us to determine the location of the phase transition. A scaling theory has already been formulated in [61] to describe the behaviour of the IPR on approach to the transition.

Similarly, the system size dependence of the IPR in Anderson location is different in the localised phase and the extended phase [2, 45–53]. Here, $L_q \sim \frac{1}{L}$ in the delocalised phase and $L_q \sim \mathcal{O}(1)$ in the localised phase.

A natural question to ask is why is there a difference in the behaviour of the IPR in the localised phase in many-body localisation and Anderson localisation. This is a question we seek at least in part to provide an answer for in chapter 5.

1.6.2 Spectral statistics

Another order parameter which has been commonly used to distinguish between localised and extended states in both MBL [65–67, 71, 79, 104, 105] and Anderson localisation [43, 44] is the average ratio of consecutive eigenvalue spacings,

$$r = \langle r_n \rangle_{n,d}; \quad r_n = \frac{\min[\delta_n, \delta_{n-1}]}{\max[\delta_n, \delta_{n-1}]}; \quad \delta_n = E_{n+1} - E_n, \tag{1.9}$$

with $\langle\rangle_{n,d}$ denoting an average over eigenstates within a certain energy window and disorder realisations. For the Gaussian orthogonal ensemble (GOE) characteristic of

delocalised/ergodic states $r_{GOE} = 0.53..$, while for Poissonian statistics appropriate to the localised/MBL phase, $r_{Pois} = 0.38..$ [65, 145]. It therefore follows that r can be used as an order parameter to detect the MBL transition.

1.6.3 Self-energy expansion

An important quantity in localisation phenomenon is the Feenberg self-energy $S(\omega)$ [35, 146], and in particular its imaginary part $\Delta(\omega)$. This has long been used as an order parameter in Anderson localisation [5, 36–42]. Physically, it corresponds to the inverse lifetime for a given real-space/FS site participating in states of energy ω.

In both one-body localisation [5, 36–42] and MBL [66, 143], $\Delta(\omega)$ is non-zero in the extended phase and $\propto \mu_E$ in many-body localisation [66, 143] , and $\Delta(\omega) \propto \eta = 0^+$ in a localised phase. Physically this occurs as in the extended phase all memory of the initial state is lost at long-times, i.e. an initial state has a finite lifetime on a given real-space/FS site, while, in the localised phase, some memory of the initial state survives at long-times, meaning the lifetime of the state is infinite in the thermodynamic limit.

Since $\Delta(\omega) \propto \mu_E \propto \sqrt{L}$ in the many-body problem, it is necessary to rescale $\Delta(\omega)$ in MBL, i.e. $\tilde{\Delta}(\omega) = \frac{\Delta(\omega)}{\mu_E}$ [66, 143]. In one-body localisation [41, 42], many-body localisation [66] and in one-body localisation with incommensurate potentials [147], a mean-field theory has been developed which explains qualitatively the behaviour of the self-energy on either side of the transition.

1.6.4 Entanglement entropy

The entanglement entropy is also known to distinguish between localised and extended states [79, 106–109]. In order to define the entanglement entropy, we first

divide up our system of L spins/fermions into two subsystems A and B with $\frac{L}{2}$ spins/fermions in each subsystem. Each FS site $|I\rangle = |I_A\rangle \times |I_B\rangle$, where $\left|I_{A(B)}\right\rangle$ is the spin/fermion configuration in subsystem A and B. The entanglement entropy of subsystem A, $S^A = -\ln[\mathrm{Tr}[\rho_A^2]]$, $\rho_A = \mathrm{Tr}_B[\rho]$, with $\rho = |\Psi\rangle\langle\Psi|$ the standard density matrix.

The entanglement entropy is known [79, 106–109] to show area law scaling, $S^A \sim \mathcal{O}(1)$ in the ergodic phase, and volume law scaling $S^A \sim L$ in the MBL phase. The difference in system size dependence of the entanglement entropy in the two phases means it is a standard order parameter [79, 106–109] for the MBL transition.

1.6.5 Magnetisation per site

In the TFI and XXZ models for a given eigenstate $|\Psi_n\rangle$ the expectation value of the $\hat{\sigma}_l^z$ operator on a given real space site l - or equivalently the magnetisation on site l - is known [61, 84] to differ for eigenstates in the ergodic and MBL phases. In the ergodic phase as spins on all real-spaces sites in an eigenstate are expected to be equally likely to be found up or down, the expectation value of the $\hat{\sigma}_l^z$ operator on any given real space site l is known to vanish in the thermodynamic limit. By contrast, in the MBL phase the spins on some real-space sites l are expected to be frozen, and for these spins the expectation value of the $\hat{\sigma}_l^z$ operator in a given eigenstate will be non-zero.

In the MBL literature several quantities have been defined which distinguish between the ergodic phase and the MBL phase based on the difference in the behaviour of magnetisation per site.

For example, Logan and Roy in [61] defined the quantity $\mathcal{M}_i = \langle\Psi_n\,|\,\hat{\sigma}_i^z\,|\,\Psi_n\rangle^2$, and examined its distribution $P_{\mathcal{M}_i}(m) = \langle\delta(m - \mathcal{M}_i)\rangle$ (with $\langle\rangle$ denoting an average over real-space sites i and disorder realisations) and it first moment $\bar{\mathcal{M}}$. The latter

acts as an order parameter for the MBL phase transition with $\bar{\mathcal{M}}$ vanishing in the ergodic phase, while $\bar{\mathcal{M}}$ remains finite in the MBL phase.

In [84] Luitz defined the quantity $\Delta_{n,n+1}S_l^z = \langle\Psi_n\,|\,\hat{\sigma}_l^z\,|\,\Psi_n\rangle - \langle\Psi_{n+1}\,|\,\hat{\sigma}_l^z\,|\,\Psi_{n+1}\rangle$, with $|\Psi_n\rangle$ and $|\Psi_{n+1}\rangle$ being nearest neighbour in energy eigenstates. $\Delta_{n,n+1}S_l^z$ is expected to show different behaviour in the ergodic phase and the MBL phase.

In the ergodic phase both due to $\langle\Psi_n\,|\,\hat{\sigma}_l^z\,|\,\Psi_n\rangle$ and $\langle\Psi_{n+1}\,|\,\hat{\sigma}_l^z\,|\,\Psi_{n+1}\rangle$ vanishing and the ETH which means $\langle\Psi_n\,|\,\hat{\sigma}_l^z\,|\,\Psi_n\rangle \simeq \langle\Psi_{n+1}\,|\,\hat{\sigma}_l^z\,|\,\Psi_{n+1}\rangle$ as eigenstate expectation values are smooth functions of energy (discussed in section 1.4), $\Delta_{n,n+1}S_l^z$ vanishes for all real-space sites l and disorder realisations. By contrast, in the MBL phase we expect $\Delta_{n,n+1}S_l^z \neq 0$ for the real-spaces sites l, $\langle\Psi_n\,|\,\hat{\sigma}_l^z\,|\,\Psi_n\rangle \neq 0$ and/or $\langle\Psi_{n+1}\,|\,\hat{\sigma}_l^z\,|\,\Psi_{n+1}\rangle \neq 0$, where as ETH does not hold in the MBL phase, generally $\langle\Psi_n\,|\,\hat{\sigma}_l^z\,|\,\Psi_n\rangle \neq \langle\Psi_{n+1}\,|\,\hat{\sigma}_l^z\,|\,\Psi_{n+1}\rangle$. As a result, the distribution $P_{\Delta_{n,n+1}S_l^z}(x) = \langle x - \Delta_{n,n+1}S_l^z)\rangle$ is found [84] to clearly distinguishes between the two phases.

1.7 Time dynamics

Having introduced some of the important order parameters used to distinguish between the ergodic phase and the MBL phase, we shall now move on to discuss what is known [7, 70, 82–87, 110–118] about the time dynamics of systems composed of ergodic eigenstates and MBL eigenstates.

1.7.1 Return probability

One time-dependent quantity which has been examined extensively in MBL [83, 148–151]) is the return probability,

$$P_{II}(t) = |G_{II}(t)|^2; \quad G_{II}(t) = \langle I|\exp[-i\mathcal{H}t]|I\rangle\,, \tag{1.10}$$

with $G_{II}(t)$ the diagonal retarded Green's function [35]. The return probability measures the probability of finding the system on FS site $|I\rangle$ at time t given its initiation on $|I\rangle$ at $t = 0$.

In MBL - similarly to Anderson localisation - the long-time behaviour of the return probability depends on the behaviour of all eigenstates in the spectrum and is known to distinguish between ergodic and MBL states [83, 148–151]. If all states - or more strictly all but a vanishing fraction of states - are ergodic then the return probability vanishes $\sim \frac{1}{N_H}$ at long times. By contrast, if a finite fraction of states in the spectrum are localised, the return probability vanishes $\sim \frac{1}{N_H^\alpha}$ $(\alpha < 1)$ at long times.

The long-time behaviour of the return probability clearly distinguishes between the ergodic and the MBL phases. It is, however, of limited use in diagnosing probability transport, since it is exponentially small in system size in both phases. This means in the thermodynamic limit, there is zero probability of the system returning to its initial state. A far greater understanding of probability transport is obtained using the quantities defined in chapters 3 and 4 and discussed in our recent paper [144].

The behaviour of the return probability in the localised phase is very different in Anderson localisation [1–5] and MBL [83, 148–151]. In Anderson localisation, when localised eigenstates are present the return probability remains finite, while in MBL it vanishes exponentially, i.e. $\sim \frac{1}{N_H^\alpha}$, but with a smaller exponent than the ergodic phase.

1.7.2 Autocorrelation function

Another time-dependent quantity which has been examined in the literature is the spin autocorrelator [70, 110, 111] which is defined by

$$C(t) = \frac{1}{L}\sum_{l=1}^{L} C_{ll}(t), \quad C_{ll}(t) = \frac{1}{N_H} Tr(\hat{\sigma}_l^z(t)\hat{\sigma}_l^z), \tag{1.11}$$

with $C_{ll}(t)$ the local real-space autocorrelator. Physically, the spin autocorrelator measures the extent to which a spin system retains memory of its initial configuration as a function of time. Its long-time value is a standard order parameter used to detect the MBL transition in real-space [70, 110, 111], and has been examined extensively in the XXZ model. Within the MBL phase, the system retains memory of its initial configuration for all times, meaning the long-time value of $C(t) > 0$. By contrast, in the ergodic phase, as the system thermalise under its own dynamics, no memory of the initial state survives for long times, and therefore $C(t \to \infty) = 0$.

The behaviour of the autocorrelation function in the TFI model shall be discussed in chapter 3.

1.7.3 Entanglement entropy

For completeness, the other time-dependent quantity commonly studied in the MBL literature [7, 112–118] is the time-dependent entanglement entropy.

In MBL it is known [7, 112–118] that deep in the ergodic phase the time-dependent entanglement entropy grows ballistically with time, while in the MBL phase the time-dependent entanglement entropy grows logarithmically with time. In both the ergodic and MBL phases, the time-dependent entanglement entropy saturates to a $\mathcal{O}(L)$ value at long-times. This is in stark contrast to Anderson localisation [112], where the time-dependent entanglement entropy remains $\mathcal{O}(1)$ for

all time .

1.8 Phenomenological approaches to MBL

In the MBL literature as well as examining relevant properties of the eigenstates and time evolution of certain quantities, a number [82, 85, 87, 152–156] of phenomenological approaches have been developed based on understanding the physics of the MBL transition.

1.8.1 Local Integrals of Motion

The failure of a system to show ergodic behaviour is believed to occur due to the system being integrable [125, 126]. Since the MBL phase shows non-ergodic behaviour, it is expected that MBL systems have some sort of integrability . This led to the concept of Local Integrals Of Motion (LIOM) [106, 108, 152–158].

To motivate the functional form of these LIOM, $\{\tau_l^z\}$, let us consider what happens asymptotically at large disorder values (i.e. $W \to \infty$) in the TFI model. Since the disorder couples to the $\{\hat{\sigma}_l^z\}$ operators, it follows that the eigenstates of the Hamiltonian in this limits are the product states of $\{\sigma_l^z\}$ spins. In this case, the value of σ_l^z on each real-space site l is an integrable of motion.

For finite disorder and interaction strengths, its is expected that the LIOM will be 'dressed' σ_l^z spins which are generated by the transformation $\hat{U}^\dagger \hat{\sigma}_l^z \hat{U}$, where $\hat{U}$ is a quasi-local unitary operator. This leads to LIOM of the form

$$\tau_i^z \sim \sigma_i^z + \sum_{j,k} \sum_{a,b=x,y,z} f_{i,jk}^{ab} \sigma_j^a \sigma_k^b + ... \tag{1.12}$$

where a, b are equal to either x, y or z. The weights $f_{i,jk}^{ab}$ decrease exponentially with

distance from i to the j and k spins. The Hamiltonian can then be rewritten as

$$\mathcal{H}_{MBL} = \sum_i \tilde{h}_i \hat{\tau}_i^z + \sum_{i>j} J_{ij} \hat{\tau}_i \hat{\tau}_j + \sum_{i>j>k} J_{ijk} \hat{\tau}_i \hat{\tau}_j \hat{\tau}_k + ... \tag{1.13}$$

where couplings between LIOMs decreases with distance between them, and the number of other LIOMs (from different sites) in the term. An effective model for the MBL phase can then be generated by only considering interactions between these LIOM [106, 108, 157, 159]. More recently, resonances between LIOMs have ben used to explain several features of the MBL phase [152–156, 158].

1.8.2 Griffith regions

In conventional phase transitions rare regions - or Griffith regions - [160, 161] have been proposed to explain sub-diffusive transport. In MBL, previous work [111, 162] has shown that on approach to the MBL transition from the ergodic phase the dynamics becomes subdiffusive. This has been explained in the literature using phenomenological theories [82, 85, 87] based on rare Griffith regions, or equivalently due to the presence of rare MBL regions in the ergodic phase which act as a 'bottlenecks' for transport. In chapter 3, we will examine the slow dynamics of the autocorrelation in the TFI model from a microscopic viewpoint.

1.9 Our work

The work in this thesis develops upon the huge amount of work which has already been done to understand the MBL transition, which we have only just touched upon in this chapter. The work in this thesis focuses on building further understanding on three separate areas of MBL in the TFI model.

Firstly in chapters 3 and 4, we will discuss the additional insight into the dynamics in MBL (previous work discussed in section 1.7) we have obtained by examining

probability transport in FS and related FS and real space properties. Secondly in chapter 5, we shall discuss our work on the IPR (discussed in section 1.6) and the insight we have obtained into the ubiquitous multifractality in the MBL phase. Finally, we shall discuss our proposed order parameters in chapter 6 (commonly used order parameters are discussed in section 1.6), and the insight these parameters gives us into the MBL transition.

Before starting to discuss our work in chapter 3, in the next chapter we shall move on to discuss the important properties of the TFI model.

Chapter 2

Transverse-field Ising model

2.1 Introducing the TFI model

Throughout this thesis we will consider different aspects of many-body localisation in the disordered transverse-field Ising (TFI) model. In this chapter, we introduce the model and discuss its important properties.

The TFI model we consider is the one-dimensional spin-1/2 model which describes a system consisting of L spins specified by the Hamiltonian

$$\mathcal{H}_{TFI} = \sum_{l=1}^{L} h_l \hat{\sigma}_l^z + \sum_{l=1}^{L-1} \mathcal{J}_l \hat{\sigma}_l^z \hat{\sigma}_{l+1}^z + \sum_{l=1}^{L} \Gamma \hat{\sigma}_l^x, \tag{2.1}$$

with $\hat{\sigma}_l^x = \hat{\sigma}_l^+ + \hat{\sigma}_l^-$, $\hat{\sigma}_l^\alpha = 2\hat{S}_l^\alpha$ with $\hat{S}_l^\alpha$ the usual $\alpha = x, y,$ or z spin-1/2 operators and $\hat{S}_l^\pm = \hat{\sigma}_l^\pm$. It follows that $(\hat{\sigma}_l^z)^2 = 1$ meaning its eigenvalues are ± 1 (rather than the usual $\pm 1/2$ for spin-1/2 operators). The commutation relations are then $[\sigma_l^\pm, \sigma_l^z] = \mp 2\hat{\sigma}_l^\pm$ and $[\hat{\sigma}_l^+, \hat{\sigma}_l^-] = \hat{\sigma}_l^z$.

The first term in eq. 2.1 describes the interaction of the spins on the real-space sites $\{l\}$ with the random magnetic fields, $\{h_l\}$. These fields are taken to be independent random variables uniformly distributed between $-W$ and W, with W the disorder strength. Their probability distribution $P(h_l) = \frac{1}{2W}\,\theta\,(W - |h_l|)$. This

is denoted throughout this thesis by $h_l \in [-W, W]$.

The second term in eq. 2.1 describes the interactions between each spin on real-space site l with its nearest neighbour spins on real-space sites $l \pm 1$. The strength of the interaction $\mathcal{J}_l$ is taken to be an independent random variable uniformly distributed between 0.8 and 1.2 with a probability distribution $P(\mathcal{J}_l) = \frac{5}{2}\,\theta\,(0.2 - |\mathcal{J}_l - 1|)$; here denoted $\mathcal{J}_l \in [0.8, 1.2]$.

Finally, the third term in eq. 2.1 is of the form $\Gamma\hat{\sigma}_l^x = \Gamma\left(\hat{\sigma}_l^+ + \hat{\sigma}_l^-\right)$ - with $\hat{\sigma}_l^+$ and $\hat{\sigma}_l^-$ the usual spin-1/2 raising and lowering operators. This term flips a spin on a given real-space site l from up to down or vice versa. Throughout this thesis, we take $\Gamma = 1$ as the basic unit of energy.

With these parameters, and the range of system sizes accessible in practice to exact diagonalisation (ED), the critical disorder strength above which all eigenstates are MBL is estimated to be $W_c \simeq 3.8$ [62]. Some recent works on standard disordered models [152, 156, 163–169] have however suggested that a genuine MBL phase, stable in the thermodynamic limit $L \to \infty$, might arise only for much larger values of W, and that the apparent localisation found for finite systems at $W > W_c$ is indicative of a pre-thermal regime. Throughout this thesis we shall take the view that the MBL phenomenology clearly observed at $W > W_c \sim 4$ for ED-accessible system sizes persists in the thermodynamic limit, albeit possibly for larger W values.

Fock space (FS) provides a natural framework for studying many-body localisation [61, 63, 64, 66, 72, 74, 94, 97, 100, 101, 124, 131–143] in part because a generic many-body Hamiltonian maps exactly onto a tight-binding model on the associated FS graph (or 'lattice'), of the form

$$\mathcal{H} = \sum_J \mathcal{E}_J |J\rangle\langle J| \;+\; \sum_{J,K}{}' T_{JK} |J\rangle\langle K|, \tag{2.2}$$

with the $'$ denoting $K \neq J$. This will be explained in more detail below.

The natural FS site basis with which to consider the TFI model is the basis of σ_l^z product states, i.e.

$$|I\rangle = \bigotimes_{l=1}^{L} |\sigma_l^z\rangle = |\{\sigma_l^z\}\rangle \,. \tag{2.3}$$

Physically, each FS site $|I\rangle$ represents a many-body quantum state, which is an eigenstate of the set of $\hat{\sigma}_l^z$ operators, where $\hat{\sigma}_l^z |I\rangle = S_{l,I} |I\rangle$ with $S_{l,I} = \pm 1$. In the limit $W \to \infty$ the wavefunction is localised on a single FS site. Clearly as each spin on real-space site l can point either up or down, the total number of FS sites is $N_H = 2^L$, which is of course the dimension of the Fock space.

Given this basis the Hamiltonian $\mathcal{H}_{TFI}$ in eq. 2.1 can be rewritten as

$$\mathcal{H}_{TFI} = \mathcal{H}_0 + \mathcal{H}_1; \quad \mathcal{H}_0 = \sum_l \left(h_l \hat{\sigma}_l^z + \mathcal{J}_l \hat{\sigma}_l^z \hat{\sigma}_{l+1}^z \right), \quad \mathcal{H}_1 = \Gamma \sum_{l=1}^{L} \hat{\sigma}_l^x. \tag{2.4}$$

From eq. 2.1 it is clear that the number of independent random variables in the TFI model is $\mathcal{O}(L)$, with L the number of real-space sites in the problem. By contrast, the number of FS sites, $N_H = 2^L$. This means there are exponentially more FS sites $\{|I\rangle\}$ than independent random variables which means the FS site energies, which are eigenstates of $\mathcal{H}_0$, i.e. $\mathcal{H}_0 |I\rangle = \mathcal{E}_I |I\rangle$ must be highly correlated. The properties of $\{\mathcal{E}_I\}$ were studied extensively in [74].

On the other hand, the $\mathcal{H}_1 = \sum_l \Gamma \hat{\sigma}_l^x$ term clearly connects the FS site $|I\rangle$ to the L FS sites $\{|J\rangle\}$ that differ from $|I\rangle$ by a single spin flip on one of the real-space sites l. It therefore follows that $\mathcal{H}_{TFI}$ can be written as a tight-binding model in FS of the form in eq. 2.2, with the hopping connecting FS sites which differ by a single spin flip.

The FS graph/lattice of the TFI model is an L-dimensional hypercube with $N_H = 2^L$ vertices, which is shown in figure 2.1. As illustrated in figure 2.1 the graph consists of $L + 1$ rows, $r = 0 - L$. A single FS site, denoted by $|I\rangle$ in figure 2.1

lies at the apex of the graph, $r = 0$. The structure of the FS graph that results is independent of this initial choice.

Links or hops on the FS graph are then generated by the $\mathcal{H}_1 = \sum_l \Gamma \hat{\sigma}_l^x$ term. Each FS site is therefore connected to L other sites which lie on adjacent rows of the graph and each of which corresponds to flipping of a single spin on a particular real-space site l. It therefore follows that starting from the initial FS site $|I\rangle$ the FS graph/lattice is generated by successively applying the $\mathcal{H}_1$ operator. On a given row r, r of the spins have been flipped in $|I\rangle$, and $L - r$ spins are the same as $|I\rangle$, with $N_r = \binom{L}{r}$ Fock-space sites on row r. The final FS site on the $r = L$ row is $\left|\overline{I}\right\rangle$ in which all real-space spins in $|I\rangle$ have been flipped.

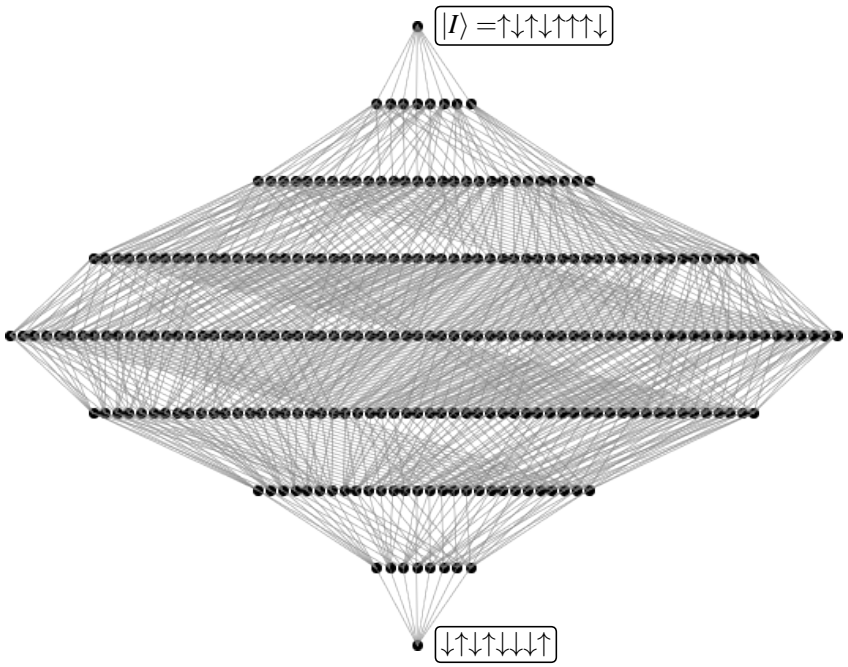


Figure 2.1: Fock-space (FS) graph of the disordered TFI model Eq. 2.1 in the basis of σ^z-product states, illustrated for $L = 8$. An arbitrary FS site, I, is placed at the apex. The graph has $L + 1$ rows, and the number of FS sites on row r is $N_r = \binom{L}{r}$. Any FS site J on row r is a Hamming distance $r_{IJ} = r$ from I. Links/hoppings can connect only FS sites on adjacent rows; with each FS site connected to precisely L others.

As a measure of distance between two sites $|I\rangle$ and $|J\rangle$ on the FS graph we shall throughout this thesis use the Hamming distance r_{IJ} which simply counts the number of real-space sites l the value of σ_l^z in $|I\rangle$ and $|J\rangle$ differ, and gives the shortest

distance between the pair of sites. When $|I\rangle$ is the apex site clearly $r_{IJ} = r$.

In the chapters that follow, we shall consider several aspects of the MBL transition in the TFI model from the FS perspective.

2.2 Analytical handles

Throughout this thesis we shall use two analytical handles, namely the gaussian random eigenvectors (GRV) model and the non-interacting limit (MBL_0), to understand deep in the ergodic phase and the MBL phase, respectively. In this section, we simply introduce both the GRV model and MBL_0, leaving the analytical results obtained to the appropriate chapters.

2.2.1 Gaussian Random Eigenvectors

Assuming that the eigenstates are gaussian random eigenvectors (GRV) is known to explain many of their properties deep in the ergodic phase [163, 170–172]. This occurs as the eigenstate amplitudes deep in the ergodic phase are uncorrelated, and are well described by random matrices.

Within the GRV model, for any given eigenstate $|n\rangle$, the sets of amplitudes of eigenstates $|n\rangle$, $\{A_{nI}\}$ across the set of FS sites, $\{|I\rangle\}$, are independent random variables. Likewise, for any given FS site $|I\rangle$, the set of $\{A_{nI}\}$ across the set of eigenstates, $\{|n\rangle\}$, are independent random variables. In both cases they are gaussian distributed, with

$$P_{A_{nI}}(x) = \frac{1}{\sqrt{2\pi\sigma^2_{A_{nI}}}} \exp\left[\frac{-x^2}{2\sigma^2_{A_{nI}}}\right], \tag{2.5}$$

with a mean of zero - as the set of amplitudes, $\{A_{nI}\}$, are equally likely to be positive or negative - and a variance $\sigma^2_{A_{nI}} = \frac{1}{N_H}$, which simply occurs as the average A^2_{nI}, $\langle A^2_{nI}\rangle = \frac{1}{N_H}$. This occurs as for all eigenstates $|n\rangle$, $\sum_I A^2_{nI} = 1$, and similarly for all FS sites $|I\rangle$, $\sum_n A^2_{nI} = 1$, which is merely a result of normalisation. This means

$\sum_n \langle A_{nI}^2 \rangle = \sum_I \langle A_{nI}^2 \rangle = 1$ and thus $N_H \langle A_{nI}^2 \rangle = 1$.

Throughout this thesis we shall use the GRV model to help us understand our numerical results deep in the ergodic phase.

2.2.2 Non-interacting problem

Sufficiently deep in the MBL phase, the interacting TFI model is known to be perturbatively connected to the non-interacting limit, $J_z = 0$ [59], which we refer to as MBL_0. Throughout this thesis we shall use MBL_0 to help us understand the interacting MBL phase. In this section, we shall discuss the eigenstates of the non-interacting problem.

When $J_z = 0$, the Hamiltonian (eq. 2.1)

$$\mathcal{H}_{TFI} = \sum_{l=1}^{L} \left(h_l \hat{\sigma}_l^z + \Gamma \hat{\sigma}_l^x \right), \tag{2.6}$$

is site separable, i.e.,

$$\mathcal{H}_{TFI} = \sum_{l=1}^{L} \hat{h}_l; \quad \hat{h}_l = \left(h_l \hat{\sigma}_l^z + \Gamma \hat{\sigma}_l^x \right). \tag{2.7}$$

The problem can be solved exactly by defining a rotated spin operator

$$\hat{\tilde{\sigma}}_l^z = \frac{h_l \hat{\sigma}_l^z + \Gamma \hat{\sigma}_l^x}{\sqrt{h_l^2 + \Gamma^2}}, \tag{2.8}$$

where the factor $\sqrt{h_1^2 + \Gamma^2}$ in the denominator ensures that $\hat{\tilde{\sigma}}_l^z$ is a bonafide spin operator, with $[\hat{\tilde{\sigma}}_l^z]^2 = 1$ using the usual spin commutation relations, and has eigenvalues of ± 1. The $|\tilde{\sigma}_l^z\rangle$ are the rotated spins, with $\hat{\tilde{\sigma}}_l^z |\tilde{\sigma}_l^z\rangle = \tilde{\sigma}_l^z |\tilde{\sigma}_l^z\rangle$, and $\tilde{\sigma}_l^z = \pm 1$, i.e. each rotated spin can point either up or down.

From eqs. 2.8, 2.7 clearly

$$\mathcal{H}_{TFI} = \sum_{l=1}^{L} \tilde{h}_l \hat{\tilde{\sigma}}_l^z : \quad \tilde{h}_l = \sqrt{h_1^2 + \Gamma^2}. \tag{2.9}$$

It follows from the site-separability of eq. 2.9 that the eigenvectors of $\mathcal{H}_{TFI}$, $\{|\Psi_n\rangle\}$, are simply product states of the $\tilde{\sigma}_\ell^z$ spins,

$$|\Psi_n\rangle = \bigotimes_{l=1}^{L} |\tilde{\sigma}_l^z\rangle = |\{\tilde{\sigma}_l^z\}\rangle\,, \tag{2.10}$$

where $\{\tilde{\sigma}_l^z\}$ is a specified configuration of the rotated spins for the different real-space sites l, with $|\Psi_n\rangle$ eigenenergy, $E_n = \sum_{l=1}^{L} \tilde{h}_l \tilde{\sigma}_l^z$.

Despite the wavefunction being site separable in real-space in MBL_0, as the FS remains fully connected, its behaviour on FS is non-trivial. We will therefore use the eigenstates discussed above to calculate the behaviour of various quantities in the non-interacting limit in the chapters that follow to help us understand the behaviour observed in our numerics in the MBL phase for $J_z \neq 0$.

2.3 Time scales in the dynamics

In the chapters that follow, we shall consider both eigenstate properties and dynamic properties of the TFI model from the FS perspective. In order to understand dynamical properties, in this section we briefly consider relevant time scales in the TFI model. Throughout this thesis we shall set $\hbar = 1$ meaning $t \sim \frac{1}{E}$.

Within the TFI model there are of course many different time scales to consider. In this section we consider the shortest and longest relevant time scales for finite sized systems, the time scale for spins to start to dephase, and the Heisenberg time, respectively.

As the initial spins in $|I\rangle$ are dephased by the $\Gamma\hat{\sigma}_l^x$ operator, then it follows that

the time scale dephasing occurs on is $\mathcal{O}(\frac{1}{\Gamma})$. Since $\Gamma = 1$ throughout this thesis, the typical time scale for spins to dephase is $\mathcal{O}(1)$.

On the other hand, the Heisenberg time t_H is the inverse of the mean-level spacing. The mean level spacing at energy ω is $[N_H D(\omega)]^{-1}$, with $D(\omega)$ the density of states/eigenvalues normalised to unity over ω. Reflecting the central limit theorem, $D(\omega)$ is known to be a Gaussian, [66, 173] with a vanishing mean for the disordered TFI model under consideration, and a variance $\mu_E^2 \propto L$ given exactly by [74] $\mu_E^2 = L\Big[\overline{\mathcal{J}}_l^2 + \frac{1}{3}(\delta\mathcal{J}_l)^2 + \frac{1}{3}W^2 + \Gamma^2\Big]$.

Since the Heisenberg time t_H is the inverse of the mean level spacing, and throughout this thesis we are shall be interested in band-centre $\omega = 0$ states (discussed further in chapter 3), $t_H = N_H D(0) = N_H/\sqrt{2\pi\mu_E^2}$ and hence

$$t_H \;=\; \frac{2^L}{\sqrt{2\pi L\Big[\overline{\mathcal{J}}_l^2 + \frac{1}{3}(\delta\mathcal{J}_l)^2 + \frac{1}{3}W^2 + \Gamma^2\Big]}}. \tag{2.11}$$

For all ED calculations, since $\{\mathcal{J}_l\}$ are uniformly distributed with $\mathcal{J}_l/\Gamma \in [0.8, 1.2]$, then $\overline{\mathcal{J}}_l/\Gamma = 1, \delta\mathcal{J}_l/\Gamma = 0.2$. Throughout this thesis, $\Gamma \equiv 1$. t_H obviously increases with L and decreases with disorder strength W. For $W = 1, 2$, and $L \in [8, 14]$, t_H ranges from ~ 20 to $\sim 10^3$, while for $W = 6, 7$ it correspondingly ranges from ~ 10 to ~ 400.

2.4 Numerical methods

All the numerical results in chapters 3-6 are calculated by exact diagonalisation (ED). In appendix A, we run step by step through the equations and numerical methods used to obtain our results. In this section, we shall simply summarise the key numerical methods used.

In chapters 3-4 we shall examine quantities related to the time evolution of

the wavefunction. In order to evolve a quantum system in time knowledge of all eigenstates in the spectrum is required (as explained in appendix A). To obtain our results for $L = 8 - 13$ we simply use a standard matrix diagonlisation algorithm in python [174] to determine all eigenstates of the system. By contrast, our numerical results for $L = 14$ are calculated using a Chebychev expansion method [175] to propagate the wavefunction in time.

On the other hand, chapters 5 and 6 examine properties of individual eigenstates typically around the band centre. In this case, our results for all system sizes $L = 8 - 14$ are obtained using a standard sparse matrix diagonalisation method known as the shift inverse method [176].

2.5 Overview of this thesis

At this point, it is helpful to give an overview of the work examined throughout the rest of this thesis.

In chapters 3 and 4 we shall discuss our work [144] on probability transport on the FS graph (figure 2.1). We shall consider initialising our system in a 'classical' spin configuration or single FS site (discussed in section 2.1). The FS graph can then be organised such that this site sits at the apex of the graph and all sites at a fixed Hamming distance from the initial FS site are arranged row-wise. Although the FS graph of a chain of L spins is an L-dimensional hypercube, this organisation of the FS graph gives rise to two natural axes along which probability transport can be defined, we refer to them as longitudinal and lateral transport.

Longitudinal transport quantifies how the probability flows down sites which are an increasing distance from the initial site. Lateral transport on the other hand measures how probability spreads across sites at the same Hamming distance from the initial site. i.e. on a given row in FS. In chapter 3 we shall examine longitudinal

transport while in chapter 4 we shall consider lateral transport.

In chapter 5 we shall then move away from considering dynamical properties to considering properties of the eigenstates themselves. In particular, we consider the IPR and related distributions alongside seeking to explain the ubiquitous (multi)fractality of eigenstates in the MBL phase.

Finally in chapter 6, we will introduce and consider several related new order parameters for the MBL transition. We will then discuss our scaling theory used to explain their behaviour on approach to the transition. Related distributions will then be discussed which provide further insight into the MBL phase.

The final chapter of the thesis will then summarise the key results obtained throughout the thesis and discuss possible areas for future research.

Chapter 3

Longitudinal probability transport

3.1 Introduction

The out-of-equilibrium dynamics of isolated quantum many-body systems can show a rich range of behaviours in the presence of disorder. For example, MBL is known to be a dynamical phase transition, meaning the time-evolution of systems in the ergodic phase and the MBL phase are very different, as briefly eluded to in chapter 1.

In contrast to the ergodic phase, systems in the MBL phase fail to thermalise under their own dynamics, and memory of the initial state survives locally for arbitrarily long times. As such behaviour falls outside the paradigm of conventional statistical mechanics, the dynamics of the MBL phase is naturally of fundamental interest. At the same time, even within the ergodic phase but at disorders proceeding the MBL transition the dynamics is known to be anomalously slow. The out-of-equilibrium dynamics of disordered quantum systems across a range of disorders straddling the MBL transition is therefore an interesting question.

Arguably, the most fundamental question one can ask is: given an initial out of equilibrium state how does this state spread out on the FS graph. Clearly to understand this, we need to understand the time evolution of the probabilities of

being on the different FS sites on the graph.

The question we therefore seek to answer in the next two chapters is given that we have initialised our system on a single (arbitrary) FS site $|I\rangle$ - an initial out of equilibrium state - how does the probability density of the state evolve on the FS graph?

The basic underlying quantities that are considered to answer this are the probabilities

$$P_{IJ}(t) = |G_{IJ}(t)|^2, \tag{3.1}$$

where as usual $G_{IJ}(t) = \langle J|\exp[-i\mathcal{H}t]|I\rangle$ is the propagator between FS sites $|I\rangle$ and $|J\rangle$. It therefore follows that

$$P_{IJ}(t) = |\langle J|\Psi(t)\rangle|^2 = |\langle J|\exp[-i\mathcal{H}t]|I\rangle|^2, \tag{3.2}$$

with $|\Psi(t)\rangle$ the time dependent wavefunction following initiation on $|I\rangle$ at $t = 0$. Physically $P_{IJ}(t)$ gives the probability that the system is found on $|J\rangle$ at time t given its initiation on $|I\rangle$ at $t = 0$ (where $P_{II}(t)$ is the commonly studied return probability [83, 148–151]).

In the TFI model, the set of amplitudes, $\{A_{nI}\}$, of $\{|I\rangle\}$ on eigenstates $\{|n\rangle\}$, $A_{nI} = \langle n|I\rangle$, can be taken to be real. From eq. 3.2 it is easy to show (by simply inserting several unit operators) that $P_{IJ}(t)$ can be expressed in terms of the eigenstate amplitudes, with

$$P_{IJ}(t) = \sum_{n,m} \exp\left[-i(E_n - E_m)t\right]\ A_{nI}A_{nJ}A_{mI}A_{mJ}, \tag{3.3}$$

where E_m and E_n are the energies of the eigenstates m and n.

Probability is of course conserved for all times (i.e. there is no loss of probability

from our system) via $\sum_J P_{IJ}(t) = 1$ for all initial sites I. For any given I, $P_{IJ}(t)$ can be regarded as a time dependent distribution over all FS sites J of a conserved 'mass' $M_I = \sum_J P_{IJ}(t) = 1$. The natural way to probe such a distribution is via relevant moments, which will be discussed later in this chapter.

At $t = 0$, $P_{IJ}(t = 0) = \delta_{IJ}$, meaning the initial state $|I\rangle$ is site localised on the FS graph (discussed in chapter 2), or equivalently it is Anderson localised in FS. We then simply seek to understand how the set of $\{P_{IJ}(t)\}$ evolve with time.

It is natural to organise our FS graph, such that our initial site $|I\rangle$ is at the apex (0th row) of the graph. As discussed in the previous chapter this means that in each row r all N_r sites are a fixed Hamming distance also equal to r away from the initial FS site. This organisation gives rise to two natural 'axes' along which probability transport can be defined; we shall refer to these as longitudinal and lateral transport.

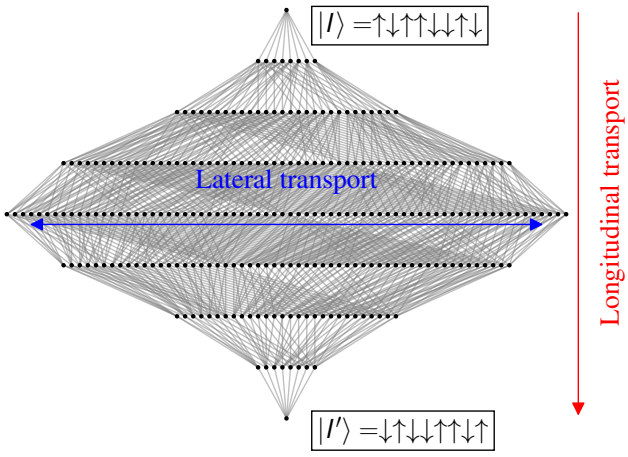


Figure 3.1: Fock space graph of the disordered TFI model in the σ_l^z basis, $L = 8$. The graph has $L + 1$ rows with the number of FS sites in row r, $N_r = \binom{L}{r}$. Any FS site $|J\rangle$ in row r is a Hamming distance r away from our initial site, $|I\rangle$. The red and blue arrows indicate the 'direction of probability flow' examined by longitudinal and lateral transport respectively.

Longitudinal transport quantifies how the probability flows down sites which are

an increasing Hamming distance from the initial site (we will further elaborate on this in the next section) . By contrast, lateral transport measures how probability spreads across sites at the same Hamming distance from the initial site, i.e. on the same row in the FS graph. In this chapter, we will discuss longitudinal transport while in the next chapter we shall discuss lateral transport.

What will emerge from the next two chapters is the rich phenomenology of probability transport in the TFI model. We shall show that at short times, the system is agnostic to which phase it is in. The $\{P_{IJ}(t)\}$ on a given row r are the same, but differ between rows. In both phases, this is followed by an intermediate time regime, where the dynamics are found to be strongly inhomogeneous, i.e. there are huge variations in the $\{P_{IJ}(t)\}$ both on a given row and on different rows. In the ergodic phase, this gives rise to homogeneity at long times, while in the MBL phase this inhomogeneity persists for all times.

In all our numerics in the next two chapter, time is shown in units of Γ^{-1} (i.e. $\Gamma = 1$). As a reminder, as is usual practise, $\hbar$ is set to one throughout this thesis, meaning the time, t, and the energy, E, are simply related by $t \equiv \frac{1}{E}$.

3.2 Longitudinal transport

3.2.1 Diagnosing Longitudinal transport

In order to understand the spread of probability down the rows of the FS graph, we define the time-dependent average probability of being on any of the N_r sites in row r, $P_I(r;t)$, which is given by

$$P_I(r;t) = \sum_{J;r_{IJ}=r} P_{IJ}(t), \tag{3.4}$$

where the J-sum is over all $N_r = \binom{N}{r}$ FS sites on a given row r of the graph. From $P_I(r;t)$ we can define its sample average over initial FS sites I,

$$P(r;t) = \frac{1}{N_H} \sum_{I=1}^{N_H} P_I(r;t). \tag{3.5}$$

This can be further averaged over disorder realisations to give

$$\overline{P}(r;t) = \left\langle \frac{1}{N_H} \sum_{I=1}^{N_H} P_I(r;t) \right\rangle_d, \tag{3.6}$$

which is the quantity we shall focus on in this chapter. An average over disorder realisations will be denoted, according to convenience, either by an overbar (e.g. $\overline{P}(r;t)$), or by angle brackets ($\langle ... \rangle_d$).

The first moments of $P_I(r;t)$, $P(r;t)$ and $\overline{P}(r;t)$,

$$r_I(t) = \sum_{r=0}^{L} P_I(r;t)\ r, \tag{3.7}$$

$$r(t) = \sum_{r=0}^{L} P(r;t)\ r, \tag{3.8}$$

and

$$\overline{r}(t) = \sum_{r=0}^{L} \overline{P}(r;t)\ r, \tag{3.9}$$

probe how the average Hamming distance varies with time for: a given initial FS site, a given disorder realisation averaged over all N_H initial FS sites $|I\rangle$ and the average over disorder realisations and FS sites respectively.

The behaviour of $r_I(t)$ will of course depend on the initial FS site $|I\rangle$ chosen and/or the disorder realisation, meaning its value will fluctuate from site to site, and realisation to realisation. We shall probe how these fluctuations vary with time in both the ergodic phase and the MBL phase at the end of chapter 4.

In this chapter, we are not interested in examining these fluctuations, but instead want to understand how systems in the ergodic phase and the MBL phase typically behave, at different times t. The structure of the FS graph does not depend on the FS site $|I\rangle$ at the apex of the graph, i.e. there are no 'special sites' on the graph. It is therefore natural to average over both the initial sites I and disorder realisations when trying to understand the typical behaviour of the dynamics in both phases. This means we will focus on the disorder-averaged quantity, $\overline{r}(t)$.

We can also define higher order moments of $\overline{P}(r;t)$. For example the second moment,

$$\overline{\delta r^2}(t) = \sum_{r=0}^{L} r^2 \ \overline{P}(r;t) - \left(\sum_{r=0}^{L} r \ \overline{P}(r;t)\right)^2 . \tag{3.10}$$

This quantity probes fluctuations of $\overline{P}(r;t)$ from its average value.

We shall examine the behaviour of $\overline{r}(t)$, $\overline{P}(r;t)$ and $\overline{\delta r^2}(t)$ both as a function of time and the disorder strength, W, throughout this chapter.

First, however, we turn to a relationship we have uncovered between $r(t)$ and the autocorrelation function (defined in the next section) for any disorder realisation. This provides a direct connection between real-space and Fock-space perspectives (discussed in chapter 2), alongside providing useful insight into the dynamics.

3.2.2 Connecting to the spin autocorrelation function

The spin autocorrelator is defined by

$$C(t) = \frac{1}{L}\sum_{l=1}^{L} C_{ll}(t), \quad C_{ll}(t) = \frac{1}{N_H} Tr(\hat{\sigma}_l^z(t)\hat{\sigma}_l^z), \tag{3.11}$$

with $C_{ll}(t)$ the local real-space autocorrelator. Physically, the spin autocorrelator measures the extent to which a spin system retains memory of its initial configuration as a function of time. Its long-time value is a standard order parameter used to detect

the MBL transition in real-space [70, 110, 111]. Within the MBL phase, the system retains memory of its initial configuration for all times, meaning the long-time value of $C(t) > 0$. By contrast, in the ergodic phase, as the system thermalise under its own dynamics, no memory of the initial state survives for long times, and therefore $C(t) = 0$.

The trace, Tr, in eq. 3.11, can be over FS sites I, i.e. $C_{ll}(t) = N_H^{-1} \sum_I C_{ll}^{[I]}(t)$, with

$$C_{ll}^{[I]}(t) = \langle I|\hat{\sigma}_l^z(t)\hat{\sigma}_l^z|I\rangle\,, \tag{3.12}$$

where $\hat{\sigma}_l^z$ is the usual spin z operator and $\hat{\sigma}_l^z(t) = \exp[i\mathcal{H}t]\hat{\sigma}_l^z \exp[-i\mathcal{H}t]$. It can be equivalently taken over all eigenstates n, where $C_{ll}(t) = N_H^{-1} \sum_I C_{ll}^{[n]}(t)$, with $C_{ll}^{[n]}(t) = \langle n|\hat{\sigma}_l^z(t)\hat{\sigma}_l^z|n\rangle$, in this case.

In order to derive the relationship between $C(t)$ and $r(t)$, we can rewrite eq. 3.12 by simply inserting three unit operators to give

$$C_{ll}^{[I]}(t) = S_{l,I} \sum_J S_{l,J}\, P_{IJ}, \tag{3.13}$$

where $S_{l,I} = \langle I|\hat{\sigma}_l^z|I\rangle$. It thus follows that

$$C^{[I]}(t) = \frac{1}{L}\sum_{l=1}^{L} C_{ll}^{[I]}(t) = \sum_J P_{IJ}(t)\, \frac{1}{L}\left(\sum_l S_{l,I}S_{l,J}\right). \tag{3.14}$$

For two FS sites I and J separated by a Hamming distance r_{IJ}, $L - r_{IJ}$ spins have $S_{l,I} = S_{l,J}$ and r_{IJ} spins have $S_{l,I} = -S_{l,J}$. It thus follows that

$$\frac{1}{L}\left(\sum_l S_{l,I}S_{l,J}\right) = 1 - \frac{2r_{IJ}}{L}. \tag{3.15}$$

and hence from eq. 3.14 that

$$C^{[I]}(t) = 1 - \frac{2r_I(t)}{L}. \tag{3.16}$$

It thus follows trivially that

$$C(t) = 1 - \frac{2r(t)}{L}, \tag{3.17}$$

and

$$\overline{C}(t) = 1 - \frac{2\overline{r}(t)}{L}. \tag{3.18}$$

These equations directly relate the real-space autocorrelator to the first moment of the FS probabilities $\{P_{IJ}(t)\}$.

The derivation above relied on the definition of the spin-autocorrelation function as a trace over all FS sites I (eqs. 3.11 and 3.12) and the relationship between the sum $\frac{1}{L}\left(\sum_l S_{l,I}S_{l,J}\right)$ and the Hamming distance r_{IJ} given by eq. 3.15, neither of which depend on the particular spin model considered. This means the relationships given by eqs. 3.16, 3.17 and 3.18 are not confined to the TFI model considered in this thesis. But apply equally to the XXZ model, and by Jordon Wigner transformation [77] to a related quantity for spinless fermion models. These other models were briefly discussed in chapter 1.

A striking feature of the relationship given by eq. 3.16, is that at times t when $C^{[I]}(t)$ departs by merely a non-vanishing amount from its $t = 0$ value of 1, the first moment $r_I(t) \propto L$, i.e. extensive in system size. Intuitively, we would expect the time scale t that $C(t)$ begins to 'decay' to be determined by the hopping scale Γ which dephases the initially synchronised spins and as such to be $\Gamma t \sim \mathcal{O}(1)$. This means $\overline{r}_I(t) \propto L$ on finite $\mathcal{O}(1)$ timescales. The resultant extensivity of $r_I(t)$ means that an excitation initially Anderson localised on the single FS site I, spreads significantly throughout the FS on the shortest timescales $\Gamma t \sim \mathcal{O}(1)$ - and would

appear to do so regardless of whether the system is ergodic or MBL. This is in stark contrast to spurious claims made in [149] which suggested that the time taken to explore the FS is exponentially large in system size.

We shall now move on to discuss our analytical results obtained for the short-time dynamics which indeed confirm that $r(t)$ becomes extensive when Γt is $\mathcal{O}(1)$.

3.2.3 Short-time universal behaviour

In order to understand the short time behaviour of $r(t)$, we need to consider the behaviour of $P_{IJ}(t) = |G_{IJ}(t)|^2$ at short times. To this end, we shall examine the behaviour of the propagator,

$$G_{IJ}(t) = \langle J|\exp[-i\mathcal{H}t]|I\rangle = \sum_{n=0}^{\infty} \frac{(-i)^n}{n!} t^n \langle J|\mathcal{H}^n|I\rangle \,. \tag{3.19}$$

As discussed in chapter 2, we can separate $\mathcal{H} = \mathcal{H}_0 + \mathcal{H}_1$. $\mathcal{H}_0 = \sum_k \mathcal{E}_K |K\rangle \langle K|$, simply determines the FS site energies, meaning it is a diagonal term in $\mathcal{H}$. By contrast, $\mathcal{H}_1$ is the hopping term connecting FS sites which differ by a single spin flip (courtesy of one of the $\{\hat{\sigma}_l^x\}$ operators), or equivalently are in a neighbouring row in FS. With K_m denoting any FS site on row m, $\mathcal{H}|K_m\rangle$ clearly connects to rows $m \pm 1$ (from the $\mathcal{H}_1$ term) and to m (from the $\mathcal{H}_0$ term).

It thus follows that each time the operator $\mathcal{H}$ is applied, $|K_m\rangle$ is able to connect to rows successively further down the FS graph. Let us consider

$$\mathcal{H}^n |K_m\rangle \equiv (\mathcal{H}_0 + \mathcal{H}_1)^n |K_m\rangle \,. \tag{3.20}$$

In this case, K_m is clearly connected to all rows from the m row to the $m \pm n$ row. The $m \pm n$ row is clearly solely connected by $\mathcal{H}_1^n |K_m\rangle = \left(\sum_{l=1}^N \hat{\sigma}_l^z\right)^n |K_m\rangle$ term. The specific terms in the sum that connects to the $m \pm n$ row is when n different

$\hat{\sigma}_l^x$ operators act on $|K_m\rangle$, i.e. n spins on different real space sites l are flipped successively.

As a concrete example, consider the randomly chosen FS site for a system of 8 spins, $|I\rangle =\uparrow\downarrow\uparrow\uparrow\downarrow\uparrow\downarrow\downarrow$, with the spins indexed left to right with indices $1-8$. A site $|J\rangle =\downarrow\uparrow\downarrow\uparrow\downarrow\uparrow\downarrow\downarrow$ sits at a Hamming distance $r=3$ away from site $|I\rangle$ and is connected to $|I\rangle$ by three spin flips on real space sites $1,2,3$. From the above discussion the smallest power of H that connects $|I\rangle$ and $|J\rangle$ is $\mathcal{H}^3$ and specifically the $\mathcal{H}_1^3$ term. In the $\mathcal{H}_1^3 = \left(\sum_{l=1}^N \hat{\sigma}_l^x\right)^3$ term, clearly the only terms to connect I and J are terms of the form $\Gamma^3\hat{\sigma}_1^x\hat{\sigma}_2^x\hat{\sigma}_3^x$, where the $\hat{\sigma}_1^x, \hat{\sigma}_2^x, \hat{\sigma}_3^x$ terms can be in any order, i.e. the spins can be flipped in any order. This gives rise to 3! identical contributions to $\mathcal{H}^3|I\rangle$ enabling hopping between FS sites $|I\rangle$ and $|J\rangle$, pictorially these different terms form different paths on the FS from $|I\rangle$ to $|J\rangle$.

Let us now move on to consider any given site J which is a Hamming distance of r from our initial site I, J_r. From the above discussion it is rather obvious that $\langle J_r|\mathcal{H}^n|I\rangle$ vanishes for all $n<r$. The smallest order t term is thus the $n=r$ term, where $\langle J_r|\mathcal{H}^n|I\rangle = \langle J_r|\mathcal{H}_1^n|I\rangle$. It follows that

$$G_{IJ_r}(t) = \frac{(-i)^r}{r!}t^r\,\langle J_r|\mathcal{H}_1^r|I\rangle + \mathcal{O}(t^{r+1}), \tag{3.21}$$

with the leading order term dominating for sufficiently small t.

The leading order term only involves $H_1^r = \left(\sum_{l=1}^N \Gamma\hat{\sigma}_l^x\right)^r$. Specifically, the non-zero contributions to

$$\langle J_r|\mathcal{H}_1^r|I\rangle = \left\langle J_r\left|\left(\sum_{l=1}^N \Gamma\hat{\sigma}_l^x\right)^r\right|I\right\rangle, \tag{3.22}$$

comes from the terms in the above expansion that involve successive application of the r different $\hat{\sigma}_l^x$ operators, for the sites l that $S_{l,I} = -S_{l,J_r}$. Pictorially, we can

think of any given order of flipping the r spins as forming a path from the FS site $|I\rangle$ and $|J_r\rangle$, connected by the $\mathcal{H}_1^r$ operator.

The r spins in $|I\rangle$ that differ from $|J_r\rangle$ can be flipped in any order, meaning there are $r!$ distinct paths connecting I and J_r by $\mathcal{H}_1^r$. It therefore follows that there are $r!$ identical contributions to $\langle J|\mathcal{H}_1^r|I\rangle$, which from eq. 3.22 clearly contribute Γ^r. These $r!$ different paths cancel the $r!$ in the denominator in eq. 3.21, meaning $G_{IJ_r}(t) \sim (-i)^r(\Gamma t)^r$ and therefore

$$P_{IJ_r}(t) \sim (\Gamma t)^{2r}. \tag{3.23}$$

This equation holds for all r, and for all FS sites on row r. This means the distribution of probabilities along any row r is homogeneous on the timescales on which eq. 3.23 holds. So far we have yet to prescribe a timescale over which this behaviour holds, this shall be discussed shortly. First, however, we shall discuss several points about eq. 3.23 itself.

Firstly, since eq. 3.23 is solely generated by the disorder independent hopping it is independent of the disorder strength, W. Physically, at short times all spins on the set of real space sites l move from being aligned along the z axis to some tilted axis in the xz plane, which is independent of the real space site l. The spins therefore remain coherent at this time scale.

Although $P_{IJ_r}(t) \sim (\Gamma t)^{2r}$ and decreases exponentially with increasing r, the number of sites on row r is $N_r = \binom{N}{r}$, which for $r < \frac{L}{2}$ grows exponentially with increasing r. It therefore follows that when calculating the first moment $r_I(t) = \sum_J P_{IJ}(t)\ r_{IJ} = \sum_{r=0}^{L} N_r\ P_{IJr}(t)\ r$, we cannot neglect contributions of sites in any row r.

The above calculation to obtain the short-time $P_{IJ_r}(t)$ relied heavily on the structure of the FS graph. In particular, the fact that there are $r!$ identical contributions

to $\langle J_r|\mathcal{H}_1^r|I\rangle$ in eq. 3.22 is due to the loops in the graph, or equivalently multiple paths between the two FS sites, I and J_r, consisting of flipping the r spins in different orders. If one instead had chosen to study a Bethe lattice [177][1] for which there is a single path between the root site I and a given J_r, $P_{IJ_r}(t) \sim \frac{1}{r!}(\Gamma t)^{2r}$, meaning only those $P_{IJ_r}(t)$ at small r would contribute significantly to $r_I(t)$ at short times.

Currently, eq. 3.23 does not conserve probability. This can however be readily resolved by writing $P_{IJ_r}(t) = g(r;t)(\Gamma t)^{2r}$. $g(r;t)$ must satisfy several criteria. For all r, $g(r;t=0) = 1$, as $P_{IJ_r}(t=0) = \delta_{IJ_r}$. Additionally, $g(r;t) > 0$ for all time t, as clearly the probabilities $P_{IJ_r}(t) \geq 0$. Finally, the overall probability must be conserved, meaning $\sum_J P_{IJ}(t) = 1$. The solution to these criteria is $g(r;t) = [1-(\Gamma t)^2]^{L-r}$. It is rather obvious that $g(r;t) > 0$ provided $\Gamma t < 1$, which sets the upper bound for the time window the calculation holds. Crucially, the maximum timescale the short-time equations hold are for small, but importantly $\mathcal{O}(1)$ times.

The essential results for the short-t behaviour of $P_{IJ_r}(t)$, is therefore

$$P_{IJ_r}(t) = (\Gamma t)^{2r}\left[1-(\Gamma t)^2\right]^{L-r}, \tag{3.24}$$

which is independent of the disorder strength, W, or the initial site, I. This means $r_I(t) = r(t) = \overline{r}(t)$ (eqs. 3.7, 3.8, 3.9, pg. 35). It therefore follows from eq. 3.24 that

$$\overline{r}(t) = r_I(t) = \sum_{r=0}^{L}\binom{N}{r} r\, P_{IJ_r}(t) = L(\Gamma t)^2, \tag{3.25}$$

independent of the disorder strength W.

The fact that $\overline{r}(t) \propto L$ is extensive for finite Γt, means of course it is $\frac{\overline{r}(t)}{L}$ which remains finite in the thermodynamic limit, and is therefore the relevant quantity to study. It thus follows that the relevant fluctuations are $\sigma^2(t) = \frac{\overline{\delta r^2}(t)}{L^2}$.

[1] A commonly used graph in Anderson localisation. A Bethe lattice is an infinite tree with nodes of connectivity K and crucially no loops. A corresponding finite tree is called a Cayley tree.

At short times,

$$\sigma^2(t) = \frac{\overline{\delta r^2}(t)}{L^2} : \quad \overline{\delta r^2}(t) = \sum_{r=0}^{L} r^2 \overline{P}(r;t) - \overline{r}(t)^2, \tag{3.26}$$

can be calculated. From eq. 3.24 it follows that

$$\sum_{r=0}^{L} r^2 \, \overline{P}(r;t) = \sum_{r=0}^{L} r^2 \binom{N}{r} P_{IJ_r}(t) = \sum_{r=0}^{L} r^2 \binom{N}{r} (\Gamma t)^{2r} \left[1 - (\Gamma t)^{2r}\right]^{L-r}. \tag{3.27}$$

This means

$$\sigma^2(t) = \frac{(\Gamma t)^2[1 - (\Gamma t)^2]}{L}. \tag{3.28}$$

It is therefore proportional to $\frac{1}{L}$ and vanishes in the thermodynamic limit $L \to \infty$, meaning $\frac{r(t)}{L}$ will be δ-distributed about its mean in that limit.

Figure 3.2 shows our ED results for $\frac{\overline{r}(t)}{L}$, for a range of disorder strengths W, in both the ergodic and the MBL phase, alongside our short-time exact result (eq. 3.25).

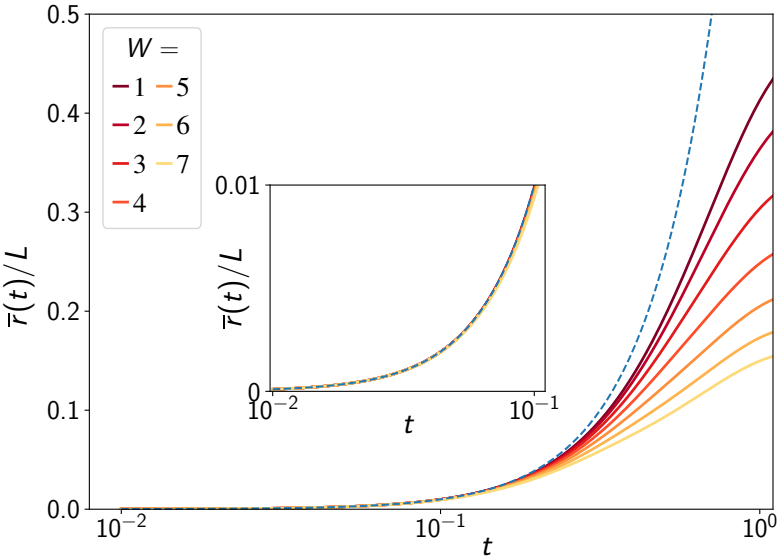


Figure 3.2: ED results for $L = 13$ $\frac{\overline{r}(t)}{L}$ *vs* t, shown over the indicated range of disorder strengths W. For $t \lesssim 0.1$, the W independent behaviour of eq. 3.25 (dashed line) is seen to arise. Identical behaviour is seen for other L values.

Figure 3.2 shows that for $\Gamma t \lesssim 0.1$, $\frac{\overline{r}(t)}{L}$ is independent of the disorder strength, W, as predicted from our short-time analytical results discussed above. In fact, eq. 3.25 (dashed line) well captures our numerical results for all W values, for $\Gamma t \lesssim 0.1$, with the time window that our numerical results for $\frac{\overline{r}(t)}{L}$ are well captured by eq. 3.25 slightly increasing with decreasing W.

A $\Gamma t \lesssim 0.1$, is clearly a small $\mathcal{O}(1)$ time. Figure 3.2 shows that for these short times, $\frac{\overline{r}(t)}{L}$ is $\mathcal{O}(1)$, meaning $\overline{r}(t) \propto L$, i.e. it is extensive in system size, independent of the disorder strength W, and thus whether the system is in the ergodic phase or the MBL phase.

Finally, a comment should be made that our short time results recover the well known behaviour for the return probability [83, 148, 149], $P_{II}(t) = \exp[-L(\Gamma t)^2]$ for $\Gamma t << 1$. It, therefore, follows that the return probability is exponentially suppressed in system size for all finite Γt and all W. Despite $P_{II}(t)$ being a well studied quantity [83, 148–151], it only really offers a limited diagnostic of probability transport, as independent of whether the system is ultimately ergodic or MBL, it is exponentially suppressed in system size. In the thermodynamic limit, in both phases there is a vanishing probability of returning to the initial site $|I\rangle$. What is therefore more relevant in MBL is how the probabilities are spread across all the FS sites J on the graph, and how this varies as a function of time. A much richer picture is therefore revealed when examining the full $\overline{P}(r;t)$, and its relevant moments, something we shall now turn our attention to.

3.2.4 Broad overview: $\overline{P}(r;t)$

To give an overview of some of the results discussed in later parts of this chapter, we shall now move on to discuss a quantity directly related to $\overline{P}(r;t)$ (eq. 3.6, pg. 35).

From the results in the previous section, we know $\overline{r}(t) \propto L$ (eq. 3.9, pg. 35), and therefore the correct quantity to examine in the thermodynamic limit is $\frac{\overline{r}(t)}{L}$. It thus follows that when comparing different system sizes L, we should examine the normalised probability distribution $\tilde{P}_y(y;t)$, which gives the probability of being at $y = \frac{r}{L}$, where

$$\tilde{P}_y(y;t) = \int dr\ \delta\left(y - \frac{r}{L}\right)\ \overline{P}(r;t). \tag{3.29}$$

In this case, for all system sizes L, $0 \leq y \leq 1$, with $y = \frac{1}{2}$ being the middle of FS graph.

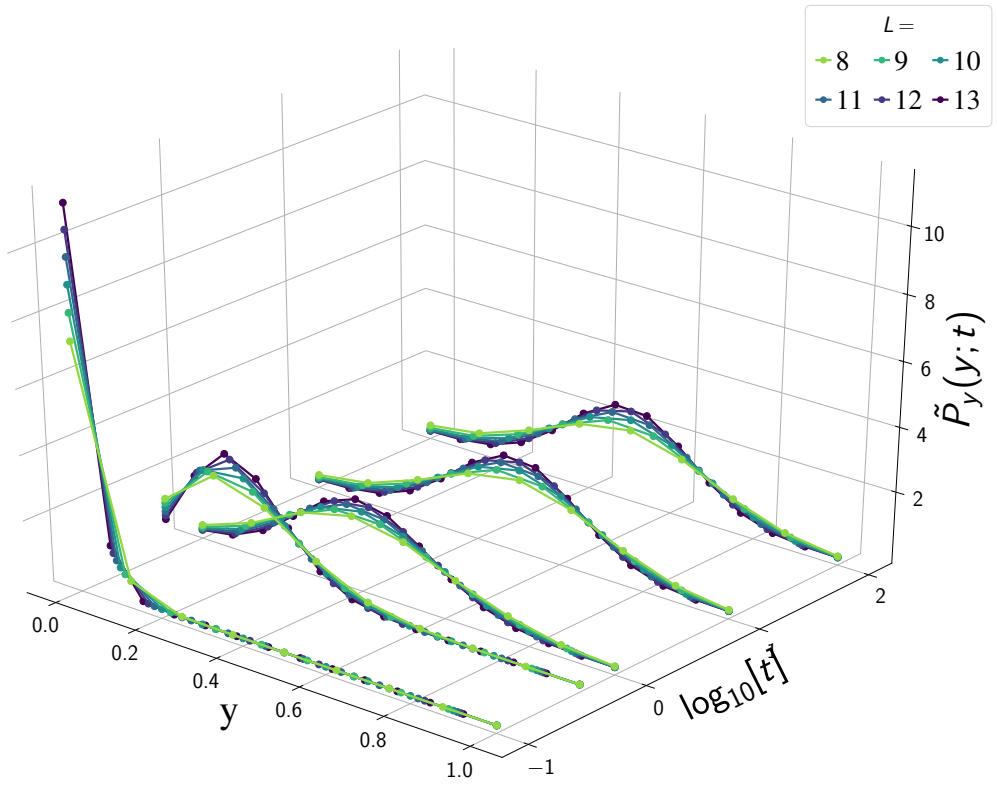


Figure 3.3: t-dependence of $\tilde{P}_y(y;t)$ for $W = 1$, for system sizes $L = 8 - 13$.

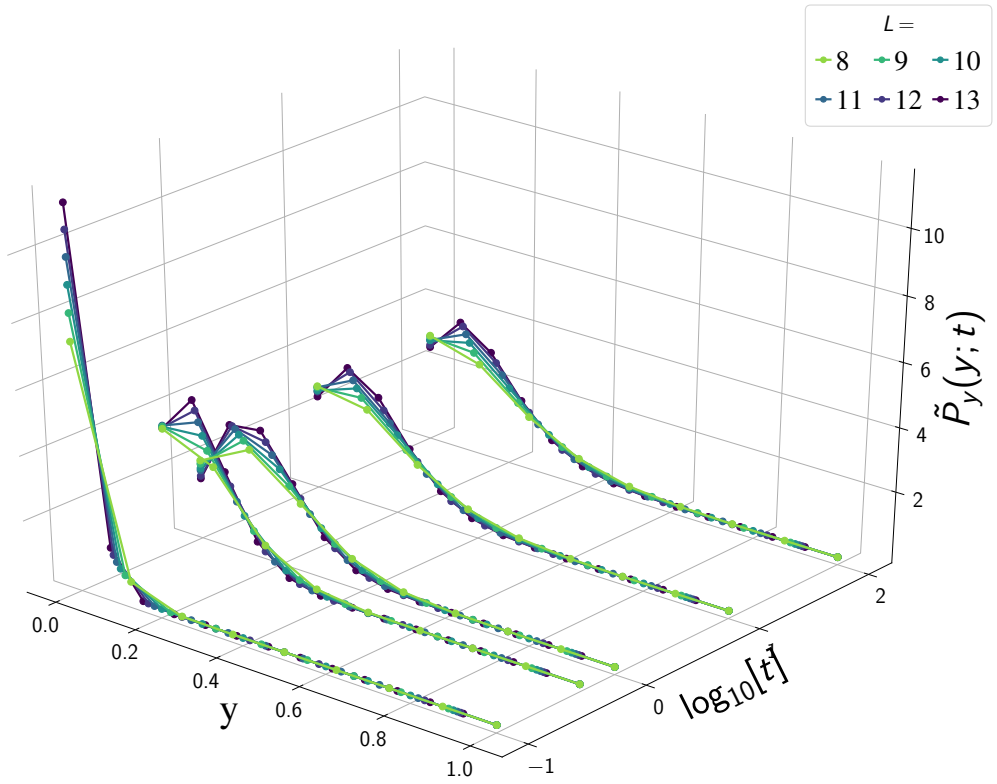


Figure 3.4: t-dependence of $\tilde{P}_y(y;t)$ for $W = 7$, for system sizes $L = 8 - 13$.

Figures 3.3 and 3.4 show how $\tilde{P}_y(y;t)$ varies with time deep in the ergodic phase ($W = 1$) and the MBL phase ($W = 7$) respectively. On the other hand, figure 3.5 shows the $L = 14$, $\overline{P}(r;t)$, for $W = 1.50$ in the ergodic phase (left column), and $W = 7$ in the MBL phase (right column). The top panels show $\overline{P}(r;t)$ as a colour map in the (r,t)-plane, while the bottom panel shows $\overline{P}(r;t)$ as a function of $\frac{r}{L}$ for different times indicated.

Figures 3.3 and 3.4 show that deep in either phase, $\tilde{P}_y(y;t)$ reaches its long-time value on finite $\mathcal{O}(1)$ time scales. This is also seen in the bottom panels of figure 3.5 where for both W values $\overline{P}(r;t)$ varies very little from $t = 10^{0.5} - 10^2$. The top panels of figure 3.5 show that $\overline{P}(r;t)$ spreads out rapidly with time in both phases.

Additionally, figures 3.3 and 3.4 show that the long-time $\tilde{P}_y(y;t)$ is centred on very different $y = \frac{r}{L}$ values in the ergodic and the MBL phases, $y \simeq 0.5$ and $y \simeq 0.1$ respectively. Physically, this reflects that $\frac{\overline{r}(t)}{L} = \frac{1}{2}$ deep in the ergodic phase, and

$\frac{\bar{r}(t)}{L} << \frac{1}{2}$, but $\mathcal{O}(1)$, deep in the MBL phase. Given the relationship $\overline{C}(t) = 1 - \frac{2\bar{r}(t)}{L}$ (derived on pgs. 36-38), this reflects that $\overline{C}(t) = 0$ deep in the ergodic phase, which means all memory of the initial alignment of spins is lost at long times. By contrast, $\overline{C}(t) > 0$ in the MBL phase, reflecting persistent memory of the initial condition at long-time. We shall discuss both $\frac{\bar{r}(t)}{L}$ and $\overline{C}(t)$ further in the coming sections.

Finally, figures 3.3 and 3.4 show that $\tilde{P}_y(y;t)$ narrows with increasing L in both phases. This shall be further examined by studying $\sigma^2(t)$ towards the end of this chapter.

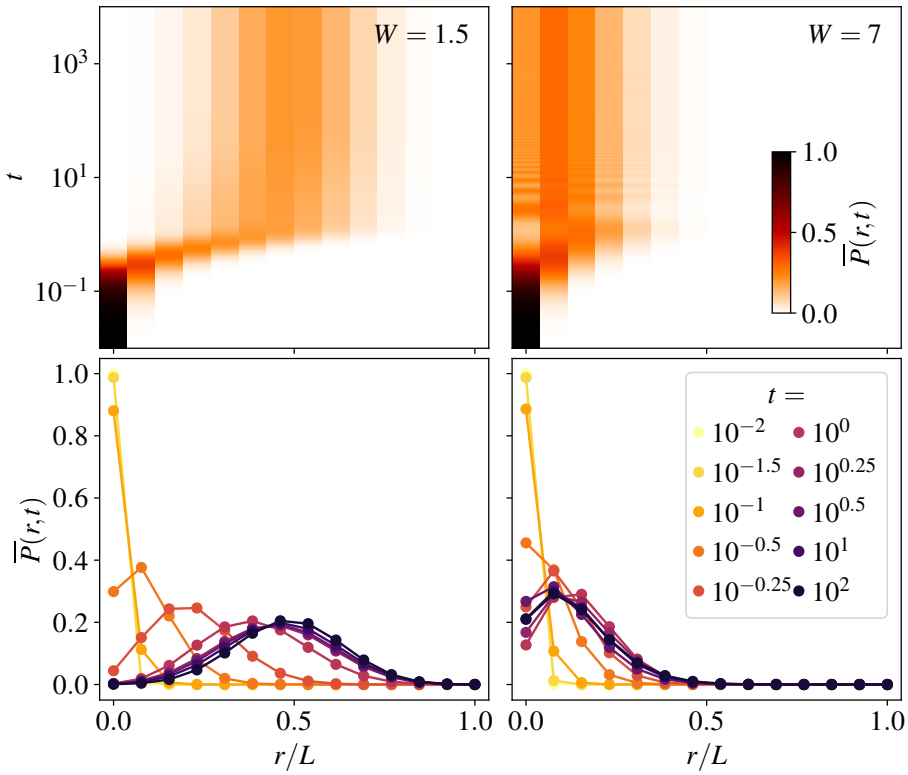


Figure 3.5: t-dependent of $\overline{P}(r;t)$ for $W = 1.5$, ergodic phase (left column) and $\overline{P}(r;t)$ for $W = 7$, MBL phase (right column). The top panels show $\overline{P}(r;t)$ as a colour map in the (r,t)-plane. Bottom plot shows $\overline{P}(r;t)$ as a function of $\frac{r}{L}$ for different times indicated. Data shown for $L = 14$.

3.2.5 Relevant bound for $\overline{C}(t)$ and $\bar{r}(t)$

Before moving on to discuss the behaviour of $\overline{C}(t)$ and $\bar{r}(t)$ in detail we shall first briefly discuss the relevant bounds on their values, remembering that the two are

simply related by $C(t) = 1 - \frac{2r(t)}{L}$ (derived on pgs. 36-38).

Since $r_I(t) = \sum_{r=0}^{L} P_{IJ}(t)\, r_{IJ}$ with $r_{IJ} \leq L$, the rather trivial bound is $r_I(t) \leq L$ and thus $r(t) \leq L$, meaning $C(t) \geq -1$. A far more useful bound is obtained in the $t \to \infty$ limit. As a reminder from pgs. 36-38, $C_{ll}(t)$ can be written as an eigenstate trace, e.g. $C_{ll}^{[n]}(t) = N_H^{-1} \sum_{n=1}^{N_H} \langle n|\hat{\sigma}_l^z(t)\hat{\sigma}_l^z|n\rangle$. In infinite-time limit this reduces to $C_{ll}(\infty) = N_H^{-1} \sum_n |\, \langle n|\hat{\sigma}_l^z|n\rangle\, |^2 \geq 0$. It thus follows that $C(\infty) \geq 0$ and thus $\overline{C}(\infty) \geq 0$. Given the relationship $\overline{C}(t) = 1 - \frac{2\overline{r}(t)}{L}$ (derived on pgs. 36-38) this means $\overline{r}(\infty) \leq \frac{L}{2}$.

Sufficiently deep in an ergodic phase, with essentially all many-body states delocalised and no remnant memory of the initial condition one expects $C(\infty)$ to vanish, which from $\overline{C}(t) = 1 - \frac{2\overline{r}(t)}{L}$ (derived on pgs. 36-38) means $r(\infty) = \frac{L}{2}$, the mid point of the FS graph. By contrast, in the MBL phase, as the system retains memory of its initial spin configuration for all times, $C(\infty) > 0$, which from $\overline{C}(t) = 1 - \frac{2\overline{r}(t)}{L}$, means $r(\infty) < \frac{L}{2}$.

3.2.6 Energy resolving $\overline{C}(t)$ and $\overline{r}(t)$

The many-body density of states,

$$D(\omega) = N_H^{-1} \sum_n \delta(\omega - E_n), \tag{3.30}$$

is known to have a Gaussian distribution [173] with a standard deviation $\sigma_E \propto \sqrt{L}$. This is simply a result of the fact that the eigenstate energies $\{E_n\}$ are given by

$$E_n = \sum_{l=1}^{L} \left\langle n \,\middle|\, h_l \hat{\sigma}_l^z + \frac{1}{2}\left(J_l \hat{\sigma}_l^z \hat{\sigma}_{l+1}^z + J_{l-1}\hat{\sigma}_{l-1}^z \hat{\sigma}_l^z\right) + \Gamma \hat{\sigma}_l^x \,\middle|\, n \right\rangle, \tag{3.31}$$

with $h_l \in [-W, W]$, and $J_l \in [0.8, 1.2]$. From eq. 3.31, E_n is clearly a sum of L independent random variables, all with a finite variance. In the thermodynamic

limit, $L \to \infty$, as a result of Central Limit Theorem [178][2], $D(\omega)$ is clearly Gaussian distributed.

States at different energies ω in the band have different propensities for localisation [78–81]. It is well known that states in the tails of the Gaussian distribution, i.e. those at very large or small ω values, are the first to localise. By contrast, the band centre ($\omega = 0$) states are the last to localise. The localisation of the band centre states therefore sets a critical disorder strength, W_c, above which *all* states in the band are MBL. At $W < W_c$, there exists mobility edges in the many-body spectrum which separate regions of the band that are MBL from those that are ergodic. For a given ω, there is a critical W, $W_c(\omega)$, above which states at that ω (and all states at larger ω) are localised. We shall now move on to discuss that it is the presence of these mobility edges that necessitates the energy resolution of $\overline{r}(t)$ and $\overline{C}(t)$.

As a reminder from pg. 32, the probability of being on FS site J at time t given its was initialised on site I at $t = 0$,

$$P_{IJ}(t) = \sum_{n,m} \exp\left[-i(E_n - E_m)t\right] \; A_{nI}A_{nJ}A_{mI}A_{mJ}. \tag{3.32}$$

In the infinite time limit, the $\exp\left[-i(E_n - E_m)t\right]$ terms rapid oscillations mean only the $m = n$ term survives meaning

$$P_{IJ}(\infty) = \sum_{n} A_{nI}^2 A_{nJ}^2, \tag{3.33}$$

and thus the disorder-averaged $P_{IJ}(t)$ is

$$\overline{P}_{IJ}(\infty) = \sum_{n} \overline{A_{nI}^2 A_{nJ}^2}. \tag{3.34}$$

[2]Central limit theorem states that the distribution of $u = \sum_{n=1}^{N} x_n$, $P(u)$ - where $\{x_n\}$ are independent random variables with a non-infinite variance - will tend to a Gaussian in the limit of large N.

On pg. 35, we introduced the quantities $r_I(t)$, $r(t)$ and $\overline{r}(t)$. $r_I(t)$ can be equivalently written as

$$r_I(t) = \sum_J P_{IJ}(t)\, r_{IJ} \tag{3.35}$$

and thus

$$\overline{r}(t) = \frac{1}{N_H} \sum_{I,J} \overline{P}_{IJ}(t)\, r_{IJ}. \tag{3.36}$$

It therefore follows that

$$\overline{r}(\infty) = N_H^{-1} \sum_{I,J} r_{IJ}\, \overline{P}_{IJ}(\infty), \tag{3.37}$$

with $P_{IJ}(\infty)$ given by eq. 3.34. This can be equivalently written as

$$\overline{r}(\infty) = N_H^{-1} \sum_n \sum_{r=0}^{L} r\, \overline{F}_n(r), \tag{3.38}$$

with $\overline{F}_n(r)$ defined by

$$\overline{F}_n(r) = \sum_{I,J;r_{IJ}=r} \overline{A_{nI}^2 A_{nJ}^2}. \tag{3.39}$$

$\overline{F}_n(r)$ was studied in the recent paper by Roy and Logan [61], where it was shown to have the form

$$\overline{F}_n(r) = \binom{L}{r} \left(1 + e^{-\frac{1}{\xi_{f,n}}}\right)^{-L} e^{-\frac{r}{\xi_{f,n}}}, \tag{3.40}$$

with $\xi_{f,n}$ a FS correlation length for eigenstates n at the particular ω considered. The band centre states were considered explicitly in [61], but there is nothing special about this energy. Eqs. 3.38, 3.40 give

$$\frac{\overline{r}(\infty)}{L} = N_H^{-1} \sum_n \frac{1}{1 + e^{\frac{1}{\xi_{f,n}}}} \equiv \int d\omega \frac{D(\omega)}{1 + e^{\frac{1}{\xi_f(\omega)}}}, \tag{3.41}$$

with $D(\omega)$ the density of states (eq. 3.30) The behaviour of $\xi_f(\omega)$ with disorder

strength W is known from detailed scaling analysis [61]. For W greater than the critical $W_c(\omega)$ at which the chosen energy ω become MBL, $\xi_f(\omega)$ remains finite. For $W < W_c(\omega)$, $\xi_f(\omega) \propto L$ and diverges in the thermodynamic limit, as expected for delocalised states.

As mentioned above the disorder strength above which all states in the band are localised is denoted W_c. For $W < W_c$, some states in the band will be delocalised, and others MBL: the spectrum hosts mobility edges. For such W then from eq. 3.41 the delocalised states contribute a factor of $\frac{1}{2}$ to the summand as $L \to \infty$, while MBL states will contribute a finite factor strictly $< \frac{1}{2}$. It is therefore only if all states in the band are delocalised, or in practise all but a vanishing fraction of them, that the long-time limit of $\frac{\overline{r}(\infty)}{L}$ will be $\frac{1}{2}$.

It would, however, be useful if the long time value distinguished whether states in a certain energy region were ergodic or MBL in nature. Eq. 3.41, expressed as a sum over all eigenstates n, shows that $\frac{\overline{r}(\infty)}{L}$ can be resolved as a sum of contributions from all eigenstates in the band. This is in fact true for all times, as now explained.

In order to energy resolve relevant time dependent quantities, we shall start by defining an energy resolved version of $P_{IJ}(t)$. To this end, $P_{IJ}(t) = |G_{IJ}(t)|^2$ (introduced previously on pg. 32) is given by:

$$P_{IJ}(t) = \mathrm{Re}\left[\langle I|\exp[i\mathcal{H}t]|J\rangle \langle J|\exp[-i\mathcal{H}t]|I\rangle\right]. \tag{3.42}$$

This can be shown (by simply inserting two unit operators) to be equal to

$$P_{IJ}(t) = \sum_{n,m} \cos\left[(E_n - E_m)t\right] A_{nI}A_{nJ}A_{mI}A_{mJ}. \tag{3.43}$$

Defining $P_{IJ}^{[n]}(t)$ as

$$N_H^{-1} P_{IJ}^{[n]}(t) = \sum_m \cos[(E_n - E_m)t] A_{nI} A_{nJ} A_{mI} A_{mJ}, \tag{3.44}$$

means

$$P_{IJ}(t) = N_H^{-1} \sum_n P_{IJ}^{[n]}(t). \tag{3.45}$$

We have thus resolved $P_{IJ}(t)$ into contributions $P_{IJ}^{[n]}(t)$ from different eigenenergies E_n. While $P_{IJ}(t)$ is a bonafide probability, with $P_{IJ}(t) \geq 0$ for all times, the same cannot however be said for $P_{IJ}^{[n]}(t)$, which is not guaranteed to be positive. Numerically, however, we find the energy resolved version of $\overline{P}(r;t)$, $\overline{P}^{[n]}(r;t)$ - the essential quantity to understanding longitudinal transport - is positive for all Hamming distances, r, and all times, t. This is shown explicitly in appendix B, alongside a discussion relating $P_{IJ}^{[n]}(t)$ to the expectation value of behemoth operators [179] (explained in detail in the appendix).

For times $\Gamma t \gtrsim 1$, $P_{IJ}^{[n]}(t)$ is controlled by states lying in a progressively narrower window $|E_m - E_n| << \Gamma$ in the vicinity of the chosen energy E_n. We shall come back to this point later in this chapter when discussing the subdiffusive behaviour of $\overline{r}^{[n]}(t)$ (defined below).

Given that $P_{IJ}(t)$ can be resolved into contributions from eigenstates in different regions of the band $P_{IJ}^{[n]}(t)$, it follows that any quantity linear in the $\{P_{IJ}(t)\}$ can also be energy resolved. For example the first moment $r_I(t) = \sum_J \ r_{IJ} \ P_{IJ}(t)$, can be resolved as $r_I(t) = N_H^{-1} \ \sum_n \ r_I^{[n]}(t)$, and similarly its sample average $r^{[n]}(t)$ can, where

$$r(t) = N_H^{-1} \ \sum_n r^{[n]}(t). \tag{3.46}$$

Given that $C(t) = 1 - \frac{2r(t)}{L}$ (derived on pgs. 36-38), it follows that

$$C(t) = N_H^{-1} \sum_n C^{[n]}(t), \tag{3.47}$$

with

$$C^{[n]}(t) = 1 - \frac{2r^{[n]}(t)}{L}. \tag{3.48}$$

Equally, $C^{[n]}(t)$ can be thought of as coming from the eigenstate trace of $C(t)$, with $C^{[n]}(t) = \frac{1}{L}\sum_l C_{ll}^{[n]}(t)$; $\quad C_{ll}^{[n]}(t) = \langle n|\hat{\sigma}_l^z(t)\hat{\sigma}_l^z|n\rangle$ (discussed previously on pgs. 36-38).

In the next few sections, we shall examine the averages over disorder realisations, $\overline{r}^{[n]}(t)$ and $\overline{C}^{[n]}(t)$.

Crucially, if the eigenstates within the energy region considered are delocalised $\overline{C}^{[n]}(\infty) = 0$ as the eigenstates thermalise, meaning they have no memory of their initial conditions at long-time. Given the relationship $C^{[n]}(t) = 1 - \frac{2r^{[n]}(t)}{L}$, clearly $\overline{r}^{[n]}(\infty) = \frac{L}{2}$. By contrast, if the eigenstates are localised, $\overline{C}^{[n]}(\infty) > 0$, as the eigenstates retain memory of their initial spin configuration for all times. From $C^{[n]}(t) = 1 - \frac{2r^{[n]}(t)}{L}$, this means $\overline{r}^{[n]}(\infty) < \frac{L}{2}$, but $\mathcal{O}(L)$.

The fact that their infinite time values distinguish whether the eigenstates within the energy region considered are MBL or ergodic makes $\overline{r}^{[n]}(t)$ and $\overline{C}^{[n]}(t)$ easier to understand quantities than the full $\overline{C}(t)$ and $\overline{r}(t)$. We shall therefore start by examining the behaviour $\overline{C}^{[n]}(t)$ and $\overline{r}^{[n]}(t)$ at the band centre, followed by considering the behaviour of $\overline{C}^{[n]}(t)$ and $\overline{r}^{[n]}(t)$ away from the band centre, before finally examining the behaviour of the full $\overline{C}(t)$ and $\overline{r}(t)$.

3.2.7 Ergodic phase: Band centre $\overline{C}^{[n]}(t)$ and $\overline{r}^{[n]}(t)$

We shall now move onto examine the behaviour of the band centre $\overline{C}^{[n]}(t)$ and $\overline{r}^{[n]}(t)$ obtained by ED in the ergodic phase. As a reminder from chapter 2, the critical disorder for band centre states to localise in the TFI model considered is $W_c \simeq 4$ [62]. For $W < W_c$, the band centre states are ergodic, while for $W > W_c$ they are MBL.

Figure 3.6 shows how $\frac{\overline{r}^{[n]}(t)}{L}$ varies with t for different W values in the ergodic phase. This figure shows that for all $W(< W_c)$ considered the largest system size $\frac{\overline{r}^{[n]}(t)}{L} = \frac{1}{2}$ at long-times, as expected from the arguments given in the previous section for the ergodic phase.

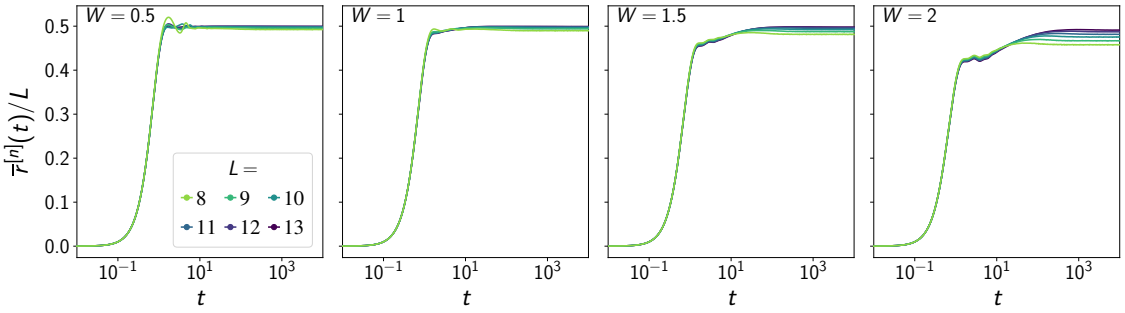


Figure 3.6: For $W = 0.5, 1, 1.5$ and 2 $\frac{\overline{r}^{[n]}(t)}{L}$ *vs* t for band centre states. For system sizes $L = 8 - 13$.

For W values deep in the ergodic phase (e.g. $W \simeq 0.5 - 1$), figure 3.6 shows that $\frac{\overline{r}^{[n]}(t)}{L}$ rapidly reaches its long-time value on timescales $\Gamma t \sim \mathcal{O}(1)$. Physically, this corresponds to the system exploring all of the FS lattice on $\mathcal{O}(1)$ time scales and reflects the extensive connectivity of the nodes on the FS graph.

On the other hand, for the larger W values (i.e. $W \gtrsim 1.5$), $\frac{\overline{r}^{[n]}(t)}{L}$ has a two-part increase. At short times, $\Gamma t \lesssim 1$, $\frac{\overline{r}^{[n]}(t)}{L}$ rapidly increases from zero to $\frac{\overline{r}^{[n]}(t)}{L} \simeq 0.45$, for $W = 1.5$, and $\frac{\overline{r}^{[n]}(t)}{L} \simeq 0.4$, for $W = 2$. A region of slower dynamics then sets in above $\Gamma t \sim 1$ until $\frac{\overline{r}^{[n]}(t)}{L}$ reaches its long-time value of $\frac{1}{2}$.

In the previous section, we mentioned that for $\Gamma t \gtrsim 1$, $\{P_{IJ}^{[n]}(t)\}$ and thus $\frac{\overline{r}^{[n]}(t)}{L}$

is controlled by states lying in a progressively narrower window $|E_m - E_n| << \Gamma$ in the vicinity of the chosen energy E_n, here chosen to be the band centre. This means in the region of slow dynamics, $\frac{\overline{r}^{[n]}(t)}{L}$ dynamics is controlled entirely by those states surrounding the band centre, which are delocalised. It thus follows that the slow dynamics for the larger W is associated with the delocalised states in the spectrum.

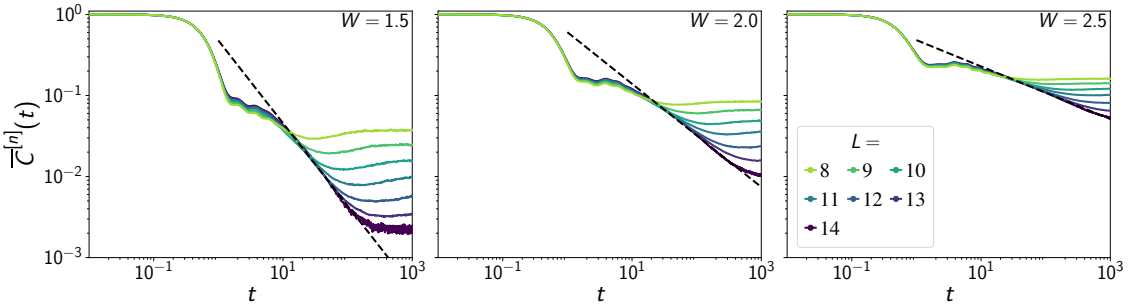


Figure 3.7: For $W = 1.5, 2, 2.5$, showing $\overline{C}^{[n]}(t)$, for band centre states n. Dashed lines show the power-law fits to the intermediate behaviour, onto which the data scales progressively with increasing L. For system sizes $L = 8 - 14$.

To further examine the slow dynamics at intermediate times, we can consider $\overline{C}^{[n]}(t)$, with $\overline{C}^{[n]}(t) = 1 - \frac{2\overline{r}^{[n]}(t)}{L}$, which is shown for $W = 1.5, 2$ and 2.5 in figure 3.7, on a log-log scale. This figure shows that $\overline{C}^{[n]}(t)$ and hence $\frac{\overline{r}^{[n]}(t)}{L}$ exhibits a power-law decay with $\overline{C}^{[n]}(t) \sim t^{-\alpha}$, with $\alpha < 1$. Figure 3.8 shows how this power-law exponent, α, varies with W. With increasing W, the exponent α is clearly seen to decrease steadily, and subject to the usual caveat of modest system sizes, appears to vanish in the vicinity of the transition, $W_c \sim 4$ [62].

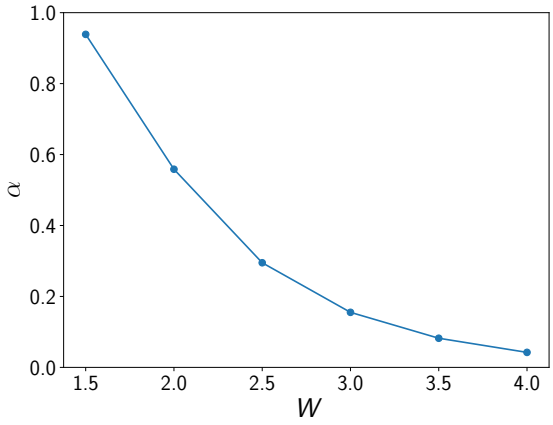


Figure 3.8: Power law exponent $\overline{C}^{[n]}(t) \sim t^{-\alpha}$, α *vs* W.

The power-law decay of $\overline{C}^{[n]}(t)$, i.e. $\overline{C}^{[n]}(t) \sim t^{-\alpha}$, indicates subdiffusive dynamics of the autocorrelation function in the TFI model. Subdiffusive dynamics of the spin autocorrelation function, in the ergodic phase for a wide range of disorder strengths proceeding the MBL phase, has been extensively studied in models with conserved magnetisation [82–87], such as the XXZ model (briefly introduced in chapter 1). In the Ising spin chain considered here, total magnetisation is clearly not conserved, meaning the spins dynamics are not 'constrained' by this requirement.

In the literature [82–87], it was thought that subdiffussion was due to the spin dynamics being constrained by a conservation law, as is the case in the XXZ model. The subdiffusive dynamics observed in our TFI model clearly warrants further explanation.

The key point to understand this, is that while total magnetisation is not conserved in the TFI model, total energy clearly is (trivially as the Hamiltonian is time independent). As a result the autocorrelator of the local energy energy density is expected to show subdiffusive dynamics, i.e. $C^E(t) \sim t^{-\alpha_E}$, where

$$C^E(t) = \frac{1}{L}\sum_{l=1}^{L} C^E_{ll}(t); \quad C^E_{ll} = \frac{1}{N_H}\sum_I \left\langle I\middle|\hat{H}_l(t)\hat{H}_l|I\right\rangle, \tag{3.49}$$

with $\hat{H}_l(t) = h_l\hat{\sigma}^z_l + \Gamma\hat{\sigma}^x_l + \frac{1}{2}\left[J_l\hat{\sigma}^z_l\hat{\sigma}^z_{l+1} + J_{l-1}\hat{\sigma}^z_{l-1}\hat{\sigma}^z_l\right]$ and $\hat{H}_l(t) = \exp[i\mathcal{H}t]\hat{H}_l\exp[-i\mathcal{H}t]$. The spin operator $\hat{\sigma}^z_l$ is not, however, orthogonal to the local energy operator, i.e. $Tr[\hat{\sigma}^z_l\hat{H}_l] \neq 0$. Therefore, at intermediate to late times, the spin autocorrelator picks up the subdiffusive tails emerging from the autocorrelator of the local energy density.

Having examined the behaviour of $\overline{C}^{[n]}(t)$ and $\overline{r}^{[n]}(t)$ in the ergodic phase, we shall now move on to consider their behaviour in the MBL phase. Before we do this, we will first discuss the analytical results for $\overline{C}(t)$ and $\overline{r}(t)$ when $J_z = 0$, denoted MBL_0 (introduced in chapter 2). The derivation will be summarised in the next

section, with the full derivation given in appendix C.

3.2.8 MBL_0 exact results for $\overline{C}(t)$ and $\overline{r}(t)$

Sufficiently deep in the MBL phase, the TFI model is known to be perturbatively connected to the non-interacting limit, $J_z = 0$ [59]. Here, although the system is 'trivially' MBL - because $\mathcal{H}$ is site-seperable in real-space and the system is a set of non-interacting spins - the behaviour on the FS is known to be non-trivial [61]. The FS Hamiltonian (discussed in chapter 2) still has the form

$$\mathcal{H} = \sum_I \mathcal{E}_I \left|I\right\rangle \left\langle I\right| + \sum_{I,J}{}' \, T_{IJ} \;\; \left|I\right\rangle \left\langle J\right|, \tag{3.50}$$

meaning the FS graph remains full connected.

As outlined in appendix C, for MBL_0 the exact disorder averaged $\overline{P}_{IJ}(t)$ can be obtained starting from the basic definition of $P_{IJ}(t) = |G_{IJ}(t)|^2$, with $G_{IJ}(t)$ the propagator between sites I and J. With I, J any pair of FS sites separated by a Hamming distance $r_{IJ} = r$, the result is

$$\overline{P}_{IJ}(t) = \left[z_0(t)\right]^r \left[1 - z_0(t)\right]^{L-r}, \tag{3.51}$$

where $z_0(t)$ given by

$$z_0(t) = \left\langle \frac{\Gamma^2}{h^2 + \Gamma^2} \;\; \sin^2\left(\sqrt{h^2 + \Gamma^2}t\right) \right\rangle_d, \tag{3.52}$$

and $\langle\rangle_d$ is the average over the disorder, i.e.

$$z_0(t) = \int_0^W \frac{dh}{W} \; \frac{\Gamma^2}{h^2 + \Gamma^2} \;\; \sin^2\left(\sqrt{h^2 + \Gamma^2}t\right). \tag{3.53}$$

Note that $\overline{P}_{IJ}(t)$ has the binomial form that we had seen on pg. 42 for the short

time analytical results. At short times,

$$\sin^2\left(\sqrt{h^2+\Gamma^2}t\right) = \frac{1}{2}\left(1-\cos\left(2\sqrt{h^2+\Gamma^2}t\right)\right). \simeq t^2\left(h^2+\Gamma^2\right) \tag{3.54}$$

From eq.3.53 it follows that

$$z_0(t) = (\Gamma t)^2 : \quad \Gamma t << 1. \tag{3.55}$$

Eq. 3.51 for $P_{IJ}(t)$ in MBL_0 recovers (as it ought to) the short-time results derived on pgs. 39-42.

Eq. 3.51 solely depends on the Hamming distance r (introduced in chapter 2) and is independent of the sites I and J, meaning $\overline{P}_I(r;t) = \overline{P}(r;t)$, with $\overline{P}_I(r;t) = \langle P_I(r;t)\rangle_d$ ($P_I(r;t)$ given by eq. 3.4, pg. 34) and $\overline{P}(r;t)$ (eq. 3.6, pg. 35). It therefore follows that

$$\overline{P}(r;t) = \binom{L}{r}\left[z_0(t)\right]^r\left[1-z_0(t)\right]^{L-r}. \tag{3.56}$$

Given that $\overline{r}(t) = \sum_{r=0}^{L}\ r\ \overline{P}(r;t)$ it follows from the binomial structure of $\overline{P}(r;t)$ that

$$\frac{\overline{r}(t)}{L} = z_0(t), \tag{3.57}$$

and therefore using the relationship $\overline{C}(t) = 1 - \frac{2\overline{r}(t)}{L}$,

$$\overline{C}(t) = 1 - 2z_0(t). \tag{3.58}$$

These results are clearly L independent for all t.

MBL_0 is therefore fully determined by $z_0(t)$ (eq. 3.53). Using the double angle

formula for $\sin^2(\theta)$ (and setting $\Gamma = 1$ as usual), we can rewrite eq. 3.53 for $z_0(t)$ as

$$z_0(t) = p - \frac{1}{2}K(t), \quad p = \frac{\tan^{-1}(W)}{2W}, \tag{3.59}$$

with $K(t) = \langle (h^2+1)^{-1} \cos\Big(2\sqrt{h^2+1}t\Big)\rangle_d$. We shall see below that $K(t)$ vanishes as $t \to \infty$. It thus follows that the long-time limits are $\frac{\overline{r}(t)}{L} = p$ and $\overline{C}(t) = 1 - 2p$, with $p < \frac{1}{2}$. This means $\overline{C}(\infty) > 0$ and subsequently $\frac{\overline{r}(t)}{L} < \frac{1}{2}$, which indicates the presence of frozen spins, or equivalently that in MBL_0 the system retains memory of the initial spin configuration for all times.

The assymptotic behaviour of $K(t)$, $t >> 1$, can be determined (derivation in appendix C), where we find

$$K(t) \sim \frac{1}{2W}\sqrt{\frac{\pi}{2}}\frac{[\cos(2t) - \sin(2t)]}{\sqrt{t}}, \tag{3.60}$$

meaning it vanishes as a power-law superimposed on oscillatory behaviour. It thus follows that from eqs. 3.58 and 3.59 that

$$\overline{C}(t) \sim \left(1 - \frac{\tan^{-1}(W)}{W}\right) + \frac{\sqrt{\pi}}{2W}\frac{1}{\sqrt{t}}. \tag{3.61}$$

In MBL_0 the oscillations in $\overline{C}(t)$ about its long-time value therefore decays as $\frac{1}{\sqrt{t}}$. We shall come back to this point when examining the decay in the oscillations of $\overline{C}^{[n]}(t)$ about its equilibrium value for our ED results.

For MBL_0 one can also determine the eigenstate resolved $\overline{C}^{[n]}(t) = 1 - \frac{2\overline{r}^{[n]}(t)}{L}$. In this case, reflecting the site separability, $\overline{C_{ll}}^{[n]}$ is independent of the site l and eigenstate n meaning $\overline{C}(t) \equiv \overline{C}^{[n]}(t)$. This means in MBL_0 that the full $\overline{C}(t)$ and the eigenstate resolved versions (for any region of the band) $\overline{C}^{[n]}(t)$ are identical. The above equations therefore also apply to $\overline{C}^{[n]}(t)$ (considered in the next section).

We shall see in the next few sections that we also observe in the MBL phase (for $J_z \neq 0$) in our ED results that $\overline{C}(t) \simeq \overline{C}^{[n]}(t)$.

3.2.9 MBL phase: Band centre $\overline{C}^{[n]}(t)$ and $\overline{r}^{[n]}(t)$

Having in the last section discussed the MBL_0 results we shall now discuss the results obtained for $\overline{C}^{[n]}(t)$ and $\overline{r}^{[n]}(t)$ by exact diagonalisation.

To this end, figure 3.9 shows how $\overline{C}^{[n]}(t)$ and $\frac{\overline{r}^{[n]}(t)}{L}$ vary with t, alongside how $\overline{C}^{[n]}(\omega)$ (defined below) varies with ω for 'relevant' ω, all for $W = 7$ (a disorder strength W representative of deep in the MBL phase). For $\overline{C}^{[n]}(t)$ and $\frac{\overline{r}^{[n]}(t)}{L}$ figure 3.9 shows the MBL_0 result for the same W value.

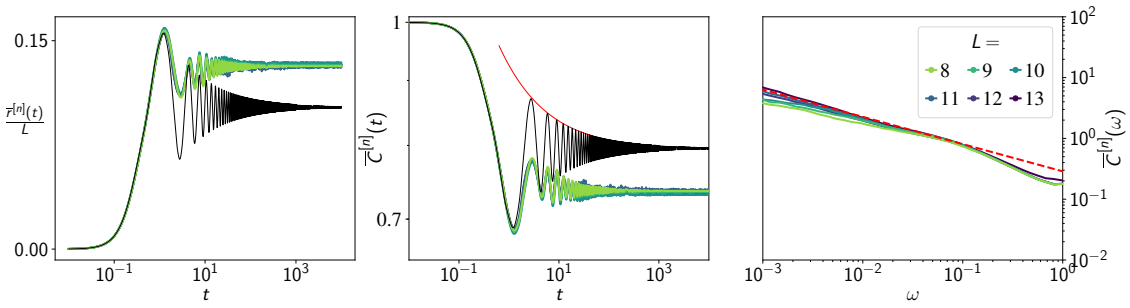


Figure 3.9: For $W = 7$, ED results for $\frac{\overline{r}^{[n]}(t)}{L}$ (left panel) and $\overline{C}^{[n]}(t)$ (middle panel) *vs* t. The solid black line shows for comparison the exact results for MBL_0 (Eqs. 3.58 and 3.53). The red line in the middle panel gives the asymptotic behaviour of eq. 3.61. The ED results for $\overline{C}^{[n]}(\omega)$ (eq. 3.62) are also shown (right panel) for 'relevant' ω values (discussed below) with the red dashed line being the fitting to a power-law decay $\overline{C}^{[n]}(\omega) \sim \omega^{-\beta}$. All ED results shown for system sizes $L = 8 - 13$.

A lot of information about the dynamics in the MBL phase is contained in figure 3.9, which we shall now start to unpack.

$\overline{C}^{[n]}(t) = 1 - \frac{2\overline{r}^{[n]}(t)}{L}$ in figure 3.9 clearly shows damped oscillatory behaviour. It plateaus to a non-zero long-time value (~ 0.7, well above zero), indicative of persistent memory of the initial condition (there are 'frozen spins'), and is barely L-dependent over the whole range studied. Equivalently, $\frac{\overline{r}^{[n]}(t)}{L} << \frac{1}{2}$, but finite. This was also seen when examining $\tilde{P}_y(y;t)$ (pg. 46), where the mode of the long-time

distribution was much less than $\frac{1}{2}$.

The exact MBL_0 results shown by the black lines (eqs. 3.57 and 3.53) in the $\frac{\overline{r}^{[n]}(t)}{L}$ and $\overline{C}^{[n]}(t)$ plots well capture much of the qualitative behaviour of our ED results for $J_z \neq 0$. For times up to $\Gamma t \sim \mathcal{O}(1)$, the MBL_0 and the ED results practically fall on top of each other. For longer times, figure 3.9 shows that while the time period for the oscillations is clearly the same, the MBL_0 oscillations are larger than in our ED results. Naturally, it is expected that oscillations will be larger in a non-interacting than interacting problem. This is simply because for a given disorder realisation in the interacting problem the spins do not decay independently of one another, as they are connected by the J_z terms in the Hamiltonian. This means we are essentially probing the collective decay of L spins, which is much less susceptible to fluctuations.

Within the field of localisation, it is well known that when $J_z = 0$ (MBL_0) in one-dimension for any non-zero disorder all eigenstates are localised [26]. In the TFI model this occurs trivially as the problem is site-separable (as briefly discussed on pg. 57, and further elaborated in appendix C). This means the 'MBL transition' occurs at $W_c = 0$. On the other hand, in our ED results for $J_z \neq 0$, $W_c \simeq 4$ [62]. This means for a given W value the MBL_0 problem is deeper in its MBL phase than the $J_z \neq 0$ problem. As a result of this $\overline{C}^{[n]}(\infty)$ is larger for MBL_0 than our ED.

The long-time value of $\overline{C}^{[n]}(t)$ is seen to be reached in practice by $\Gamma t \sim 10^2$, damped oscillations about that limit set in at shorter time scales $\Gamma t \sim \mathcal{O}(1)$ in our ED results. This is also seen in the MBL_0 results. In the MBL_0 results, eq. 3.61, shows that at long times the oscillations decay $\frac{1}{\sqrt{t}}$.

In order to determine how the oscillations decay with t in our ED results, it is

easiest to examine the Fourier transform of $\overline{C}^{[n]}(t)$,

$$\overline{C}^{[n]}(\omega) = \int_0^\infty dt\ \exp[i\omega t]\ \overline{C}^{[n]}(t). \tag{3.62}$$

Equivalently, $\overline{C}^{[n]}(\omega)$ is the average over disorder realisations of

$$C^{[n]}(\omega) = \sum_l C_l^{[n]}(\omega); \quad C_l^{[n]}(\omega) = \sum_m \delta(\omega - (E_m - E_n)) \left|\langle n|\hat{\sigma}_l^z|m\rangle\right|^2. \tag{3.63}$$

Figure 3.9 shows that clear oscillations in $\overline{C}^{[n]}(t)$ - whose decay we are interested in - occurs on timescales $1 \lesssim t \lesssim 10^2$. Given that $t \equiv \frac{1}{\omega}$ (as $\hbar = 1$) , it follows that the relevant ω scale the power law decay in $\overline{C}^{[n]}(t)$ will show up in $\overline{C}^{[n]}(\omega)$ (with $\overline{C}^{[n]}(\omega)$ and $\overline{C}^{[n]}(t)$ related by eq. 3.62) is $\mathcal{O}(10^0 - 10^{-2})$. The right hand panel of figure 3.9 shows that for these relevant ω values, $\overline{C}^{[n]}(\omega) \sim \omega^{-\beta}$ with $\beta = 0.46$ or equivalently $\beta \simeq 0.5$ (within the numerical error in the calculation).

From eq. 3.62 using a change of variables $u = \omega t$ it is easy to show that the two exponents of the power-law decays $\overline{C}^{[n]}(\omega) \sim \omega^{-\beta}$ and $\overline{C}^{[n]}(t) \sim t^{-\alpha}$ are simply related by $\alpha = 1 - \beta$. It therefore follows from the above results that the decay in the oscillation in $\overline{C}^{[n]}(t) \sim t^{-0.5}$ in our ED results, exactly as obtained for MBL_0.

Throughout this section, we have thus seen that much of the behaviour of $\overline{C}^{[n]}(t)$ and $\frac{\overline{r}^{[n]}(t)}{L}$ in the MBL phase is well captured by the MBL_0 results.

3.2.10 Moving away from the band centre

We shall now move onto consider how $\overline{C}^{[n]}(t)$ and $\frac{\overline{r}^{[n]}(t)}{L}$ vary as the energy E_n of the eigenstate $|n\rangle$, whose $\overline{C}^{[n]}(t)$ and $\frac{\overline{r}^{[n]}(t)}{L}$ we are considering, moves away from the band centre.

The many-body density of states, $D(\omega)$, is known to have a Gaussian distribution [173] with a standard deviation $\sigma_E \propto \sqrt{L}$, or equivalently '$D(\omega)$ exists on the $\sqrt{L}$

scale'. It follows that when comparing how $\overline{C}^{[n]}(t)$ and $\frac{\overline{r}^{[n]}(t)}{L}$ vary with ω for different system sizes, we should examine them at $\omega = n_s\sigma_E$, where n_s is the number of standard deviations that ω is from the band centre.

Figure 3.10 shows how the $\frac{\overline{r}^{[n]}(t)}{L}$ *vs* t plots differ for different number of standard deviations, n_s, away from the band centre for $W = 1$ and $W = 2$. This figure shows that for $W = 1$, $\frac{\overline{r}^{[n]}(t)}{L}$ *vs* t plots for $n_s = 0.1 - 2$ are all practically identical, with minor differences observed for $n_s = 2$. All plots have $\frac{\overline{r}^{[n]}(\infty)}{L} = \frac{1}{2}$, and have a $\frac{\overline{r}^{[n]}(t)}{L}$ which rapidly saturates to a half, meaning all regions of the band considered are deeply ergodic. This is naturally what we would expect as $W = 1$ is deep in the ergodic phase.

By contrast, figure 3.10 shows that the $W = 2$, $\frac{\overline{r}^{[n]}(t)}{L}$ *vs* t plots vary as the number of standard deviations away from the band centre the eigenstates are taken from, n_s increases. For $W = 2$, for the largest system size considered, $\frac{\overline{r}^{[n]}(\infty)}{L} = \frac{1}{2}$ for $n_s = 0.1, 0.5$, but $\frac{\overline{r}^{[n]}(\infty)}{L} < \frac{1}{2}$ for $n_s = 1, 2$.

Given the accessible system sizes we are able to examine using numerics, it is expected that the long-time value of $\frac{\overline{r}^{[n]}(t)}{L}$ for a given ω will show a 'crossover W window' surrounding $W_c(\omega)$, where $\frac{\overline{r}^{[n]}(\infty)}{L}$ varies continuously from its value of $\frac{1}{2}$ expected in the ergodic phase to a value much less than $\frac{1}{2}$ in the MBL phase. Without detailed scaling analysis for a given ω value, it preludes substantial consideration of W's in the vicinity of $W_c(\omega)$.

The eigenstates at one and two standard deviations away from the band centre are clearly in this crossover region, and without doing a detailed scaling analysis, which is not our aim here, it is not possible to tell what the critical disorder $W_c(\omega)$ is, and thus categorically whether these eigenstates are in the ergodic phase or the MBL phase. The results for $\overline{C}^{[n]}(t)$ (discussed below), however, suggest, the eigenstates are probably on the ergodic side of the transition, but at different 'distances' from

the transition.

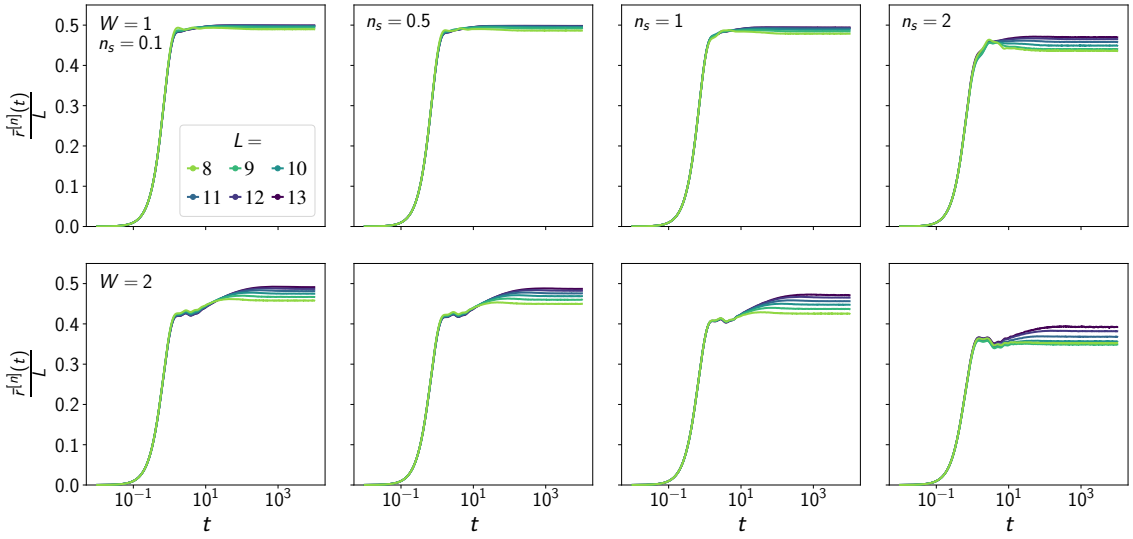


Figure 3.10: $W = 1, 2$, $\frac{\overline{r}^{[n]}(t)}{L}$ *vs* t, for different number of standard deviations, n_s, away from the band centre, for system sizes $L = 8 - 13$.

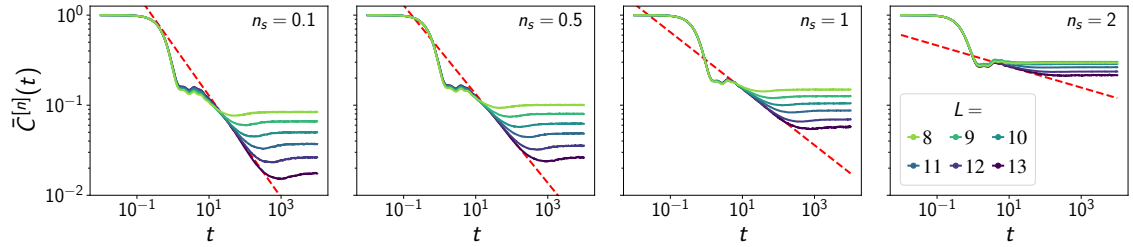


Figure 3.11: $W = 2$, $\overline{C}^{[n]}(t)$ *vs* t for different number of standard deviations, n_s, away from the band centre. The red dotted line show the power law decay $\overline{C}^{[n]}(t) \sim t^{-\alpha_n}$ at intermediate times. For system sizes $L = 8 - 13$.

Figure 3.11 shows how $\overline{C}^{[n]}(t)$ for $W = 2$ varies as the number of standard deviations away from the band centre, n_s, increases. This figure shows that for all n_s values $\overline{C}^{[n]}(t)$ has a power-law decay, i.e. $\overline{C}^{[n]}(t) \sim t^{-\alpha_n}$, with the exponent decreasing from $\alpha_n = 0.56$ at $n_s = 0.1$ to $\alpha_n = 0.12$ for $n_s = 2$. Since we know from our results at the band centre, that on approach to the transition from the ergodic side the power law exponent decreases, and vanishes at the transition, we expect that two standard deviations away from the band centre is close to the mobility edge for $W = 2$.

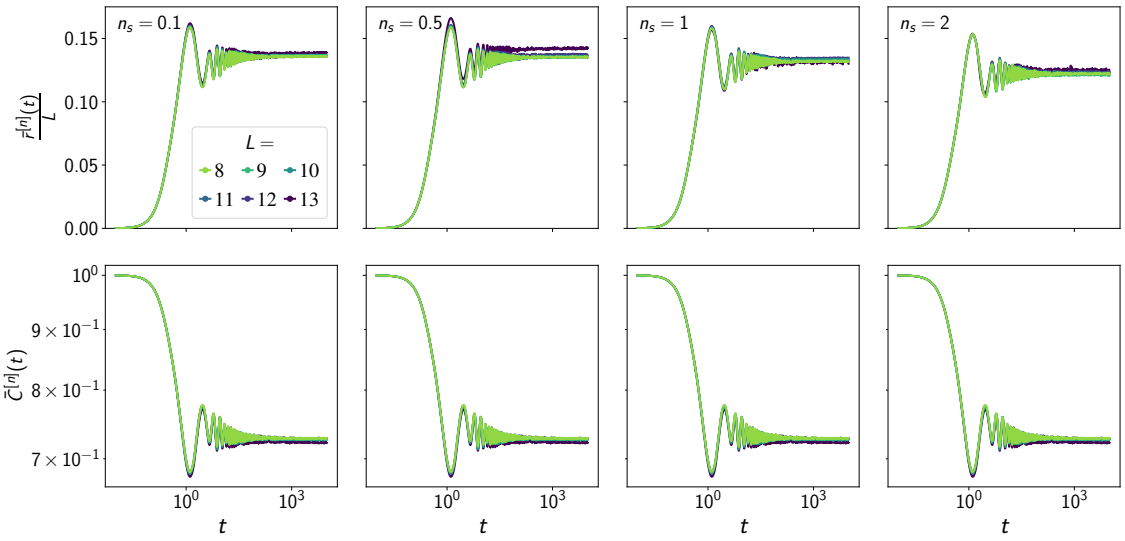


Figure 3.12: $W = 7$, $\overline{C}^{[n]}(t)$ *vs* t and $\frac{\overline{r}^{[n]}(t)}{L}$ *vs* t, for different number of standard deviations, n_s, away from the band centre. For system sizes $L = 8 - 13$.

Above the critical disorder, W_c, that band centre states are localised, all states in the band are MBL. Our exact results for MBL_0 (pgs. 57-59) suggest that in the MBL phase, $\frac{\overline{r}^{[n]}(t)}{L}$ and $\overline{C}^{[n]}(t)$ will not depend on the region of the band the eigenstates are taken from. Figure 3.12 shows that this is exactly what we observe in our ED results.

3.2.11 Full $\overline{C}(t)$ and $\overline{r}(t)$

In the last section, we showed how $\frac{\overline{r}^{[n]}(t)}{L}$ and $\overline{C}^{[n]}(t)$ vary as the eigenstate n is taken from different regions of the band. In this section, for completeness, we shall now examine how the band centre $\frac{\overline{r}^{[n]}(t)}{L}$ and $\overline{C}^{[n]}(t)$ compare to the full $\frac{\overline{r}(t)}{L}$ and $\overline{C}(t)$.

To this end, figures 3.13 and 3.14 show how the band centre $\overline{C}^{[n]}(t)$ and $\frac{\overline{r}^{[n]}(t)}{L}$ compare to the full $\overline{C}(t)$ and $\frac{\overline{r}(t)}{L}$, for $W = 2$ and $W = 7$.

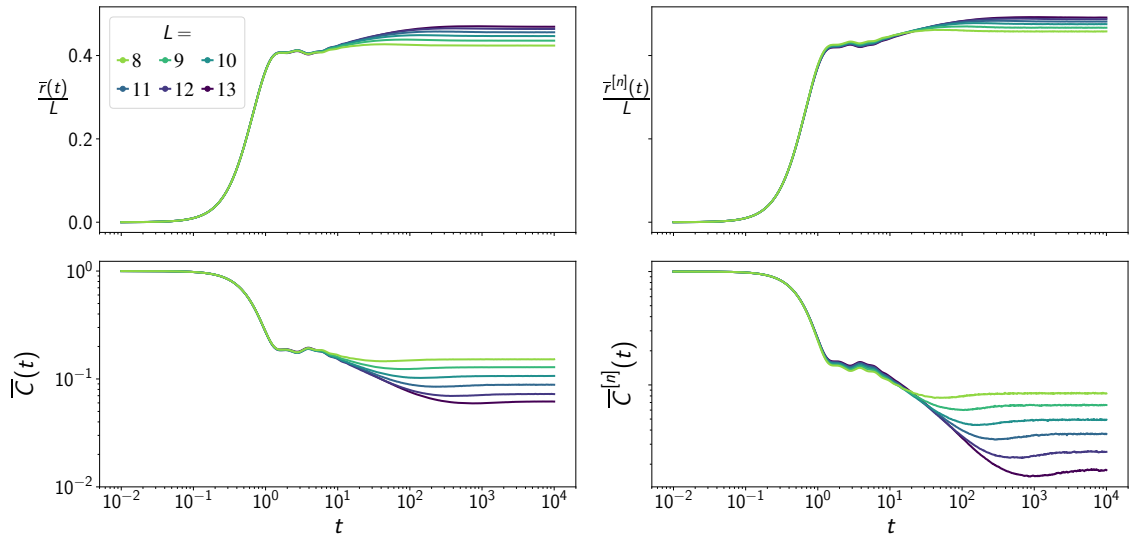


Figure 3.13: $W = 2$, $\overline{C}^{[n]}(t)$ and $\overline{C}(t)$ *vs* t and $\frac{\overline{r}^{[n]}(t)}{L}$ and $\frac{\overline{r}(t)}{L}$ *vs* t, for system sizes $L = 8 - 13$.

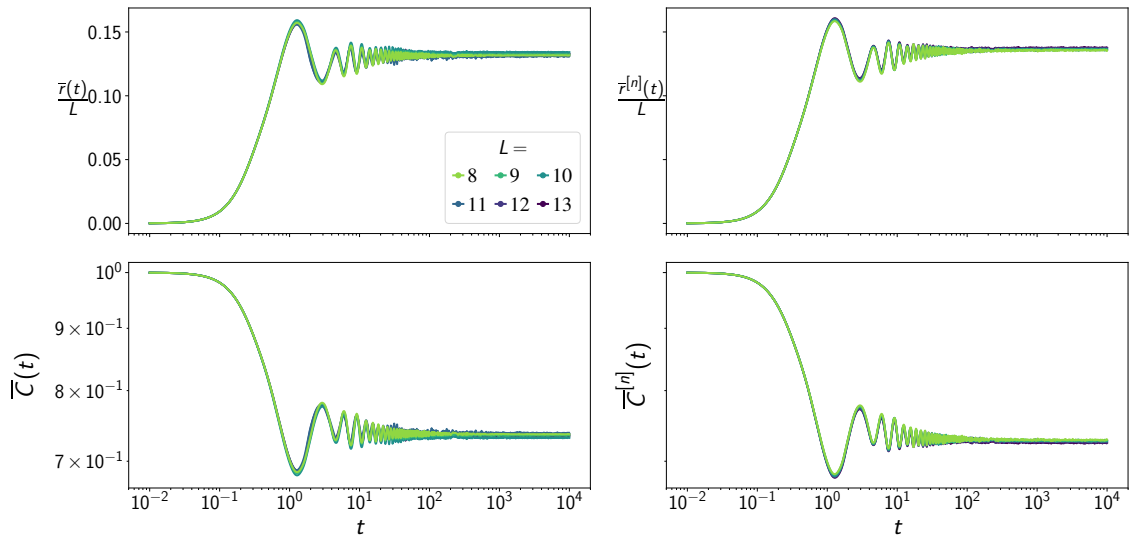


Figure 3.14: $W = 7$, $\overline{C}^{[n]}(t)$ and $\overline{C}(t)$ *vs* t and $\frac{\overline{r}^{[n]}(t)}{L}$ and $\frac{\overline{r}(t)}{L}$ *vs* t, for system sizes $L = 8 - 13$.

Figure 3.13 shows that for $W = 2$ the full $\frac{\overline{r}(\infty)}{L} < \frac{\overline{r}^{[n]}(\infty)}{L} = \frac{1}{2}$. As discussed in the previous sections, this is simply due to mobility edges present for $W < W_c$, which led to the full $\frac{\overline{r}(t)}{L}$ having contributions from eigenstates with different propensities to localisation (both ergodic and MBL states), which localise at smaller W than the band centre states. This subsequently means that $\overline{C}^{[n]}(t) = 1 - \frac{2\overline{r}^{[n]}(t)}{L}$ has a smaller long-time limit than $\overline{C}(t) = 1 - \frac{2\overline{r}(t)}{L}$.

On the other hand, figure 3.14 shows that for $W = 7$ the band centre $\frac{\overline{r}^{[n]}(t)}{L}$ and the full $\frac{\overline{r}(t)}{L}$ and subsequently $\overline{C}^{[n]}(t)$ and $\overline{C}(t)$ are practically identical. This is exactly as we had seen analytically for MBL_0.

We shall move onto discuss $W < W_c$ (the ergodic phase for band centre states) a little further.

Similarly to $\overline{C}^{[n]}(t)$ (figure 3.7, pg. 55), figure 3.15 shows that the full $\overline{C}(t)$ decays by a power-law at intermediate times, for $W < W_c$.

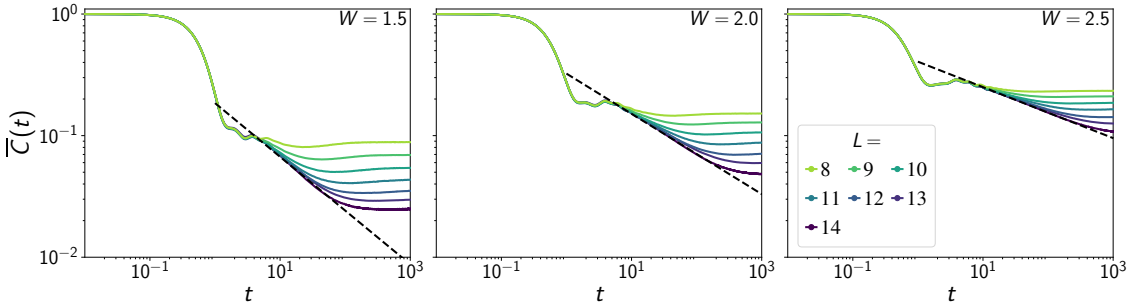


Figure 3.15: For $W = 1.5, 2, 2.5$, showing the full $\overline{C}(t)$. Dashed lines show the power-law fits to the intermediate behaviour, onto which the data scales progressively with increasing L. For system sizes $L = 8 - 14$. $W < W_c$.

Naturally, we would expect that for a given W the full $\overline{C}(t) \sim t^{-\alpha'}$ to decay by a smaller exponent than the band-centre $\overline{C}^{[n]}(t) \sim t^{-\alpha}$. Figure 3.16 shows this is exactly what is observed numerically. The full $\overline{C}(t)$ decaying slower than $\overline{C}^{[n]}(t)$ for the band centre eigenstates, is simply because the former has contributions from states in different regions of the band, with different propensities to localisation.

Our results for $\overline{C}^{[n]}(t)$ at the band centre showed that $\overline{C}^{[n]}(t) \sim t^{-\alpha}$, with the exponent α vanishing on approach to the transition from the ergodic phase (figure 3.8, pg. 55), i.e. only ergodic states show this power-law decay. It thus follows that for a given W ($< W_c$) the full $\overline{C}(t)$ power-law only has contributions from $\overline{C}^{[n]}(t)$ whose eigenstate energies E_n are within the ergodic region of the band.

The full $\overline{C}(t)$ has contributions from different eigenstates within the ergodic region of the band, where $W < W_c(\omega)$. These eigenstates are at 'different distances'

from the localisation transition, with the band centre states the furthest from the transition.

Figure 3.8 (pg. 55) showed that the exponent α, with the band centre $\overline{C}^{[n]}(t) \sim t^{-\alpha}$, decreased with increasing W on approach to the localisation transition, meaning the full $\overline{C}(t)$ has contributions from eigenstates with different exponents α_n which must be less than or equal to the band-centre exponent α. This means clearly $\alpha' < \alpha$. We expect as W approaches W_c, α and α' would approach each other, as the region of the band contributing to the decay of $\overline{C}(t)$ becomes a smaller region around the band-centre states, with α and α' vanishing at W_c.

Figures 3.16 and 3.17 show that numerically we do indeed find that $\overline{C}(t)$ decays slower than $\overline{C}^{[n]}(t)$, $\alpha' < \alpha$, and α and α' approach each other on approach to the transition.

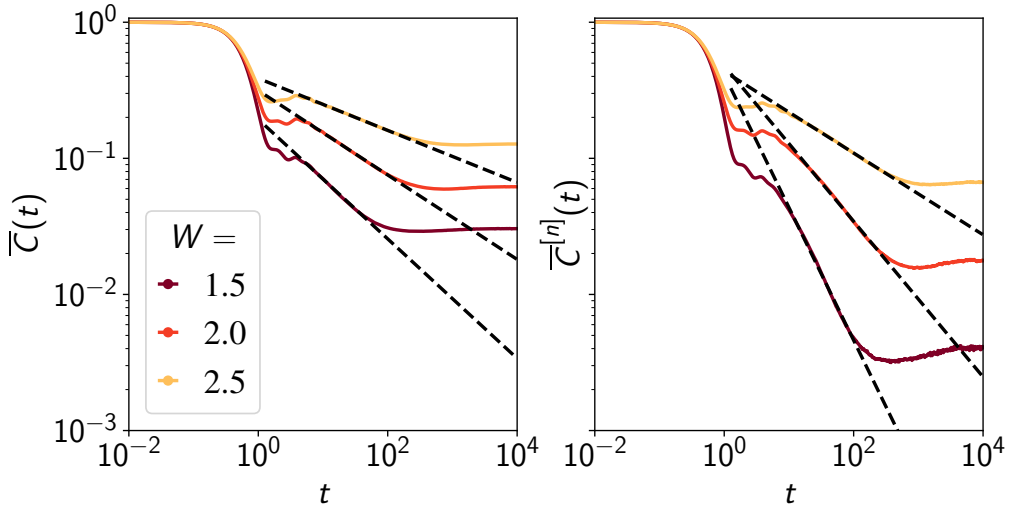


Figure 3.16: For $L = 13$, $W = 1.5, 2, 2.5$, showing the full $\overline{C}(t)$ and $\overline{C}^{[n]}(t)$. Dashed lines show the power-law fits to the intermediate behaviour.

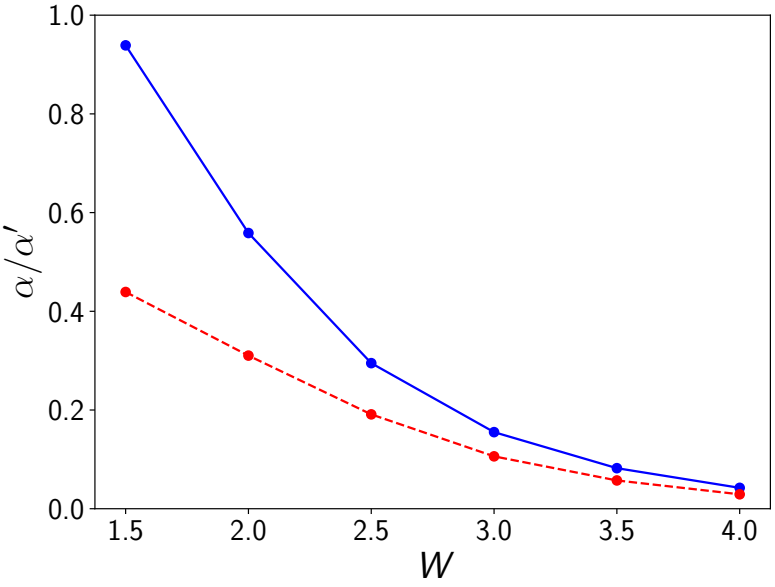


Figure 3.17: The power-law exponent α' , $\overline{C}(t) \sim t^{-\alpha'}$ (red dashed-line) and α, $\overline{C}^{[n]}(t) \sim t^{-\alpha}$ (blue line) *vs* W.

At this point, it is worth briefly discussing the similarity in the behaviour of $\overline{C}(t)$ in MBL and the return probability in Anderson (one-body) localisation [1, 2]. The full $\overline{C}(t)$ only vanishes in the thermodynamic limit, if all but a vanishing fraction of the states in the many-body spectrum are delocalised. This is just as is observed for the return probability in Anderson localisation, which only vanishes if all but a vanishing fraction of states in the one-body spectrum are delocalised. In Anderson localisation this necessitates us to energy resolve time-dependent quantities. Throughout this chapter, we have discussed that in MBL due to mobility edges present, we similarly need to energy resolve such time-dependent quantities.

3.2.12 Examining fluctuations

For most of this chapter, we have focused on the average r of the distribution, $\overline{P}(r;t)$, $\overline{r}(t)$, and useful quantities related to this. A natural question to ask is what are the fluctuation of $\overline{P}(r;t)$ about this average.

Given that $\overline{r}(t) \propto L$, the relevant quantity to probe these fluctuations is

$$\sigma^2(t) = \frac{\overline{\delta r^2}(t)}{L^2}; \quad \overline{\delta r^2}(t) = \sum_{r=0}^{L} \overline{P}(r;t)\, r^2 - \left(\sum_{r=0}^{L} \overline{P}(r;t)\, r \right)^2 . \tag{3.64}$$

Figure 3.18 shows how $\sigma^2(t)$ varies with t for different W values in both the ergodic and the MBL phase. This figure shows that in both the ergodic and the MBL phase the fluctuations probed by $\sigma^2(t)$ are very small, and decrease steadily with increasing system size L, meaning they vanish in the thermodynamic limit. The fact that $\sigma^2(t)$ decreases with increasing system size was also seen in the distributions $\tilde{P}_y(y;t)$, which were shown on pgs. 45-46 to narrow with increasing system size L.

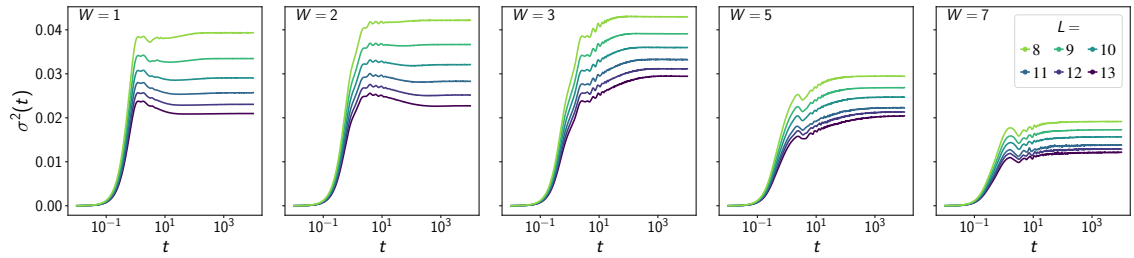


Figure 3.18: $\sigma^2(t)$ *vs* t, for different W and system sizes $L = 8 - 13$ indicated.

Our analytical results also suggest that $\sigma^2(t)$ decreases with increasing L. Our short time results discussed on pgs. 39-42, show explicitly that at short times $\sigma^2(t) \sim \frac{1}{L}$. Additionally, for all times using our exacts results for $\overline{P}(r;t)$ for MBL_0 eqs. 3.56 and 3.53 (pg. 58) give $\sigma^2(t) = \frac{z_0(t)(1-z_0(t))}{L}$, which is proportional to $\frac{1}{L}$ and thus vanishes in the thermodynamic limit.

Since $\sigma^2(t)$ vanishes in the thermodynamic limit, the only 'relevant' moment of $\overline{P}(r;t)$ is $\overline{r}(t)$ examined extensively in this chapter.

3.2.13 Summary of Longitudinal transport

In this chapter we have extensively discussed our understanding of longitudinal transport in the TFI model. Our keys findings are:

- We have uncovered a simple relationship between the average Hamming distance $\overline{r}(t)$ and the autocorrelator, $\overline{C}(t)$, with $\overline{C}(t) = 1 - \frac{2\overline{r}(t)}{L}$. This provides new insight by connecting between the real-space and Fock-space perspectives.

- At short times, $t << 1$, we have found that the system is agnostic to which phase it is in, ergodic or MBL. The Fock-space length scale $\overline{r}(t) \sim \mathcal{O}(L)$, for finite t however small; this ensures the autocorrelator is less than unity.

- We have discussed the need to energy resolve $\overline{r}(t)$ and $\overline{C}(t)$ to give $\overline{r}^{[n]}(t)$ and $\overline{C}^{[n]}(t)$, and linked this to the need to energy resolve time-dependent quantities in Anderson (one-body) localisation.

- In the ergodic phase, we found $\overline{C}^{[n]}(t)$ decays subdiffusively at intermediate times, i.e. $\overline{C}^{[n]}(t) \sim t^{-\alpha}$, with an exponent that vanishes as we approach the transition. $\frac{\overline{r}^{[n]}(\infty)}{L} = \frac{1}{2}$, which means $\overline{C}^{[n]}(\infty) = 0$.

- On the other hand, we found in the MBL phase that while $\overline{C}^{[n]}(t)$ reaches its long-time value at $\Gamma t \simeq 10^2$, damped oscillations set in at $\Gamma t \simeq 1$ about this value. We also find that $\overline{C}^{[n]}(\infty) > 0$, which implies $\frac{\overline{r}^{[n]}(t)}{L} < \frac{1}{2}$. We find that the dynamics for $\overline{r}(t)$ and $\overline{C}(t)$ are very similar to our exact results for MBL_0.

- Finally, we found that the relevant fluctuations of $\overline{P}(r;t)$ vanish in both phases, meaning the only relevant moment to examine is its first moment, $\overline{r}(t)$.

Having in this chapter developed a through understanding of how probability spreads out down the different rows in the FS graph, we shall now turn our attention to examine the transport of probability across rows: so called lateral transport.

Chapter 4

Lateral probability transport and the emergence of multifractality

In this chapter, we will continue to examine probability transport within the TFI model, originally introduced on pg. 32.

In the last chapter, we discussed extensively how probability spreads down the rows of the FS graph, which are an increasing Hamming distance r away from the initial FS site; so called longitudinal transport. We shall start this chapter by discussing lateral transport, or equivalently how probability spreads out across the FS sites within a given row, i.e. across sites which are at the same Hamming distance away from the initial FS site. The quantities we will examine to probe this will be introduced in the next section.

We will then move on to examine two further quantities which probe how the time dependent wavefunction $|\Psi(t)\rangle$ is spread out across FS, namely the time-dependent versions of the inverse participation ratio (IPR) and the first participation entropy. These are commonly studied quantities in localisation phenomenon [79, 88–103], and will be defined in a later section (section 4.2.1).

Finally we shall examine the extent to which the probability of being a Hamming distance r away from our initial site I depends on the particular site chosen, or on

the disorder realisation. The relevant quantities to examine this will be defined in a later section (section 4.3).

4.1 Lateral transport

4.1.1 Diagnosing Lateral transport

For any given disorder realisation and initial FS site I, $P_I(r;t) = \sum_{J;r_{IJ}=r} P_{IJ}(t)$ (eq. 3.4, pg. 34) - the essential quantity discussed in the last chapter - gives the total probability on row r. We studied its r-and t-dependence, which revealed how the probability flows with time down the graph; so called longitudinal transport. It does not however give any information on how the probabilities are spread out laterally, and in general inhomogeneously, within a given row of the graph, and how this inhomogeneity evolves with time. Understanding this lateral transport is our objective here.

To this end, we can define

$$R_I(r;t) = \frac{\frac{1}{N_r}\sum_{J;r_{IJ}=r} P_{IJ}^2(t)}{\left(\frac{1}{N_r}\sum_{J;r_{IJ}=r} P_{IJ}(t)\right)^2}, \tag{4.1}$$

with $N_r = \binom{N}{r}$. For any given disorder realisation, this is simply the ratio of the mean squared probability per FS site on row r to the square of the mean, $[N_r^{-1}P_I(r;t)]^2$. It, therefore, provides an obvious measure of the fluctuations in the distributions of P_{IJ}'s within a given row. Clearly as the mean square is always greater than or equal to the square of the mean, $R_I(r;t) \geq 1$, for all r and t. In particular, $R_I(r;t) = 1$ in the limit of extreme homogeneity where all the $P_{IJ}(t)$ on the row are the same, and hence $R_I(t) > 1$ reflects at least some inhomogeneity in the distribution.

We can take the average of $R_I(r;t)$ over initial FS sites I and disorder realisations, to give

$$\langle R \rangle = N_H^{-1} \sum_I \langle R_I(r;t) \rangle_d, \tag{4.2}$$

with $\langle\rangle_d$ here denoting the average over disorder realisations.

The value of $R_I(r;t)$ will clearly depend on the particular eigenstate and/or on the disorder realisation considered. The mean of $R_I(r;t)$ take over initial FS sites and disorder realisations, $\langle R \rangle$, (introduced above) provides only a limited understanding of the behaviour of the $\{R_I(r;t)\}$. A fuller picture is obtained by examining the probability distribution of $R_I(r;t)$,

$$P_R(x) = N_H^{-1} \sum_I \langle \delta \left(x - R_I(r;t) \right) \rangle_d \,. \tag{4.3}$$

This distribution enables us to understand how the inhomogeneity of the $P_{IJ}(t)$ on a given row r varies depending on the initial FS site $|I\rangle$ and/or on the disorder realisation, and on the typical values of $R_I(r;t)$. The first moment of $P_R(x)$, $\int dx \; P_R(x) \; x = \langle R \rangle$ (introduced above), and its width (second moment) probes the fluctuations in $R_I(t)$ over disorder realisations and initial FS sites. We shall come back to this second point, when discussing $P_R(x)$ in a later part of this chapter (section 4.1.5).

As a complement to $P_R(x)$, we can also study the probability distribution

$$P_{\rm rel}(x) = \frac{1}{N_H} \sum_I \frac{1}{N_r} \sum_{J;r_{IJ}=r} \left\langle \delta \left(x - \frac{P_{IJ}(t)}{\frac{1}{N_r} \sum\limits_{J;r_{IJ}=r} P_{IJ}} \right) \right\rangle . \tag{4.4}$$

For any given row r on the graph this gives the distribution of $P_{IJ}(t)$ relative to its mean value on the row, $x = \frac{P_{IJ}(t)}{[N_r^{-1} P_I(r;t)]}$, i.e. it probes the spread of the correctly normalised probabilities in a given row. The first moment of this distribution is by

construction 1, and the second moment $\int dx\ x^2 P_{\rm rel}(x) = \langle R \rangle$, mentioned above, eq. 4.2, pg. 75.

In our definitions above, for the three key quantities studied in this chapter to understand lateral transport, $\langle R \rangle$, $P_R(x)$ and $P_{\rm rel}(x)$, eqs. 4.2, 4.3 and 4.4, we averaged over all initial FS sites $|I\rangle$. There is, however, no *a priori* requirement here to average over all FS sites when studying lateral transport. We shall therefore choose in our numerics that follow - in the interest of numerical efficiency - to average only over a small number of FS sites I, typically 50, whose site energies $\mathcal{E}_I$ lie close to their mean value of zero. The distribution of FS site energies,

$$\mathcal{D}(\omega) = \frac{1}{N_H} \sum_{I=1}^{N_H} \langle \omega - \mathcal{E}_I \rangle_d, \tag{4.5}$$

is known to have a gaussian distribution [173] centred on $\omega = 0$. The densities of FS site energies, $\mathcal{D}(\omega)$, is largest at $\omega = 0$, meaning that when choosing a specified number of FS sites $|I\rangle$, those chosen at zero will be the closest in energy. It is therefore common practise within the field of many-body localisation to average over a small set of FS sites whose energies $\mathcal{E}_I$ are around 0. In appendix D we show that the key qualitative features of the distribution of $P_{IJ}(t)$ on a given row r, is independent of whether we averaged over all initial FS sites $|I\rangle$, or a restricted number with FS site energies, $\mathcal{E}_I$, around zero.

Since we are interested in dynamics we shall focus on one particular representative r throughout the next few sections. We shall choose the middle of the FS graph, $r = \frac{L}{2}$ for even L or $r = \frac{L-1}{2}$ for odd L. Numerically, we find that the key qualitative features of the time evolution of $\langle R \rangle$, $P_{\rm rel}(x)$ and $P_R(x)$, in the ergodic phase and the MBL phase, do not depend on the row r chosen. In appendix D we show this explicitly by showing some result for $\langle R \rangle$, $P_{\rm rel}(x)$ and $P_R(x)$ for other r values.

Throughout this chapter, we shall examine how $P_R(x)$, $\langle R \rangle$ and $P_{\rm rel}(x)$ vary as a function of time, t, and the disorder strength, W. First, we shall discuss how these quantities behave at short times.

4.1.2 Short-time results

In the previous chapter (pgs. 39-43) we discussed our exact results for the short-time universal behaviour of $\{P_{IJ}(t)\}$. In particular, we showed that at short times,

$$P_{IJ_r} = (\Gamma t)^{2r} \left[1 - (\Gamma t)^2\right]^{(L-r)} : \quad \Gamma t << 1, \tag{4.6}$$

independent of the initial FS site I, or site J_r on row r, with $\Gamma t < 1$, setting the upper bound for the time regime in which the calculation is valid.

It therefore follows that at short-time, all $N_r = \binom{N}{r}$ sites on row r have identical probabilities, or equivalently the probabilities are homogenously distributed across a given row r over the time-scale that eq. 4.6 holds, which from our numerical results in chapter 1 (figure 3.2, pg. 43) is $\Gamma t \lesssim 0.1$.

From eq. 4.1, as at short times all the $\{P_{IJ_r}(t)\}$ on row r are the same (and given by eq. 4.6), clearly

$$R_I(r;t) = 1, \tag{4.7}$$

for all initial FS sites $|I\rangle$ and disorder realisations. This means from eq. 4.2 that

$$\langle R \rangle = 1, \tag{4.8}$$

and from eq. 4.3 that

$$P_R(x) = \delta\left(x - 1\right). \tag{4.9}$$

Similarly as at short times $\{P_{IJ_r}(t)\}$ on a row are the same, it follows from eq. 4.4

that

$$P_{\text{rel}}(x) = \delta\left(x - 1\right). \tag{4.10}$$

We shall come back to these results when discussing our numerical results for $\langle R \rangle$, $P_R(x)$ and $P_{\text{rel}}(x)$ in the next few sections (4.1.4, 4.1.5, and 4.1.6). Before doing this, we shall first discuss the relationship between $R_I(r;t)$ and a time-dependent row-resolved IPR (defined in the next section).

4.1.3 Connecting to a row-resolved IPR

To further motivate studying $R_I(r;t)$, we can directly relate it to another natural measure of fluctuations in the distribution of $P_{IJ}(t)$'s: the row-resolved inverse participation ratio (IPR) (defined in eq. 4.14).

The usual IPR, $L_q = \frac{\sum_I |A_{nI}|^{2q}}{\sum_I |A_{nI}|^2}$ with $L_q = \sum_I |A_{nI}|^{2q}$ if the wavefunction is normalised, is a standard order parameter used in MBL [79, 88–99, 180]. It was briefly introduced in chapter 1, and will be further discussed in the next chapter on multifractality and related distributions.

In order to understand how $R_I(t)$ is related to a time-dependent row-resolved IPR, we need to consider the time-dependent wavefunction, $|\Psi(t)\rangle$, for a system initialized on $|I\rangle$ at $t = 0$,

$$|\Psi(t)\rangle = \exp[-i\mathcal{H}t]\,|I\rangle\,. \tag{4.11}$$

This can be expanded out (by simply inserting the unit operator $\sum_J |J\rangle\langle J|$) to give

$$|\Psi(t)\rangle = \sum_J \mathcal{A}_J^{[I]}(t)\,|J\rangle\,, \tag{4.12}$$

with $\mathcal{A}_J^{[I]}(t) = G_{IJ}(t) = \langle J|\exp[-i\mathcal{H}t]|I\rangle$, such that $|\mathcal{A}_J^{[I]}(t)|^2 = P_{IJ}(t)$. We now in-

troduce time-dependent wavefunction densities normalised on a given row r, defined by

$$\left|\mathcal{B}_J^{[I]}(t)\right|^2 = \frac{\left|\mathcal{A}_J^{[I]}(t)\right|^2}{\sum\limits_{J;r_{IJ}=r}\left|\mathcal{A}_J^{[I]}(t)\right|^2}. \tag{4.13}$$

Having defined the time-dependent wavefunction densities normalised on a given row r, $\left|\mathcal{B}_J^{[I]}(t)\right|^2$, we can now define the row-resolved IPR,

$$\mathcal{I}_{I,q}(r;t) = \sum_{J;r_{IJ}=r}\left|\mathcal{B}_J^{[I]}(t)\right|^{2q} = \frac{\sum\limits_{J;r_{IJ}=r}\left|\mathcal{A}_J^{[I]}(t)\right|^{2q}}{\left(\sum\limits_{J;r_{IJ}=r}\left|\mathcal{A}_J^{[I]}(t)\right|^2\right)^q}. \tag{4.14}$$

For the previously studied case of $q = 2$, $\mathcal{I}_{I,2}(r;t)$, [61] - which examined the long-time behaviour of $\mathcal{I}_{I,2}(r;t)$ - given that $P_{IJ}(t) = |\mathcal{A}_J^{[I]}(t)|^2$, it follows that

$$\mathcal{I}_{I,2}(r;t) = \frac{\sum\limits_{J;r_{IJ}=r} P_{IJ}^2(t)}{\left(\sum\limits_{J;r_{IJ}=r} P_{IJ}(t)\right)^2}. \tag{4.15}$$

From eq. 4.1 (pg. 74) clearly

$$\mathcal{I}_{I,2}(r;t) = N_r^{-1}\, R_I(r;t), \tag{4.16}$$

and hence (using eqs. 4.1 and 4.2) that

$$\langle\mathcal{I}_2\rangle = N_H^{-1}\sum_I \langle\mathcal{I}_{I,2}(r;t)\rangle_d = N_r^{-1}\langle R\rangle, \tag{4.17}$$

with $\langle I_2\rangle$ here denoting an average over both initial FS sites, $|I\rangle$, and disorder realisations.

We can therefore use our physical understanding of how the conventional IPRs (discussed further in chapter 5) behave in MBL [79, 88–100] to further understand

the relation

$$\langle R \rangle = N_r \, \langle \mathcal{I}_2 \rangle. \tag{4.18}$$

Let us first suppose that at some particular time t, the amplitudes $|B_J^{[I]}(t)|^2 = \frac{P_{IJ}(t)}{\sum\limits_{J;r_{IJ}=r} P_{IJ}(t)}$ (previously introduced in eq. 4.13), and hence the probabilities $P_{IJ}(t)$, are essentially uniformly distributed over the $N_r = \binom{N}{r}$ sites on row r, for all initial FS sites $|I\rangle$ and disorder realisations. Then $\sum\limits_{J;r_{IJ}=r} P_{IJ}(t) \sim N_r \, P_{IJ}(t)$, which means $|B_J^{[I]}(t)|^2 \sim N_r^{-1}$. From eq. 4.14 this means $I_{I,2}(r;t) = N_r^{-1}$ for all FS sites I and disorder realisations. Hence from eq. 4.17, $\langle \mathcal{I}_2 \rangle \sim N_r^{-1}$, which in turn means (using eq. 4.18) that $\langle R \rangle \sim \mathcal{O}(1)$. In this case, $\langle R \rangle$ will be independent of the system size L.

This behaviour is seen to arise in our numerical results for $\langle R \rangle$, discussed in the next section (4.1.4), at short times independent of the disorder strength, W, and at long times in the ergodic phase. The former can be understood from our exact short-time results discussed in the previous section (pg. 77), where the probabilities $P_{IJ_r}(t)$ are homogeneously distributed on any given row r. The latter occurs at long times deep in the ergodic phase, as here there is complete homogeneity of the probabilities across the entire FS lattice.

If by contrast, the wavefunction is strongly inhomogeneously distributed on the row, one might anticipate from previous work on the long-time row-resolved IPRs [61] that $\langle \mathcal{I}_2 \rangle \sim N_r^{-\nu}$ with $\nu < 1$, and hence $\langle R \rangle \sim N_r^{1-\nu}$. In this case, $\langle R \rangle$ will increase exponentially with increasing system size, L. We will see in the next section (4.1.4) that in our numerical results $\langle R \rangle \sim N_r^{1-\nu}$, with $\nu < 1$, in both the ergodic and the MBL phase at intermediate times, and in the MBL phase at long times.

From the above discussion, $\langle R \rangle$ clearly shows distinctly different dependence on system size depending on whether the wavefunction is homogeneously or inhomogeneously distributed on a given row. The system size dependence of $\langle R \rangle$, at different

times, for different disorder strengths W, therefore provides a clear indicator of the homogeneity or inhomogeneity of the probabilities on a given row, at the time of interest, something we shall now turn to examine.

4.1.4 Time evolution of $\langle R \rangle$

In the previous section, we discussed that the L-dependence of $\langle R \rangle$ (eq. 4.2) revealed whether the set of $\{P_{IJ_r}(t)\}$ on a given row r were homogeneously or inhomogeneously distributed at the time t of interest. In this section, we shall therefore examine how $\langle R \rangle \equiv \langle R \rangle(t)$ evolves with time in both the ergodic and the MBL phases. As a reminder the critical disorder strength for the TFI model considered, $W_c \simeq 4$ [62]. For $W < W_c$, the band-centre eigenstates are ergodic, and for $W > W_c$, they are MBL.

Figure 4.1 shows the t-dependence of $\langle R \rangle$ for $L = 8 - 13$, with $W = 1, 2$ characteristic of the ergodic phase, and $W = 5, 7$ of the MBL phase.

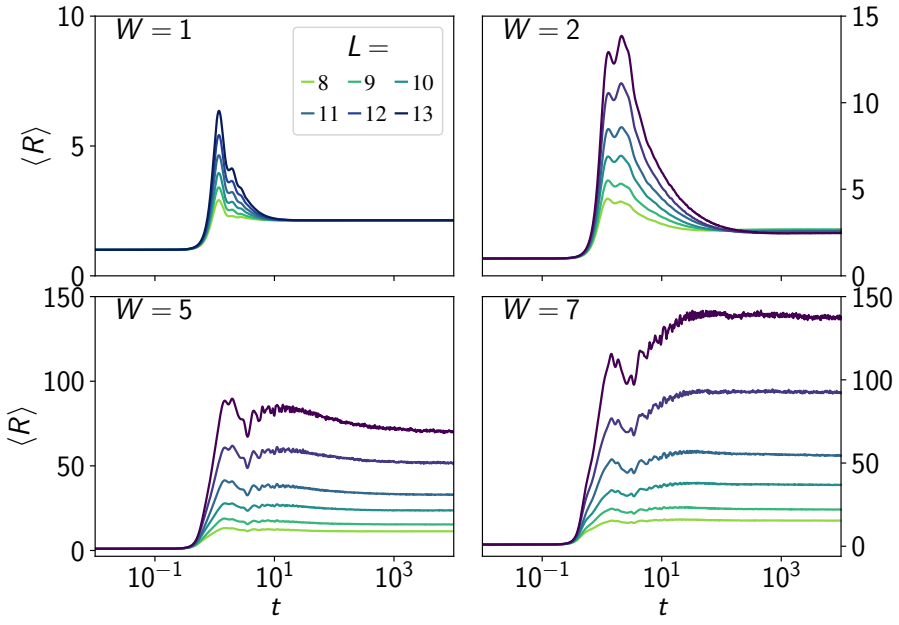


Figure 4.1: t-dependence of the average $\langle R \rangle$ ($= N_r \langle \mathcal{I}_2 \rangle$ from eq. 4.18). Shown for $r = \frac{L}{2}$ with $W = 1, 2, 5, 7$ for system sizes $L = 8 - 13$.

Figure 4.1 shows several notable points, which we shall now go on to discuss.

First, in the short time domain $t \lesssim 0.1$, $\langle R \rangle$ is independent of L, for all disorder strengths W. As pointed out in a previous section of this chapter (eqs. 4.7, 4.8, pg. 77), this is the limit of complete homogeneity, where all $P_{IJ}(t)$'s in a given row r are the same (and given by eq. 4.6). In consequence from eq. 4.1, $R_I(r;t) = 1$ for all FS sites I and disorder realisations. Hence from eq. 4.2, $\langle R \rangle = 1$. Using the relation $\langle R \rangle = N_r \langle I_2 \rangle$ (eq. 4.18), it follows that $\langle \mathcal{I}_2 \rangle = N_r^{-1}$.

Second, consider the opposite limit in figure 4.1, the long-time behaviour. For $W = 1, 2$, $\langle R \rangle$ is here $\mathcal{O}(1)$ and L-independent, just as it was at short times. Physically, this occurs as at long times in the ergodic phase, there is complete homogeneity of the probabilities across the Fock space. This means clearly $\{P_{IJ_r}(t)\}$ in a given row r are homogeneously distributed across the $N_r = \binom{N}{r}$ FS sites. From the arguments above it follows that $\langle \mathcal{I}_2 \rangle \sim N_r^{-1}$ and thus $\langle R \rangle$ is $\mathcal{O}(1)$.

By contrast, for $W = 5, 7$, figure 4.1 shows that the long-time value of $\langle R \rangle$ grows with increasing system size L. As discussed in the previous section (pg. 80) this reflects that the probabilities, $\{P_{IJ}(t)\}$, and hence the wavefunction are strongly inhomogeneously distributed across a given row at long times in the MBL phase. From previous work on the long-time row-resolved IPRs [61] it follows that such inhomogeneity leads to $\langle \mathcal{I}_2 \rangle \sim N_r^{-\nu}$ with $\nu < 1$, and hence $\langle R \rangle \sim N_r^{1-\nu}$, increasing with increasing system size L. The exact scaling of the long-time $\langle R \rangle$ with N_r shall be discussed shortly.

Third, consider in figure 4.1 the ergodic phase ($W = 1, 2$), $\langle R \rangle$ at intermediate times. Although in the ergodic phase $\langle R \rangle \equiv \langle R \rangle(t)$ is L-independent at both short and long times (discussed above), for times t of order unity , $\langle R \rangle$ is L-dependent. This reflects that even in the ergodic phase the wavefunction is inhomogeneously distributed across a given row at these intermediate times, as discussed on pg. 80.

It is clearly of interest to know how $\langle R \rangle$ scales with N_r, at long times in both

phases, and at intermediate times in the ergodic phase, as in both cases it is anticipated $\langle R \rangle \sim N_r^{1-\nu}$, with $\nu < 1$. To this end, figure 4.2 shows how: the long-time $\langle R \rangle$ varies with W for different system sizes (left panel), the long-time $\ln[\langle R \rangle]$ varies with $\ln[N_r]$ for different W values (middle panel) and the intermediate time $\ln[\langle R \rangle]$ varies with $\ln[N_r]$ in the ergodic phase (right panel).

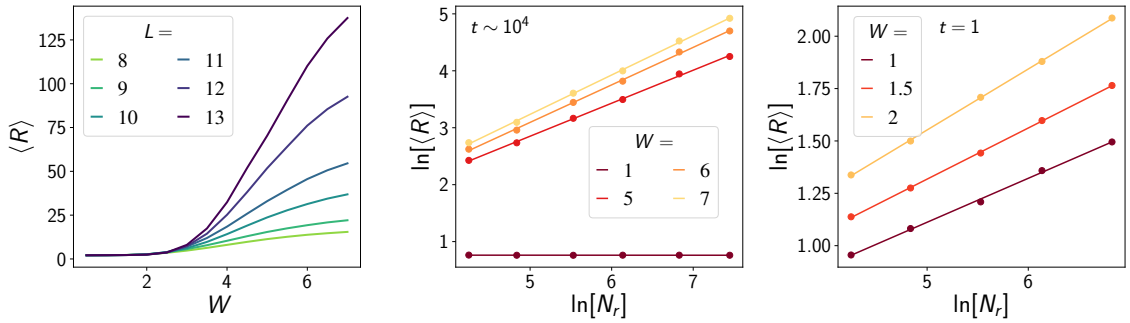


Figure 4.2: The first two panels show the long-time behaviour of $\langle R \rangle$. The middle shows $\ln[\langle R \rangle]$ *vs* $\ln[N_r]$ for $W = 5, 6, 7$, and $W = 1$; showing the scaling behaviour $\langle R \rangle \sim N_r^{1-\nu}$ and $\langle \mathcal{I}_2 \rangle \sim N_r^{-\nu}$, with $\nu < 1$ in the MBL phase and $\nu = 1$ in the ergodic phase. The left panel shows $\langle R \rangle$ *vs* W for system sizes $L = 8 - 13$. The final right hand panel shows for intermediate times $t = 1$ the scaling behaviour $\langle R \rangle \sim N_r^{1-\nu}$ and $\langle \mathcal{I}_2 \rangle \sim N_r^{-\nu}$ in the ergodic phase, here $\nu < 1$.

Figure 4.2 (left-panel) gives the late-time $\langle R \rangle$ as a function of W, confirming the strong L-dependence of $\langle R \rangle$ in the MBL phase, and its corresponding absence in the ergodic phase. This reflects (as discussed above) that the $\{P_{IJ_r}(t)\}$ are homogeneously distributed across a given row r (and the entire FS) at long times in the ergodic phase. While in the MBL there is strong inhomogeneity in $\{P_{IJ_r}(t)\}$ in a given row.

Given the accessible system sizes we are able to examine using numerics, $\langle R \rangle$ is expected to show a 'crossover W window', where the long-time $\langle R \rangle$ change continuously from ergodic to MBL behaviour. The left-hand panel of figure 4.2, shows this typical crossover W window, which without considering detailed scaling analysis, which is not our aim here, preludes consideration of W around W_c.

The centre panel of figure 4.2 shows that the long-time $\langle R \rangle \sim N_r^{1-\nu}$. In the MBL

phase ($W = 5, 6, 7$), $\nu < 1$ and decreases with increasing W, for example $\nu = 0.4$ for $W = 5$ and $\nu = 0.3$ for $W = 7$. This reflects (as discussed above) that $\{P_{IJ_r}(t)\}$ are inhomegeneously distributed across a given row r at long times in the MBL phase, with this inhomogeneity increasing with increasing W. By contrast, the $W = 1$ long-time $\langle R \rangle$ is independent of N_r, corresponding to $\nu = 1$. Since at long times in the ergodic phase, the probabilities $P_{IJ}(t)$ are uniformly distributed across the entire FS lattice.

Finally, figure 4.2 (right-panel) shows how $\langle R \rangle$ varies with N_r, for t of order unity, in the ergodic phase. This figure shows that $\langle R \rangle (t \simeq 1) \sim N_r^{1-\nu(t \simeq 1)}$, with $\nu(t \simeq 1) < 1$. The exponent $\nu(t \simeq 1)$ is found to decrease with increasing W, e.g. $\nu(t \simeq 1) = 0.8$ for $W = 1$ and $\nu(t \simeq 1) = 0.7$ for $W = 2$. This reflects that at intermediate times in the ergodic phase, the $\{P_{IJ_r}(t)\}$ are inhomegeneously distributed across a given row r, with this inhomogeneity increasing with increasing W. From figure 4.1 as in the MBL phase, there is essentially no real change in $\langle R \rangle (t)$ for $t \sim \mathcal{O}(10)$ (and very little change after $t \sim \mathcal{O}(1)$) for all system sizes L, meaning clearly $\langle R \rangle \sim N_r^{1-\nu}$ with $\nu < 1$ at intermediate times in the MBL phase. It thus follows that at intermediate times $\{P_{IJ_r}(t)\}$ are inhomogeneously distributed in the MBL phase as well.

The physical picture arising from our results for $\langle R \rangle (t)$ (discussed above) are as follows. Following the W-independent, short-time complete homogeneity of the squared wavefunction amplitudes/probabilities along a given row of the graph predicted by our exact results (pg. 77), at $t \sim 1$ - again for all W - the probabilities along a given row become inhomogeneously distributed (as seen by the $\langle R \rangle$ scaling with N_r in figure 4.2 discussed above). In the MBL phase figure 4.1 shows that this inhomogeneity persists with increasing time, and reaches its long-time value by $t \simeq 10$. By contrast, in the ergodic phase, this evolution is arrested; and the system

regains homogeneity of the probabilities along a given row, with $\langle R \rangle \sim \mathcal{O}(1)$ (figure 4.1). In a later section of this chapter, we shall see that this is related to how the full conventional IPR evolves with time (section 4.2).

Our discussion in this section has focused on the average $R_I(r;t)$, $\langle R \rangle$. We shall now move on to consider the full probability distribution of $R_I(r;t)$, $P_R(x)$ whose first moment is $\langle R \rangle$.

4.1.5 Examining $P_R(x)$ time dependence

The value of $R_I(r;t)$ will clearly depend on the particular eigenstate and/or on the disorder realisation considered. The mean of $R_I(r;t)$ take over initial FS sites and disorder realisations, $\langle R \rangle$, (eq. 4.2), considered in the previous section, provides only a limited understanding of the behaviour of the $\{R_I(r;t)\}$. A fuller picture is obtained by examining the probability distribution of $R_I(r;t)$, $P_R(x)$, which we shall now move on to discuss.

As a reminder the distribution of $R_I(r;t)$ (eq. 4.3, pg. 75),

$$P_R(x) = \langle \delta \left(x - R_I(r;t) \right) \rangle_{d,I} \,, \tag{4.19}$$

with $\langle \rangle_{d,I}$ here denoting an average over initial FS sites I and disorder realisations. The first moment of this distribution $\int dx \; P_R(x) \; x = \langle R \rangle$, considered in the previous section.

Figure 4.3 shows $P_R(x)$ *vs* x for $W = 1$ (top row) and $W = 7$ (bottom row), at a sequences of t's indicated, and over a range of system sizes studied ($L = 8 - 13$).

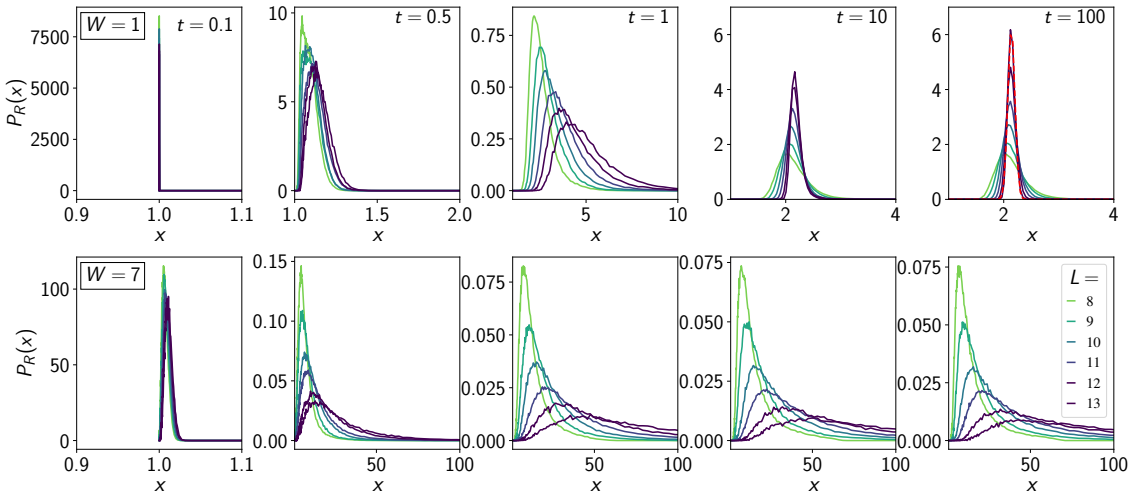


Figure 4.3: Probability distribution $P_R(x)$ of x for $W = 1$ (top row) and $W = 7$ (bottom row) at a sequence of t's specified and for different system sizes $L = 8 - 13$. Dashed red line shows the fit of the $W = 1$, $L = 13$, $t = 100$, $P_R(x)$ to a normal distribution.

Figure 4.3 shows that for either W, $P_R(x)$ for $t = 0.1$ is δ-distributed at $x = 1$. This simply reflects the short-time regime ($t \lesssim 0.1$), where all $\{P_{IJ_r}(t)\}$ on row r are identical (and given by eq. 4.6, pg. 77). In this limit, the probabilities $P_{IJ_r}(t)$ are homogeneously distributed across a given row r, independent of the initial FS site or disorder realisation, meaning $R_I(r;t) = 1$ for all initial FS sites I and disorder realisations. It therefore follows from eq. 4.3 that $P_R(x) = \delta(x - 1)$.

Let us now consider the time evolution $P_R(x)$ in the ergodic phase, illustrated by $W = 1$ in figure 4.3. For a given L, $P_R(x)$ evolves most significantly over $0.1 \lesssim t \lesssim 1$. In this time regime, $P_R(x)$ clearly broadens with increasing t, with the broadening being largest for the largest L values considered. It is evident from $P_R(x)$ than in this time-regime, the mean of $P_R(x)$, $\langle R \rangle(t)$, also clearly increases, which was seen in figure 4.1 (pg. 81).

At $t \simeq 1$ in the ergodic phase, the probabilities $\{P_{IJ_r}(t)\}$ are inhomogeneously distributed across a given row r. This is reflected in $\langle R \rangle$ increasing with L (discussed in the previous section). The extent to which the $\{P_{IJ_r}(t)\}$ are inhomogeneously distributed will depend on the initial FS site and/or disorder realisation. From eq.

4.1, this means $R_I(r;t)$ depends on the initial FS site and/or the disorder realisation, with $P_R(x)$ (eq. 4.3) measuring the extent it does. Figure 4.3 shows that $t \simeq 1$ in the ergodic phase, $P_R(x)$ has a broad distribution with tails at large-x values, which means there are significant variations in $R_I(r;t)$. We shall come to examine the functional form of this distribution, and meaning of this, later in this section.

By contrast, on further increasing t from $t \simeq 1$, $P_R(x)$ narrows with increasing t, and its mean $\langle R \rangle$ decreases with increasing time (previously seen in figure 4.1, pg. 81). By $t = 100$, the mean of the evidently symmetrical $P_R(x)$ ($=\langle R \rangle$) appears rather well converged over the accessible L-range; and the distribution narrows and sharpens with increasing L. A simple fit (indicated by the dashed red line in plot which shows the fit for $L = 13$) shows that $P_R(x)$ is normally distributed with a variance that decreases with L, with a δ-function expected in the thermodynamic limit.

This is exactly as expected, as at long times in the ergodic phase, the $\{P_{IJ}(t)\}$ are homogeneously distributed across the entire FS. This means for all initial sites $|I\rangle$ or disorder realisation, $R_I(r;t) \sim \mathcal{O}(1)$. We therefore expect $P_R(x) = \delta(x - \langle R \rangle)$ with $\langle R \rangle \sim \mathcal{O}(1)$ in the thermodynamic limit.

The situation is rather different in the MBL phase, illustrated by $W = 7$ in figure 4.3. Here, again $P_R(x)$ evolves most significantly over the interval $0.1 \lesssim t \lesssim 1$. For a given L, the distributions are practically converged to their long-time value by $t \sim 1$, above which little further temporal evolution occurs. Clearly, however, the late time $P_R(x)$ is much broader than its counter part in the ergodic phase (note the greatly increased x-scale compared to $W = 1$). With increasing L, the mean and mode of $P_R(x)$ clearly increase (as seen in figure 4.1, pg.81). The distribution is not only broad but appears to be heavy tailed.

This reflects that at long times in the MBL phase the set of probabilities,

$\{P_{IJ_r}(t)\}$, are inhomogeneously distributed across a given row r. This was seen in the previous section, where $\langle R\rangle$ increased with L. The extent to which the $\{P_{IJ_r}(t)\}$ are inhomogeneously distributed will depend on the initial FS site and/or the disorder realisation. From eq. 4.1, this means $R_I(r;t)$ depends on the initial FS site and/or the disorder realisation. Figure 4.3 shows $P_R(x)$ (eq. 4.3) has a heavy-tailed distribution for all but the shortest times in the MBL phase. This means that there are significant variations in this inhomogeneity in the MBL phase, reflected in large variations in the $R_I(r;t)$ value for all but the shortest times. We shall now move on to examine the functional form of this heavy-tailed distribution.

In the MBL phase in contrast to the ergodic phase the long-time mean $\langle R\rangle(\infty)$ is increasing with L. To distill this out from the large-x tails of $P_R(x)$ we need to consider the distribution

$$P_{\tilde{R}}(x) = \langle \delta(x - \tilde{R})\rangle_{d,I} : \quad \tilde{R} = \frac{R_I(r;t)}{\langle R\rangle}, \tag{4.20}$$

which has a mean of unity for all t.

Figure 4.4, pg. 90 (left panel) shows the long-time $P_{\tilde{R}}(x)$ for $W = 7$. $P_{\tilde{R}}(x)$ given the accessible L-range shows reasonable scaling behaviour; and shows power-law tails $P_{\tilde{R}}(x) \sim x^{-\alpha}$ with $\alpha \simeq 2.5$, such that the variance and all higher order moments are unbounded.

It appears that $P_R(x)$ itself is described by a generalised Lévy distribution [181],

$$P_{R,Lévy}(x) = \frac{A^{\alpha-1}}{\Gamma(\alpha-1)}\frac{1}{x^{\alpha}}\exp\left(\frac{-A}{x}\right), \tag{4.21}$$

which for large $x >> A$, $\propto x^{-\alpha}$, with A an L-dependent constant, and as usual $\Gamma(z)$ is the gamma function. This heavy-tailed distribution is known to be stable, provided $\alpha < 3$ [181]. The mode, or equivalently the peak in the generalised

Lévy, distribution, $P_{R,Lévy}(x)$, can be determined, by simply working out the x-value $\frac{\mathrm{d}P_{R,Lévy}(x)}{\mathrm{d}x} = 0$, which gives

$$x_{mode} = \frac{A}{\alpha}. \tag{4.22}$$

The mean of $P_{R,Lévy}(x)$, $\overline{x} = \int_0^\infty dx\ x\ P_{R,Lévy}(x)$, is finite provided $\alpha > 2$, and is given by:

$$\overline{x} = \frac{A\Gamma(\alpha-2)}{\Gamma(\alpha-1)} := A/f(\alpha). \tag{4.23}$$

The corresponding Lévy distribution for $\tilde{R}$ is then

$$P_{\tilde{R},Lévy}(x) = \frac{[f(\alpha)]^{\alpha-1}}{\alpha-1} x^{-\alpha} \exp\left(-\frac{f(\alpha)}{x}\right): \quad f(\alpha) = \frac{\Gamma(\alpha-1)}{\Gamma(\alpha-2)}, \tag{4.24}$$

and depends solely on α and not A.

The inset in the left panel of figure 4.4 shows $P_R(x)$ for $L = 13$ compared to the two-parameter fit (obtaining α and A) to $P_{R,Lévy}(x)$ (eq. 4.21), leading to $\alpha \simeq 2.5$. The left panel in figure 4.4 shows $P_{\tilde{R}}(x)$ for increasing system size, compared to $P_{\tilde{R},Lévy}(x)$ (eq. 4.24) with $\alpha \simeq 2.5$.

We add that the L-dependence of the fit $P_{R,Lévy}(x)$ itself arises largely from the L-dependence of A, over the accessible L range α varies very little. It is for this reason that $P_{\tilde{R},Lévy}(x)$ shows reasonable convergence to $P_{\tilde{R}}(x)$ with increasing L.

Earlier in this section, we discussed that for $t \simeq 1$, $P_R(x)$ for a W characteristic of the ergodic phase, $W = 1$, has a broad distribution with a mean, $\langle R \rangle$, that increases with increasing system size, and large-x power-law tails. A natural question then to ask is whether the $t \simeq 1$ $P_{\tilde{R}}(x)$ in the ergodic phase also have the form of a generalised Lévy distribution?

The right panel of figure 4.4 shows $P_{\tilde{R}}(x)$ for $W = 2$ (a disorder strength that clearly shows the behaviour typical of the ergodic phase) and $t \simeq 1$ alongside its fit to eq. 4.24. The Lévy form again appears to describe the data well; now with a

larger tail exponent ($\alpha \simeq 7$), with $\alpha > 3$ meaning the variance of $P_{\tilde{R}}(x)$ is finite.

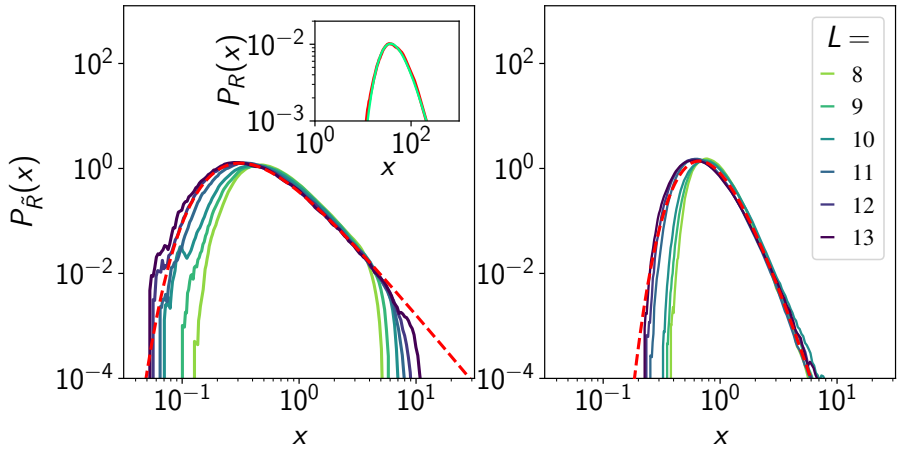


Figure 4.4: The left panel shows for $W = 7$ at $t = 100$, $P_{\tilde{R}}(x)$ *vs* x. Dashed line shows comparison to Lévy distribution, $P_{\tilde{R},Lévy}(x)$ (eq. 4.24). The inset on the left-hand side show how $P_R(x)$ compares to the two-parameter fit to $P_{R,Lévy}(x)$ (eq. 4.21). Right panel shows for $W = 2$ at $t = 1$, $P_{\tilde{R}}(x)$. Dashed line again shows fit to $P_{\tilde{R},Lévy}(x)$ (eq. 4.24). Both panels show our ED results for system sizes $L = 8 - 13$.

Physically the distribution of $P_{\tilde{R}}(x)$ examines the variation in $\frac{R_I(r;t)}{\langle R\rangle(t)}$ for different initial FS sites and disorder realisations. $\frac{R_I(r;t)}{\langle R\rangle}$ itself probes the inhomogeneity in the P_{IJ}'s on row r for a given initial FS site and disorder realisation compared to the average inhomogeneity (taken over FS sites and disorder realisations).

The fact that $P_{\tilde{R}}(x)$ has a generalised Lévy distribution, in the MBL phase for long times and in the ergodic phase for times of order unity, means that in both cases that the inhomogeneity of the $P_{IJ}(t)$'s in row r varies substantially depending on the particular initial FS site chosen and/or the disorder realisation. Given that in both cases $P_{\tilde{R}}(x)$ has converged to a common form for the modest system sizes amenable to numerics, it appears that these significant variations in $\frac{R_I(r;t)}{\langle R\rangle(t)}$ 'survive' in the thermodynamic limit.

Having extensively examined $P_R(x)$, we shall now move on to examine the distribution $P_{\text{rel}}(x)$ (eq. 4.4, pg. 75).

4.1.6 Further probing inhomogeneity in a row using $P_{\rm rel}(x)$

Complementary insight into the spread of probabilities across a row of the FS graph come from

$$P_{\rm rel}(x) = \frac{1}{N_H}\sum_I \frac{1}{N_r}\sum_{J;r_{IJ}=r}\left\langle \delta\left(x - \frac{P_{IJ}(t)}{\frac{1}{N_r}\sum\limits_{J;r_{IJ}=r} P_{IJ}}\right)\right\rangle. \tag{4.25}$$

For a given row r, this gives the distribution - over disorder realisations, FS sites J on the row, and initial sites I - of $P_{IJ}(t)$ relative to its mean on the row,

$$x = \frac{P_{IJ}(t)}{\frac{1}{N_r}\sum\limits_{J;r_{IJ}=r} P_{IJ}(t)} = \frac{P_{IJ}(t)}{N_r^{-1}P_I(r;t)}. \tag{4.26}$$

The first moment of $P_{\rm rel}(x)$, $\int dx\ x\ P_{\rm rel}(x)$, is one by construction, while the second moment $\int dx\ x^2\ P_{\rm rel}(x) = \langle R\rangle$ (eq. 4.2) studied in a previous section (4.1.4).

We shall now move onto examine $P_{rel}(x)$ for W characteristic of the ergodic phase ($W = 1$) and the MBL phase ($W = 7$). To this end, figures 4.5 and 4.6 show how $P_{rel}(x)$ and its corresponding cumulative distribution,

$$P_{\rm rel,c}(x) = \int_0^x dy\ P_{\rm rel}(y), \tag{4.27}$$

vary with t for system sizes $L = 8 - 13$, for $W = 1$ and $W = 7$.

Let us first consider $W = 1$. The top row of figure 4.5 shows $P_{\rm rel}(x)$ *vs* x at the sequence of t's specified, and for different system sizes $L = 8 - 13$. Corresponding cumulative distributions, $P_{\rm rel,c}(x)$ (eq. 4.27), are shown on the bottom row. While $P_{\rm rel}(x)$ is not converged with system size at $t \simeq 1$ - as expected from our previous discussion on $\langle R\rangle$ and $P_R(x)$, figures 4.1 and 4.3 - the distributions appear converged with L for all other t's shown. The long-time value of $P_{\rm rel}(x)$ is reached by $t = 10^2$ (indeed essentially by $t \sim 10$); and consistent with the convergence of $P_{\rm rel}(x)$ with L, the long-time value of $\langle R\rangle = \int dx\ x^2\ P_{\rm rel}(x)$ discussed previously (figure 4.1, pg.

81) is $\mathcal{O}(1)$, and L-independent.

This long-time $P_{\rm rel}(x)$ is in fact rather well captured by a half-Gaussian distribution [182], of the form

$$P_G(x) = \frac{2}{\pi} \exp\left(\frac{-x^2}{\pi}\right), \tag{4.28}$$

for $x > 0$, with a mean of unity and a cumulative distribution $Erf(\frac{x}{\sqrt{\pi}})$. The latter is compared to our ED results in figure 4.5, and seen to agree with them.

The important physical point here is $P_{\rm rel}(x)$ has a mean of unity and fluctuations that are also $\mathcal{O}(1)$. This means the probabilities are essentially uniformly distributed across a row; as evident from eq. 4.26, where if all the $P_{IJ}(t)$ on a row are comparable $x \sim \mathcal{O}(1)$. This is of course symptomatic of the ergodic behaviour one expects at weak disorder, where at long times the $P_{IJ}(t)$ are homogeneously distributed across all sites of the FS graph.

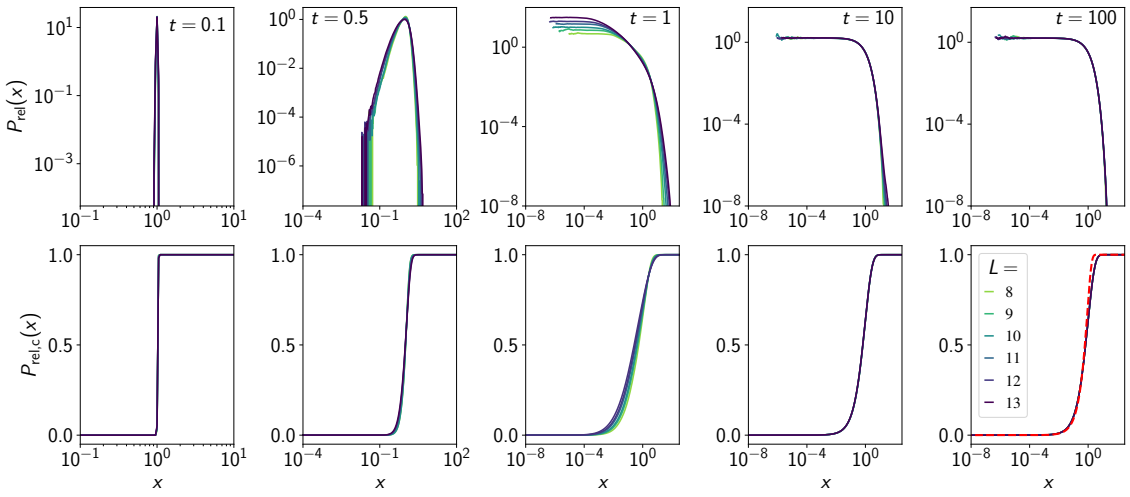


Figure 4.5: For $W = 1$. The top panel shows the distribution of $P_{\rm rel}(x)$ of x (eq. 4.25), at the t's specified, and for system sizes $L = 8 - 13$. The bottom panel shows the cumulative distribution $P_{{\rm rel},c}(x)$ (eq. 4.27). Red dashed line in final panel shows the half-Gaussian fit to the data.

We shall now consider the case of $W = 7$, representative of the MBL phase, for which the results are shown in figure 4.6. The situation is very different here since - particularly in the wings of $P_{\rm rel}(x)$ - the distribution is clearly not converging with L for any t, save for $t \lesssim 0.1$, as known from our short time analytical results

(discussed on pg. 77). This is exactly what is expected as the long-time value of $\langle R \rangle = \int dx\ x^2\ P_{\rm rel}(x)$ grows with increasing L (discussed in section 4.1.4).

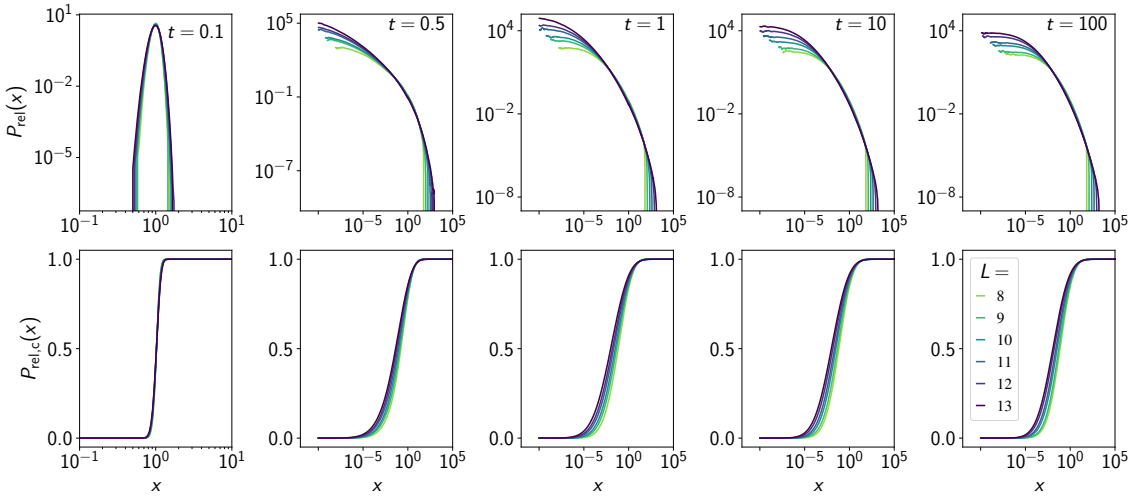


Figure 4.6: For $W = 7$. The top panel shows the distribution of $P_{\rm rel}(x)$ of x (eq. 4.25), at the t's specified, and for system sizes $L = 8 - 13$. The bottom panel shows the cumulative distribution $P_{{\rm rel},c}(x)$ (eq. 4.27).

The question then is: what feature of the long-time distribution $P_{\rm rel}(x)$ determines this behaviour? It must surely arise from the long-tails in $P_{\rm rel}(x)$ which are 'filling out' in an obvious sense with increasing L.

To examine this consider the effective cumulative distribution,

$$F_c(x) = \int_0^x dy\ y^2\ P_{\rm rel}(y), \tag{4.29}$$

giving the contribution to $\langle R \rangle$ arising from different parts of the $P_{\rm rel}(x)$ distribution, with

$$\langle R \rangle = \int_0^\infty dy\ y^2\ P_{\rm rel}(y) = F_c(\infty). \tag{4.30}$$

$F_c(x)$ is shown in figure 4.7 (dashed line and right axis), together with $P_{\rm rel}(x)$ itself, eq. 4.25 (solid line and left axis) for system sizes $L = 8 - 13$. We add in passing that while the large x behaviour of $P_{\rm rel}(x)$ does not appear to be a pure power-law, it is quite well captured by $P_{\rm rel}(x) \sim a x^{-n} \ln[x]$ (with $n \simeq 2.3$), which is shown as a

dashed line in figure 4.7. The fact that $P_{\rm rel}(x)$ has a modified power-law distribution, means that there are significant fluctuation in $\{P_{IJ_r}(t)\}$ within a given row r, in the MBL phase at long times.

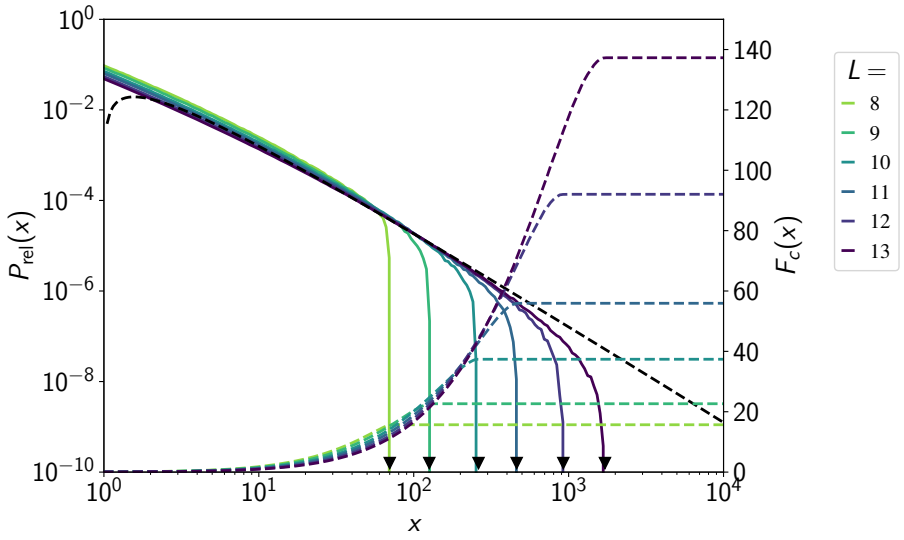


Figure 4.7: For $W = 7$, with $t = 100$. $F_c(x)$ *vs* x (dashed lines, right hand scale), shown for $x > 1$ and $L = 8 - 13$; and $P_{\rm rel}(x)$ (solid line, left scale). Black arrows shown $N_r = \binom{L}{\frac{L}{2}}$ for even L and $N_r = \binom{L}{\frac{L\pm1}{2}}$ for odd L. Dashed black line shows fit of $P_{\rm rel}(x)$ data to $P_{\rm rel}(x) \sim ax^{-n}\ln[x]$ (with $n \simeq 2.3$).

Figure 4.7 shows that $F_c(x)$ saturates at $x = x_m(L)$, the x value $P_{\rm rel}(x)$ crashes out in a self-evident senses. $x_m(L)$ grows strongly with L, and the $F_c(x)$ collapse onto an essentially common curve.

As shall be discussed below the maximum possible value of x (eq. 4.26) in $P_{\rm rel}(x)$ is $N_r = \binom{N}{r}$, and is thus exponentially large in L for a fixed $\frac{r}{L}$. That this is indeed the $x_m(L)$ that $P_{\rm rel}(x)$ crashes out is shown in figure 4.7, where the black arrows show $N_r = \left(\frac{L}{\frac{L}{2}}\right)$ for even L and $N_r = \left(\frac{L}{\frac{L\pm1}{2}}\right)$ for odd L.

The fact that the $\max(x) = N_r$ is evident from eq. 4.26 (pg. 91). Since all $P_{IJ} \geq 0$ then over the set of probabilities P_{IJ} for all N_r sites on row r, it arises when one probability call it P^*_{IJ} dominates all the others (such that $P_I(r;t) = \sum_{J;r_{IJ}=r} P_{IJ} = P^*_{IJ}$). More generally, if the set of P_{IJ} that are non-negligible are an $\mathcal{O}(1)$ number of FS sites J on row r then the associated x is $\mathcal{O}(N_r)$.

Figure 4.7 shows that it is the large-x behaviour of $P_{\mathrm{rel}}(x)$ which governs the second moment $\langle R \rangle$ and consequently all higher order moments of the distribution. Physically, this arises due to FS sites J that greatly exceed the mean probability $N_r^{-1} \sum_{J;r_{IJ}=r} P_{IJ}$ on a row, which is symptomatic of the MBL phase for sufficiently long time. It is expected that there are strong inhomogeneity in the $\{P_{IJ_r}(t)\}$ on a given row r.

In the first part of this chapter, we have examined lateral transport within the TFI model. We have shown that there are three time-regimes for lateral transport. A short time regime which is agnostic to whether the system is in the ergodic or the MBL phase, with the $\{P_{IJ_r}(t)\}$ distributed homogeneously within a given row. This is followed by an intermediate time regime, which is again independent of whether the system is in the ergodic phase or the MBL phase, there is strong inhomogeneity in the set of $\{P_{IJ_r}(t)\}$ within a given row r. In the ergodic phase, this gives way to homogeneity in the $\{P_{IJ_r}(t)\}$ at long times. While in the MBL phase, this inhomogeneity persists for all times.

Having extensively discussed lateral transport, we shall now move on to consider two quantities which probe how the inhomogeneity in the probabilities across the entire FS evolve with time; namely the time dependent IPR and participation entropy.

4.2 Time dependent IPR and participation entropy

4.2.1 Introducing the relevant quantities

In a previous section of this chapter (pgs. 81-83) we studied the time evolution of

$$\langle R \rangle(t) = N_r \; I_{2,r}(t), \tag{4.31}$$

with $I_{2,r}(t)$ a row-resolved IPR. This quantity enabled us to understand how homogeneously the $\{P_{IJ}(t)\}$ are distributed on a given row r, a Hamming distance r away from our initial site, and how this depended on time.

It is clearly also of interest to understand how homogeneously spread the probabilities are across the entire FS graph. To this end, we shall now examine two quantities that probe this; namely the time dependent IPR and participation entropy.

As a reminder, the time-dependent wavefunction $|\Psi(t)\rangle$ for a system initialised on $|I\rangle$ at $t = 0$ is given by:

$$|\Psi(t)\rangle = \sum_J A_J^{[I]}(t) \, |J\rangle \, , \tag{4.32}$$

with the time-dependent probability amplitude of being on $|J\rangle$, $A_J^{[I]}(t) = G_{IJ}(t) = \langle J \, | \exp[-i\mathcal{H}t] \, | \, I \rangle$, such that $|A_J^{[I]}(t)|^2 = P_{IJ}(t)$. The usual studied inverse participation ratio [79, 88–100] is given by:

$$L_q = \frac{\sum_I |A_{nI}|^{2q}}{\sum_I |A_{nI}|^2} \tag{4.33}$$

with

$$L_q = \sum_I |A_{nI}|^{2q} \tag{4.34}$$

if the wavefunction is normalised. Probability is of course conserved for all times, meaning $\sum_J P_{IJ}(t) = \sum_J |A_J^{[I]}(t)|^2 = 1$. This means using eq. 4.33 the analogous time-dependent inverse participation ratio, for a given site I and disorder realisation,

$$L_{I,q}(t) = \sum_J |A_J^{[I]}(t)|^{2q} = \sum_J P_{IJ}^q(t). \tag{4.35}$$

This can be averaged over FS sites to give

$$L_q(t) = \frac{1}{N_H} \sum_I L_{I,q}(t), \tag{4.36}$$

which can then be further averaged over disorder realisations to give

$$\overline{L}_q(t) = \langle L_q(t) \rangle_d \tag{4.37}$$

with $\langle\rangle_d$ denoting the average over disorder realisations. The overline here denote an average over both initial FS sites $|I\rangle$ and disorder realisations.

From $\overline{L}_q(t)$ we can define a time-dependent multifractal exponent $\tau_q(t)$, where

$$\overline{L}_q(t) = C_q(t)\ N_H^{-\tau_q(t)}, \tag{4.38}$$

with $C_q(t)$ a system size-independent constant and N_H the FS dimension. It is well known in localisation phenomenon that the multifractal exponent distinguishes whether the wavefunction is Anderson localised, multifractal or extended [79, 88–100].

First, suppose the time-dependent wavefunction $|\Psi(t)\rangle$ is Anderson localised on

$\mathcal{O}(1)$ sites of the FS graph/lattice for any specified t, then clearly only $|A_J^{[I]}(t)|^2 \sim \mathcal{O}(1)$ for those sites, and zero for all other sites. From eqs. 4.35, 4.36 it therefore follow $L_q(t) \sim \mathcal{O}(1)$, and thus $\tau_q(t) = 0$. Second, suppose the time-dependent wavefunction $|\Psi(t)\rangle$ is essentially uniformly spread across all FS sites on the graph, and as such ergodic. In this case, $|A_J^{[I]}(t)|^2 \sim \frac{1}{N_H}$, which from eqs. 4.35, 4.36 means $L_q(t) \sim N_H^{1-q}$, and thus $\tau_q(t) = q - 1$. Finally, suppose the time-dependent wavefunction $|\Psi(t)\rangle$ is localised on a macroscopic number of sites which is a vanishing fraction of the total number of FS sites, e.g. N_H^{α} sites with $\alpha < 1$, it is known from previous work [79, 88–100] $0 < \tau_q < q - 1$ and that the wavefunction is fractal, and specifically if τ_q is a non-linear function of q the wavefunction is multifractal. Our numerical results in section 4.2.3 shall show that these three different behaviours of $\tau_q(t)$ occur for different times t in the dynamics in the ergodic phase and the MBL phase.

A complementary quantity which is known to probe how homogenously the wavefunction is distributed on FS is the first participation entropy [79, 101–103], which is given by:

$$S_1 = \sum_I |A_{nI}|^2 \ln[|A_{nI}|^2] \tag{4.39}$$

From the time-dependent wavefunction (eq. 4.32), given that $P_{IJ}(t) = |A_J^{[I]}(t)|^2$, with $A_J^{[I]}(t)$ the probability amplitude of $|\Psi(t)\rangle$ on $|J\rangle$ at time t given its initialization on $|I\rangle$ at $t = 0$, we can define a time-dependent first participation entropy

$$S_1(t) = \frac{1}{N_H} \sum_{I=1}^{N_H} S_{I,1}(t) : \quad S_{1,q} = -\sum_J P_{IJ}(t) \ln[P_{IJ}(t)]. \tag{4.40}$$

We will focus on the disorder-averaged $S_1(t)$,

$$\overline{S}_1(t) = \langle S_1(t) \rangle_d. \tag{4.41}$$

The overline here again denotes an average over FS sites and disorder realisations.

From $\overline{S}_1(t)$ we can define $a_1(t)$ and $b_1(t)$, where

$$\overline{S}_1(t) = a_1(t)\ln[N_H(t)] + b_1(t)\ln[\ln[N_H]], \tag{4.42}$$

with $a_1(t)$ and $b_1(t)$ independent of the system size L.

Similarly to τ_q, a_1 [79, 101–103] is known to distinguish whether the wavefunction is Anderson localised, fractal or extended.

Let us first suppose that the time-dependent wavefunction $|\Psi(t)\rangle$ is Anderson localised on $\mathcal{O}(1)$ sites of the FS graph/lattice. Clearly $P_{IJ}(t) = |A_J^{[I]}(t)|^2 \sim \mathcal{O}(1)$ for these sites, and zero for all other sites. From eq. 4.40, $S_1(t) \simeq 0$, meaning (from eq. 4.42) $a_1(t) = 0$. If by contrast, the wavefunction is uniformly spread across the entire FS graph and is therefore ergodic, $P_{IJ}(t) = |A_J^{[I]}(t)|^2 \sim \frac{1}{N_H}$. This mean $S_1(t) \sim \ln[N_H]$, meaning - using eq. 4.42 - $a_1(t) = 1$. While if $0 < a_1(t) < 1$ it is known from the literature [79, 101–103] that the wavefunction is fractal. We shall observe these different behaviours for $a_1(t)$ in our numerical results in section 4.2.3.

Throughout section 4.2.3 we shall focus on the time-dependence of $\tau_q(t)$ and $a_1(t)$ in both the ergodic phase and the MBL phase. But first we shall return to our exact short-time analytical results to discuss the short-time behaviour of $\tau_q(t)$, and hence the emergence of multifractality.

4.2.2 Emergent multifractality

In the previous chapter of this thesis (pgs. 39-43) we showed that at short times,

$$P_{IJ_r}(t) = (\Gamma t)^{2r}\left[1 - (\Gamma t)^2\right]^{L-r} : \quad \Gamma t << 1, \tag{4.43}$$

independent of the initial site I, final site J_r in row r, or the disorder strength, W. Clearly eq. 4.43 can be equivalently written in binomial form as

$$P_{IJ_r}(t) = z(t)^r[1 - z(t)]^{L-r}, \tag{4.44}$$

with

$$z(t) = (\Gamma t)^2 . \tag{4.45}$$

Since $P_{IJ_r}(t)$ is independent of the disorder realisation or initial site I, $L_{I,q}(t) = L_q(t) = \overline{L}_q(t)$ (eqs. 4.35, 4.36, 4.37). This means

$$\overline{L}_q(t) = \sum_{r=0}^{L} \binom{N}{r} P_{IJ_r}(t)^q. \tag{4.46}$$

Using eq. 4.44 for $P_{IJ_r}(t)$ it follows that

$$\overline{L}_q(t) = \left((1 - z(t))^q + z(t)^q\right)^L . \tag{4.47}$$

Assuming $C_q(t) = 1$ for short times, from eq. 4.47 and the definition of $\tau_q(t)$ (eq. 4.38, pg. 97), clearly

$$\tau_q(t) = -\log_2\left[(1 - z(t))^q + z(t)^q\right] = \frac{-\ln\left[(1 - z(t))^q + z(t)^q\right]}{\ln[2]}. \tag{4.48}$$

From eq. 4.48, for $t = 0$, as $z(0) = 0$ (eq. 4.45), $\tau_q = 0$, reflecting the fact that $|\Psi(t = 0)\rangle = |I\rangle$ is Anderson localised on a single FS site $|I\rangle$. However, for any non-zero $\Gamma t << 1$ - the time regime this calculation is valid - $z(t) << 1$. From eq. 4.48 it is clear that $\tau_q(t)$ is a non-linear function of q with $0 < \tau_q(t) << q - 1$.

The wavefunction is therefore multifractal at these short-time scales. Moreover the behaviour arises for any disorder strength W. Emergent multifractality is there-

fore common both to W's for which the system is ergodic at long times, as well as for W's the system is MBL at long times. We shall see that this is observed in our numerics in the next section (4.2.3).

In the next section, we will consider explicitly $\tau_2(t)$ and $a_1(t)$. We will therefore consider the analytical short-time result for $\tau_2(t)$. From eq. 4.48 it follows that

$$\tau_2(t) = \frac{-1}{\ln[2]} \ln\left[1 - 2(\Gamma t)^2 + 2(\Gamma t)^4\right]. \tag{4.49}$$

This means the short-time $\tau_2(t)$ (using a Taylor expansion) is given by:

$$\tau_2(t) \sim \frac{2}{\ln[2]} (\Gamma t)^2. \tag{4.50}$$

We will compare this result to our results obtained by ED at short times in the next section.

Having extensively discussed the short-time behaviour, we shall now move onto discuss our ED results for $\tau_2(t)$ and $a_1(t)$.

4.2.3 Numerical results for $\tau_2(t)$ and $a_1(t)$

As a reminder $\tau_q(t)$ is defined as

$$\overline{L}_q(t) = C_q(t) N_H^{-\tau_q(t)}, \tag{4.51}$$

with $C_q(t)$ an L-independent constant. In order to determine $\tau_2(t)$ for a chosen time t, $\overline{L}_2(t)$ has to be calculated for a range of different system sizes L (in our calculations $L = 8 - 13$). For a chosen t, a plot of $\ln[\overline{L}_2(t)]$ *vs* $\ln[N_H]$ gradient gives $-\tau_2(t)$. Appendix E shows that the $\ln[\overline{L}_2(t)]$ *vs* $\ln[N_H]$ data has a good linear fit.

Figure 4.8 shows $\tau_2(t)$ obtained by ED for a range of disorder strengths W in both

the ergodic phase and the MBL phase. This figure shows that at $\Gamma t \lesssim 0.1$, $\tau_2(t)$ is W-independent and is well captured by our short-time exact result $\tau_2(t) \sim \frac{2}{\ln[2]} (\Gamma t)^2$ (derived in the previous section 4.2.2). Figure 4.8 shows that for these short times, $0 < \tau_2(t) < 1$ (and finite) for all W, meaning $|\Psi(t)\rangle$ in both phases has become multifractal. Multifractality therefore emerges from the dynamics at $\mathcal{O}(1)$ times independent of whether the system is in the ergodic phase or the MBL phase.

Figure 4.8 shows that for $W = 6, 7$, illustrative of the MBL phase, $\tau_2(t) < 1$ for all times. This means this emergent multifractality found at short times persists for all times in the MBL phase. Physically this reflects that the $\{P_{IJ}(t)\}$ remain inhomogeneously distributed across the FS sites of the graph in the MBL phase for all times.

By contrast, figure 4.8 shows that for $W = 1, 1.5, 2$, illustrating the ergodic phase, $\tau_2(t)$ grows with t, and ultimately ends at $\tau_2(t) = 1$ $(q - 1)$. As discussed in section 4.2.1, the long-time value of $\tau_2(t) = 1$ reflects that the $\{P_{IJ}(t)\}$ are uniformly distributed across the FS at long times in the ergodic phase, with the long-time $P_{IJ}(t) \sim \frac{1}{N_H}$ for all sites J.

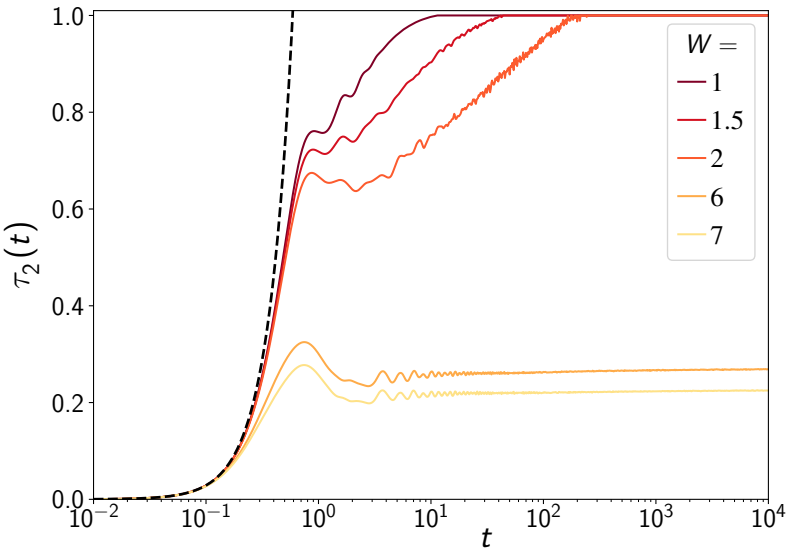


Figure 4.8: t-dependence of the IPR exponent $\tau_2(t)$ obtained by ED calculations with $W = 1, 1.5, 2$ exemplifying ergodic behaviour and $W = 6, 7$ MBL behaviour. Dashed line shows the low-t asymptotic behaviour, $\tau_2(t) \sim \frac{2(\Gamma t)^2}{\ln[2]}$.

We can also examine $a_1(t)$, where

$$\overline{S}_1(t) = a_1(t)\ln[N_H] + b_1(t)\ln[\ln[N_H]]. \tag{4.52}$$

In our exact diagonalisation calculations, for a given t and W, $\overline{S}_1(t)$ is calculated for $L = 8 - 13$, and then the curves fitted to eq. 4.52. Appendix E shows that $S_1(t)$ is well-fitted to eq. 4.52.

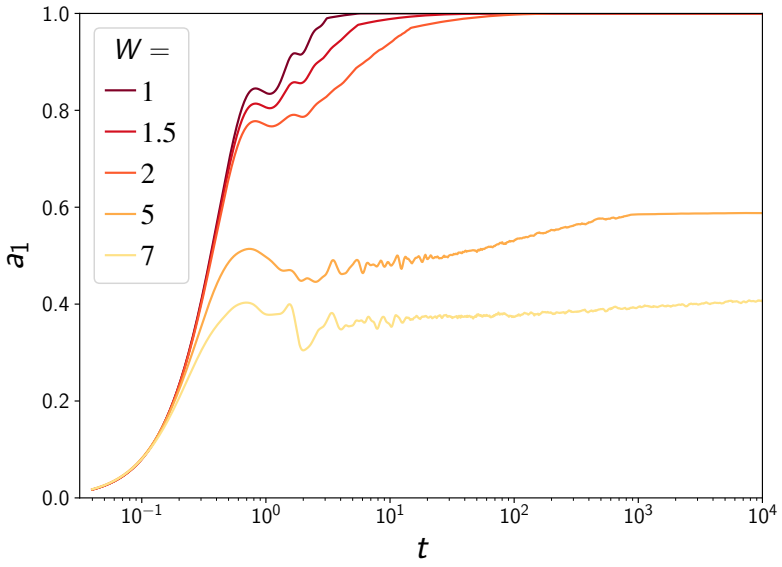


Figure 4.9: t-dependence of the first participation entropy exponent $a_1(t)$ obtained by ED calculations with $W = 1, 1.5, 2$ exemplifying ergodic behaviour and $W = 6, 7$ MBL behaviour.

Figure 4.9 shows how $a_1(t)$ obtained by ED varies with t for a range of disorder strengths W, in both the ergodic phase and the MBL phase. This figure again shows that at $\Gamma t \lesssim 0.1$, $a_1(t)$ is W-independent, with $0 < a_1(t) < 1$. It thus follows that at short times that the time-dependent wavefunction, $|\Psi(t)\rangle$, in both phases has become multifractal. The time evolution of $\overline{S}_1(t)$ therefore provides further evidence of the emergence of multifractality on $\mathcal{O}(1)$ timescales.

Figure 4.9 shows that for $W = 6, 7$, illustrative of the MBL phase, $a_1 < 1$ for all times. Just as for $\tau_2(t)$ this means that multifractality persists for all times in the MBL phase. While for $W = 1, 1.5, 2$, illustrating the ergodic regime, a_1 grows with

t, and ultimately ends at $a_1 = 1$, indicative of ergodic behaviour.

The essential result from this section is that in either phase there is an emergent multifractality of the wavefunction at $t \sim \mathcal{O}(1)$. While at long times this is arrested in the ergodic phase, this multifractality persists for all times in the MBL phase.

4.3 Examining 'self-averaging': $P_{m;rel}(x)$

In the last two chapters, we have discussed extensively various ways to probe probability transport on the FS graph in the TFI model. We shall now change tact, and briefly discuss how the probability of being found on a row r depends on the FS site $|I\rangle$ or the disorder realisation considered.

As a reminder, the essential quantity examined in chapter 3 was $P_I(r;t) = \sum_{J;r_{IJ}=r} P_{IJ}(t)$ (eq. 3.4, pg. 34), which measures the probability of being found on row r, a Hamming distance of r away from the initial FS site $|I\rangle$. In particular, in chapter 3, we focused on the average $P_I(r;t)$, taken over the initial FS sites $|I\rangle$ and disorder realisations, $\overline{P}(r;t)$. The question we seek to answer in this section is how does $P_I(r;t)$ vary with the initial FS site I and/or the disorder realisation?

To this end, we can define the distribution,

$$\tilde{P}_{m;rel}(x) = N_H^{-1} \sum_I \left\langle \delta\left(x - \frac{P_I(r;t)}{\overline{P}(r;t)}\right)\right\rangle_d, \tag{4.53}$$

with $\overline{P}(r;t) = \langle P_I(r;t)\rangle_{d,I}$, the disorder and FS-site averaged $P_I(r;t)$. Just as in the last section, we shall choose to examine $\tilde{P}_{m;rel}(x)$ for the middle point of the FS graph, $\frac{r}{2}$ for even L, and $\frac{r-1}{2}$ for odd L. The key results are not, however, dependent on this choice. This is shown explicitly in appendix F, by showing $\tilde{P}_{m;rel}(x)$ for other r values.

The top row of figures 4.10 and 4.11 show $\tilde{P}_{rel;m}(x)$ of x at the t's specified, for $L-8-13$ for $W = 1$ (characteristic of the ergodic phase) and $W = 7$ (characteristic

of the MBL phase) respectively. While, the bottom row of these figures show the corresponding cumulative distribution,

$$\tilde{P}_{m;rel,c}(x) = \int_0^x dy\ \tilde{P}_{m;rel}(y). \tag{4.54}$$

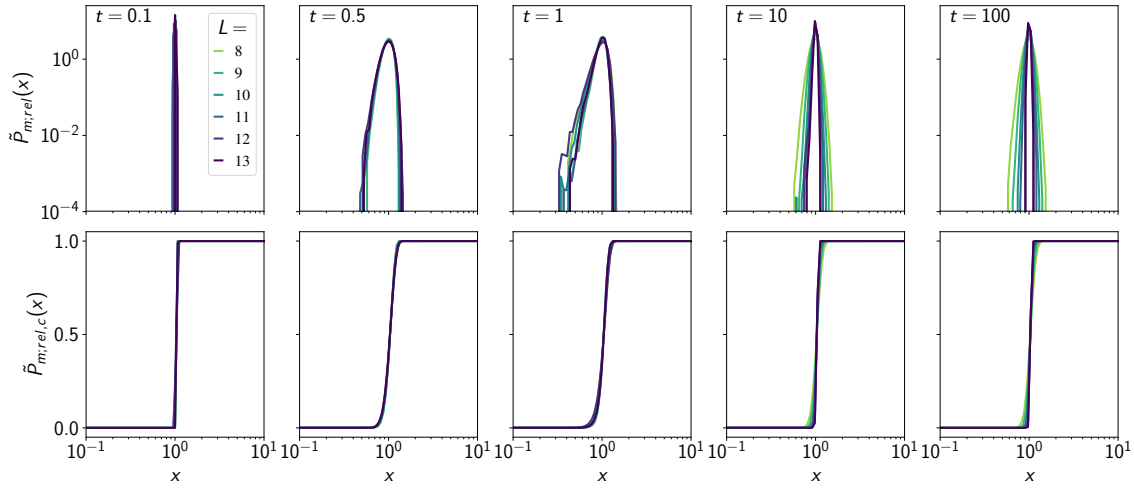


Figure 4.10: For $W = 1$. Top panel shows the distribution of $\tilde{P}_{rel;m}(x)$ of x (eq. 4.53), at the t's specified, and $L = 8 - 13$. The bottom panel shows the cumulative distribution $\tilde{P}_{rel;m,c}(x)$ (eq. 4.54)

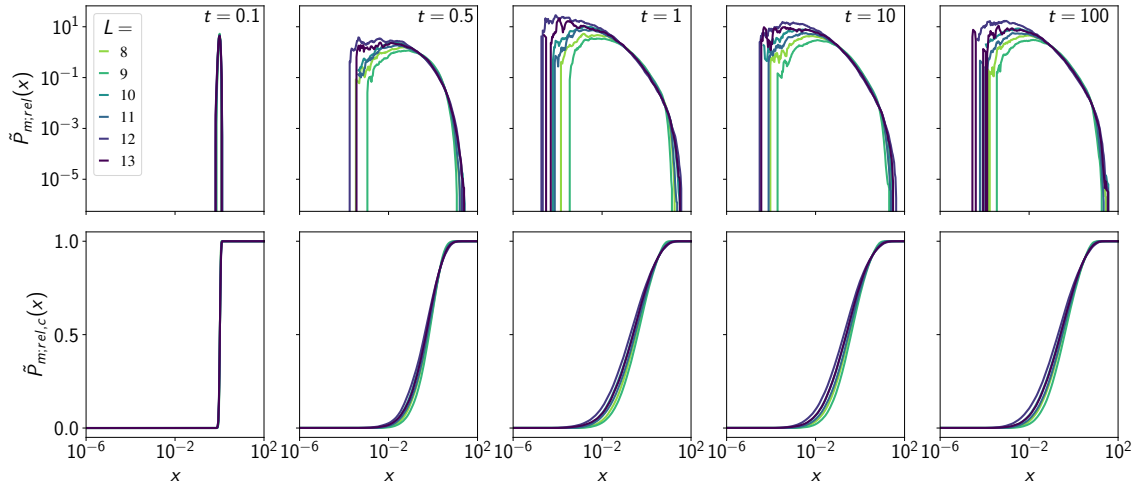


Figure 4.11: For $W = 7$. The top panel shows the distribution of $\tilde{P}_{rel;m}(x)$ of x (eq. 4.53), at the t's specified, and for system sizes $L = 8 - 13$. The bottom panel shows the cumulative distribution $\tilde{P}_{rel;m,c}(x)$ (eq. 4.54).

Figures 4.10 and 4.11 show that for $t \lesssim 0.1$, $\tilde{P}_{rel;m}(x)$ is δ-distributed on $x = 1$, as expected from our short-time analytical results (pgs. 39-42). Physically, this occur

as at short times $\{P_{IJ_r}(t)\}$ are independent of the initial FS site $|I\rangle$ or disorder realisation, and depend only on the Hamming distance between a pair of sites $|I\rangle$ and $|J_r\rangle$.

Figure 4.10 shows that in the ergodic phase for $t \gtrsim 10$, $\tilde{P}_{rel;m}(x)$ rapidly narrows with increasing L, and is thus δ-distributed on $x = 1$ in the thermodynamic limit. This means at long times in the ergodic phase $P_I(r;t)$ is independent of the disorder realisation or the initial FS site. This occurs as deep in the ergodic phase, at long times there is homogeneity in the set $\{P_{IJ}(t)\}$ across the FS graph. The difference in $P_I(r;t)$ for different rows solely occurs due to each row having a different number of FS sites, $N_r = \binom{N}{r}$, which is an inherent property of the FS graph, and is independent of the initial FS site I at the apex of the graph (discussed in chapter 2). For $t \simeq 1$, figure 4.10 shows that $\tilde{P}_{rel;m}(x)$ appear converged with system size. It, however, remains a very narrow distribution. It therefore follows that there are only small fluctuations in the intermediate time, $t \simeq 1$, $P_I(r;t)$, depending on the initial FS site or disorder realisation. This means for all times in the ergodic phase $\{P_I(r;t)\}$ all are well-captured by the average $\overline{P}(r;t)$.

By contrast, figure 4.11 shows that in the MBL phase ($W = 7$) that for all but the smallest t values - for which our short-time analytical results apply - $\tilde{P}_{rel;m}(x)$ is a broad distribution, which broadens with increasing L. The cumulative distribution, $\tilde{P}_{rel;m,c}(x)$, confirms this, as $\tilde{P}_{rel;m}(x)$ has significant weight over several orders of magnitude. This means that $P_I(r;t)$ in the MBL phase depend strongly on the initial FS site and/or disorder realisation. Physically, this reflect the strong inhomogeneity of the $\{P_{IJ}(t)\}$ in the MBL, which changes depending on the FS site $|I\rangle$ or the disorder realisation considered.

4.4 Issues with the 'simple' spin flipping picture

To conclude this chapter, we shall briefly discuss the issue with a 'simple spin flipping picture'. This shall link into our next chapter on multifractality and related distributions.

The long-time multifractality of the eigenstates in the MBL phase is often explained by considering the system to be composed of 'frozen spins' and spins that are able to 'flip' [96, 97]. Our analytical results in the TFI model, however, suggest that this simple minded picture may not be entirely correct.

Our short-time analytical results for $P_{IJ_r}(t)$, show that within a given row the short-time $P_{IJ_r}(t)$ for all sites J_r on the row are the same. As each site correspond to a different set of r spins being flipped from $|I\rangle$, this means the extent each of the l spin has flipped is the same, meaning their autocorrelation function decay by the same amount at short times. Physically, at short times this is due to all spins on the set of real space sites l moving from being aligned along the z axis to some tilted axis in the xz plane, which is independent of the real space site l (discussed on pg. 41) . The spins therefore remain coherent at this time scale. It is the fact that all the spins rotate from being aligned along the z axis to some tilted axis in the xz plane which leads to the emergent multifractality at $\mathcal{O}(1)$ times.

This result is entirely due to the quantum mechanical nature of the problem, and cannot be recovered by any toy classical model based on the mental picture of 'flipping spins'.

Similarly, when $J_z = 0$, as the Hamiltonian is site-separable the spins on real space sites l time evolution simply occurs as the spins individually move from being aligned along the z axis to somewhere in xz plane, with the exact angle depending on the strength of the field, h_l, relative to the strength of the hopping, Γ (discussed

in chapter 2 and 5). As discussed in the next chapter it is the fact that $\mathcal{O}(1)$ spins are rotated away from the z axis which leads to the emergent multifractality of $|\Psi(t)\rangle$ at long times, not as is claimed in the literature due to a mixture of frozen and flippable spins [96, 97].

As our $J_z \neq 0$ problem is perturbatively connected to MBL_0 [59], we expect this effect leads to the emergent multifractality and decay of $\overline{C}(t)$ in the interacting problem also at short times.

In appendix G, we briefly consider a quantity which measures the difference in decay of $C_{ll}^{[n]}(t)$ for each of the different real-space sites l. This quantity further confirms that at short times independent of W the decay of all $\{C_{ll}^{[n]}(t)\}$ are the same. Something that is clearly recovered from our short-time analytical results.

4.5 Overview of probability transport

The essential question we set to answer in the last two chapters was: given an initial spin configuration, how do the probability densities of the time evolving state spread out on the FS graph of the TFI model?

In the course of investigating this question a rather rich phenomenology was uncovered. This can be summarised by considering three time windows, which are shown in figure 4.12 and discussed below. In the following discussion t_H denotes the Heisenberg time, which was introduced in chapter 2, and sets the natural 'maximum' timescale for our problem. As a reminder throughout this thesis $\Gamma = 1$.

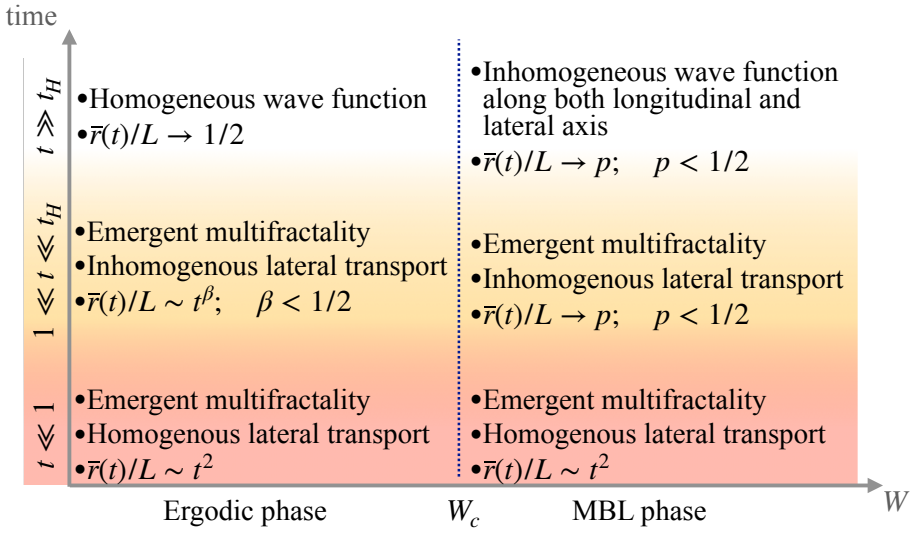


Figure 4.12: Schematic summary of the three main time windows for the dynamics, and their characteristic features in the ergodic phase and the MBL phase.

- **Short times** $t << 1$: In this regime, the system is agnostic to which phase it is in, ergodic or MBL. The dynamics on these scales is characterised by an emergent multifractality of the time evolving state, but homogenous probability transport across rows of the FS graph. Another feature of this time regime is that $\overline{r}(t) \sim \mathcal{O}(L)$ for any t, however small. By the relationship we have uncovered, $\overline{C}(t) = 1 - \frac{2\overline{r}(t)}{L}$, this ensures that $\overline{C}(t) < 1$. The fractal exponent $\tau_2(t)$ as well as the emergent length scale, $\overline{r}(t)$, grow $\propto t^2$ in this regime.

- **Intermediate times** $1 \lesssim t << t_H$: This is arguably the most interesting dynamical regime. While the emergent multifractality of the wavefunction persists, albeit with increasing $\tau_2(t)$, strong inhomogeneity in the lateral transport set in. This manifests itself in $P_R(x)$ and $P_{rel}(x)$ not converging with L. On these time scales in the ergodic phase $\overline{r}(t)$ grows subdiffusively, with an anomalous power law decay of $\overline{C}(t)$. In the MBL there is a power law envelope to the decay of the oscillations of $\overline{C}(t)$, but with a clear signatures of the incipient saturation to a finite value.

- **Long times** $t \gtrsim t_H$: This is the regime where the dynamics is essentially

saturated and one sees eigenstate properties. In the ergodic phase, the multifractality gives way to a fully extended homogeneous state, reflected in $\tau_2 = 1$, $\langle R \rangle \sim \mathcal{O}(1)$, and $P_R(x)$ and $P_{rel}(x)$ converging with increasing system size L. This is qualitatively different from the MBL phase, where multifractality and inhomogeneity persists for all times, meaning $\tau_2 < 1$, $\langle R \rangle$ grows with increasing L, and $P_R(x)$ exhibits a heavy-tailed Lévy distribution.

Throughout the last two chapters, we have extensively discussed probability transport within the TFI model. We shall now move away from considering time-dependent properties to examining properties of the eigenstates themselves. In the next chapter, we shall start this discussion by considering quantities relevant to probing the multifractality of the many-body eigenstates on the FS graph.

Chapter 5

Multifractality and associated distributions

5.1 Introduction

The properties of the many-body eigenstates are known to be qualitatively different on either side of the MBL transition. This is reflected in the very different behaviour of e.g. the IPR [79, 88–103] and the Entanglement Entropy [8, 60, 107, 183–185] (discussed in chapter 1).

In the previous two chapters, we showed that at long times in the ergodic phase, the time-dependent wavefunction, $|\Psi(t)\rangle$, is uniformly distributed across the FS graph, while in the MBL phase, the long-time $|\Psi(t)\rangle$ remains inhomogeneous. This was reflected in the time-dependent multifractal exponent $\tau_2(t)$ (figure 4.8, pg. 102), where the long-time $\tau_2(t) = 1$ in the ergodic phase, and $\tau_2(t) < 1$ in the MBL phase.

The long-time behaviour of a quantum system is well known to reflect the properties of its eigenstates [61, 84, 129, 186]. This can be understood from the equation for $P_{IJ}(t)$ (eq. 3.2, pg. 32), with

$$P_{IJ}(t) = \sum_{n,m} \exp\left[-i(E_n - E_m)t\right] \; A_{nI}A_{nJ}A_{mI}A_{mJ}. \tag{5.1}$$

At long-time, the rapid oscillations in the $\exp\left[-i(E_n - E_m)t\right]$ term means only the

$m = n$ terms survive in the sum in eq. 5.1, and hence

$$P_{IJ}(\infty) = \sum_n A_{nI}^2 A_{nJ}^2. \tag{5.2}$$

The essential quantities in eq. 5.2 are the set of squared amplitudes of the eigenstates, $\{|n\rangle\}$, on FS sites $|J\rangle$, $\{A_{nJ}^2\}$.

In order to understand how at long times, the time-dependent wavefunction is distributed across the FS sites of the graph, we clearly need to understand how for a given eigenstate $|n\rangle$, the $\{A_{nJ}^2\}$ are distributed across the FS graph. Additionally, since the many-body localisation transition is an eigenstate transition - the properties of the eigenstates are fundamentally different in the ergodic phase and the MBL phase - studying how $\{A_{nJ}^2\}$ are distributed across the FS is clearly of central interest. It is well known in the literature [79, 88–100] that this can be understood by examining the generalised IPR, L_q, and its corresponding multifractal exponent, τ_q (defined in the next section). These two quantities - and related distributions - shall be the main focus of this chapter.

In chapter 3 (pgs. 48-49), we discussed that it is well known in localisation phenomena [78–81] that eigenstates with eigenenergies $E_n = \omega$, from different regions of the band, $D(\omega)$ (eq. 3.30, pg. 48), localise at different disorder strengths, denoted $W_c(\omega)$. Throughout this chapter, we shall therefore focus on one region of the band - the band-centre - whose critical disorder strength is known to be $W_c \simeq 4$ [62] from calculations obtained using the system sizes amenable to numerics, with the thermodynamic limit W_c believed to be much larger [152, 156, 163, 164, 166–169, 187] (discussed in chapter 1).

5.1.1 Defining relevant quantities

In chapter 2 we discussed that the Hamiltonian,

$$\mathcal{H}_{TFI} = \sum_{l=1}^{L} \left(h_l \hat{\sigma}_l^z + \Gamma \hat{\sigma}_l^x + J_z \hat{\sigma}_l^z \hat{\sigma}_{l+1}^z \right), \tag{5.3}$$

can be rewritten as a tight-binding model in FS, i.e.

$$\mathcal{H}_{TFI} = \sum_{I} \mathcal{E}_I \left| I \right\rangle \left\langle I \right| + \sum_{I,J}{}' \Gamma \left| I \right\rangle \left\langle J \right|. \tag{5.4}$$

The FS sites $\{|I\rangle\}$ are simply product states of the $\hat{\sigma}_l^z$ operator, i.e. $|I\rangle = \bigotimes_{l=1}^{N} |\sigma_l^z\rangle = |\{\sigma_l^z\}\rangle$, whose FS site energies, $\mathcal{E}_I = \left\langle I \left| \sum_{l=1}^{L} \left(h_l \hat{\sigma}_l^z + J_z \hat{\sigma}_l^z \hat{\sigma}_{l+1}^z \right) \right| I \right\rangle$. The prime in eq. 5.4 indicates the hopping is between nearest neighbour FS sites which differ by a single spin flip, and are connected by one of the $\{\hat{\sigma}_l^x\}$ operators.

The eigenstates of $\mathcal{H}_{TFI}$, $\{|\Psi_n\rangle\}$, can be written as a sum over all FS sites $\{|I\rangle\}$, i.e.

$$|\Psi_n\rangle = \sum_{I} A_{nI} \left| I \right\rangle, \tag{5.5}$$

with $A_{nI} = \langle n|I\rangle$, the probability amplitude of eigenstate $|\Psi_n\rangle$ on FS site $|I\rangle$. We would like to understand how a given eigenstate $|\Psi_n\rangle$ is distributed across the FS lattice/graph. The essential quantity considered to understand this is the generalised IPR [79, 88–100], for a given eigenstate and disorder realisation,

$$L_q = \sum_{I} |A_{nI}|^{2q}. \tag{5.6}$$

From L_q we can define the fractal exponent τ_q which gives the dependence of the

IPR on the FS dimension N_H, with

$$L_q = C_q N_H^{-\tau_q} : \quad \tau_q = \frac{-\ln\left[\frac{L_q}{C_q}\right]}{L\ln[2]}. \tag{5.7}$$

C_q is customarily assumed to be a W-dependent constant, which is independent of the disorder realisation considered. In both the ergodic and MBL phases L_q is found to decrease exponentially with increasing L (discussed in sections 5.2.3 and 5.3), it is therefore sensible to define

$$u_q = \ln[L_q], \tag{5.8}$$

which only depends linearly on the system size L.

The three quantities we shall focus on in this chapter are u_q, L_q and τ_q. The values of L_q, u_q and τ_q will clearly depend on the particular disorder realisation considered. It evidently would be of interest to determine how these quantities vary between different disorder realisations. To this end, we define the probability distributions,

$$P_{L_q}(x) = \langle \delta(x - L_q)\rangle_{n,d}, \quad P_{u_q}(x) = \langle \delta(x - u_q)\rangle_{n,d}, \quad P_{\tau_q}(x) = \langle \delta(x - \tau_q)\rangle_{n,d}, \tag{5.9}$$

where $\langle\rangle_{n,d}$ here denotes the average taken over band-centre eigenstates - typically we choose to examine the 25 eigenstates nearest the band centre per disorder realisation - and disorder realisations.

Given the distributions $P_{L_q}(x)$, $P_{u_q}(x)$ and $P_{\tau_q}(x)$ we can define their first moments

$$\langle L_q\rangle = \int dx\ x\ P_{L_q}(x), \quad \langle u_q\rangle = \int dx\ x\ P_{u_q}(x), \quad \langle \tau_q\rangle = \int dx\ x\ P_{\tau_q},(x), \tag{5.10}$$

which shall be examined throughout this chapter.

It will also prove helpful for later use to define

$$P_{\tilde{u}_q}(x) = \int du\ P_{u_q}(u)\ \delta\left(x - \frac{u - \langle u_q \rangle}{\sigma_{u_q}}\right), \tag{5.11}$$

$$P_{\overline{u}_q}(x) = \int du\ P_{u_q}(u)\ \delta\left(x - \frac{u}{\langle u_q \rangle}\right), \tag{5.12}$$

and

$$P_{\overline{\tau}_q}(x) = \int du\ P_{\tau_q}(u)\ \delta\left(x - \frac{u}{\langle \tau_q \rangle}\right), \tag{5.13}$$

where $\langle u_q \rangle$ is the mean and $\sigma^2_{u_q} = \langle u_q^2 \rangle - \langle u_q \rangle^2$ is the variance of the distribution $P_{u_q}(x)$, and $\langle \tau_q \rangle$ is the mean of $P_{\tau_q}(x)$. It is worth pointing out here that as

$$u_q = \ln[C_q] - \tau_q\ L \ln[2], \tag{5.14}$$

we expect the behaviour of $P_{\overline{u}_q}(x)$ and $P_{\overline{\tau}_q}(x)$ to be very similar, which will indeed be shown numerically later in this chapter (section 5.2.4).

Throughout this chapter, we shall examine how the relevant probability distributions and their first moments, $\langle u_q \rangle$, $\langle L_q \rangle$ and $\langle \tau_q \rangle$, vary with system size L and disorder strength, W, in both the ergodic phase and the MBL phase.

5.1.2 Insight from one-body localisation

The generalised IPR L_q (eq. 5.6) is known to distinguish between localised and extended states in Anderson localisation [2, 45–53]. In one-body localisation the one-particle eigenstate,

$$|\psi_n\rangle = \sum_{i=1}^{N} \alpha_{in}\, |i\rangle\,, \tag{5.15}$$

with $\alpha_{in} = \langle i|\psi_n\rangle$ the probability amplitude of $|\psi_n\rangle$ on real-space site $|i\rangle$. The analogous generalised IPR (introduced in eq. 5.6) is given by

$$L_q = \sum_{i=1}^{N} |\alpha_{in}|^{2q}. \tag{5.16}$$

The one-particle τ_q is then defined as

$$L_q = c_q \; N^{-\tau_q}, \tag{5.17}$$

with the c_q a (W-dependent) constant.

In the extended phase, the one-particle wavefunction $|\psi_n\rangle$ (eq. 5.15) is distributed essentially uniformly across all real-space sites i, meaning the fraction of real-space sites the wavefunction is spread across is $\mathcal{O}(1)$. This means that a typical $|\alpha_{in}|^2 \sim \frac{1}{N}$. It follows from eq. 5.16 that $L_q \sim N^{-(q-1)}$, and therefore from eq. 5.17 that $\tau_q = q - 1$, which is the symptom of ergodic eigenfunctions.

By contrast, in the localised phase in one-body localisation the wavefunction $|\psi_n\rangle$ is exponentially localised on a finite $\mathcal{O}(1)$ number of sites n, with the fraction of sites $\frac{n}{N}$ occupied by the wavefunction $|\psi_n\rangle$ vanishing in the thermodynamic limit, $N \to \infty$. On the n sites the wavefunction is spread across $|\alpha_{in}|^2 \sim \frac{1}{n}$ and is zero otherwise. From eq. 5.16 it follows that L_q will be $\mathcal{O}(1)$, and thus from eq. 5.17 that $\tau_q = 0$ for all q in the localised phase.

From the above discussion it follows that the exponent $\tau_q = 0$ in an Anderson localised phase and $\tau_q = q - 1$ in a fully extended phase. By contrast, an eigenstate is said to be fractal when $0 < \tau_q < q - 1$ (for $q > 1$) and is multifractal if τ_q is a non-linear function of q also. Within Anderson localisation, multifractality only typically occurs at the critical point [2, 45–53].

On the other hand it is well known in many-body localisation [79, 88–103] that

in the MBL phase the many-body wavefunction $|\Psi_n\rangle$ is (multi)fractal. This occurs because in the MBL phase the wavefunction $|\Psi_n\rangle$ is spread across a macroscopic number N_H^α of FS sites $|I\rangle$, with $\alpha < 1$, with the fraction of sites the wavefunction occupies $N_H^{\alpha-1}$ vanishing in the thermodynamic limit. The typical $|A_{nI}|^2 \sim N_H^{-\alpha}$ which from eqs. 5.6, 5.7 leads to $\tau_q = \alpha(q-1)$ with $\alpha < 1$; whence $0 < \tau_q < q-1$ follows. This simple minded calculation just gives fractal behaviour for the MBL states, i.e. $\tau_q \propto q-1$. Such a calculation naturally cannot pick up the actual multifractal behaviour (i.e. $0 < \tau_q < q-1$ and is a non-linear function of q) of the wavefunction observed in the MBL phase.

The similarities and differences between Anderson localised and MBL states are summarised in the table below.

Property	Anderson localised	MBL
Number of sites occupied	$n \sim \mathcal{O}(1)$	N_H^α with $\alpha < 1$
Fraction of sites occupied	$\frac{n}{N} \to 0$ as $N \to \infty$	$N_H^{\alpha-1} \to 0$ as $N \to \infty$
Typical $\lvert A_{nI}\rvert^2$	$\sim \frac{1}{n} \sim \mathcal{O}(1)$	$\sim \frac{1}{N_H^\alpha}$
L_q	$\sim \mathcal{O}(1)$	$\sim N_H^{-\tau_q}$ with $0 < \tau_q < q-1$

Previous studies have shown that the MBL eigenstates are ubiquitously multifractal in a range of models typically used to examine MBL [79, 88–103]. Several papers e.g. [96, 97] have tried to use qualitative physical arguments to discuss the possible origins of this multifractality as being due to a mixture of flippable and unflippable spins in the system. That this explanation does not agree with the insight gained from MBL_0 (section 4.4) was discussed in chapter 4.

In this chapter we will extend upon previous work by first examining the relevant distributions of the IPRs - certain distributions were briefly discussed in [92, 98] - before moving on to discuss generally the origins of multifractality in MBL using relevant mathematical bounds.

5.2 Generalised IPR distributions

Before discussing our numerical results for the IPR distributions we shall now discuss the analytical results for the distributions and their moments, for the non-interacting problem, MBL_0, and a model typically used to understand the weak disorder limit - gaussian random eigenvectors (GRV) [163, 170–172]. MBL_0 and GRV provide analytical handles to enable us to understand the strong disorder and weak disorder limits respectively.

5.2.1 Exact results for MBL_0

Sufficiently deep in the MBL phase, the TFI model is known to be perturbatively connected to the non-interacting limit, $J_z = 0$ [59], MBL_0. Our results in chapter 3, showed that much of the important qualitative features of the $J_z \neq 0$, $\overline{C}^{[n]}(t)$ and $\overline{r}^{[n]}(t)$, were captured by MBL_0 (figure 3.9, pg. 60). In this section, we shall therefore outline the derivation of the exact MBL_0 results for $P_{u_q}(x)$, $P_{L_q}(x)$ and $P_{\tau_q}(x)$, with the full derivation given in appendix H.

As outlined in appendix H, L_q can be determined from the definition of $L_q = \sum_I |A_{nI}|^{2q} = \sum_I |\langle n|I\rangle|^{2q}$ (eq. 5.6, pg. 113), alongside the site separability of $\mathcal{H}_{TFI}$ which means *both* $|I\rangle$ and $|n\rangle$ are simple product states. The result is

$$L_q = \prod_{l=1}^{L} \left[(p_{l+})^q + (p_{l-})^q\right]; \quad p_{l\pm} = \frac{1}{2}\left[1 \pm \frac{h_l}{\sqrt{h_l^2+1}}\right]. \tag{5.18}$$

It follows from eq. 5.8 that

$$u_q = \ln[L_q] = \sum_{l=1}^{L} x_l; \quad x_l = \ln\left[(p_{l+})^q + (p_{l-})^q\right]. \tag{5.19}$$

From eq. 5.19, u_q is seen to be a sum of L independent random variables x_l,

each with a finite variance. It thus follows from central limit theorem [178] that in the thermodynamic limit $L \to \infty$, the distribution $P_{u_q}(x)$ (eq. 5.9) of $u_q = \ln[L_q]$ will be a normal distribution, with

$$P_{u_q}(x) = \frac{1}{\sqrt{2\pi\sigma^2_{u_q}}} \exp\left(\frac{-[x - \langle u_q \rangle]^2}{2\sigma^2_{u_q}}\right). \tag{5.20}$$

Given this, it follows directly that in the thermodynamic limit $P_{L_q}(x)$ (eq. 5.9) will be a log-normal distribution,

$$P_{L_q}(x) = \frac{1}{\sqrt{2\pi\sigma^2_{u_q}}} \frac{1}{x} \exp\left(\frac{-[\ln[x] - \langle u_q \rangle]^2}{2\sigma^2_{u_q}}\right). \tag{5.21}$$

Since $P_{u_q}(x)$ is a gaussian distribution (eq. 5.20), it only has two 'relevant' moments, $\langle u_q \rangle$ and $\sigma^2_{u_q}$, which we now calculate.

From eq. 5.19 - and $p_{l+}(h) = p_{l-}(-h)$ (eq. 5.18) - we can calculate the mean of $P_{u_q}(x)$, which as u_q is a sum of L independent variables,

$$\langle u_q \rangle = L\langle x \rangle, \tag{5.22}$$

with

$$\langle x \rangle = \frac{1}{W} \int_0^W dh \ln\left[(p_{l+})^q + (p_{l-})^q\right]. \tag{5.23}$$

We can also calculate the variance of $P_{u_q}(x)$, $\sigma^2_{u_q} = \langle u_q^2 \rangle - \langle u_q \rangle^2$, which using eq. 5.19 gives $\sigma^2_{u_q} = \sum_{l,m} \langle x_l x_m \rangle - \sum_{l,m} \langle x_l \rangle \langle x_m \rangle$. The $\{x_l\}$ (given by eq. 5.19) are independent of one another, meaning clearly for $l \neq m$, $\langle x_l x_m \rangle = \langle x_l \rangle \langle x_m \rangle$. It thus follows that

$$\sigma^2_{u_q} = L\left(\langle x^2 \rangle - \langle x \rangle^2\right), \tag{5.24}$$

which again is proportional to L, since u_q is a sum of L independent random variables

x_l. Within MBL_0 it thus follows that the mean of $P_{u_q}(x)$, $\langle u_q \rangle \propto L$ (eq. 5.23), and its width (i.e. standard deviation) $\sigma_{u_q} \propto \sqrt{L}$ (eq. 5.24).

When examining our numerics later we shall examine the distribution $\overline{u}_q = \frac{u_q}{\langle u_q \rangle}$ (eq. 5.12) which from eq. 5.20 is clearly given by

$$P_{\overline{u}_q}(x) = \frac{1}{\sqrt{2\pi\tilde{\sigma}^2_{u_q}}} \exp\left(\frac{-[x-1]^2}{2\tilde{\sigma}^2_{u_q}}\right); \quad \tilde{\sigma}^2_{u_q} = \frac{\sigma^2_{u_q}}{\langle u_q \rangle^2}. \tag{5.25}$$

The standard deviation of $P_{\overline{u}_q}(x)$ is equal to $\tilde{\sigma}^2_{u_q} = \frac{\sigma^2_{u_q}}{\langle u_q \rangle^2} \propto \frac{1}{L}$. This means $P_{\overline{u}_q}(x)$ is clearly δ-distributed on $x = 1$ in the thermodynamic limit. We shall come back to this when examining our numerics in section 5.2.5.

Within MBL_0, $L_q = N_H^{-\tau_q}$ (or equivalently from eq. 5.7, $C_q = 1$). It thus follows that $\tau_q = -L \ln[2] u_q$. This means that the probability distribution $P_{\tau_q}(x)$ of fractal exponents,

$$P_{\tau_q}(x) = \int dy \; P_{u_q}(y) \; \delta\left(y - \frac{x}{-L\ln[2]}\right), \tag{5.26}$$

which from eq. 5.20 gives

$$P_{\tau_q}(x) = \frac{1}{\sqrt{2\pi\sigma^2_{\tau_q}}} \exp\left(\frac{-[x - \langle \tau_q \rangle]^2}{2\sigma^2_{\tau_q}}\right). \tag{5.27}$$

The first moment $\langle \tau_q \rangle = \frac{\langle x \rangle}{-\ln[2]}$, and the standard deviation $\sigma_{\tau_q} \propto \frac{1}{L}$. The latter result means $P_{\tau_q}(x)$ will be δ-distributed on its mean in the thermodynamic limit. The only relevant moment of $P_{\tau_q}(x)$ in MBL_0 is thus $\langle \tau_q \rangle$, which will be examined in section 5.2.3.

We shall come back to these predictions from MBL_0 when discussing our results for $\langle \tau_q \rangle$, and the distributions, $P_{u_q}(x)$, $P_{\tau_q}(x)$ and $P_{L_q}(x)$, in sections 5.2.3-5.2.6.

It is important to note that the result that $P_{u_q}(x)$ has a gaussian distribution - which arises from central limit theorem [178]- is exact when $L \to \infty$. The typical

L values amenable to numerics are however quite small, $8 \leq L \leq 14$. It is therefore sensible at this point to examine the finite-size distributions for MBL_0, which we now discuss.

When $J_z = 0$, the Hamiltonian, $\mathcal{H}_{TFI}$, is site-separable, i.e.

$$\mathcal{H}_{TFI} = \sum_{l=1}^{N} (J\hat{\sigma}_l^x + h_l\hat{\sigma}_l^z) = \sum_{l=1}^{N} \hat{h}_l. \tag{5.28}$$

This means the spins on real-space sites $\{l\}$ behave independently of one another. $P_{u_q}(x) = \langle \delta(x - u_q) \rangle_{d,I}$ can therefore be obtained by simply averaging over the different possible values of the fields for each of the L real-space sites in the system, i.e.

$$P_{u_q}(x) = \int \cdots \int_{-W}^{W} \prod_{l=1}^{L} \left(\frac{dh_l}{2W} \right) \delta \left(x - u_q \right). \tag{5.29}$$

Using eq. 5.19 for $u_q = \ln[L_q]$ it follows that

$$P_{u_q}(x) = \int \cdots \int_{-W}^{W} \prod_{1}^{L} \left(\frac{dh_l}{2W} \right) \delta \left(x - \sum_{l} x_l \right). \tag{5.30}$$

For finite-size L values $P_{u_q}(x)$ can be calculated using a Fourier transform method, which will now be briefly explained. In order to calculate $P_{u_q}(x)$ we can define the Fourier transform of $P_{u_q}(x)$, $\hat{P}_{u_q}(k)$ with

$$\hat{P}_{u_q}(k) = \int_{-\infty}^{\infty} dx \ \exp[ikx] P_{u_q}(x), \tag{5.31}$$

or equivalently using eq. 5.30 that

$$\hat{P}_{u_q}(k) = \left[\hat{P}_{u_q,1}(k) \right]^L : \quad \hat{P}_{u_q,1}(k) = \frac{1}{2W} \int_{-W}^{W} dh \ \exp[ik \ x_l(h)], \tag{5.32}$$

with $x_l(h_l) = \ln \left[(p_{l+}(h))^q + (p_{l-}(h))^q \right]$ (eq. 5.19) and $p_{l\pm}(h) = \frac{1}{2} \left[1 \pm \frac{h}{\sqrt{h^2+1}} \right]$ (eq.

5.18) introduced on pg. 118. It therefore follows that to calculate the MBL_0 $P_{u_q}(x)$ for finite-size systems, we can calculate $\hat{P}_{u_q,1}(k)$ numerically, and raise it to the Lth power for a range of different k values to determine $\hat{P}_{u_q}(k)$. We can then use a Fast Fourier Transform method [188] to inverse Fourier transform $\hat{P}_{u_q}(k)$ to determine $P_{u_q}(x)$.

This Fourier transform method will be used to calculate the finite-size MBL_0 $P_{u_q}(x)$ throughout this chapter. We now move on to compare the finite-size $P_{u_q}(x)$ functional form to the gaussian expected in the thermodynamic limit.

Within MBL_0 both σ_{u_q} (eq. 5.24) and $\langle u_q \rangle$ (eq. 5.23) depend on the system size L. Therefore, in order to compare conveniently the functional form of the finite-size $P_{u_q}(x)$ to the gaussian expected in the thermodynamic limit, we define the distribution

$$P_{\tilde{u}_q}(x) = \int dy\ P_{u_q}(y)\ \delta\left(x - \frac{(y - \langle u_q \rangle)}{\sigma_{u_q}}\right), \tag{5.33}$$

which has a mean of zero and a variance of one.

Figure 5.1 shows how the finite-size $P_{\tilde{u}_2}(x)$ (eq. 5.33) compares to the unit gaussian expected in the thermodynamic limit, for $W = 1, 4, 8$ for the typical system sizes amenable to numerics, $L = 8 - 14$, alongside $W = 8$ for larger system sizes ($L = 25$ and $L = 300$).

Figure 5.1 shows that for all W values $P_{\tilde{u}_2}(x)$ is reasonably well captured by a unit gaussian for the system sizes amenable to numerics. The finite-size deviations from the gaussian increase as W increases, for example the $W = 8$ $P_{\tilde{u}_2}(x)$ has larger deviations from the central limit theorem [178] result than $W = 1$. Figure 5.1 , however, shows that for $W = 8$ at larger system sizes, i.e. $L \simeq 300$, $P_{\tilde{u}_2}(x)$ indeed converges to the gaussian distribution expected in the thermodynamic limit.

Figure 5.1 shows that small deviations from the unit gaussian distribution - expected in the thermodynamic limit - for $P_{\tilde{u}_2}(x)$ arise in MBL_0 for the W and

L values, relevant for examining the MBL phase for $J_z \neq 0$, i.e. $L = 8 - 14$ and $W \gtrsim 4$. It therefore make sense when examining our numerics in the MBL phase to compare $P_{u_q}(x)$ for $J_z \neq 0$ to the finite-size MBL_0 result, as deviations from the gaussian are even seen to arise for MBL_0.

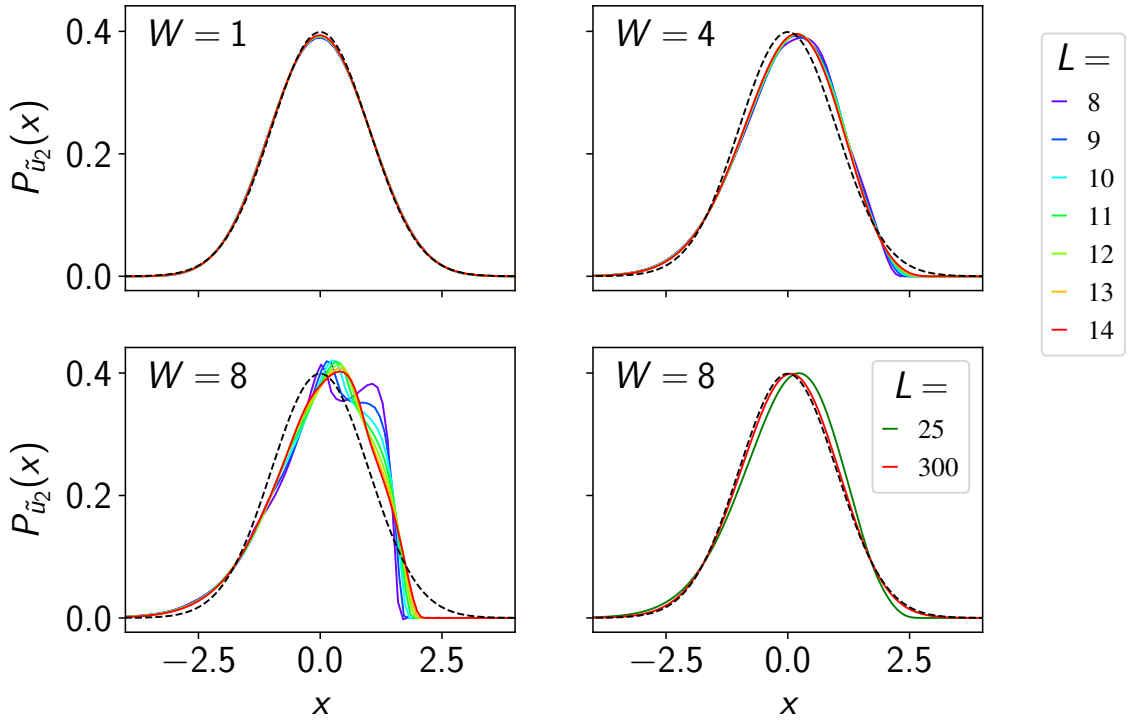


Figure 5.1: For $W = 1, 4, 8$, MBL_0, $P_{\tilde{u}_2}(x)$ for $L = 8 - 14$ compared to the unit gaussian (dashed line) expected in the thermodynamic limit. For $W = 8$, $P_{\tilde{u}_2}(x)$ compared to the unit gaussian for larger system sizes ($L = 25$ and $L = 300$).

Having in this section extensively examined the analytical results for MBL_0, we now consider the results obtained using gaussian random eigenvectors, commonly used to understand properties deep in the ergodic phase [163, 170–172].

5.2.2 Results obtained using gaussian random eigenvectors

Assuming that the eigenstates are gaussian random eigenvectors is known to explain many of their properties deep in the ergodic phase [163, 170–172]. In this section, we shall outline the derivation of the results arising for the IPR distributions; further details can be found in appendix I.

As a reminder to the reader, the sets of amplitudes $A_{nI} = \langle n|I\rangle$, refer to amplitude of eigenstate $|n\rangle$ on FS site $|I\rangle$. Within the gaussian random vectors (GRV) model, for any given eigenstate $|n\rangle$, $\{A_{nI}\}$ across the set of FS sites, $\{|I\rangle\}$, are independent random variables. Likewise, for any given FS site $|I\rangle$, the set of $\{A_{nI}\}$ across the set of eigenstates, $\{|n\rangle\}$, are independent random variables. In both cases they are gaussian distributed, with

$$P_{A_{nI}}(x) = \frac{1}{\sqrt{2\pi\sigma^2_{A_{nI}}}} \exp\left[\frac{-x^2}{2\sigma^2_{A_{nI}}}\right], \tag{5.34}$$

with a mean of zero - as the set of amplitudes, $\{A_{nI}\}$, are equally likely to be positive or negative - and a variance $\sigma^2_{A_{nI}} = \frac{1}{N_H}$, which simply occurs as the average A^2_{nI}, $\langle A^2_{nI}\rangle = \frac{1}{N_H}$ in order for the wavefunction to be normalised, $N_H\langle A^2_{nI}\rangle = 1$.

From $P_{A_{nI}}(x)$ the distribution of $|A_{nI}|^{2q}$,

$$P_{|A_{nI}|^{2q}}(x) = \int dy\ P_{A_{nI}}(y)\ \delta\left(x - |y|^{2q}\right) \tag{5.35}$$

can be calculated. Using eq. 5.34 and a simple change of variables, it follows that

$$P_{|A_{nI}|^{2q}}(x) = \frac{1}{q}\frac{1}{\sqrt{2\pi\sigma^2_{A_{nI}}}} x^{\frac{-(2q-1)}{2q}} \exp\left[\frac{-x^{\frac{1}{q}}}{2\sigma^2_{A_{nI}}}\right]\theta(x), \tag{5.36}$$

with $\theta(x)$ the usual step function. For all $q > 0$ these distributions clearly have a non-infinite mean and variance, since $|A_{nI}|^{2q} \leq 1$.

Within the GRV model, the generalised IPR,

$$L_q = \sum_{I=1}^{N_H} |A_{nI}|^{2q}, \tag{5.37}$$

is clearly given by a sum of N_H terms, each of which are independent random variables, with a non-infinite variance, whose distribution is given by eq. 5.36. This

means from central limit theorem [178] that in the thermodynamic limit $P_{L_q}(x)$ (eq. 5.9, pg. 114) is a gaussian distribution,

$$P_{L_q}(x) = \frac{1}{\sqrt{2\pi\sigma^2_{L_q}}} \exp\left(\frac{-[x - \langle L_q\rangle]^2}{2\sigma^2_{L_q}}\right), \tag{5.38}$$

where both $\sigma^2_{L_q}$ and $\langle L_q\rangle$ can be calculated using GRV (both derived in appendix I), and are given by:

$$\langle L_q\rangle = \frac{2^q\,\Gamma\left(\frac{1}{2}+q\right)}{\sqrt{\pi}} N_H^{1-q}; \quad \sigma^2_{L_q} = N_H^{1-2q}\frac{2^{2q}}{\sqrt{\pi}}\left(\Gamma\left(2q+\frac{1}{2}\right) + \frac{\Gamma(q+\frac{1}{2})^2}{\sqrt{\pi}}\right), \tag{5.39}$$

with $\Gamma(z)$ the usual Gamma function [189].

For e.g. $q = 2$, $\langle L_2\rangle = \frac{3}{N_H}$ and $\sigma^2_{L_2} = \frac{96}{N_H^3}$. Here, the central limit theorem result is likely to be a very good approximation even for our modest L, as the sum in eq. 5.37 for L_q is over $N_H = 2^L$ terms, where $256 \leq N_H \leq 16384$, for $8 \leq L \leq 14$.

Given that $P_{L_q}(x)$ is a gaussian distribution, we can calculate $P_{u_q}(x)$, where the two are related by $P_{u_q}(x) = \int\ dy\ P_{L_q}(y)\delta\left(x - \ln[y]\right)$. Using eq. 5.38 for $P_{L_q}(x)$ it follows that

$$P_{u_q}(x) = \frac{\exp[x]}{\sqrt{2\pi\sigma^2_{L_q}}} \exp\left(\frac{-[\exp[x] - \langle L_q\rangle]^2}{2\sigma^2_{L_q}}\right). \tag{5.40}$$

As outlined in appendix I, in our problem as $\sigma^2_{L_q}$ is exponentially small in L, we can use steepest descents to find $P_{u_q}(x)$ functional form. This gives

$$P_{u_q}(x) = \frac{1}{\sqrt{2\pi\sigma^2_{u_q}}} \exp\left(\frac{-[x - \langle u_q\rangle]^2}{2\sigma^2_{u_q}}\right); \quad \sigma^2_{u_q} = \frac{\sigma^2_{L_q}}{\langle L_q\rangle^2} \sim \frac{1}{N_H}, \quad \langle u_q\rangle = \langle \ln[L_q]\rangle \sim L. \tag{5.41}$$

Given that $u_q = \ln[C_q] - \tau_q L \ln[2]$ it follows that

$$P_{\tau_q}(x) = \frac{1}{\sqrt{2\pi\sigma^2_{\tau_q}}} \exp\left(\frac{-[x - \langle \tau_q\rangle]^2}{2\sigma^2_{\tau_q}}\right), \tag{5.42}$$

with

$$\langle \tau_q \rangle = \frac{\langle u_q \rangle - \ln[C_q]}{-L \ln[2]} = q - 1; \quad \sigma^2_{\tau_q} = \frac{\sigma^2_{u_q}}{(L \ln[2])^2} \sim \frac{1}{L^2} N_H^{-1}. \tag{5.43}$$

It therefore follows that within the model $P_{u_q}(x)$, $P_{\tau_q}(x)$ and $P_{L_q}(x)$ are all gaussian distributions, with widths that decrease exponentially (rather than algebraically) with L. All three of these distributions are therefore δ-functions in the thermodynamic limit.

We shall come back to the analytical results obtained in the last two sections when discussing our numerical results for $P_{\tau_q}(x)$, $P_{u_q}(x)$ and $P_{L_q}(x)$ in the next few sections (sections 5.2.4-5.2.6).

5.2.3 Average fractal exponent, $\langle \tau_q \rangle$

The fractal exponent τ_q is known [79, 88–100] to distinguish whether an eigenstate is Anderson localised, (multi)fractal or extended (as discussed in section 5.1.2). If $\tau_q = 0$, the eigenstate is Anderson localised on $\mathcal{O}(1)$ sites of the FS graph/lattice. While if $\tau_q = q - 1$, the eigenstate is spread across all the FS sites on the graph, and is as such ergodic. If by contrast, $0 < \tau_q < q - 1$ the eigenstate $|n\rangle$ is fractal; and specifically if τ_q is a non-linear function of q the state is multifractal. Multifractality is characteristic of eigenstates in the MBL phase. The origins of this multifractality shall be discussed in a later section of this chapter (section 5.3).

In this section, we shall focus on the average τ_q and $u_q = \ln[L_q]$, $\langle \tau_q \rangle$ and $\langle u_q \rangle$. As a reminder, from eq. 5.7

$$u_q = \ln[L_q] = -\tau_q \ln[N_H] + C_q; \quad \langle u_q \rangle = -\langle \tau_q \rangle \ln[N_H] + \ln[C_q], \tag{5.44}$$

where C_q is an L-independent constant (but naturally dependent on disorder strength W).

Figure 5.2 shows how the $\langle \tau_q \rangle$ *vs* q plots vary with the disorder strength, W, both for MBL_0 (left-hand panel) and our ED results for $J_z \neq 0$ (right-hand panel). In particular, our $J_z \neq 0$ results are for a uniformly distributed $J_z \in [0.8, 1.2]$, whose critical disorder strength is known to be $W_c \simeq 4$ [62]. The black dotted line shows $\langle \tau_q \rangle = q - 1$, expected for ergodic eigenstates. The inset of figure 5.2 shows how $\langle u_2 \rangle$ varies with $\ln[N_H]$, similar behaviour is seen for other q values. We shall now move on to comment on the plots shown in this figure.

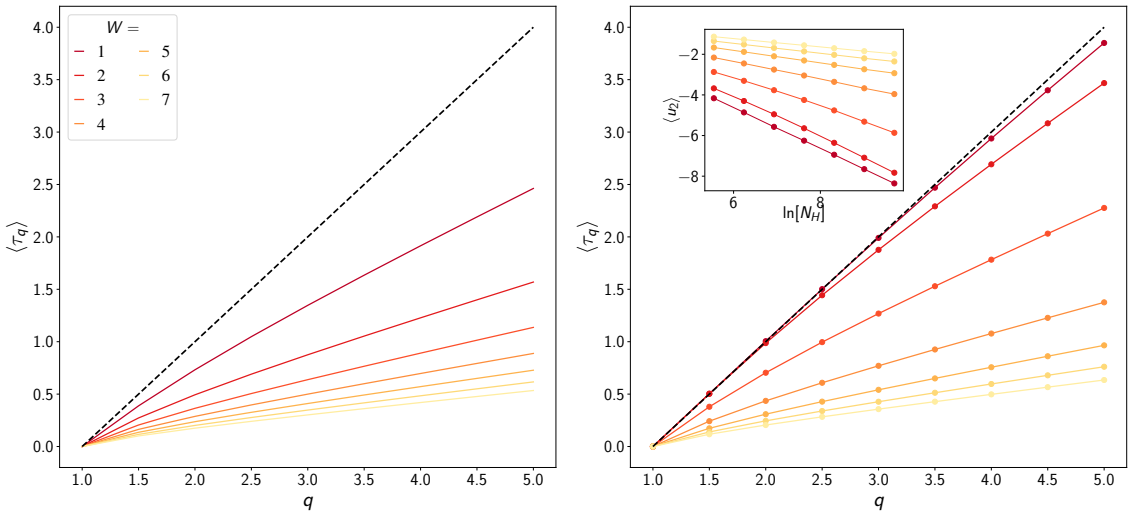


Figure 5.2: For $W = 1 - 7$ as indicated, $\langle \tau_q \rangle$ *vs* q for MBL_0 (left panel) and our ED results for a uniformly distributed $J_z \in [0.8, 1.2]$ (right panel) calculated using system sizes $L = 8 - 13$. Black dotted line $\langle \tau_q \rangle = q - 1$ (expected in the ergodic phase). The inset shows the linear behaviour of $\langle u_2 \rangle$ ($\propto -\tau_2 L \ln[2]$, eq. 5.14) *vs* $\ln[N_H]$ plots, deep in the ergodic phase and the MBL phase.

From eq. 5.44, it is expected that in our ED results deep in either the ergodic phase or the MBL phase - where finite size effects are expected to be small - that the plots of $\langle u_2 \rangle$ *vs* $\ln[N_H]$ are straight lines, with their gradients equal to $-\langle \tau_2 \rangle$. The inset in figure 5.2 shows that this is indeed the case.

For both disorder strengths W deep in the ergodic phase ($W = 1 - 2$), and deep in the MBL phase ($W \gtrsim 4.5$), the $\langle u_2 \rangle$ ($\propto -\tau_2 L \ln[2]$, eq. 5.14) *vs* $\ln[N_H]$ plots are clearly straight lines. By contrast, for $2 < W < 4$, the $\langle u_2 \rangle$ *vs* $\ln[N_H]$ plots, for the system sizes ($L = 8 - 14$) amenable to numerics, are not quite straight lines, with the

slope between the lines connecting adjacent L values increasing with increasing L. As W increases on approach to the transition it is well known that larger and larger system sizes are needed to see thermodynamic behaviour [61, 62, 91, 187, 190–192]. For the W region $2.5 \lesssim W \lesssim 4$ our modest system sizes $L = 8 - 14$ are not large enough to have converged to the behaviour expected in the thermodynamic limit, but with increasing L their behaviour approaches that expected in the thermodynamic limit; reflected in the $\langle u_2 \rangle$ *vs* $\ln[N_H]$ plots by the slope between the lines connecting adjacent L values increasing with increasing L. To get a more precise description of $\langle u_2 \rangle$ for W values close to the transition a scaling theory would be required, which is not our aim here.

The quantity from the above discussion that is naturally of interest is $\langle \tau_q \rangle$, as this quantity clearly distinguishes between extended, (multi)fractal and Anderson localised phases. The left panel of figure 5.2 shows how the MBL_0 $\langle \tau_q \rangle$ varies with q for different disorder W values. For all non-zero W, $\langle \tau_q \rangle < q - 1$ and is a non-linear function of q, meaning the MBL_0 eigenstates are indeed multifractal.

Within the field of localisation, it is well known that in the non-interacting limit in one-dimension for any non-zero disorder, all eigenstates are localised [26]. In the TFI model with $J_z = 0$, this occurs trivially as the problem is site-separable. This means the 'MBL transition' occurs at $W_c = 0$. As a result for all W values, MBL_0 is in the MBL phase, and thus its eigenstates are multifractal.

On the other hand, our ED results for $J_z \neq 0$, shown on the right panel of figure 5.2 show different behaviour depending on the particular disorder strength, W, chosen. Deep in the ergodic phase, e.g. $W = 1$, $\langle \tau_q \rangle = q - 1$ (shown by the black dotted line in the figure), as expected for extended states. For slightly larger W, i.e. $W = 2$, while for smaller q, $\langle \tau_q \rangle \simeq q - 1$, for the larger q small deviations from $q - 1$ arise. This occurs as finite-size effects are larger for the larger q values. By

contrast, in the MBL phase, figure 5.2 shows that $\langle \tau_q \rangle < q - 1$ and is a non-linear function of q, meaning the eigenstates are multifractal, as expected.

The MBL_0 results for $\langle \tau_q \rangle$ are qualitatively similar to our ED results in the MBL phase. As W increases our ED results and the MBL_0 results numerical values become more similar, as is expected to be the case. This occurs as deep in the MBL phase, the $J_z \neq 0$ problem is known to be perturbatively connected to the $J_z = 0$ problem [59].

We shall now move on to examine how the distributions $P_{u_q}(x)$, $P_{L_q}(x)$ and $P_{\tau_q}(x)$ behave in the ergodic phase and the MBL phase. For the rest of this chapter, we shall focus on the distributions for $q = 2$. Appendix J shows result for other q values, where the essential qualitative features seen for $q = 2$ are also seen to arise for other q values.

5.2.4 $P_{\tau_2}(x)$

The distribution that is of central importance is the distribution of the multifractal exponent itself, $P_{\tau_2}(x)$, and its relevant moments.

Figure 5.3 shows how the average of $P_{\tau_2}(x)$, $\langle \tau_2 \rangle$, and its variance, $\sigma^2_{\tau_2}$, varies with W for different system sizes $L = 8 - 14$. While figure 5.4 shows how the distribution of $\overline{u}_2 = \frac{u_2}{\langle u_2 \rangle}$, $P_{\overline{u}_2}(x)$ (eq. 5.12, pg. 115) and the distribution of $\overline{\tau}_2 = \frac{\tau_2}{\langle \tau_2 \rangle}$, $P_{\overline{\tau}_2}(x)$(eq. 5.13, pg. 115) vary with L for different disorder strengths, W.

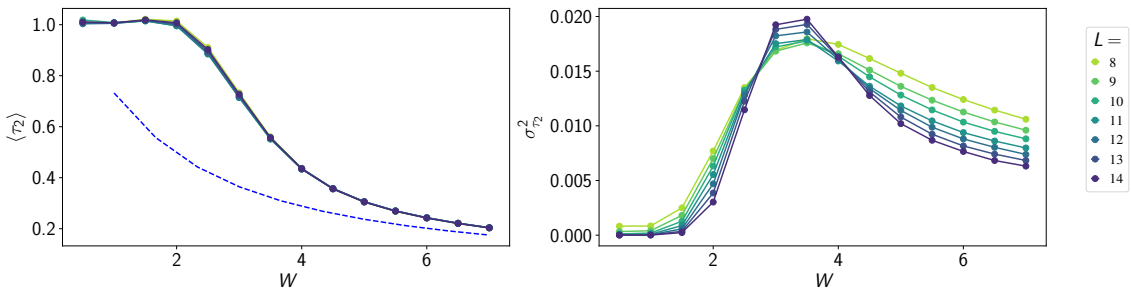


Figure 5.3: Left hand panel: $\langle \tau_2 \rangle$ *vs* W for different system sizes L with the blue dotted line showing the $J_z = 0$ results. Right hand panel: $\sigma^2_{\tau_2}$ *vs* W, $L = 8 - 14$.

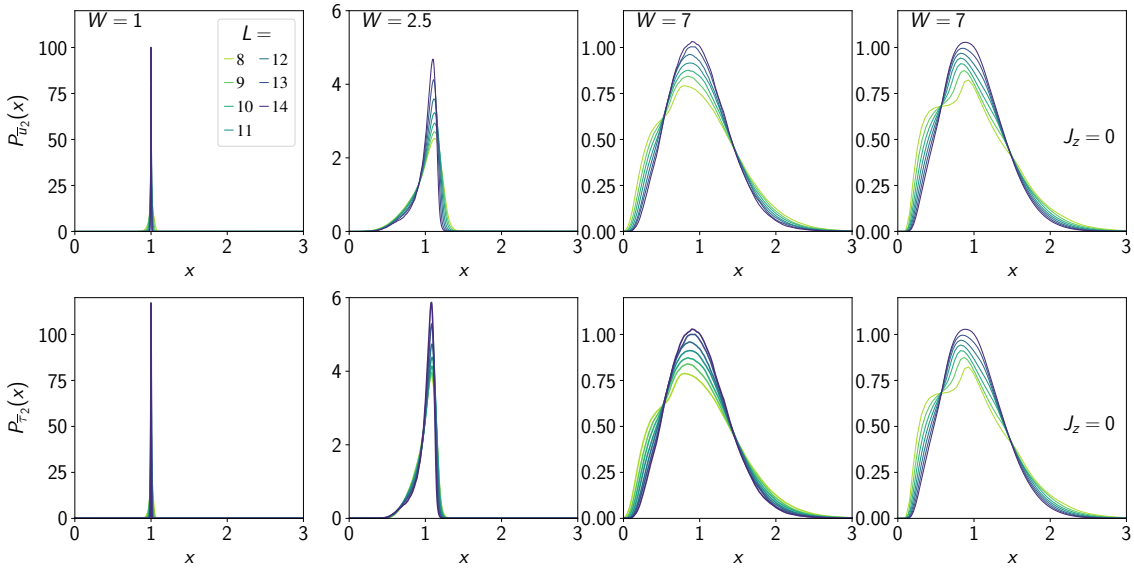


Figure 5.4: Top panels: The distribution of $\overline{u}_2 = \frac{u_2}{\langle u_2 \rangle}$, $P_{\overline{u}_2}(x)$ (eq. 5.12, pg. 115) for different W (indicated in plot), $L = 8 - 14$. Bottom panels: The distribution of $\overline{\tau}_2 = \frac{\tau_2}{\langle \tau_2 \rangle}$, $P_{\overline{\tau}_2}(x)$(eq. 5.13, pg. 115) for different W, $L = 8 - 14$. In both the set of panels on the top and the bottom the first three panels on the left-hand side show results for uniformly distributed $J_z \in [0.8, 1.2]$ and different W values (indicated in plot). The final set of panels on the right-hand side show the results for $J_z = 0$ and $W = 7$.

The left-hand panel of figure 5.3 shows that deep in the ergodic phase $\langle \tau_2 \rangle \simeq 1 (\equiv q - 1)$. By contrast, in the MBL phase $\langle \tau_2 \rangle << 1$.

Given the accessible system sizes we are able to examine using numerics, it is expected that $\langle \tau_2 \rangle$ will show a 'crossover W window' surrounding W_c , where $\langle \tau_2 \rangle$ varies continuously from its value of 1 expected in the ergodic phase to a value much less than 1 in the MBL phase. For $2.5 \lesssim W \lesssim 4$, $\langle \tau_2 \rangle$ shows this typical crossover behaviour expected for finite system sizes. Without a detailed scaling analysis, it preludes substantial consideration of W's in the vicinity of W_c. In [61] Logan and Roy developed such a scaling theory for the IPR, $\langle L_2 \rangle = \langle \exp[u_2] \rangle$.

The right-hand panel of figure 5.3 shows how the variance of the distribution $P_{\tau_2}(x)$ (eq. 5.9), $\sigma^2_{\tau_2}$, varies with W for different system sizes L. For all W values $\sigma^2_{\tau_2}$ is very small indeed $\sigma^2_{\tau_2} < 0.02$. Additionally, for all W values except those in the cross-over region $\sigma^2_{\tau_2}$ decreases with L, meaning it will vanish in the thermodynamic limit. This means $P_{\tau_2}(x)$ will be δ-distributed on its mean $\langle \tau_2 \rangle$ in the thermodynamic

limit.

The right-hand panel of figure 5.3 shows that $\sigma^2_{\tau_2}$ decreases much more rapidly with increasing L in the ergodic phase than the MBL phase as expected from our results using the GRV model (section 5.2.2) and MBL_0 (section 5.2.1). In the GRV model $\sigma^2_{\tau_2} \sim \frac{1}{L^2} N_H^{-1}$, while our results for MBL_0 give $\sigma^2_{\tau_2} \sim \frac{1}{L}$. These analytical handles thus predict that $\sigma^2_{\tau_2}$ decreases exponentially with L in the ergodic phase and algebraically with L in the MBL phase. Since $\sigma^2_{\tau_2} = \frac{\sigma^2_{u_2}}{(L \ln[2])^2}$ we shall show in the next section when examining the distribution of $u_2 = \ln[L_2]$, $P_{u_2}(x)$, that the expected behaviour of $\sigma^2_{\tau_2}$ from GRV and MBL_0 is observed in our numerics.

Since $\sigma^2_{\tau_2}$ decreases with L, it follows that in the thermodynamic limit $P_{\tau_2}(x)$ will be δ-distributed on its mean, $\langle \tau_2 \rangle$, as predicted by GRV and MBL_0. The only relevant moment of $P_{\tau_2}(x)$ is thus $\langle \tau_2 \rangle$ examined in detail in the previous section.

Figure 5.4 additionally shows that for all W values $P_{\overline{\tau}_2}(x) = \int du\ P_{\tau_q}(u)\ \delta\left(x - \frac{u}{\langle \tau_q \rangle}\right)$ (eq. 5.13) and $P_{\overline{u}_2}(x) = \int du\ P_{u_q}(u)\ \delta\left(x - \frac{u}{\langle u_q \rangle}\right)$ (eq. 5.12) are very similar. This occurs as $u_q = \ln[C_q] - \tau_q\ L \ln[2]$ (eq. 5.14), which means the two distributions are simply are related by a change of variables (discussed in section 5.1.1). We shall therefore move on to consider the distribution $P_{u_2}(x)$ in the next section to gain further insight into $P_{\tau_2}(x)$.

5.2.5 Examining $P_{u_2}(x)$

We shall move on to consider the distribution of

$$u_2 = \ln[L_2] : \quad L_2 = \sum_{I=1}^{N_H} |A_{nI}|^4, \tag{5.45}$$

$$P_{u_2}(x) = \langle \delta(x - u_2) \rangle_{n,d}, \tag{5.46}$$

where $\langle\rangle_{n,d}$ denotes an average over band centre eigenstates and disorder realisations. The inset in figure 5.2 from the previous section showed that the mean value $\langle u_2\rangle \propto \ln[N_H] = L\ln[2]$. This means $\langle u_2\rangle$ increases with increasing system size L. To distill this out from the change in the functional form of $P_{u_2}(x)$ with increasing L, we consider the distribution

$$P_{\overline{u}_2}(x) = \int dy\ P_{u_2}(y)\ \delta\left(x - \frac{y}{\langle u_2\rangle}\right), \tag{5.47}$$

which has a mean of unity and a standard deviation $\sigma^2_{\overline{u}_2} = \frac{\sigma^2_{u_2}}{\langle u_2\rangle^2}$.

The first three left-hand panels of figure 5.5 show the $W = 1, 2.5, 7$, $P_{\overline{u}_2}(x)$, for system sizes $L = 8-14$. The final right-hand panel in figure 5.5 shows the finite-size MBL_0, $P_{\overline{u}_2}(x)$ for the same system sizes, i.e. $L = 8-14$. The red-dashed line in both the $W = 7$ plots (our ED results and MBL_0) show the fit to a gaussian distribution - expected in the thermodynamic limit for MBL_0 - with a mean of one and a standard deviation $\sigma^2_{\overline{u}_2}$ which is the same as the $L = 14$ numerical data. Finally, the insert in figure 5.5 shows how $\langle\tau_2\rangle$ varies with W - where $\langle u_2\rangle = \ln[C_q] - \tau_2 L\ln[2]$ - for our ED results and MBL_0. $\langle\tau_2\rangle$ determines $\langle u_2\rangle$ system size dependence and distinguishes between extended, multifractal and Anderson localised states.

On the other hand, figure 5.6 shows plots of the standard deviation of $P_{\overline{u}_2}(x)$, $\sigma^2_{\overline{u}_2} = \frac{\sigma^2_{u_2}}{\langle u_2\rangle^2}$ *vs* W, $L = 8-14$. The inset on the upper left-hand side shows $\frac{\sigma^2_{u_2}}{\langle u_2\rangle^2}$ *vs* $\frac{1}{L}$ for $W = 7$, while the inset on the lower right-hand side shows $\ln[\sigma^2_{u_2}]$ *vs* $\ln[N_H]$ for $W = 1$.

There is a lot of information contained in figures 5.5 and 5.6, which we shall now unpack.

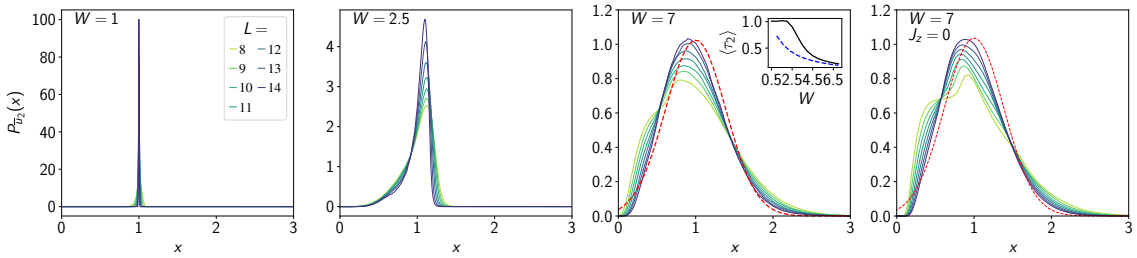


Figure 5.5: For $W = 1, 2.5, 7$, $P_{\overline{u}_2}(x)$ for system sizes $L = 8 - 14$ (first three panels on left-hand side). For $W = 7$, MBL_0, $P_{\overline{u}_2}(x)$ for system sizes amenable to numerics $L = 8 - 14$ (right hand panel). The red dashed line in the $W = 7$ plots shows the fit to a gaussian distribution with a mean of one and a standard deviation $\sigma^2_{\overline{u}_2}$ which is the same as the $L = 14$ numerical data. The inset shows how $\langle \tau_2 \rangle$ varies with W with the blue line indicating the MBL_0 results.

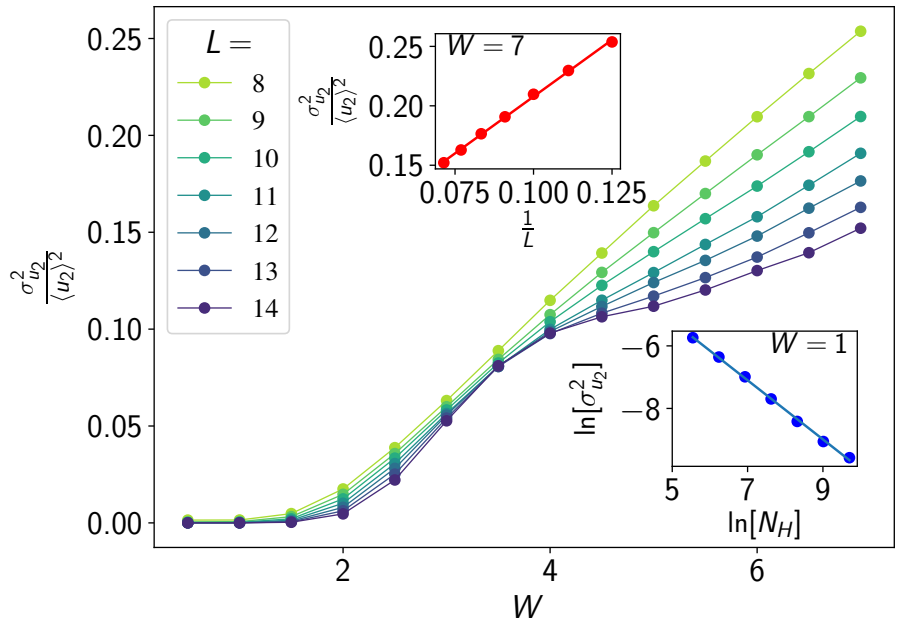


Figure 5.6: The standard deviation of $P_{\overline{u}_2}(x)$, $\sigma^2_{\overline{u}_2} = \frac{\sigma^2_{u_2}}{\langle u_2 \rangle^2}$ *vs* W, $L = 8 - 14$. Upper left-hand inset: $W = 7$, $\frac{\sigma^2_{u_2}}{\langle u_2 \rangle^2}$ *vs* $\frac{1}{L}$. Lower right-hand inset: $W = 1$, $\ln[\sigma^2_{u_2}]$ *vs* $\ln[N_H]$.

Figure 5.5 shows that in both the ergodic phase ($W = 1, 2.5$) and the MBL phase ($W = 7$) $P_{\overline{u}_2}(x)$ narrows with increasing system size L. This is also seen in figure 5.6, where $\sigma^2_{\overline{u}_2} = \frac{\sigma^2_{u_2}}{\langle u_2 \rangle^2}$ decreases with increasing L for all W values.

In our gaussian random eigenvectors (GRV) results (pgs. 124-125 and appendix I), we obtained that in this limit, $P_{u_2}(x)$ has a Gaussian distribution with $\sigma^2_{u_2} = \frac{\sigma^2_{L_2}}{\langle L_2 \rangle^2}$, where as $\langle L_2 \rangle = \frac{3}{N_H}$ and $\sigma^2_{L_2} = \frac{26}{N_H^3}$, gives $\sigma^2_{u_2} \sim N_H^{-1}$. The right-hand inset in figure 5.6 shows that for $W = 1$, $\ln[\sigma^2_{u_2}]$ indeed decreases linearly with $\ln[N_H]$,

with a gradient $= -0.95$ ($\simeq -1$ within numerical error), meaning $\sigma^2_{u_2} \sim N_H^{-1}$, and $\sigma^2_{\overline{u}_2} \sim \frac{1}{L^2} N_H^{-1}$. This implies in the ergodic phase that since the variances of $P_{u_2}(x)$ and $P_{\overline{u}_2}(x)$ decrease with increasing system size, both will be δ-distributed in the thermodynamic limit. This is reflected in figure 5.5, where for $W = 1$, $P_{\overline{u}_2}(x)$ rapidly narrows with increasing L in the ergodic phase.

By contrast, in the MBL phase we expect from our MBL_0 results (discussed on pgs. 118-123 and appendix H) that the standard deviation of $P_{\overline{u}_2}(x)$, $\sigma^2_{\overline{u}_2} = \frac{\sigma^2_{u_2}}{\langle u_2 \rangle^2} \propto \frac{1}{L}$. The inset on the left-hand side of figure 5.6 shows that for $W = 7$ (a disorder strength W characteristic of deep in the MBL phase), the plot of $\frac{\sigma^2_{u_2}}{\langle u_2 \rangle^2}$ *vs* $\frac{1}{L}$ is a straight line, meaning in our ED results for the $J_z \neq 0$ MBL phase $\frac{\sigma^2_{u_2}}{\langle u_2 \rangle^2} \propto \frac{1}{L}$ also. As $\sigma^2_{\overline{u}_2}$ decreases with increasing system size we would expect $P_{\overline{u}_2}(x)$ to narrow with increasing L, exactly as is seen in figure 5.5, with a δ-function again expected in the thermodynamic limit.

Additionally, figure 5.5 shows that our ED results for $W = 7$ and the MBL_0 results for the same system sizes as for $J_z \neq 0$ are very similar. In both cases, the largest system sizes $P_{\overline{u}_2}(x)$ is reasonably well captured by a gaussian, with the fit indicated by the red dotted line in the plot. Figure 5.1 (pg. 123) showed that even for MBL_0 the finite-size $P_{\tilde{u}_2}(x)$ (eq. 5.11) are not gaussian distributed, but converge to gaussian distributions in the thermodynamic limit. Given the similarity in $P_{\overline{u}_2}(x)$ for the same system sizes L for $J_z = 0$ and $J_z \neq 0$, we naturally expect the $J_z \neq 0$ $P_{\overline{u}_2}(x)$ to be gaussian distributed in the thermodynamic limit.

Finally figure 5.5 shows that for W values on approach to the transition from the ergodic phase e.g. $W \simeq 2.5$, the $P_{\overline{u}_2}(x)$ distribution - at least for the modest system sizes amenable to numerics - is no longer gaussian distributed and becomes a left-hand skewed distribution. This will also be seen to be reflected in the form of $P_{L_2}(x)$ in the next section. For a given system size L the distribution $P_{\overline{u}_2}(x)$ clearly

broadens from $W \simeq 1$ to $W \simeq 2.5$. In both cases, however, as $P_{\overline{u}_2}(x)$ narrows with increasing L we expect $P_{\overline{u}_2}(x) = \delta(x-1)$ in the thermodynamic limit.

Both the model for deep in the ergodic phase, gaussian random eigenvectors, and deep in the MBL phase, MBL_0, suggest that $P_{\overline{u}_2}(x)$ will have a gaussian distribution with a variance $\sigma^2_{\overline{u}_2}$ that decreases with increasing system size L. However, the rate at which the variance of $P_{\overline{u}_2}(x)$, $\sigma^2_{\overline{u}_2}$, decreases is very different in the two phases. In the ergodic phase, $\sigma^2_{\overline{u}_2} \propto \frac{1}{L^2} N_H^{-1}$, i.e. decreases exponentially rapidly with increasing L. While in the MBL phase, $\sigma^2_{\overline{u}_2} \propto \frac{1}{L}$, meaning it only decreases algebraically with increasing L. This means the distribution of $P_{\overline{u}_2}(x)$ is more inhomogeneous in the MBL phase than the ergodic phase. This is reflected in figure 5.5, where $P_{\overline{u}_2}(x)$ for a given system size is seen to be much broader in the MBL phase than the ergodic phase.

Within both the GRV model and MBL_0, $P_{\overline{u}_2}(x)$ (discussed above) is predicted to have a gaussian distribution, but with very different standard deviations (previously seen in figure 5.6). In order to compare the extent to which our ED results are captured by a gaussian expected in the GRV and MBL_0 limits, it is useful to define a related distribution

$$P_{\tilde{u}_2}(x) = \int dy\ P_{u_2}(y)\ \delta\left(x - \frac{(y - \langle u_2 \rangle)}{\sigma_{u_2}}\right), \tag{5.48}$$

which has a mean of zero and a variance of one.

Figure 5.7 shows $P_{\tilde{u}_2}(x)$ for $L = 8 - 14$ for a disorder strength, W, characteristic of the ergodic phase ($W = 1$) and the MBL phase ($W = 7$), alongside the finite-size MBL_0 result. This figure shows that our ED results for $P_{\tilde{u}_2}(x)$ for $W = 1$ and $W = 7$ are well captured by a gaussian distribution. Additionally, it shows that our ED results in the MBL phase ($W = 7$) are very well captured by the finite-size MBL_0 result. It is clear from the above discussion that much of the important

physics of the MBL phase, is captured by that of the non-interacting problem. We shall return to this point when discussing the origins of multifractality later in this chapter (section 5.3).

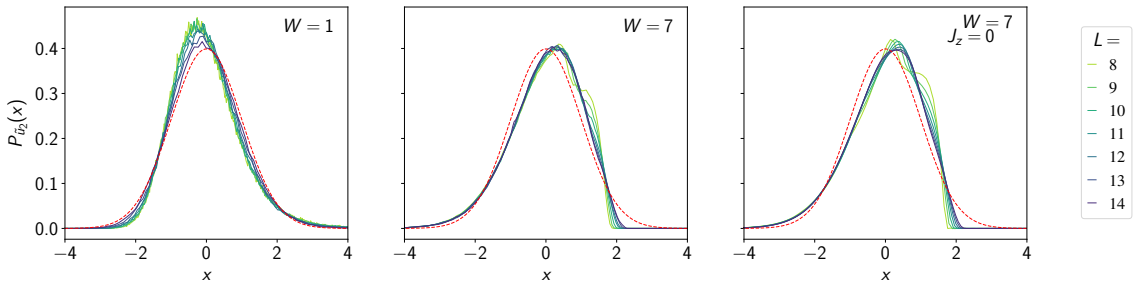


Figure 5.7: For $W = 1, 7$, our ED results for $P_{\tilde{u}_2}(x)$ (eq. 5.48), $L = 8 - 14$. Final panel shows the $W = 7$ finite-size MBL_0 results fo $P_{\tilde{u}_2}(x)$, $L = 8 - 14$. Red dotted line shows the unit gaussian expected from the $L \to \infty$, MBL_0 and GRV results.

5.2.6 Results for $P_{L_2}(x)$

We shall now move on to consider the distribution of the IPR which has a different functional form in the GRV and MBL_0 limit. It is given by

$$P_{L_2}(x) = \langle \delta(x - L_2) \rangle_{n,d} : \quad L_2 = \sum_{I=1}^{N_H} |A_{nI}|^4, \tag{5.49}$$

where $\langle \rangle_{n,d}$ denotes an average over band-centre eigenstates and disorder realisations, previously introduced in eq. 5.9.

The reason for considering the distribution itself is as follows. In the last section we showed that the distribution of $u_2 = \ln[L_2]$, $P_{u_2}(x)$, is a gaussian distribution deep in both the ergodic and MBL phases; albeit with qualitatively different variances. On the other hand, our results obtained using GRV (discussed on pgs. 124-125 and appendix I) and MBL_0 (discussed on pgs. 118-123 and appendix H) predict different functional forms for $P_{L_2}(x)$ in the ergodic phase and the MBL phase. It is clearly of interest to show that if these different functional forms for $P_{L_2}(x)$ are indeed observed in our numerics.

Within the GRV model, typically used to understand the ergodic phase, $P_{L_2}(x)$ is a predicted to have a gaussian distribution in the thermodynamic limit $L \to \infty$, with

$$P_{L_2}(x) = \frac{1}{\sqrt{2\pi\sigma_{L_2}^2}} \exp\left(\frac{-[x - \langle L_2\rangle]^2}{2\sigma_{L_2}^2}\right), \tag{5.50}$$

where $\langle L_2\rangle = \frac{3}{N_H}$ and $\sigma_{L_2}^2 = \frac{96}{N_H^3}$. By contrast, in MBL_0, we found that the thermodynamic limit, $L \to \infty$, $P_{L_2}(x)$ had a log-normal distribution, which is given by:

$$P_{L_q}(x) = \frac{1}{\sqrt{2\pi\sigma_{u_q}^2}} \frac{1}{x} \exp\left(\frac{-[\ln[x] - \langle u_q\rangle]^2}{2\sigma_{u_q}^2}\right), \tag{5.51}$$

with

$$\langle u_q\rangle = L\langle x\rangle, \quad \sigma_{u_q}^2 = L\left(\langle x^2\rangle - \langle x\rangle^2\right). \tag{5.52}$$

$\langle x\rangle$ and $\langle x^2\rangle$ are $\mathcal{O}(1)$ quantities discussed in section 5.2.1.

Figure 5.8 shows $P_{L_2}(x)$ for $W = 1, 2.5, 7$ for system sizes $L = 8 - 14$. $P_{L_2}(x)$ for $L = 14$ is fitted to a gaussian distribution in the ergodic phase and to a log-normal distribution in the MBL phase, which are indicated by the dashed red lines in the plots.

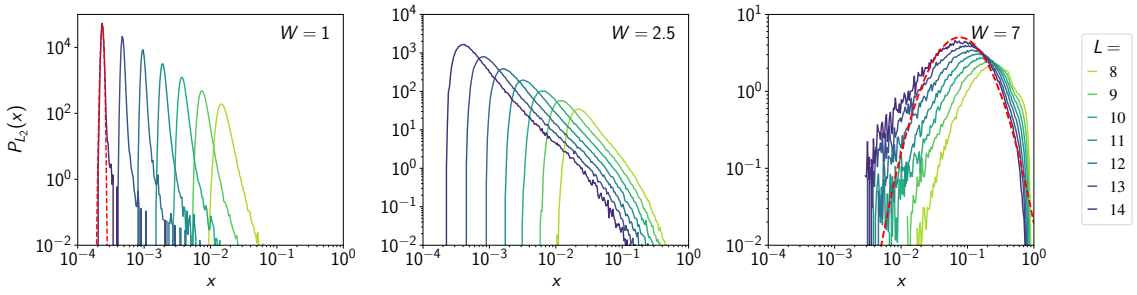


Figure 5.8: For $W = 1, 2.5, 7$, $P_{L_2}(x)$ for system sizes $L = 8 - 14$. The red dashed line in the $W = 1$ plot (left-hand panel) shows the fit to a gaussian distribution. The red dashed line in the $W = 7$ plot (right-hand panel) shows the fit to a log-normal distribution.

Figure 5.8 shows that the quite different functional forms predicted by GRV and MBL_0 discussed above are indeed observed in our numerics. The left-hand panel of figure 5.8 shows that deep in the ergodic phase ($W = 1$) the largest system

size, $L = 14$, $P_{L_2}(x)$ has a good fit to a gaussian distribution (indicated by the red dashed line in the plot); exactly as predicted by our results using the GRV model. By contrast, the right-hand panel of figure 5.8 shows that deep in the MBL phase, the largest system size, $L = 14$, $P_{L_2}(x)$, is well captured by a log-normal distribution (indicated by the red dashed line); as found in our MBL_0 exact results.

Additionally, figure 5.8 shows that deep in the ergodic phase ($W = 1$) $P_{L_2}(x)$ has a very narrow distribution, which becomes narrower and moves to smaller x values as L increases. This is exactly as predicted by our GRV results, where both the mean and the variance of $P_{L_2}(x)$ decrease exponentially with L. Specifically our gaussian random eigenvector exact results give the average of $P_{L_2}(x)$ $\langle L_2 \rangle = \int dx\ x P_{L_2}(x)$, as $\langle L_2 \rangle = \frac{3}{N_H}$, and its variance $\sigma^2_{L_2} = \frac{96}{N_H^3}$ (derived in appendix I). For $W = 1$, we find numerically that $\langle L_2 \rangle = \frac{3.8}{N_H}$ and $\sigma^2_{L_2} \sim N_H^{-2.9}$ (shown in appendix K). This means within numerical error our results for the two 'relevant' moments of $P_{L_2}(x)$ for $W = 1$ are well captured by the GRV results.

By contrast, figure 5.8 shows that in the MBL phase $P_{L_2}(x)$ has a broad log-normal distribution which broadens in an obvious sense with increasing L. In the MBL phase, the wavefunction is known to be inhomogeneously distributed across the FS, with the extent of inhomogenity varying between different disorder realisations [61, 91, 97, 122]. As a result there are large fluctuations in L_2 between disorder realisations. This means $P_{L_2}(x)$ has a broad distribution.

Finally, figure 5.8 shows that at larger disorder strengths in the ergodic phase, i.e. $W = 2.5$, $P_{L_2}(x)$ is very broad and covers a larger-x range than in either the ergodic phase or the MBL phase. This is naturally what we had expected as $W = 2.5$ is the in the crossover region between ergodic and MBL behaviour.

Having extensively discussed the IPR distributions we shall move on to a general discussion of the origins of multifractality in many-body localisation.

5.3 Understanding the origins of multifractality

It is well known that eigenstates in the MBL phase are generically multifractal [79, 88–103]. By contrast, within the field of one-body/Anderson localisation multifractality is known to be the exception rather than the rule (discussed in section 5.1.2), typically occurring at critical points between the localised and the extended regime [45–49], or requiring fine tuning to persist as a stable phase [193, 194]. An obvious question therefore arises: what is the origin of the ubiquitous multifractality in the MBL phase? This is the question we seek to answer at least in part, within this final section of the chapter.

We shall start by examining the non-interacting problem within both the TFI model and a generic spinless fermion model, before extending somewhat our discussion to interacting problems.

5.3.1 Non-interacting problem $J_z = 0$: TFI model

The TFI model has a useful advantage to other commonly studied models in many-body localisation: the MBL eigenstates of the non-interacting problem (i.e. $J_z = 0$) can be calculated explicitly. We shall now consider their construction, and in consequence, as will be shown, the origins of multifractality in the non-interacting problem.

When $J_z = 0$, the Hamiltonian

$$\mathcal{H}_{TFI} = \sum_{l=1}^{L} \left(h_l \hat{\sigma}_l^z + \Gamma \hat{\sigma}_l^x \right), \tag{5.53}$$

is site separable, i.e.,

$$\mathcal{H}_{TFI} = \sum_{l=1}^{L} \hat{h}_l; \quad \hat{h}_l = \left(h_l \hat{\sigma}_l^z + \Gamma \hat{\sigma}_l^x \right). \tag{5.54}$$

The problem can be solved exactly by defining a rotated spin operator

$$\hat{\tilde{\sigma}}_l^z = \frac{h_l \hat{\sigma}_l^z + \Gamma \hat{\sigma}_l^x}{\sqrt{h_l^2 + \Gamma^2}}, \tag{5.55}$$

where the factor $\sqrt{h_1^2 + \Gamma^2}$ in the denominator ensures that $\hat{\tilde{\sigma}}_l^z$ is a bonafide spin operator, with $[\hat{\tilde{\sigma}}_l^z]^2 = 1$ using the usual spin commutation relations, and has eigenvalues of ± 1. The $|\tilde{\sigma}_l^z\rangle$ are the rotated spins, with $\hat{\tilde{\sigma}}_l^z |\tilde{\sigma}_l^z\rangle = \tilde{\sigma}_l^z |\tilde{\sigma}_l^z\rangle$, and $\tilde{\sigma}_l^z = \pm 1$, i.e. each rotated spin can point either up or down.

From eqs. 5.55, 5.54 clearly

$$\mathcal{H}_{TFI} = \sum_{l=1}^{L} \tilde{h}_l \hat{\tilde{\sigma}}_l^z : \quad \tilde{h}_l = \sqrt{h_1^2 + \Gamma^2}. \tag{5.56}$$

It follows from the site-separability of eq. 5.56 that the eigenvectors of $\mathcal{H}_{TFI}$, $\{|\Psi_n\rangle\}$, are simply product states of the $\tilde{\sigma}_\ell^z$ spins,

$$|\Psi_n\rangle = \bigotimes_{l=1}^{L} |\tilde{\sigma}_l^z\rangle = |\{\tilde{\sigma}_l^z\}\rangle\,, \tag{5.57}$$

where $\{\tilde{\sigma}_l^z\}$ is a specified configuration of the rotated spins for the different real-space sites l, with $|\Psi_n\rangle$ eigenenergy, $E_n = \sum_{l=1}^{L} \tilde{h}_l \tilde{\sigma}_l^z$. By contrast - as discussed in chapter 2 - the FS sites $|I\rangle$ are product states of the original $\hat{\sigma}_l^z$ operators, i.e.

$$|I\rangle = \bigotimes_{l=1}^{L} |\sigma_l^z\rangle = |\{\sigma_l^z\}\rangle\,. \tag{5.58}$$

We can now calculate the amplitude of eigenstate $|\Psi_n\rangle$ on FS site $|I\rangle$,

$$|A_{nI}|^2 = |\,\langle \Psi_n | I \rangle\,|^2 = \prod_{l=1}^{L} |\,\langle \tilde{\sigma}_l^z | \sigma_l^z \rangle\,|^2. \tag{5.59}$$

From eq. 5.55 since $\Gamma \neq 0$ ($\Gamma = 1$ in our calculations) for all finite fields h_l the $\tilde{\sigma}_l^z$

spin is rotated in the xz plane away from the σ_l^z spin. This is illustrated pictorially in figure 5.9.

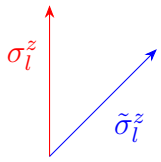


Figure 5.9: Illustration of a typical $\tilde{\sigma}_l^z$ spin compared to σ_l^z spin in xz plane.

Since the $\tilde{\sigma}_l^z$ spin is rotated away from the original σ_l^z spin, their overlap,

$$|\langle\tilde{\sigma}_l^z|\sigma_l^z\rangle|^2 < 1, \tag{5.60}$$

for all spins L (and eigenstates $|\Psi_n\rangle$). It follows from eq. 5.59 that $|A_{nI}|^2$ is a product of L terms; each of which is less than 1. This means $|A_{nI}|^2$ is exponentially small in the number of spins L, for all FS sites $|I\rangle$ and eigenstates $|\Psi_n\rangle$. As the set of $\{|A_{nI}|^2\}$ are all exponentially small in L, clearly $|\Psi_n\rangle$ cannot be Anderson localised, since in this case a finite number of $|A_{nI}|^2$ would be $\mathcal{O}(1)$. As a result, within the non-interacting TFI model states are either fractal or ergodic, with the latter only occurring when $W = 0$.

Physically in the MBL_0 problem, the eigenstates are fractal as all of the rotated spins on the real-space sites l have been rotated away from the z axis of the original $\hat{\sigma}_l^z$ spins - in which the product states $|I\rangle$ are defined - by the hopping $\Gamma\hat{\sigma}_l^x$, which is illustrated in figure 5.9.

It is important to note that the same result would also apply if we had chosen the FS sites $|I\rangle$ to be product states of any other spin operator $\frac{a\hat{\sigma}_l^z+b\hat{\sigma}_l^x}{\sqrt{a^2+b^2}}$ in the xz plane, which was the same for all real-space sites l. This occurs as the set of fields, $\{h_l\}$, are independent random variables, meaning the rotated spins $\hat{\tilde{\sigma}}_l^z$ in different real-space sites l lie at different orientations in the xz plane, with an $\mathcal{O}(1)$ fraction of spins rotated away from any given defined axis.

Fractality of the non-interacting eigenstates is thus generically true, independent of the basis states chosen to form the FS sites $|I\rangle$ within the non-interacting TFI model. The essential point is not however confined to this model. To illustrate this we shall now consider another commonly studied model in MBL; namely spinless fermion models [8, 65–69, 165, 190, 195].

5.3.2 Non-interacting problem $J_z = 0$: Spinless fermions

Spinless fermion models were briefly introduced in chapter 1, and we shall consider them further in this section.

A standard spinless fermion model used in MBL has a Hamiltonian of the form [8, 65–69]

$$\mathcal{H} = \sum_{i=1}^{N} \epsilon_i \hat{n}_i + \sum_{\langle ij \rangle} t(\hat{c}_i^\dagger \hat{c}_j + \hat{c}_j^\dagger \hat{c}_i) + \sum_{\langle ij \rangle} V \hat{n}_i \hat{n}_j, \tag{5.61}$$

where $\{\epsilon_i\}$ are the site energies of the orbitals on real-space sites i, and are taken to be independent random variables. The hopping (t) and the interactions (V) are taken to be nearest neighbour (NN), denoted in eq. 5.61 by $\langle ij \rangle$. As usual $\hat{n}_i = \hat{c}_i^\dagger \hat{c}_i$ is the number operator on real-space site i, which simply counts whether there is a fermion or not on this real-space site, and $\hat{c}_i^\dagger$ and $\hat{c}_i$ are respectively the creation and annhilation operators for a fermion on real-space site i. The chain has N real-space sites and N_e fermions. The filling fraction $\nu = \frac{N_e}{N} \in [0, 1]$, and in MBL we are generally interested in the thermodynamic limit $N \to \infty$ holding ν fixed and non-vanishing.

In this section, since we consider the non-interacting problem ($V = 0$), here eq. 5.61 simplifies to

$$\mathcal{H} = \sum_{i=1}^{N} \epsilon_i \hat{n}_i + \sum_{\langle ij \rangle} t(\hat{c}_i^\dagger \hat{c}_j + \hat{c}_j^\dagger \hat{c}_i). \tag{5.62}$$

As the spins do not interact with each other, from $\mathcal{H}$ (eq. 5.62) we can calculate

the N orthogonal single-particle eigenstates $\{|\psi_\alpha\rangle\}$, which are of the form

$$|\psi_\alpha\rangle = \sum_{i=1}^{N} a_{i\alpha} |i\rangle : \quad \sum_{i=1}^{N} |a_{\alpha i}|^2 = 1, \tag{5.63}$$

where $\{|i\rangle\}$ are the real-space site-orbitals. Given the $\{|\psi_\alpha\rangle\}$, the many-particle eigenfunction $|\Psi_n\rangle$, can constructed as a single Slater determinant (SD) in which N_e of the single-particle states $\{|\psi_\alpha\rangle\}$ are occupied. Likewise, the Fock-Space sites $|I\rangle$ are constructed from a single SD formed by an arbitrary set of N_e site-orbitals $\{|i\rangle\}$ being occupied.

Just as in the TFI model, the many-particle eigenfunction $|\Psi_n\rangle$ can be written as a linear combination of FS sites $\{|I\rangle\}$, i.e.,

$$|\Psi_n\rangle = \sum_I A^0_{nI} |I\rangle , \tag{5.64}$$

with $A^0_{nI} = \langle \Psi_n | I \rangle$, where the superscript 0 denotes we are considering the non-interacting problem. The $|A^0_{nI}|^2$ themselves are given by :

$$|A^0_{nI}|^2 = |\det \mathcal{M}|^2, \tag{5.65}$$

where the matrix $\mathcal{M}$ is an $N_e \times N_e$ overlap matrix whose elements are $\langle i|\psi_\alpha\rangle$, for the N_e $|\psi_\alpha\rangle$ in $|\Psi_n\rangle$ and the N_e $|i\rangle$ in $|I\rangle$. The matrix columns are simply column vectors $v_\alpha = \{\langle \psi_\alpha | i \rangle\}_{i\in I}$ for each of the different $|\psi_\alpha\rangle$ in $|\Psi_n\rangle$.

But Hadamard's inequality states [196] that if $\mathcal{M}$ is a square matrix containing m column vectors v_α, then

$$\det \mathcal{M} \leq \prod_{\alpha=1}^{m} \|v_\alpha\|, \tag{5.66}$$

with $\|v_\alpha\|$ denoting the norm of a column vector v_α, and m $(=N_e)$ the number of columns in the matrix . Given that the norm $\|v_\alpha\|^2 = \sum_{i\in I} |a_{i\alpha}|^2$ with $a_{i\alpha} = \langle \psi_\alpha | i \rangle$,

it follows that

$$|A^0_{nI}|^2 = |\det \mathcal{M}|^2 \leq \prod_{\alpha=1}^{N_e} \sum_{i\in I} |a_{i\alpha}|^2. \tag{5.67}$$

For any finite W, all eigenstates $|\psi_\alpha\rangle$ are known to be exponentially localised [2, 3, 26, 29] in the $|i\rangle$ basis with a finite localisation length. As the wavefunction is normalised the sum over all i $\sum_i |a_{i\alpha}|^2 = 1$. In eq. 5.67, however, the sum $(\sum_{i\in I} |a_{i\alpha}|^2)$ is only over a finite fraction $\nu = \frac{N_e}{N}$ of the sites $|i\rangle$, meaning $\sum_{i\in I} |a_{i\alpha}|^2 < 1$.

Eq. 5.67 tells us that $|A^0_{nI}|^2$ must be less than or equal to a product of $N_e = \nu N$ terms which are all less than one, and therefore is exponentially small in system size N. It thus follows that a typical $|A^0_{nI}|^2$ is exponentially small in system size N. This precludes Anderson localisation on the FS graph, meaning that the eigenstates $|\Psi_n\rangle$ are either ergodic or fractal. In the non-interacting problem in one dimension for any $W > 0$ ergodic states do not exist, meaning the eigenstates $|\Psi_n\rangle$ are fractal.

A natural question to ask is does Anderson localisation ever occur in the one-dimensional non-interacting spinless fermion problem for finite disorder strength W? The answer is that it can occur but only in the special case of $N = N_e$. Here the situation is simple as all single-particle states $|\psi_\alpha\rangle$ are occupied, meaning there is just one eigenstate $|\Psi_n\rangle$ and FS site $|I\rangle$, such that $|A^0_{nI}|^2 = 1$. Trivially in this special case $|\Psi_n\rangle$ is Anderson localised, as there is only one FS site in the problem. This simply occurs as while single-fermion hopping is generally present in $\mathcal{H}$, it is completely inoperative due to Pauli blocking.

While we framed our discussion above on the 'standard' fermion model in 1 dimension, none of the derivation relied on any properties of this particular model; it was simply determined by the Hadamard bound. The derivation would therefore equally apply to other spinless fermion models. Similarly it would apply for any generic single-particle basis $\{|i\rangle\}$, which is not the single-particle eigenbasis, $\{|\psi_\alpha\rangle\}$.

The important conclusion from this section is that it does not matter whether the single-particle states $|\psi_\alpha\rangle$ are spatially localised or extended, the $|A^0_{nI}|^2$ vanish exponentially with increasing N, for any fermion model. Such behaviour rules out Anderson localised states on the FS graph for such models, meaning any state that is not ergodic must be fractal. This means fractality is a general feature of the many-particle MBL wavefunctions in the non-interacting problem for fermion models, and by Jordan Wigner transformation to XXZ-like models [77].

5.3.3 Interacting problem

In the last two sections, we have shown that the many-particle wavefunctions $|\Psi_n\rangle$ are generally either ergodic or fractal for a range of non-interacting models. In this section, we shall extend our discussion to consider some aspects of the interacting problem.

With this aim in mind, we can write a generalised eigenstate of the interacting problem $|\phi_m\rangle$ as a linear combination of eigenstates of the non-interacting problem $|\Psi_n\rangle$, i.e.,

$$|\phi_m\rangle = \sum_n c_{n,m} |\Psi_n\rangle : \quad \sum_n |c_{n,m}|^2 = 1. \tag{5.68}$$

This means $A_{mI} = A_{Im} = \langle I|\phi_m\rangle$ is given by:

$$A_{mI} = \sum_n c_{n,m} \langle I|\Psi_n\rangle = \sum_n c_{n,m} A^0_{nI}. \tag{5.69}$$

Clearly we want to understand the behaviour of $|A_{mI}|^2$ generally in the interacting problem. In order to do this we need to introduce the Hölder inequality [197] which states

$$\left|\sum_i a_i b_i\right| \leq \left(\sum_i |a_i|^p\right)^{\frac{1}{p}} \left(\sum_i |b_i|^r\right)^{\frac{1}{r}} : \quad p > 1, \quad \frac{1}{p} + \frac{1}{r} = 1. \tag{5.70}$$

This inequality will allow us to show that in the two diametrically opposed limits

of the behaviour of the set of $\{|c_{n,m}|^2\}$, we obtain that the typical $|A_{mI}|^2$ decrease exponentially with increasing system size L, preluding Anderson localisation in FS in the interacting problem also.

To this end, let us consider $|A_{mI}|^2$ (eq. 5.69), using the Hölder inequality (eq. 5.70) clearly there are 2 inequalities that can be generated,

$$|A_{mI}|^2 \leq \left(\sum_n |c_{n,m}|^r\right)^{\frac{2}{r}} \left(\sum_n |A^0_{nI}|^p\right)^{\frac{2}{p}}, \tag{5.71}$$

and

$$|A_{mI}|^2 \leq \left(\sum_n |c_{n,m}|^p\right)^{\frac{2}{p}} \left(\sum_n |A^0_{nI}|^r\right)^{\frac{2}{r}}. \tag{5.72}$$

Now suppose that $r = 2q$ and taking logs from eqs. 5.71, 5.72 it follows that

$$\ln[|A_{mI}|^2] \leq \frac{2q-1}{q} \ln\left[\sum_n |c_{n,m}|^{\frac{2q}{2q-1}}\right] + \frac{1}{q} \ln\left[\sum_n |A^0_{nI}|^{2q}\right] \tag{5.73}$$

and

$$\ln[|A_{mI}|^2] \leq \frac{1}{q} \ln\left[\sum_n |c_{n,m}|^{2q}\right] + \frac{2q-1}{q} \ln\left[\sum_n |A^0_{nI}|^{\frac{2q}{2q-1}}\right]. \tag{5.74}$$

At this point it is useful to define the exponent ϕ for the interacting problem by $|A_{mI}|^2 = N_H^{-\phi}$, i.e.

$$\phi = \frac{-\ln[|A_{mI}|^2]}{\ln[N_H]}, \tag{5.75}$$

as well as to remind the reader that

$$L_q = \sum_n |A^0_{nI}|^{2q} = N_H^{-\tau^0_q}, \tag{5.76}$$

with τ^0_q the multifractal exponent for the non-interacting problem, whose average in the TFI model was considered explicitly in figure 5.2, pg. 127.

Using eqs. 5.73, 5.74 and the definition of ϕ (eq. 5.75) it follows

$$\phi \geq \frac{\tau_q^0}{q} - \frac{2q-1}{q}\frac{1}{\ln[N_H]}\ln\left[\sum_n |c_{n,m}|^{2q_{eff}}\right], \tag{5.77}$$

$$\phi \geq \frac{2q-1}{q}\tau^0_{q_{eff}} - \frac{1}{q}\frac{1}{\ln[N_H]} ln\left[\sum_n |c_{n,m}|^{2q}\right], \tag{5.78}$$

where

$$q_{eff} = \frac{2q}{2q-1} \in \left[\frac{1}{2}, 1\right]. \tag{5.79}$$

In the non-interacting problem as the eigenstates are either fractal or ergodic, clearly

$$0 < \tau_q^0 < q-1: \quad q > 1, \tag{5.80}$$

which was shown explicitly in the TFI model in figure 5.2, pg. 127. Additionally, since $\frac{1}{2} < q_{eff} < 1$, given that the non-interacting eigenstates are multifractal,

$$-\frac{q-1}{2q-1} < \tau^0_{q_{eff}} < 0. \tag{5.81}$$

We shall make use of both these inequalities below.

Let us now consider the two diametrically opposed limits for the behaviour of the set of $\{|c_{n,m}|^2\}$, and use one of the two eqs. 5.77, 5.78 to give a bound for ϕ.

Firstly, the case where the number of non-interacting states whose $c_{n,m}$ is non-negligible is not exponentially large in system size, which encompasses a possible limit when $\mathcal{O}(1)$ number of $|c_{n,m}|^2$ are non-negligible. In this case, since the second-term in eq. 5.77 vanishes, clearly from eq. 5.77

$$\phi > \frac{\tau_q^0}{q} > 0, \tag{5.82}$$

meaning $|A_{mI}|^2 = N_H^{-\phi}$ is exponentially small in system size, and thus $|\phi_m\rangle$ is expected to be fractal. This is expected to occur close to the non-interacting limit,

where the interacting eigenstates are expected to be perturbatively connected to non-interacting limit.

Secondly, the case when the $|c_{n,m}|^2$ are expected to be uniformly distributed over the N_H sites, $|c_{n,m}|^2 \sim \frac{1}{N_H}$. This is likely to hold deep in the ergodic phase. In this case, eq. 5.78 gives

$$\phi \geq \frac{2q-1}{q}\tau^0_{q_{eff}} + \frac{q-1}{q}. \tag{5.83}$$

Given that the bound $-\frac{q-1}{2q-1} < \tau^0_{q_{eff}} < 0$ (eq. 5.81), it follows that

$$\phi > 0. \tag{5.84}$$

This again means $|A_{mI}|^2 = N_H^{-\phi}$ decreases exponentially with increasing system size.

The substantive point from the above discussion is that for the extreme cases of the $c_{n,m}$ distributions, we use the Hölder bound to show that $\phi > 0$ strictly; preluding as such Anderson localised eigenstates in Fock Space in the interacting problem, just as we showed in the non-interacting problem. This means that if the eigenstates are not extended, they must be fractal. In a sense, fractality arising in the interacting problem can be regarded as having its origins in the non-interacting but many-particle limit.

5.4 Conclusion

Throughout this chapter, we have discussed the relevant distributions of the IPR and the origins of multifractality in the MBL phase. Our key findings are:

- The average of τ_q taken over band-centre eigenstates and disorder realisations, $\langle\tau_q\rangle$ shows very different behaviour in the ergodic and the MBL phase. Deep in the ergodic phase, we find that $\langle\tau_q\rangle = q - 1$, as expected for extended states. While in the MBL phase, $\langle\tau_q\rangle < q - 1$, and is a non-linear function of

q, meaning the eigenstates are multifractal. The $J_z \neq 0$ numerical results for $\langle \tau_q \rangle$ are well captured by our MBL_0 results.

- The distribution $P_{u_q}(x)$ is found to be gaussian in both the ergodic phase and the MBL phase; exactly as predicted by the GRV model and MBL_0. The variance of $P_{u_q}(x)$ is found to differ significantly, with larger inhomogeneity in the distributions in the MBL phase than in the ergodic phase.

- The distributions $P_{L_q}(x)$ are found to have very different functional forms in the ergodic and the MBL phase, with a gaussian distribution found in the ergodic phase and a log-normal distribution in the MBL phase. Again these different functional forms were predicted by the GRV model and MBL_0.

- Finally, we discussed more generally the origins of multifractality in MBL, showing that multifractality arising in the interacting problem can be regarded as having its origins in the non-interacting but many-particle limit.

Having extensively examined the multifractality of eigenstates in the ergodic and the MBL phase, we shall now move on to introduce in the next chapter our new order parameters used to detect the MBL transition. These parameters probe the overlap between nearest neighbour eigenstates.

Chapter 6

New order parameters

6.1 Introduction

It has been well known since the early days of Anderson localisation that the extent to which nearest neighbour eigenstates overlap - or equivalently are found in the same region of space - differs significantly between localised and extended states [2, 198–200].

In the one-body problem in the absence of disorder the one-particle eigenstates are known to be Bloch states [34], plane waves. This means that the wavefunction is uniformly distributed across all real-space sites of the system. As a result eigenstates of the same energy will occupy the same region of space. This is generically true for extended eigenstates at finite disorder values also. By contrast, it is known in Anderson localisation [2, 198–200] that localised eigenstates of the same energy cannot occupy the same region of space: even an infinitesimal coupling present between the two states - which will occur if they overlap - will mix the two states and split their energies apart.

Similarly, in many-body localisation the spatial overlap of nearest neighbour in energy eigenstates on the Fock space differs significantly between ergodic and MBL states (by nearest neighbour in energy, we mean eigenstates whose energies are

adjacent when energy ordered). In the ergodic phase, as the many-body eigenstates are essentially uniformly distributed across the FS graph/lattice, nearest neighbour in energy eigenstates clearly overlap. By contrast, in the MBL phase, just as in one-body localisation nearest neighbour in energy eigenstates typically do not overlap, as they are found in different regions of the FS graph. It follows that defining a quantity that measures the extent to which nearest neighbour many-body eigenstates overlap in MBL may act as an order parameter for the MBL transition.

In this chapter, we shall therefore introduce and study two quantities L_{nm} and S_{nm} (defined in the next section) which measure the overlap between two eigenstates $|n\rangle$ and $|m\rangle$ with energies E_n and E_m. We shall focus on nearest neighbour in energy eigenstates, which will allow us to define two new order parameters for the MBL phase transition.

6.1.1 Defining relevant quantities

For two eigenstates $|n\rangle$ and $|m\rangle$ we can define two quantities which measure the wavefunction overlap as

$$L_{nm} = \frac{\sum\limits_I A_{nI}^2 A_{mI}^2}{\frac{1}{2}\sum\limits_I \left(A_{nI}^4 + A_{mI}^4\right)} \tag{6.1}$$

and

$$S_{nm} = \sum_I \frac{A_{nI}^2 A_{mI}^2}{\frac{1}{2}\left(A_{nI}^2 + A_{mI}^2\right)}, \tag{6.2}$$

where $A_{nI} = \langle n|I\rangle$ is the amplitude of eigenstate $|n\rangle$ on FS site $|I\rangle$. We now provide motivation for the functional forms of L_{nm} and S_{nm}.

Let us first consider L_{nm} (eq. 6.1). The term in the numerator in eq. 6.1 ($\sum_I A_{nI}^2 A_{mI}^2$) clearly measures the overlap in FS of the two eigenstates $|n\rangle$ and $|m\rangle$. If $|n\rangle \equiv |m\rangle$ this reduces to the IPR $\sum_I A_{nI}^4$ (examined in detail in chapter 5). This is known to vanish in both the ergodic phase and the MBL phase [79, 88–103]. To

account for this, when defining L_{nm} in eq. 6.1 we divide through by the average IPR of the two eigenstates $\frac{1}{2}\sum_I (A_{nI}^4 + A_{mI}^4)$. This ensures that if the eigenstates are identical, i.e. $|n\rangle \equiv |m\rangle$, $L_{nn} = 1$. By contrast, if the two eigenstates occupy entirely different regions of the FS, meaning $A_{nI}^2 A_{mI}^2 = 0$ everywhere, then $L_{nm} = 0$. L_{nm} thus provides a measure of the similarity of spatial extent or 'overlap' of the two eigenstates $|n\rangle$ and $|m\rangle$.

Now let us consider the functional form of S_{nm} in eq. 6.2. Here we take the sum of a single fraction $\frac{A_{nI}^2 A_{mI}^2}{\frac{1}{2}\left(A_{nI}^2 + A_{mI}^2\right)}$, which is simply the product of the amplitudes of the two eigenstates $|n\rangle$ and $|m\rangle$ $A_{nI}^2 A_{mI}^2$ divided by the average amplitude of the two eigenstates $\frac{1}{2}(A_{nI}^2 + A_{mI}^2)$. If $|n\rangle \equiv |m\rangle$ the fraction in eq. 6.2 reduces to A_{nI}^2, which given that the wavefunction is normalised means $S_{nm} = 1$. By contrast, if the two eigenstates $|n\rangle$ and $|m\rangle$ occupy entirely different regions of the FS space $A_{nI}^2 A_{mI}^2$ is equal to zero everywhere, which from eq. 6.2 means $S_{nm} = 0$. Again, S_{nm} provides a measure of the extent to which two eigenstates $|n\rangle$ and $|m\rangle$ occupy the same region of space.

From the discussion in the previous section it is clear that the value of L_{nm} and S_{nm} for nearest neighbour eigenstates $|n\rangle$ and $|n+1\rangle$, L_{nn+1} and S_{nn+1}, are particularly of interest. These shall be denoted

$$L^{NN} = L_{nn+1}, \quad S^{NN} = S_{nn+1} \tag{6.3}$$

respectively. Here the superscript NN denotes that these are L_{nm} and S_{nm} for nearest neighbour (in energy) eigenstates.

In chapter 3 (pgs. 48-49), we discussed that it is well known in localisation phenomenon [78–81] that eigenstates with eigenenergies $E_n = \omega$, from different regions of the band, $D(\omega)$ (eq. 3.30, pg. 48), localise at different disorder strength, denoted $W_c(\omega)$. Throughout this chapter, we shall therefore focus on eigenstates

$|n\rangle$ from one region of the band - the band-centre - whose critical disorder strength is known to be $W_c \simeq 4$ [62].

The value of L^{NN} and S^{NN} for band-centre states will differ between disorder realisations. It is therefore important to examine the probabilities distributions of L^{NN} and S^{NN}, $\mathcal{P}_{L^{NN}}(x)$ and $\mathcal{P}_{S^{NN}}(x)$ which are given by:

$$\mathcal{P}_{L^{NN}}(x) = \left\langle \delta(x - L^{NN}) \right\rangle_{n,d}; \quad \mathcal{P}_{S^{NN}}(x) = \left\langle \delta(x - S^{NN}) \right\rangle_{n,d}, \tag{6.4}$$

with $\langle\rangle_{n,d}$ denoting an average over disorder realisations and band centre eigenstates (typically the 25 eigenstates either side of the band centre). These distributions shall be examined in section 6.3.

Given the distributions $\mathcal{P}_{L^{NN}}(x)$ and $\mathcal{P}_{S^{NN}}(x)$ we can calculate their average and typical values. These are given by:

$$L^{NN}_{avg} = \int dx\ x\ \mathcal{P}_{L^{NN}}(x); \quad \ln\left[L^{NN}_{typ}\right] = \int dx\ \ln[x]\ \mathcal{P}_{L^{NN}}(x), \tag{6.5}$$

and

$$S^{NN}_{avg} = \int dx\ x\ \mathcal{P}_{S^{NN}}(x); \quad \ln\left[S^{NN}_{typ}\right] = \int dx\ \ln[x]\ \mathcal{P}_{S^{NN}}(x). \tag{6.6}$$

In a later section (section 6.2) we shall show that L^{NN}_{typ}, L^{NN}_{avg}, S^{NN}_{typ} and S^{NN}_{avg} act as order parameters for the MBL phase transition. We will then go on to develop a scaling theory for their behaviour on either side of the transition.

But first, we move to consider in the next two sections (6.1.2 and 6.1.3) the information obtained on the distributions $P_{L^{NN}}(x)$ and $P_{S^{NN}}(x)$ using GRV and MBL_0. These standard analytical handles have been used throughout this thesis to understand the behaviour of relevant quantities deep in the ergodic phase and the MBL phase respectively.

6.1.2 Gaussian Random Eigenvector results

As we have seen many times throughout this thesis, assuming that the eigenstates are gaussian random eigenvectors (GRV) is known to explain many of their properties deep in the ergodic phase [163, 170–172]. Before discussing our numerical results for various quantities introduced in the previous section, we shall now discuss the analytical results for L_{nm} and S_{nm} obtained using this model.

As a reminder to the reader, the sets of amplitudes $A_{nI} = \langle n|I\rangle$, refer to amplitude of eigenstate $|n\rangle$ on FS site $|I\rangle$. Within the GRV model, for any given eigenstate $|n\rangle$, $\{A_{nI}\}$ across the set of FS sites, $\{|I\rangle\}$, are treated as independent random variables. Likewise, for any given FS site $|I\rangle$, the set of $\{A_{nI}\}$ across the set of eigenstates, $\{|n\rangle\}$, are independent random variables. In both cases they are gaussian distributed, with

$$P_{A_{nI}}(x) = \frac{1}{\sqrt{2\pi\sigma^2_{A_{nI}}}} \exp\left[\frac{-x^2}{2\sigma^2_{A_{nI}}}\right], \tag{6.7}$$

with a mean of zero - as the set of amplitudes, $\{A_{nI}\}$, are equally likely to be positive or negative - and a variance $\sigma^2_{A_{nI}} = \frac{1}{N_H}$, which simply occurs as the average A^2_{nI}, $\langle A^2_{nI}\rangle = \frac{1}{N_H}$ in order for the wavefunction to be normalised, $N_H\langle A^2_{nI}\rangle = 1$.

Let us first consider the behaviour of L_{nm} within the GRV model. As a reminder L_{nm} is given by eq. 6.1 on pg. 151. In order to determine the distribution of $P_{L_{nm}}(x)$ it is helpful to first consider the distributions of the numerator and denominator in eq. 6.1. Let us first consider the distribution, $P_{x_N}(x)$, of the numerator, $x_N = \sum_I A^2_{nI}A^2_{mI}$. As x_N is a sum of N_H independent random variables with a non-infinite variance, it follows from the central limit theorem [178] that $P_{x_N}(x)$ is a gaussian distribution. Its mean and variance can be readily calculated using eq. 6.7 (this is done explicitly in appendix I) to give $\langle x_n\rangle = \frac{1}{N_H}$ and $\sigma^2_{x_N} = \frac{8}{N_H^3}$. The distribution of

the denominator, $P_{x_D}(x)$ is simply the distribution of $P_{L_2}(x)$ calculated in chapter 5. $P_{x_D}(x)$ is therefore a gaussian distribution with a mean $\langle x_D \rangle = \frac{3}{N_H}$ and variance $\sigma^2_{x_D} = \frac{26}{N_H^3}$ (discussed in section 5.2.2).

Given the distributions of the numerator and the denominator it follows that

$$P_{L_{nm}}(x) = \int dy\ P_{x_N}(y) \int dz\ P_{x_D}(z)\ \delta\left(x - \frac{y}{z}\right), \tag{6.8}$$

which clearly can be calculated. As both distributions used to calculate $P_{L_{nm}}(x)$ have a variance $\sim \frac{1}{N_H^3}$ - and are therefore δ-distributed in the thermodynamic limit - we expect the variance of $P_{L_{nm}}(x)$ will decrease with increasing system size L, and will be δ-distributed in the thermodynamic limit. The L_{nm} value the δ-distribution is centre on is evidently $L_{nm} = \frac{\langle x_N \rangle}{\langle x_D \rangle}$. As $\langle x_n \rangle = \frac{1}{N_H}$ and $\langle x_D \rangle = \frac{3}{N_H}$ (discussed above), clearly $P_{L_{nm}}(x) = \delta(x - \frac{1}{3})$. As the GRV model results do not depend on the region of the band the eigenstates $|n\rangle$ and $|m\rangle$ come from, it follows that $\mathcal{P}_{L^{NN}}(x)$ will also be δ-distributed on $x = \frac{1}{3}$, i.e. $P_{L^{NN}}(x) = \delta(x - \frac{1}{3})$. As a result $L^{NN}_{typ} = L^{NN}_{avg} = \frac{1}{3}$. We shall come back to these results for $\mathcal{P}_{L^{NN}}(x)$, L^{NN}_{typ} and L^{NN}_{avg} when discussing our numerical results for these quantities in sections 6.2 and 6.3.

We now move on to consider the behaviour of S_{nm} within the GRV model. To this end, we remind the reader that S_{nm} is given by eq. 6.2 on pg. 151. The amplitudes A_{nI} in eq. 6.2 for $S_{nm;I}$ are independent random variables with a gaussian probability distribution $P_{A_{nI}}(x)$ given by eq. 6.7, with a mean of 0 and a variance $\frac{1}{N_H}$. It thus follows that $S_{nm;I}$ is an independent random variable with a probability distribution $P_{S_{nm;I}}(x)$ which can be calculated using eq. 6.7, where

$$P_{S_{nm;I}}(x) = \int dy\ P_{A_{nI}}(y) \int dz\ P_{A_{nI}}(z)\ \delta\left(x - \frac{y^2 z^2}{\frac{1}{2}(y^2 + z^2)}\right) \tag{6.9}$$

The two important quantities to determine for $P_{S_{nm;I}}(x)$ are its mean

$$\langle S_{nm;I}\rangle = \int dx\ x\ P_{S_{nm;I}}(x) \tag{6.10}$$

and its variance

$$\sigma^2_{S_{nm;I}} = \langle S^2_{nm;I}\rangle - \langle S_{nm;I}\rangle^2; \quad \langle S^2_{nm;I}\rangle = \int dx\ x^2\ P_{S_{nm;I}}(x). \tag{6.11}$$

These can both be readily calculated using eq. 6.9 to give

$$\langle S_{nm;I}\rangle = \frac{1}{2N_H}; \quad \sigma^2_{S_{nm;I}} = \frac{1}{2N_H^2}. \tag{6.12}$$

From eq. 6.2 it follows that S_{nm} is a sum of N_H independent random variables, which from the central limit theorem [178] means $P_{S_{nm}}(x)$ will be a gaussian distribution. Using eq. 6.12 for the mean and variance of $S_{nm;I}$ and the fact that $\{S_{nm;I}\}$ are uncorrelated gives the mean and variance of $P_{S_{nm}}(x)$ as

$$\langle S_{nm}\rangle = \frac{1}{2}; \quad \sigma^2_{S_{nm}} = \frac{1}{2N_H}. \tag{6.13}$$

As the variance vanishes in the thermodynamic limit, it follows that here $\langle S_{nm}\rangle = \exp\left(\langle \ln[S_{nm;I}]\rangle\right) = \frac{1}{2}$, or equivalently the arithmetic and geometric mean of $P_{S_{nm}}(x)$ are both $\frac{1}{2}$.

The results obtained using the GRV do not depend on the region of the band the eigenstates $|n\rangle$ and $|m\rangle$ are taken from. It thus follows that

$$S^{NN}_{avg} = S^{NN}_{typ} = \frac{1}{2}. \tag{6.14}$$

$\mathcal{P}_{S^{NN}}(x)$ itself is a gaussian distribution centred on $\frac{1}{2}$ with a variance $\sigma^2_{S^{NN}} = \frac{1}{2N_H}$

which rapidly decreases with system size L, with a δ-distribution expected in the thermodynamic limit. We shall come back to these results for S^{NN}_{avg}, S^{NN}_{typ} and $\mathcal{P}_{S^{NN}}(x)$ when discussing our numerical results in sections 6.2 and 6.3.

6.1.3 MBL_0 results

As discussed many times throughout this thesis, sufficiently deep in the MBL phase, the TFI model is known to be perturbatively connected to the non-interacting limit, $J_z = 0$ [59], MBL_0. Our results in chapter 3, showed that much of the important qualitative features of the $J_z \neq 0$, $\overline{C}^{[n]}(t)$ and $\overline{r}^{[n]}(t)$, were captured by MBL_0 (figure 3.9, pg. 60). Similarly our results in chapter 5 showed that much of the important features of the IPR distributions can be obtained from the non-interacting problem. In this section, we will discuss the unfortunately limited insight gained into the behaviour of $P_{L^{NN}}(x)$ and $P_{S^{NN}}(x)$ from MBL_0. Unlike in previous chapters, even in MBL_0 we have been unable to determine an analytical expression for these distributions.

We shall therefore start this section by discussing the general equation we have obtained for S_{nm}. We then move to discuss when L_{nm} and S_{nm} can be $\mathcal{O}(1)$ even in MBL_0. The latter will help us understand the distributions $P_{L^{NN}}(x)$ and $P_{S^{NN}}(x)$ in section 6.3. Since no analytical expressions for these distributions have been obtained, in section 6.3 we calculate even the non-interacting problem distributions by exact diagonalisation (ED) studies using modest system sizes (i.e. $L = 8 - 13$).

As a reminder,

$$S_{nm} = \sum_I \frac{A^2_{nI} A^2_{mI}}{\frac{1}{2}\left(A^2_{nI} + A^2_{mI}\right)} \equiv \sum_I \frac{1}{2}\left(\frac{1}{A^2_{nI}} + \frac{1}{A^2_{mI}}\right)^{-1}. \tag{6.15}$$

In order to calculate S_{nm} we require knowledge of the set of squared amplitudes for

all FS sites I, $\{A^2_{nI}\}$ and $\{A^2_{mI}\}$, for the two eigenstates $|\Psi_m\rangle$ and $|\Psi_n\rangle$. In section 5.3.1 (pg. 139-141) we discussed that the MBL_0 eigenstates $|\Psi_n\rangle = \bigotimes_{l=1}^{N} |\tilde{\sigma}^z_l\rangle = |\{\tilde{\sigma}^z_l\}\rangle$, where $\{\tilde{\sigma}^z_l\}$ is a specified configuration of the rotated spins for the different real-space sites l. Given this, the amplitude of eigenstate $|\Psi_n\rangle$ on FS site $|I\rangle$, $|A_{nI}|^2 = |\langle\Psi_n|I\rangle|^2 = \prod_{l=1}^{N} |\langle\tilde{\sigma}^z_l|\sigma^z_l\rangle|^2 = \prod_{l=1}^{L} p^{(n)}_{l,I}$, where $p^{(n)}_{l,I}$ is the projection of the rotated spin on real-space site l, $\tilde{\sigma}^z_l$, onto the original σ^z_l spin on the same site. This leads to

$$S_{nm} = 2\sum_{I=1}^{N_H}\prod_{l=1}^{L}\frac{p^{(n)}_{l,I}p^{(m)}_{l,I}}{p^{(n)}_{l,I}+p^{(m)}_{l,I}}. \tag{6.16}$$

Unfortunately, no further progress has been made to understand analytically the distribution $P_{S^{NN}}(x)$ from this rather complicated expression.

From the discussion in section 6.1.1, it is clear that both L^{NN} and S^{NN} measure the overlap of nearest neighbour eigenstates, or equivalently the extent to which nearest neighbour eigenstates occupy the same region of Fock-space. Since nearest neighbour MBL eigenstates do not usually occupy the same region of Fock-space, we expect typical L^{NN} and S^{NN} values to be small and vanish with increasing system size L. This means we expect the bulk of the distributions $P_{L^{NN}}(x)$ and $P_{S^{NN}}(x)$ in the MBL phase to be at small x values which vanish with increasing L. This is indeed found to be the case, as will be shown in section 6.3.

One question that naturally arises is can $\mathcal{O}(1)$ L^{NN} and S^{NN} values occur even in MBL_0? From the equations for L_{nm} (eq. 6.1, pg. 151) and S_{nm} (eq. 6.2, pg. 151), it is clear that $\mathcal{O}(1)$ L_{nm} and S_{nm} values occur when $A^2_{nI} \simeq A^2_{mI}$ for all FS sites I. We will now discuss when this may occur within MBL_0.

At this point it is helpful to remind the reader that for two FS sites $|I\rangle$ and $|J\rangle$ the Hamming distance r_{IJ} measures the number of real-space sites for which the value of σ^z_l $(= \pm 1)$ are different in $|I\rangle$ and $|J\rangle$. Similarly in MBL_0 the Hamming distance r_{nm} measures the number of real-space sites for which the two eigenstates

$|\Psi_n\rangle$ and $|\Psi_m\rangle$ have different values for the rotated spin $\tilde{\sigma}_l^z (= \pm 1)$.

In order to have $A_{nI}^2 \simeq A_{mI}^2$ for all FS sites $|I\rangle$, given that $A_{nI}^2 = \prod_{l=1}^{L} p_{l,I}^{(n)}$ and $A_{mI}^2 = \prod_{l=1}^{L} p_{l,I}^{(m)}$ (derived in appendix H), it follows that for all real-space sites l $p_{l,I}^{(n)} \simeq p_{l,I}^{(m)}$. For the $L - r_{nm}$ real-space sites for which the value of $\tilde{\sigma}_l^z$ is identical in both eigenstates, trivially $p_{l,I}^{(n)} \equiv p_{l,I}^{(m)}$. On the other hand, for the r_{nm} real-space sites for which the value of $\tilde{\sigma}_l^z$ differ, we require $p_{l,+} \simeq p_{l,-}$, with $p_{l,\pm} = \frac{1}{2}\left(1 \pm \frac{h_l}{\sqrt{h_l^2+1}}\right)$ (derived in appendix H). Clearly $p_{l,+} \simeq p_{l,-}$ when $h_l \to 0$. It follows that in order for two different eigenstates $|\Psi_m\rangle$ and $|\Psi_n\rangle$ to have $A_{nI}^2 \simeq A_{mI}^2$ for all FS sites $|I\rangle$, the r_{nm} real-space sites on which the $\tilde{\sigma}_l^z$ spins are different must have 'tiny' fields. If this is the case, even within MBL_0, $L_{nm} \simeq 1$ and $S_{nm} \simeq 1$. The probability of having r real-space sites l with small fields decreases exponentially with increasing r, meaning there will be very few such sites in a given disorder realisation, as such naturally making these eigenstates 'rare states'.

6.2 L_{avg}^{NN}, L_{typ}^{NN}, S_{avg}^{NN} and S_{typ}^{NN}

6.2.1 Numerical results

In this section, we discuss our numerical results obtained by exact diagonalisation (ED) for L_{avg}^{NN}, L_{typ}^{NN}, S_{avg}^{NN} and S_{typ}^{NN} for the full TFI model - discussed in chapter 2, eq. 2.1, pg. 21 - with a uniformly distributed $J_z \in [0.8, 1.2]$, $\Gamma = 1$ and different disorder strength (W) values. As a reminder the critical disorder strength for the TFI model considered $W_c \simeq 4$ [62].

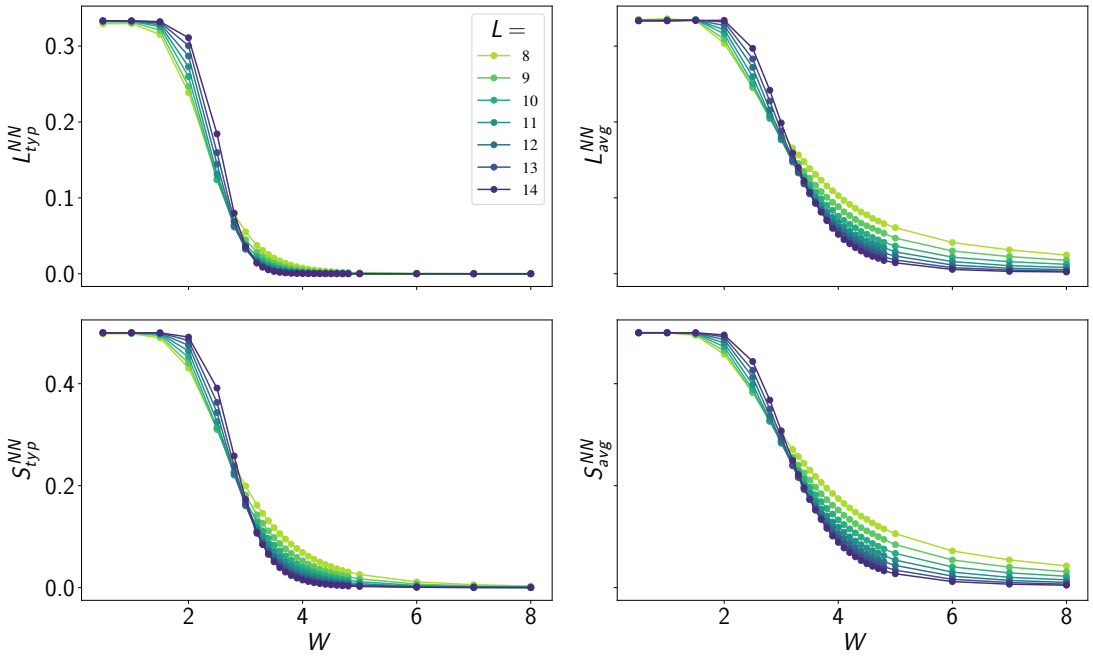


Figure 6.1: L_{typ}^{NN}, L_{avg}^{NN}, S_{typ}^{NN} and S_{avg}^{NN} *vs* W, $L = 8 - 13$ (indicated in plot).

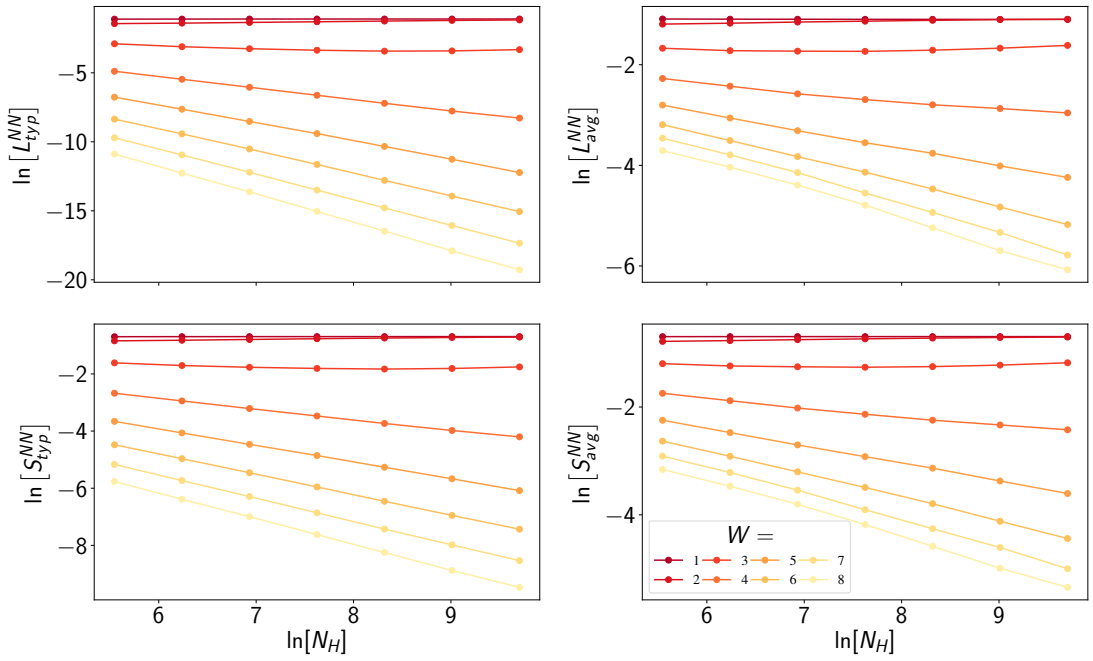


Figure 6.2: $\ln[L_{typ}^{NN}]$, $\ln[L_{avg}^{NN}]$, $\ln[S_{typ}^{NN}]$ and $\ln[S_{avg}^{NN}]$ *vs* $\ln[N_H] = L\ln[2]$ for different disorder strengths, $W = 1 - 7$ (indicated in plot).

To this end, figure 6.1 shows how L_{avg}^{NN}, L_{typ}^{NN}, S_{avg}^{NN} and S_{typ}^{NN} vary with W for different system sizes $L = 8 - 13$. By contrast, figure 6.2 shows how $\ln[L_{typ}^{NN}]$, $\ln[L_{avg}^{NN}]$, $\ln[S_{typ}^{NN}]$ and $\ln[S_{avg}^{NN}]$ vary with $\ln[N_H] = L\ln[2]$ for different disorder

strengths, $W = 1 - 7$. We shall start this section by discussing figure 6.1, before moving on to discuss figure 6.2.

Figure 6.1 shows that deep in the ergodic phase ($W \lesssim 2$), independent of the system size L, $L^{NN}_{typ} = L^{NN}_{avg} \simeq \frac{1}{3}$, as predicted by the GRV model in section 6.1.2. Similarly, deep in the ergodic phase, $S^{NN}_{typ} = S^{NN}_{avg} \simeq \frac{1}{2}$ independent of the system size L, again as predicted by GRV. The figure also shows that deep in the MBL phase ($W \gtrsim 5$), L^{NN}_{typ}, L^{NN}_{avg}, S^{NN}_{typ} and S^{NN}_{avg} all decrease with increasing system size L, and therefore vanish in the thermodynamic limit.

At intermediate W values - on approach to the transition from the ergodic phase, $2 \lesssim W \lesssim 4$ - figure 6.1 shows that L^{NN}_{typ}, L^{NN}_{avg}, S^{NN}_{typ} and S^{NN}_{avg} all decrease with increasing disorder strength W. Crucially, however, these quantities increase with increasing system size L. We therefore expect that they will converge to a finite value in the thermodynamic limit. This will be confirmed by our scaling analysis in section 6.2.2. On the other hand, on approach to the transition from the MBL phase the figure shows that all quantities decrease with increasing system size L, and therefore we expect them to vanish in the thermodynamic limit.

From the above discussion it is clear that figure 6.1 shows a 'crossover region' where, despite all these quantities decreasing continuously with increasing W, in the two W regimes there is different system-size dependence. At small W (left-hand side of plots) L^{NN}_{typ}, L^{NN}_{avg}, S^{NN}_{typ} and S^{NN}_{avg} increase with increasing system size L, while at large W (right-hand side of plots) they decrease with increasing L. This leads in figure 6.1 to L^{NN}_{typ}, L^{NN}_{avg}, S^{NN}_{typ} and S^{NN}_{avg} plots for different system sizes L crossing each other, with the larger L plots crossing at slightly larger W values. This crossing behaviour is known [65–67, 71, 79, 104–109] to occur for other order parameters used to locate the MBL phase transition. This suggests L^{NN}_{typ}, L^{NN}_{avg}, S^{NN}_{typ} and S^{NN}_{avg} are indeed bonafide order parameters for the transition.

We now move to consider figure 6.2. This figure further confirms that deep in the ergodic phase ($W \lesssim 2$) L^{NN}_{typ}, L^{NN}_{avg}, S^{NN}_{typ} and S^{NN}_{avg} are all independent of the system size L, since the $\ln[L^{NN}_{typ}]$, $\ln[L^{NN}_{avg}]$, $\ln[S^{NN}_{typ}]$, and $\ln[S^{NN}_{avg}]$ *vs* $\ln[N_H]$ plots are all horizontal straight lines. By contrast, the figure shows that deep in the MBL phase the $\ln[L^{NN}_{typ}]$, $\ln[L^{NN}_{avg}]$, $\ln[S^{NN}_{typ}]$, and $\ln[S^{NN}_{avg}]$ *vs* $\ln[N_H]$ plots are all straight lines with a negative gradient, i.e. all quantities decrease as $N_H^{-\gamma}$ with $\gamma > 0$, and will vanish in the thermodynamic limit.

On approach to the transition the $\ln[L^{NN}_{typ}]$, $\ln[L^{NN}_{avg}]$, $\ln[S^{NN}_{typ}]$, and $\ln[S^{NN}_{avg}]$ *vs* $\ln[N_H]$ plots in figure 6.2 are seen to be slightly curved, reflecting the finite-size effects known [61, 62, 91, 187, 190–192] to occur on approach to the MBL transition.

In order to understand the behaviour of L^{NN}_{typ}, L^{NN}_{avg}, S^{NN}_{typ} and S^{NN}_{avg} for W values close to the transition a scaling theory is required, and to which we shall now turn.

6.2.2 Introducing the scaling theory

A scaling theory for the behaviour of S^{NN}_{avg}, S^{NN}_{typ}, L^{NN}_{avg} and L^{NN}_{typ} is clearly desirable as it will shed light on the critical behaviour of the overlap of nearest neighbour eigenstates. In this chapter we shall focus on the scaling theory for L^{NN}_{typ} and S^{NN}_{typ}, as the scaling collapse is better than for S^{NN}_{avg} and L^{NN}_{avg}. This can be understood from the probability distributions $\mathcal{P}_{L^{NN}}(x)$ and $\mathcal{P}_{S^{NN}}(x)$ examined later in section 6.3 (the scaling collapse obtained using S^{NN}_{avg} and L^{NN}_{avg} themselves - which uses the same scaling form as for L^{NN}_{typ} and S^{NN}_{typ} discussed below - are shown in appendix L).

Since L_{nm} (eq. 6.1) and S_{nm} (eq. 6.2) are natural generalisations of the IPR to include distinct eigenstates, we might intuitively expect L^{NN}_{typ} and S^{NN}_{typ} to have the same scaling functional form as the IPR. In [94] - inspired by a scaling theory of an Anderson problem on a random regular graph [201] - Macé *et al* showed that the MBL transition in the disordered XXZ chain can be described by a scaling theory

for the participation entropy (PE, introduced in chapter 1) in which the functional form was asymmetrical on the two sides of the transition. On the ergodic side the PE showed 'volumic' scaling, while on the MBL side the PE showed 'linear' scaling (explained in detail below). In [61], Roy and Logan showed that the same scaling form well described the behaviour of the average IPR ($\langle L_2 \rangle$ in our notation, defined in chapter 5) and Sutradhar *et al* [143] showed the same scaling form well described the imaginary part of the self energy (introduced in chapter 1).

Following on from these works, we use the following scaling ansatz for L_{typ}^{NN},

$$\ln\left[\frac{L_{typ}^{NN}(L,W)}{L_{typ}^{NN}(L,W_c)}\right] = \begin{cases} \mathcal{G}_{vol}\left[\frac{N_H}{\Lambda(W)}\right] & W < W_c, \\ \mathcal{G}_{lin}\left[\frac{\ln[N_H]}{\xi(W)}\right] & W > W_c, \end{cases} \tag{6.17}$$

with an identical scaling form assumed for S_{typ}^{NN}.

If the scaling ansatz in eq. 6.17 is correct, in the ergodic phase $\ln\left[\frac{L_{typ}^{NN}(L,W)}{L_{typ}^{NN}(L,W_c)}\right]$ is solely a function of $x = N_H/\Lambda(W)$, where $N_H = 2^L$ is the number of sites or equivalently the 'volume' of the FS lattice, and $\Lambda(W)$ is a characteristic volume on the FS for a given disorder strength W. If our numerical data satisfies this scaling form, then our results for different L and W values will collapse onto a common curve $\mathcal{G}_{vol}(x)$ which solely depends on $x = N_H/\Lambda(W)$.

On the other hand, if the scaling form in eq. 6.17 is correct in the MBL phase, $\ln\left[\frac{L_{typ}^{NN}(L,W)}{L_{typ}^{NN}(L,W_c)}\right]$ is solely a function of $x = \ln[N_H]/\xi(W)$, where $\ln[N_H] = L\ln[2]$ is a length scale on the FS graph and $\xi(W)$ is a characteristic length scale on the FS for a given disorder strength W. Similarly to the ergodic phase, if our numerical data in the MBL phase satisfies this scaling ansatz, then our results for different L and W values will collapse onto a common curve $\mathcal{G}_{lin}(x)$, which solely depends on $x = \ln[N_H]/\xi(W)$.

We shall now move on to discuss the asymptotic forms of the two curves $\mathcal{G}_{vol}(x)$

and $\mathcal{G}_{lin}(x)$ at small and large x values in the ergodic phase and the MBL phase respectively.

From the arguments and results in the previous sections of this chapter, we expect L_{typ}^{NN} and S_{typ}^{NN} to go to a constant in the ergodic phase, and to decrease exponentially with L in the MBL phase. Equivalently we expect,

$$L_{typ}^{NN}(L >> 1, W) = \begin{cases} a(W) & W < W_c, \\ b(W) N_H^{-\gamma(W)} & W > W_c, \end{cases} \tag{6.18}$$

with $\gamma(W)$ increasing with increasing W and $a(W)$ decreasing with increasing W.

Since it is believed that the MBL transition is a Kosterlitz-Thouless-like (KT-like) transition [97, 202–206], the MBL critical point is part of the MBL phase (in renormalisation group language, it is the terminal end point of the line of fixed points characteristic of the MBL phase [207]). We thus expect it to behave as

$$L_{typ}^{NN}(L, W_c) = b_c N_H^{-\gamma_c} \tag{6.19}$$

with $b_c \equiv b(W_c)$ and $\gamma_c \equiv \gamma(W_c)$, just as for $W > W_c$.

In the ergodic phase this means using eqs. 6.18, 6.19 that

$$\ln\left[\frac{L_{typ}^{NN}(L, W)}{L_{typ}^{NN}(L, W_c)}\right] = \ln\left[\frac{a(W)}{b_c}\right] + \gamma_c \ln[N_H], \tag{6.20}$$

which can be rewritten as

$$\ln\left[\frac{L_{typ}^{NN}(L, W)}{L_{typ}^{NN}(L, W_c)}\right] = \gamma_c \ln\left[\frac{N_H}{\Lambda(W)}\right] : \quad \Lambda(W)^{-\gamma_c} = \frac{a(W)}{b_c}. \tag{6.21}$$

With $x \equiv N_H/\Lambda(W)$, the asymptotic form of the scaling function in the ergodic

phase is therefore

$$\mathcal{G}_{vol}(x) = \begin{cases} \gamma_c \ln[x] & x >> 1, \\ 0 & x \to 0. \end{cases} \tag{6.22}$$

The $x \to 0$ result follows simply since, on to approach to the transition, $L_{typ}^{NN}(L, W) \to L_{typ}^{NN}(L, W_c)$, which from eqs. 6.21, 6.17 means $\mathcal{G}_{vol}(x) = 0$.

By contrast in the MBL phase, using eqs. 6.18, 6.19 it follows that

$$\ln\left[\frac{L_{typ}^{NN}(L, W)}{L_{typ}^{NN}(L, W_c)}\right] = (\gamma_c - \gamma(W)) \ln[N_H] + \ln\left[\frac{b(W)}{b_c}\right], \tag{6.23}$$

which can be equivalently written as

$$\ln\left[\frac{L_{typ}^{NN}(L, W)}{L_{typ}^{NN}(L, W_c)}\right] = -\gamma_c \frac{\ln[N_H]}{\xi(W)} + \ln\left[\frac{b(W)}{b_c}\right] : \quad \frac{1}{\xi(W)} = \left(\frac{\gamma(W)}{\gamma_c} - 1\right). \tag{6.24}$$

With $x \equiv \ln[N_H]/\xi(W)$ in this case, it follows from eq. 6.17 that the asymptotic form of the scaling function in the MBL phase is

$$\mathcal{G}_{lin}(x) = \begin{cases} -\gamma_c x & x >> 1, \\ 0 & x \to 0. \end{cases} \tag{6.25}$$

The latter result occurs as $x = \ln[N_H]/\xi(W) \to 0$ means the location length $\xi(W) \to \infty$, which occurs on approach to the transition from the MBL phase. Clearly in this case, $L_{typ}^{NN}(L, W) \to L_{typ}^{NN}(L, W_c)$, which from eqs. 6.24, 6.17 means $\mathcal{G}_{lin}(x) \to 0$.

We now turn to discuss the results obtained using our scaling theory. Details of the numerical procedure used in the scaling analysis are given in appendix M.

6.2.3 Results from scaling theory

Figures 6.3 and 6.4 show the scaling collapse obtained for L_{typ}^{NN} and S_{typ}^{NN} respectively.

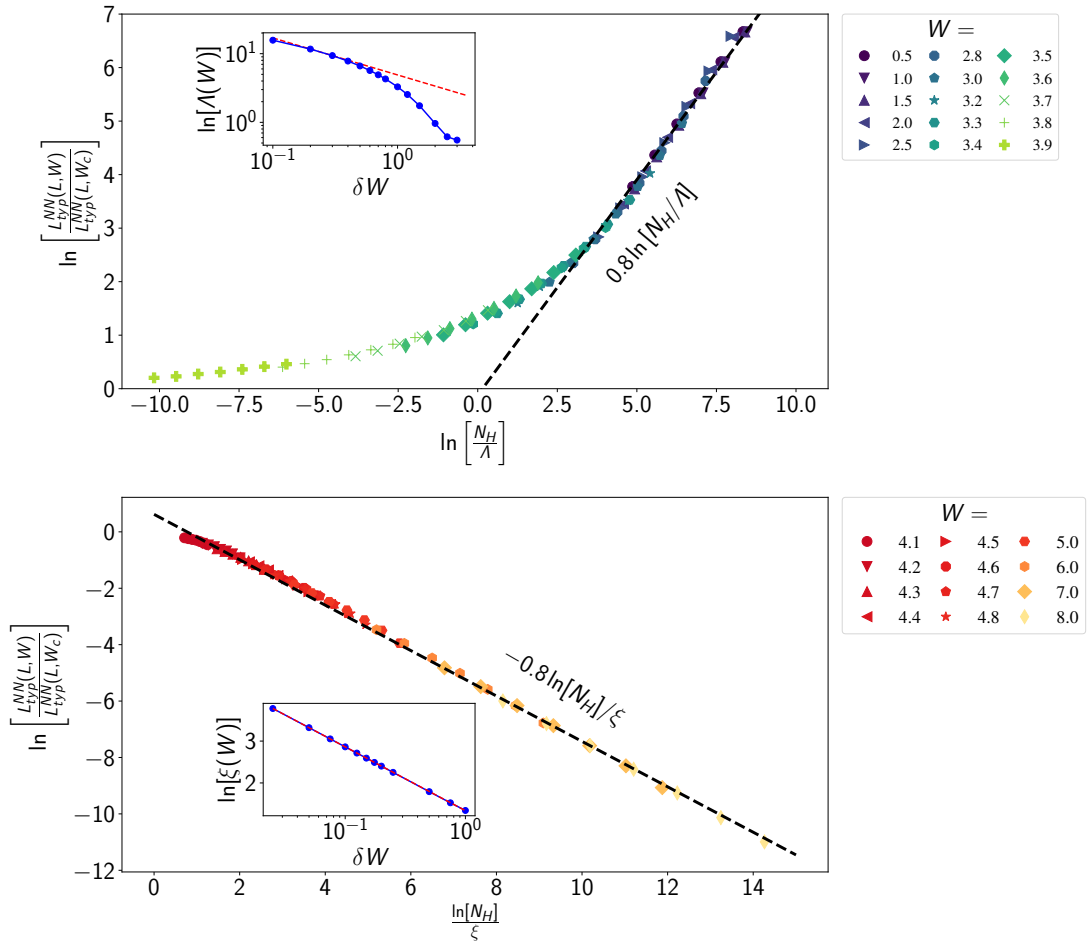


Figure 6.3: Top panel: Ergodic phase scaling analysis $\ln\left[\frac{L_{typ}^{NN}(L,W)}{L_{typ}^{NN}(L,W_c)}\right]$ *vs* $x = N_H/\Lambda(W)$. The black dotted line shows the fitting of the large x data to $\gamma_c \ln[x]$. Bottom panel: MBL scaling analysis $\ln\left[\frac{L_{typ}^{NN}(L,W)}{L_{typ}^{NN}(L,W_c)}\right]$ *vs* $x = \ln[N_H]/\xi(W)$. The black dotted line shows the fitting of the large x data to $-\gamma_c x$. $\Lambda(W)$ and $\xi(W)$ are determined by a fitting procedure discussed in appendix M. Top inset: $\ln[\Lambda(W)]$ *vs* $\delta W = W_c - W$ in the ergodic phase. Bottom inset: $\ln[\xi(W)]$ *vs* $\delta W = W - W_c$ in the MBL phase.

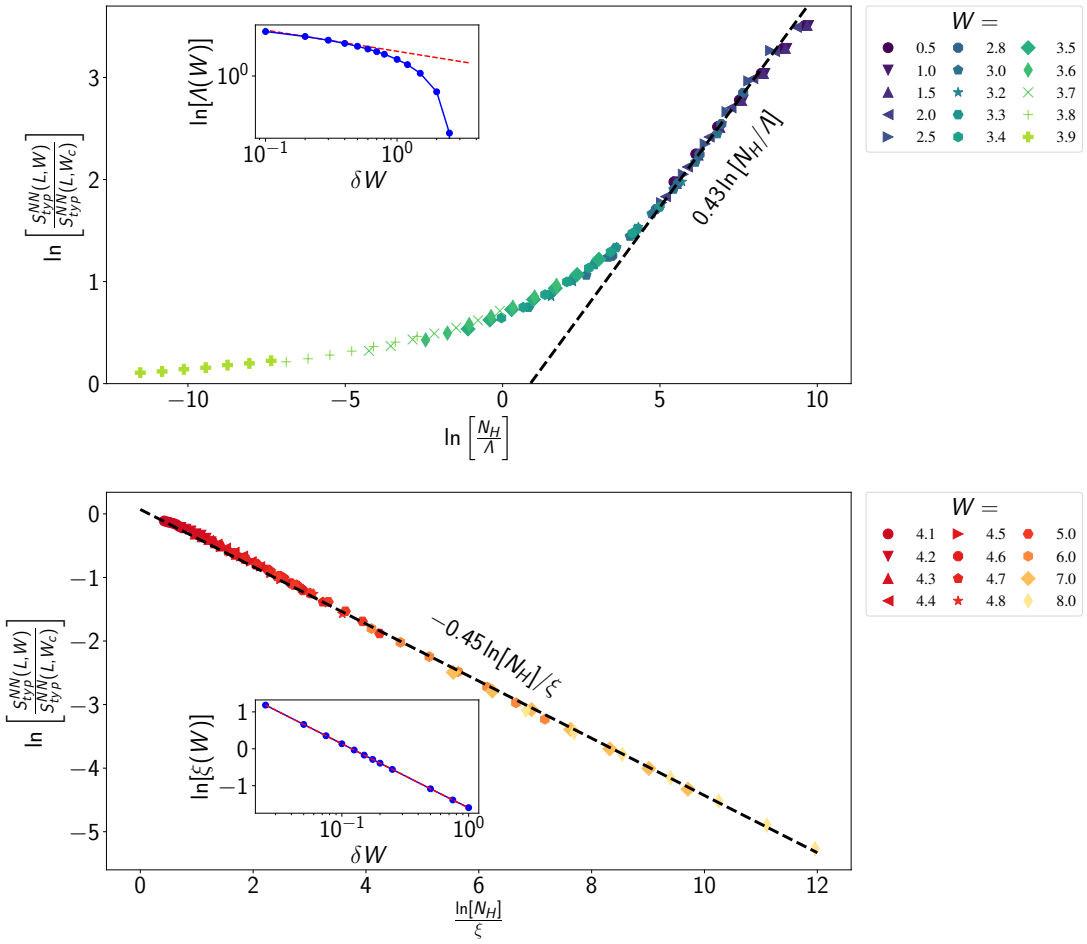


Figure 6.4: Top panel: Ergodic phase scaling analysis $\ln\left[\frac{S^{NN}_{typ}(L,W)}{S^{NN}_{typ}(L,W_c)}\right]$ *vs* $x = N_H/\Lambda(W)$. The black dotted line shows the fitting of the large x data to $\gamma_c \ln[x]$. Bottom panel: MBL scaling analysis $\ln\left[\frac{S^{NN}_{typ}(L,W)}{S^{NN}_{typ}(L,W_c)}\right]$ *vs* $x = \ln[N_H]/\xi(W)$. The black dotted line shows the fitting of the large x data to $-\gamma_c x$. $\Lambda(W)$ and $\xi(W)$ are determined by a fitting procedure discussed in appendix M. Top inset: $\ln[\Lambda(W)]$ *vs* $\delta W = W_c - W$ in the ergodic phase. Bottom inset: $\ln[\xi(W)]$ *vs* $\delta W = W - W_c$ in the MBL phase.

These results in figures 6.3 and 6.4 are obtained by determining $\Lambda(W)$ and $\xi(W)$ from our numerical data for different L and W values in the ergodic phase and the MBL phase respectively. The fitting procedure used to determine $\Lambda(W)$ and $\xi(W)$ is discussed in appendix M. Numerically, we find the collapse of the data onto common curves is best when the critical disorder $W_c = 4$ is chosen. Appendix M shows that visually the scaling collapse of the data using $W_c = 3.9, 4.1$ (i.e. either side of this W_c) is slightly worse than for $W_c \simeq 4$.

The essential result shown in figure 6.3 is that our numerical results for $\ln\left[\frac{L_{typ}^{NN}(L,W)}{L_{typ}^{NN}(L,W_c)}\right]$ for different L and W values collapse onto a universal function of $N_H/\Lambda(W)$ in the ergodic phase and of $\ln[N_H]/\xi(W)$ in the MBL phase. For a given W value, as L increases $N_H/\Lambda(W)$ and $\ln[N_H]/\xi(W)$ increase. This leads to our results in figure 6.3 for two different W values and different L overlapping, with our results in the ergodic and the MBL phases for $\ln\left[\frac{L_{typ}^{NN}(L,W)}{L_{typ}^{NN}(L,W_c)}\right]$ forming continuous curves. The same behaviour is also seen for $\ln\left[\frac{S_{typ}^{NN}(L,W)}{S_{typ}^{NN}(L,W_c)}\right]$ in figure 6.4.

Figures 6.3 and 6.4 show that in the ergodic phase, our data for $\ln\left[\frac{L_{typ}^{NN}(L,W)}{L_{typ}^{NN}(L,W_c)}\right]$ and $\ln\left[\frac{S_{typ}^{NN}(L,W)}{S_{typ}^{NN}(L,W_c)}\right]$ collapse onto common curves, $\mathcal{G}_{vol}(x)$, which are solely a function of $x = N_H/\Lambda(W)$. This means our data in the ergodic phase satisfies the volumic scaling ansatz (eq. 6.17). These plots also have the correct asymptotic behaviour given by eq. 6.22. In both figures, in our numerical data clearly $\mathcal{G}_{vol}(x) \to 0$ as $x \to 0$. Similarly, the black dotted lines in figures 6.3 and 6.4 show that at large x, $\mathcal{G}_{vol}(x)$ is well described by $\gamma_c \ln[x]$.

On the other hand, figures 6.3 and 6.4 show that in the MBL phase, our data for $\ln\left[\frac{L_{typ}^{NN}(L,W)}{L_{typ}^{NN}(L,W_c)}\right]$ and $\ln\left[\frac{S_{typ}^{NN}(L,W)}{S_{typ}^{NN}(L,W_c)}\right]$ collapse onto common curves, $\mathcal{G}_{lin}(x)$, which are solely a function of $x = \ln[N_H]/\xi(W)$. This means our data satisfies the linear scaling ansatz (eq. 6.17). These plots also have the correct asymptotic behaviour given by eq. 6.25. In both figures, in our numerical data clearly $\mathcal{G}_{lin}(x) \to 0$ as $x \to 0$. Similarly, the black dotted lines in figures 6.3 and 6.4 show that at large x, $\mathcal{G}_{lin}(x)$ is well described by $-\gamma_c x$.

Crucially, the values of γ_c obtained by the scaling analysis in the ergodic phase for L_{typ}^{NN} and S_{typ}^{NN} are almost identical to the corresponding values obtained in the MBL phase. Figure 6.3 shows that our results for $\ln\left[\frac{L_{typ}^{NN}(L,W)}{L_{typ}^{NN}(L,W_c)}\right]$ give $\gamma_c \simeq 0.8$ in both phases. An estimate for γ_c can also be obtained by fitting the results for $W_c \simeq 4$ in figure 6.2 to the form $\ln[L_{typ}^{NN}] = -\gamma_c \ln[N_H] + C$. This gives $\gamma_c \simeq 0.82$,

which within numerical error is in agreement with our results for γ_c obtained from the scaling analysis. Similarly figure 6.4 shows that our results for $\ln\left[\frac{S^{NN}_{typ}(L,W)}{S^{NN}_{typ}(L,W_c)}\right]$ give $\gamma_c \simeq 0.43$ in ergodic phase and $\gamma_c \simeq 0.45$ in the MBL phase. An estimate for γ_c can also be obtained by fitting the results for $W_c \simeq 4$ in figure 6.2 to the form $\ln[S^{NN}_{typ}] = -\gamma_c \ln[N_H] + C$. This gives $\gamma_c \simeq 0.39$. It therefore follows that within numerical error, the three estimate for γ_c are in agreement with one another. Clearly, the γ_c obtained for L^{NN}_{typ} differs from the value obtained for S^{NN}_{typ}, this is not however a problem as there is no reason why the two should be the same.

Additionally, figures 6.3 and 6.4 show that the correlation volume $\Lambda(W)$ and correlation length $\xi(W)$ diverge on approaching the transition from the ergodic and MBL side as

$$\Lambda \sim \exp\left[\frac{-c}{(\delta W)^{\alpha}}\right]; \quad \xi \sim (\delta W)^{-\beta}; \quad \delta W = |W - W_c|. \tag{6.26}$$

Our results from the scaling collapse of L^{NN}_{typ} give $\alpha \simeq 0.54$ and $\beta \simeq 0.66$, while our results for the scaling collapse of S^{NN}_{typ} give $\alpha \simeq 0.58$ and $\beta \simeq 0.75$. The values obtained for the exponents α and β for S^{NN}_{typ} and L^{NN}_{typ} are essentially the same. This means that in the ergodic phase $\ln\left[\frac{L^{NN}_{typ}(L,W)}{L^{NN}_{typ}(L,W_c)}\right]$ and $\ln\left[\frac{S^{NN}_{typ}(L,W)}{S^{NN}_{typ}(L,W_c)}\right]$ are both functions of $x = N_H/\Lambda(W)$, with the same functional form for the characteristic volume $\Lambda(W)$ on approach to the transition. Similarly, in the MBL phase $\ln\left[\frac{L^{NN}_{typ}(L,W)}{L^{NN}_{typ}(L,W_c)}\right]$ and $\ln\left[\frac{S^{NN}_{typ}(L,W)}{S^{NN}_{typ}(L,W_c)}\right]$ are both functions of $x = \ln[N_H]/\xi(W)$, with the same functional form for the characteristic length scale $\xi(W)$ on approach to the transition. Since for both S^{NN}_{typ} and L^{NN}_{typ}, $\Lambda(W)$ represents a characteristic volume in the ergodic phase, and $\xi(W)$ represents a characteristic length scale in the MBL phase, independent of which quantity is considered, we would expect $\Lambda(W)$ and $\xi(W)$ to diverge in the same way on approach to the transition. This is indeed as we observe numerically for L^{NN}_{typ} and S^{NN}_{typ}. The values for α and β are indeed also consistent to those

obtained using the scaling collapse of the participation entropies [94], the IPRs [61] and the imaginary part of the self-energy [143]. This means all these quantities have the same scaling form. Importantly, in the scaling analysis of both L_{typ}^{NN} and S_{typ}^{NN}, $\alpha \simeq 0.5$ which is symptomatic of a KT-like transition [97, 202–206].

From eq. 6.26 for $\Lambda(W)$, for any W and L in the ergodic phase ($W < W_c$), $\Lambda(W)$ may be large but importantly it is finite (and independent of system size L). This means in the thermodynamic limit, $x = N_H/\Lambda(W) \to \infty$, as $N_H \to \infty$. The thermodynamic limit clearly corresponds to the large x limit of our scaling analysis (eq. 6.22, pg. 165), which means

$$\ln\left[\frac{L_{typ}^{NN}(L,W)}{L_{typ}^{NN}(L,W_c)}\right] = \gamma_c \ln\left[\frac{N_H}{\Lambda(W)}\right]. \tag{6.27}$$

Since $L_{typ}^{NN}(L,W_c) = b_c N_H^{-\gamma_c}$ (with b_c a finite constant), it follows that

$$\ln\left[L_{typ}^{NN}(L,W)\right] = -\gamma_c \ln\left[\Lambda(W)\right] + \ln[b_c]. \tag{6.28}$$

The same argument also applies for S_{typ}^{NN}, which means evidently

$$L_{typ}^{NN} \sim \Lambda(W)^{-\gamma_c}; \quad S_{typ}^{NN} \sim \Lambda(W)^{-\gamma_c}. \tag{6.29}$$

The fitting in figures 6.3 and 6.4 (eq. 6.26) show that $\Lambda(W)$ diverges exponentially on approach to the transition, which from eq. 6.29 leads to L_{typ}^{NN} and S_{typ}^{NN} vanishing exponentially rapidly on approach to the transition. This means they are indeed order parameters for the MBL phase transition. Note that this is not the same as for 'normal' critical phenomena, where quantities vanish/diverge as powers of δW on approach to the transition. Here, since $\Lambda(W)$ diverges exponentially on approach to the transition, L_{typ}^{NN} and S_{typ}^{NN} vanish exponentially rapidly, with γ_c merely changing

the amplitude with which the exponential vanishes.

Having discussed our scaling theory for L^{NN}_{typ} and S^{NN}_{typ} in detail we shall now move on to consider the distributions $\mathcal{P}_{L^{NN}}(x)$ and $\mathcal{P}_{S^{NN}}(x)$.

6.3 Nearest neighbour distributions

In section 6.2.1 (figure 6.1, pg. 160) we found that deep in the ergodic phase the average and typical L^{NN} and S^{NN} values were essentially identical, while in the MBL phase, the average L^{NN} and S^{NN} values were far greater than the typical values. Additionally, as discussed in section 6.2.2 - and shown in section 6.2.3 and appendix L - we obtain better scaling collapse for the typical values, L^{NN}_{typ} and S^{NN}_{typ}, than for the average values, L^{NN}_{avg} and S^{NN}_{avg}. In this section we shall examine the probability distributions $\mathcal{P}_{L^{NN}}(x)$ and $\mathcal{P}_{S^{NN}}(x)$ (eq, 6.4, pg. 153), which shall enable us to understand these observations.

As a reminder,

$$\mathcal{P}_{L^{NN}}(x) = \langle \delta(x - L^{NN}) \rangle_{n,d}; \quad \mathcal{P}_{S^{NN}}(x) = \langle \delta(x - S^{NN}) \rangle_{n,d}, \tag{6.30}$$

where $\langle \rangle_{n,d}$ denotes an average over disorder realisations and band centre eigenstates (typically the 25 eigenstates either side of the band centre). $L^{NN} = L_{nn+1}$ and $S^{NN} = S_{nn+1}$ are the nearest neighbour (in energy) eigenstates, L_{nm} (eq. 6.1, pg. 151) and S_{nm} (eq. 6.2, pg. 151) values.

6.3.1 Numerical results $\mathcal{P}_{L^{NN}}(x)$ and $\mathcal{P}_{S^{NN}}(x)$

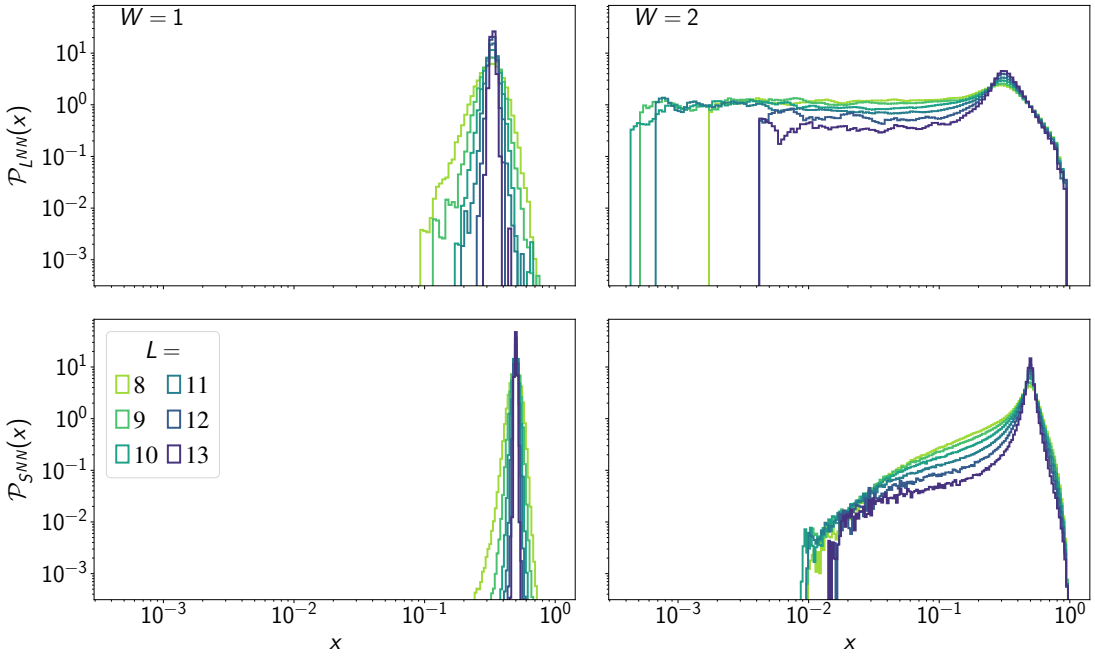


Figure 6.5: Top panels: $\mathcal{P}_{L^{NN}}(x)$ for $W = 1, 2$, and for system sizes $L = 8 - 13$. Bottom panels: $\mathcal{P}_{S^{NN}}(x)$ for the same range of W and L.

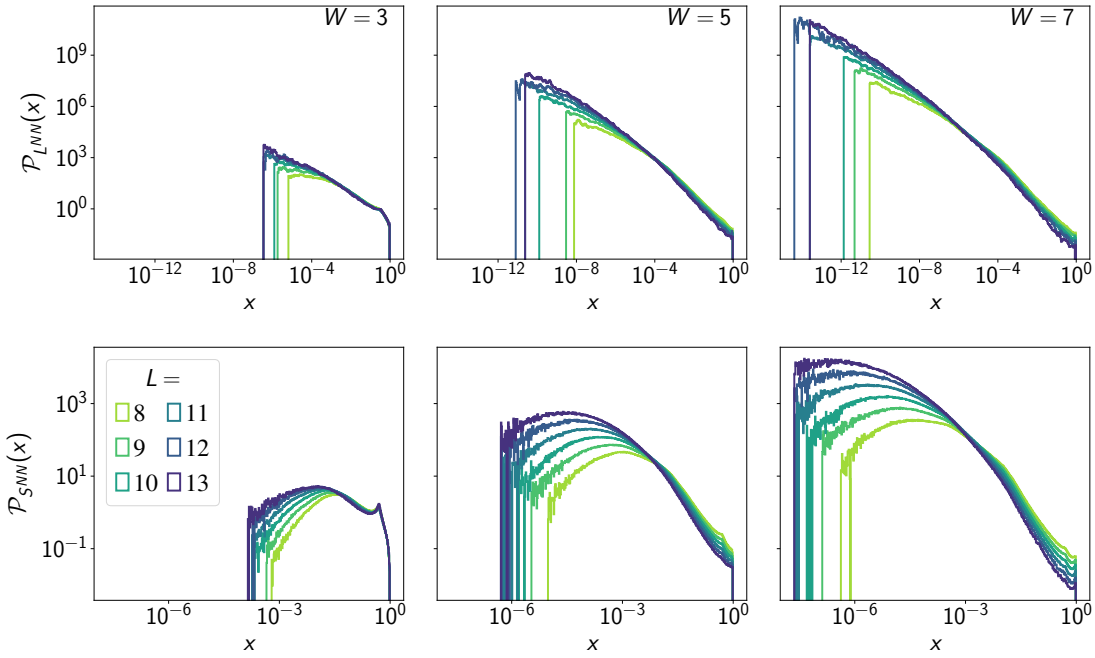


Figure 6.6: Top panels: $\mathcal{P}_{L^{NN}}(x)$ for $W = 3, 5, 7$, and for system sizes $L = 8 - 13$. Bottom panels: $\mathcal{P}_{S^{NN}}(x)$ for the same range of W and L.

In this section and the next, we discuss our numerical results obtained by exact diagonalisation (ED) for $\mathcal{P}_{L^{NN}}(x)$ and $\mathcal{P}_{S^{NN}}(x)$ for the full TFI model - discussed in chapter 2, eq. 2.1, pg. 21 - with a uniformly distributed $J_z \in [0.8, 1.2]$, $\Gamma = 1$ and different disorder strengths, W. To this end, figures 6.5 and 6.6 show how $\mathcal{P}_{L^{NN}}(x)$ and $\mathcal{P}_{S^{NN}}(x)$ vary with disorder strength (W) for $W = 1, 2$ and $W = 3, 5, 7$, $L = 8-13$. As a reminder the critical disorder strength for the TFI model considered $W_c \simeq 4$ [62].

Figure 6.5 shows that deep in the ergodic phase (i.e. $W = 1$), $\mathcal{P}_{L^{NN}}(x)$ and $P_{S^{NN}}(x)$ are very narrow distributions centred on $x \simeq \frac{1}{3}$ and $x \simeq \frac{1}{2}$ respectively. These distributions narrow with increasing L, becoming δ-functions in the thermodynamic limit, i.e. $\mathcal{P}_{L^{NN}}(x) = \delta(x - \frac{1}{3})$ and $\mathcal{P}_{S^{NN}}(x) = \delta(x - \frac{1}{2})$. This is exactly as predicted by the GRV model in section 6.1.2.

The $W = 2$ $\mathcal{P}_{L^{NN}}(x)$ and $\mathcal{P}_{S^{NN}}(x)$ while slightly broader and more skewed than the $W = 1$ distributions for the system sizes amenable to numerics, both become narrower and less skewed distributions with increasing L. This means they are again expected to be δ distributed on $\frac{1}{3}$ and $\frac{1}{2}$ respectively in the thermodynamic limit.

By contrast, figure 6.6 shows that in the MBL phase ($W = 5, 7$) $\mathcal{P}_{L^{NN}}(x)$ and $\mathcal{P}_{S^{NN}}(x)$ have very broad distributions, and appear to have a power-law tail at larger x values (i.e. x around 1). The functional form of these power-law tails shall be examined in the next section (section 6.3.2).

As L increases figure 6.6 shows that for $W = 5, 7$, the modes of $\mathcal{P}_{L^{NN}}(x)$ and $\mathcal{P}_{S^{NN}}(x)$ (peaks of the distributions) move to smaller x values. A brief inspection of the distributions show that they have not converged with L for any of the x range. This is naturally what we would have expected from our results discussed in section 6.2.1 (figures 6.1 and 6.2, pg. 160) which showed that $\mathcal{P}_{L^{NN}}(x)$ and $\mathcal{P}_{S^{NN}}(x)$ means, L^{NN}_{avg} and S^{NN}_{avg}, and their geometric means, L^{NN}_{typ} and S^{NN}_{typ}, decreased with

L. We shall define a rescaled distribution in the next section, which will collapse the distributions in the MBL phase for different L values onto a common functional form.

Finally, figure 6.6 shows that on approach to the transition from the ergodic phase ($W = 3$), $\mathcal{P}_{L^{NN}}(x)$ and $\mathcal{P}_{S^{NN}}(x)$ are broad distributions, which show the usual crossover behaviour [61, 84] between the two forms of the distribution expected in the ergodic and the MBL phases.

6.3.2 Rescaled distributions

In the last section (figure 6.6) we saw that in the MBL phase the distributions $\mathcal{P}_{L^{NN}}(x)$ and $\mathcal{P}_{S^{NN}}(x)$ have not converged with L, and clearly show power-law behaviour at larger x values (i.e. $x \sim \mathcal{O}(1)$). In this section, we shall examine this power-law behaviour.

To this end, we define the rescaled distributions,

$$\mathcal{P}_{\tilde{L}^{NN}}(x) = \int dy\, \mathcal{P}_{L^{NN}}(y)\, \delta\left(x - \frac{y}{L^{NN}_{typ}}\right); \quad \mathcal{P}_{\tilde{S}^{NN}}(x) = \int dy\, \mathcal{P}_{S^{NN}}(y)\, \delta\left(x - \frac{y}{S^{NN}_{typ}}\right), \tag{6.31}$$

alongside their corresponding cumulative distributions,

$$\mathcal{C}_{\tilde{L}^{NN}}(x) = \int_0^x dy\, \mathcal{P}_{\tilde{L}^{NN}}(y); \quad \mathcal{C}_{\tilde{S}^{NN}}(x) = \int_0^x dy\, \mathcal{P}_{\tilde{S}^{NN}}(y). \tag{6.32}$$

Figures 6.7 and 6.8 show, $\mathcal{P}_{\tilde{L}^{NN}}(x)$ and $\mathcal{C}_{\tilde{L}^{NN}}(x)$, and $\mathcal{P}_{\tilde{S}^{NN}}(x)$ and $\mathcal{C}_{\tilde{S}^{NN}}(x)$, for different W values in the MBL phase, $L = 8 - 13$. These figures show that the rescaled distributions $\mathcal{P}_{\tilde{L}^{NN}}(x)$ and $\mathcal{P}_{\tilde{S}^{NN}}(x)$ and their corresponding cumulative distributions $\mathcal{C}_{\tilde{L}^{NN}}(x)$ and $\mathcal{C}_{\tilde{S}^{NN}}(x)$ for different L values clearly collapse onto a common functional form, which extends to both smaller and larger x values as L increases. Given this rescaling, full knowledge of $\mathcal{P}_{L^{NN}}(x)$ and $\mathcal{P}_{S^{NN}}(x)$ for all system

sizes L is possible simply by understanding the system size dependence of L_{typ}^{NN} and S_{typ}^{NN} - examined in section 6.2.1 - and the functional form of these distributions, particularly at large x, to which we now turn.

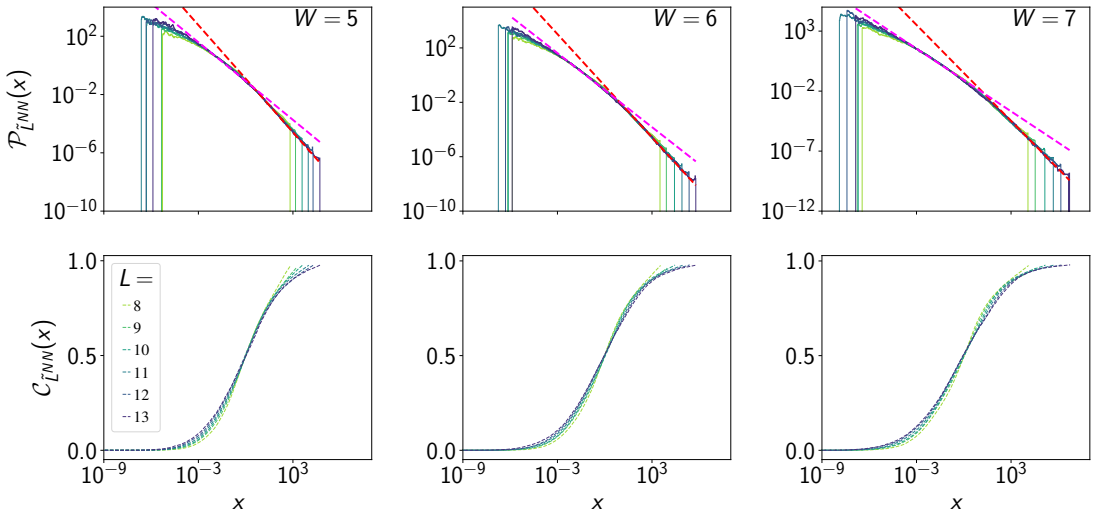


Figure 6.7: Top panels: $\mathcal{P}_{\tilde{L}^{NN}}(x)$ (eq. 6.31) for different W values (indicated in plot), $L = 8 - 13$. Bottom panels: $\mathcal{C}_{\tilde{L}^{NN}}(x)$ (eq. 6.32) for different W values, $L = 8 - 13$. The red dotted line shows the fit for the large-x power-law tail, $\mathcal{P}_{\tilde{L}^{NN}}(x) \sim x^{-a}$. The pink dotted line shows the fit for the small-x power-law behaviour $\mathcal{P}_{\tilde{L}^{NN}}(x) \sim x^{-b}$.

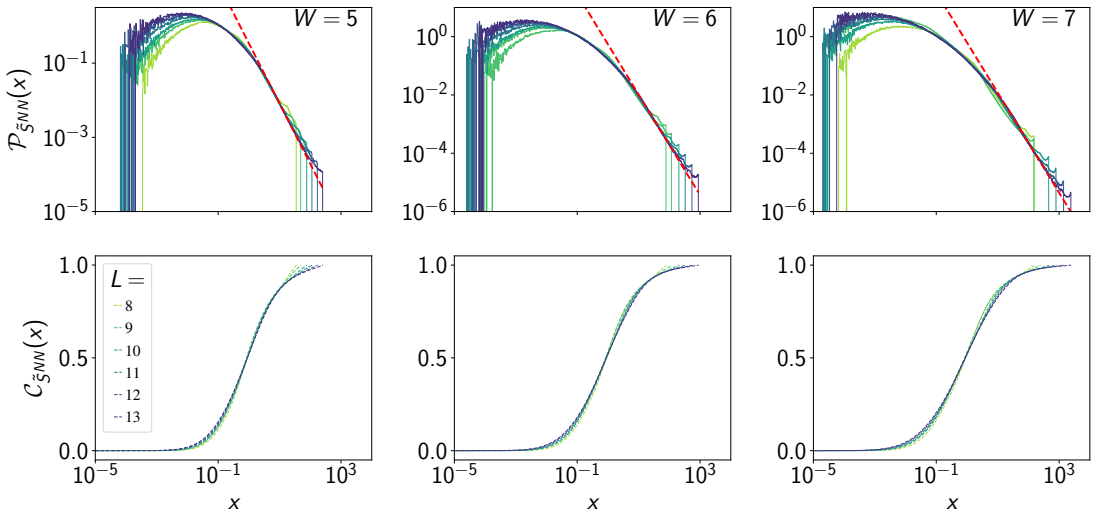


Figure 6.8: $\mathcal{P}_{\tilde{S}^{NN}}(x)$ (eq. 6.31) for different W values (indicated in plot), $L = 8 - 13$. Bottom panels: $\mathcal{C}_{\tilde{S}^{NN}}(x)$ (eq. 6.32) for different W values, $L = 8 - 13$. The red dotted line shows the fit for the large-x power-law tail, $\mathcal{P}_{\tilde{S}^{NN}}(x) \sim x^{-a}$.

At large-x values, figures 6.7 and 6.8 show that both $\mathcal{P}_{\tilde{L}^{NN}}(x)$ and $\mathcal{P}_{\tilde{S}^{NN}}(x)$ have power-law tails $\sim x^{-a}$, with the tails filling out in an obvious sense with increasing

L. $\mathcal{P}_{\tilde{L}^{NN}}(x)$ has a power-law tail exponent a which increases with increasing W. For example, when $W = 5$ $a \simeq 1.23$, while for $W = 7$ $a \simeq 1.33$. The power law exponent a behaves similarly for $\mathcal{P}_{\tilde{S}^{NN}}(x)$ in figure 6.8.

Additionally, figure 6.7 shows that for small-x values $\mathcal{P}_{\tilde{L}^{NN}}(x)$ also displays power-law behaviour, $\mathcal{P}_{\tilde{L}^{NN}}(x) \sim x^{-b}$ (with $b \simeq 0.89$ for $W = 5$ and $b \simeq 0.87$ for $W = 7$). Importantly, $b < 1$, meaning the extension of $\mathcal{P}_{\tilde{L}^{NN}}(x)$ to very small x values ($x << 1$) contributes negligible weight to the distribution. This is exactly as seen in the cumulants $\mathcal{C}_{\tilde{L}^{NN}}(x)$ in the bottom panels of figure 6.7.

The fact that in the MBL phase the large-x power-law tail of $\mathcal{P}_{\tilde{L}^{NN}}(x)$ and $\mathcal{P}_{\tilde{S}^{NN}}(x) \sim x^{-a}$ with $a < 2$ means that the average of $\mathcal{P}_{\tilde{L}^{NN}}(x)$ and $\mathcal{P}_{\tilde{S}^{NN}}(x)$

$$\frac{L^{NN}_{avg}}{L^{NN}_{typ}} = \int dx\, x\, \mathcal{P}_{\tilde{L}^{NN}}(x); \quad \frac{S^{NN}_{avg}}{S^{NN}_{typ}} = \int dx\, x\, \mathcal{P}_{\tilde{S}^{NN}}(x), \tag{6.33}$$

will diverge in the thermodynamic limit.

Figure 6.9 shows how $\frac{L^{NN}_{avg}}{L^{NN}_{typ}}$ and $\frac{S^{NN}_{avg}}{S^{NN}_{typ}}$ vary with W for different system sizes $L = 8 - 13$. This shows that deep in the ergodic phase ($W \lesssim 2$) $\frac{L^{NN}_{avg}}{L^{NN}_{typ}}$ and $\frac{S^{NN}_{avg}}{S^{NN}_{typ}}$ are $\mathcal{O}(1)$, and become closer to one with increasing L. This is simply because as seen in figure 6.5 (pg. 172) deep in the ergodic phase $\mathcal{P}_{L^{NN}}(x)$ and $\mathcal{P}_{S^{NN}}(x)$ narrow with increasing L, becoming δ-functions in the thermodynamic limit. This means the average and typical values approach each other with increasing L, meaning both $\frac{L^{NN}_{avg}}{L^{NN}_{typ}}$ and $\frac{S^{NN}_{avg}}{S^{NN}_{typ}}$ tend to one.

By contrast, figure 6.9 shows that deep in the MBL phase $\frac{L^{NN}_{avg}}{L^{NN}_{typ}}$ and $\frac{S^{NN}_{avg}}{S^{NN}_{typ}}$ increase with increasing L. This simply occurs as $\frac{L^{NN}_{avg}}{L^{NN}_{typ}}$ and $\frac{S^{NN}_{avg}}{S^{NN}_{typ}}$ are the mean of $\mathcal{P}_{\tilde{L}^{NN}}(x)$ and $\mathcal{P}_{\tilde{S}^{NN}}(x)$ (eq. 6.33), which both have power-law tails at large-x values, $\sim x^{-a}$ ($a < 2$), which extend to larger x values as L increases. This means $\frac{L^{NN}_{avg}}{L^{NN}_{typ}}$ and $\frac{S^{NN}_{avg}}{S^{NN}_{typ}}$ will increase with increasing L, and diverge in the thermodynamic limit.

Since it is the tails in $\mathcal{P}_{\tilde{L}^{NN}}(x)$ and $\mathcal{P}_{\tilde{S}^{NN}}(x)$ that cause $\frac{L^{NN}_{avg}}{L^{NN}_{typ}}$ and $\frac{S^{NN}_{avg}}{S^{NN}_{typ}}$ to diverge

in the thermodynamic limit in the MBL phase, it follows that it is the larger L^{NN} and S^{NN} $\mathcal{O}(1)$ values which cause this behaviour. In section 6.1.3 we discussed that S_{nm} and L_{nm} values of $\mathcal{O}(1)$ can even occur in MBL_0 ($J_z = 0$), and discussed the physical reason for this. We shall now compare the rescaled distributions for $J_z = 0$ and a uniformly distributed $J_z \in [0.8, 1.2]$, both obtained by ED, to try and gain some further understanding of these distributions in the interacting problem.

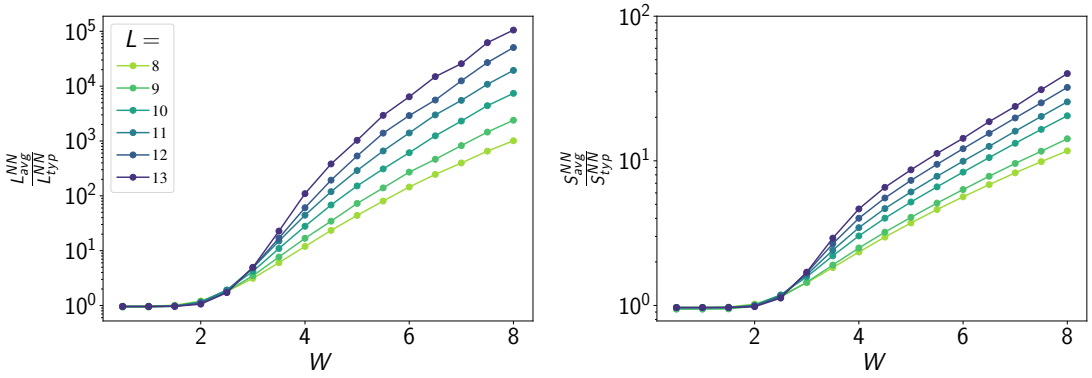


Figure 6.9: $\frac{L^{NN}_{avg}}{L^{NN}_{typ}}$ and $\frac{S^{NN}_{avg}}{S^{NN}_{typ}}$ (eq. 6.33) *vs* W, $L = 8 - 13$.

6.3.3 Comparing to the non-interacting problem

To this end, figures 6.10 and 6.11 show the rescaled distributions $\mathcal{P}_{\tilde{L}^{NN}}(x)$ and $\mathcal{P}_{\tilde{S}^{NN}}(x)$ for $J_z = 0$ and a uniformly distributed $J_z \in [0.8, 1.2]$ (i.e. $J_z \neq 0$) and disorder strengths $W = 5$ and $W = 7$ (all indicated in plots). The figures show that the $\mathcal{P}_{\tilde{L}^{NN}}(x)$ and $\mathcal{P}_{\tilde{S}^{NN}}(x)$ for $J_z = 0$ and $J_z \neq 0$ are very similar, and become increasingly so with increasing W. The figure also shows that both the $J_z = 0$ and the uniformly distributed $J_z \in [0.8, 1.2]$ $\mathcal{P}_{\tilde{L}^{NN}}(x)$ and $\mathcal{P}_{\tilde{S}^{NN}}(x)$ have a power-law decay at large-x values, i.e. $\sim x^{-a}$ (indicated by red line in plot). The power-law exponent a is found to be somewhat larger for $J_z = 0$ than $J_z \neq 0$.

Within the field of localisation, it is well known that when $J_z = 0$ (MBL_0) in one-dimension for any non-zero disorder all eigenstates are localised [26]. In the TFI model this occurs trivially as the problem is site-separable (discussed in appendix

H). This means the 'MBL transition' occurs at $W_c = 0$. On the other hand, in our ED results for $J_z \neq 0$, $W_c \simeq 4$ [62]. This means for a given W value the MBL_0 problem is deeper in its MBL phase than the $J_z \neq 0$ problem.

Figures 6.7 and 6.8 (pg. 175) showed that as W increases in the MBL phase - or equivalently the system moves further into the MBL phase - the power-law exponents a of the large-x tails of $\mathcal{P}_{\tilde{L}^{NN}}(x)$ and $\mathcal{P}_{\tilde{S}^{NN}}(x)$ (which go as x^{-a}) increase. The fact that the power-law exponent a is larger for the $J_z = 0$ problem than the $J_z \neq 0$ problem simply reflects that the $J_z = 0$ problem is deeper in its MBL phase than the $J_z \neq 0$ problem. This is also reflected in figure 6.12 which shows that S^{NN}_{typ} and L^{NN}_{typ} are smaller in the MBL phase ($W \gtrsim 4$) for the $J_z = 0$ problem than the $J_z \neq 0$ problem. The $J_z = 0$ and $J_z \neq 0$ S^{NN}_{typ} and L^{NN}_{typ} values naturally become closer as W increases.

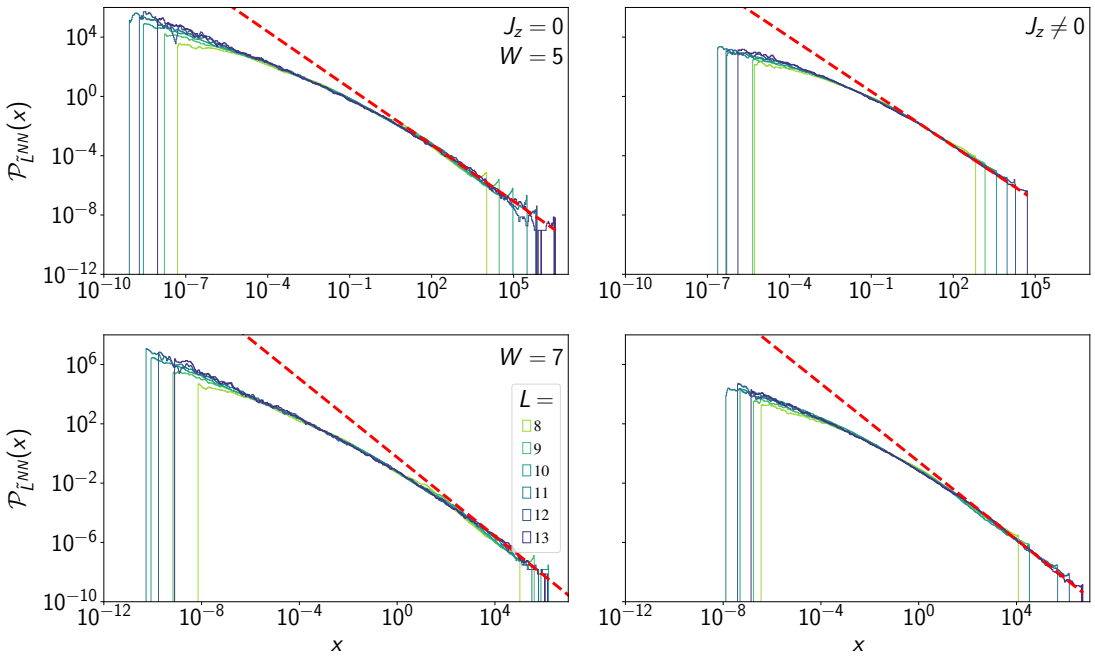


Figure 6.10: $\mathcal{P}_{\tilde{L}^{NN}}(x)$ for $J_z = 0$ and a uniformly distributed $J_z \in [0.8, 1.2]$ ($J_z \neq 0$) and disorder strengths $W = 5$ and $W = 7$. The red dotted line shows the fit of the large-x power-law tails for $\mathcal{P}_{\tilde{L}^{NN}}(x) \sim x^{-a}$. For $W = 5$ $a \simeq 1.27$ for $J_z = 0$ and $a \simeq 1.23$ for uniformly distributed $J_z \in [0.8, 1.2]$, while for $W = 7$ $a \simeq 1.32$ for $J_z = 0$ and $a \simeq 1.33$ for uniformly distributed $J_z \in [0.8, 1.2]$.

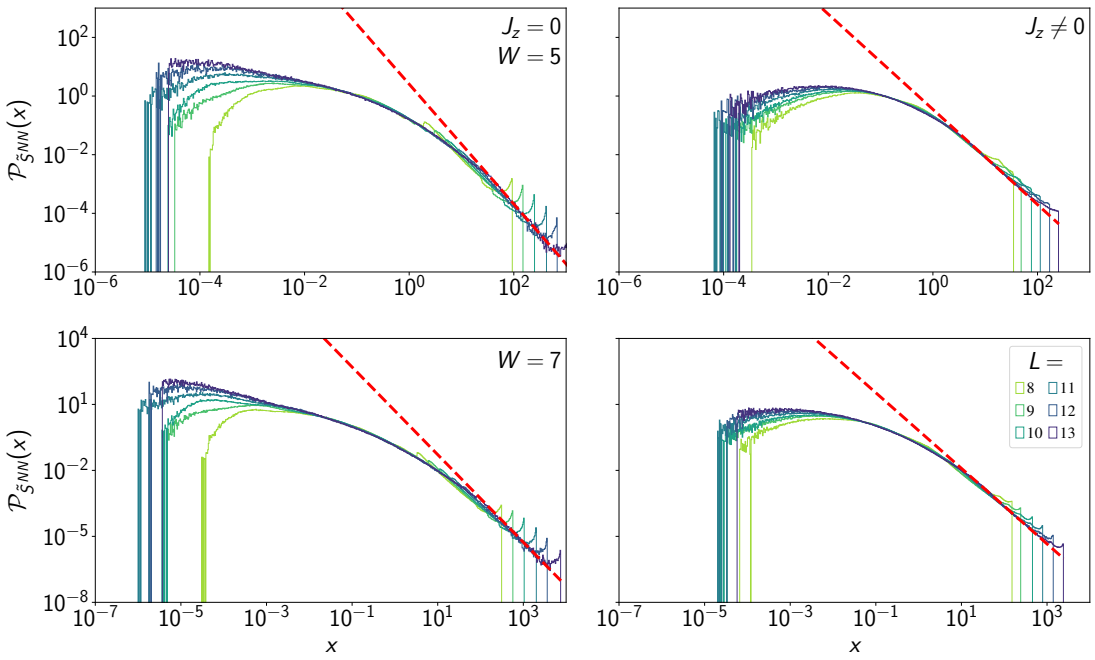


Figure 6.11: $\mathcal{P}_{\tilde{S}^{NN}}(x)$ for $J_z = 0$ and a uniformly distributed $J_z \in [0.8, 1.2]$ $(J_z \neq 0)$ and disorder strengths $W = 5$ and $W = 7$. Red dotted line shows the fit of the large-x power-law tails for $\mathcal{P}_{S^{\tilde{N}N}}(x) \sim x^{-\alpha}$. For $W = 5$ $a \simeq 2$ for $J_z = 0$ and $a \simeq 1.62$ for uniformly distributed $J_z \in [0.8, 1.2]$, while for $W = 7$ $a \simeq 2$ for $J_z = 0$ and $a \simeq 1.72$ for uniformly distributed $J_z \in [0.8, 1.2]$.

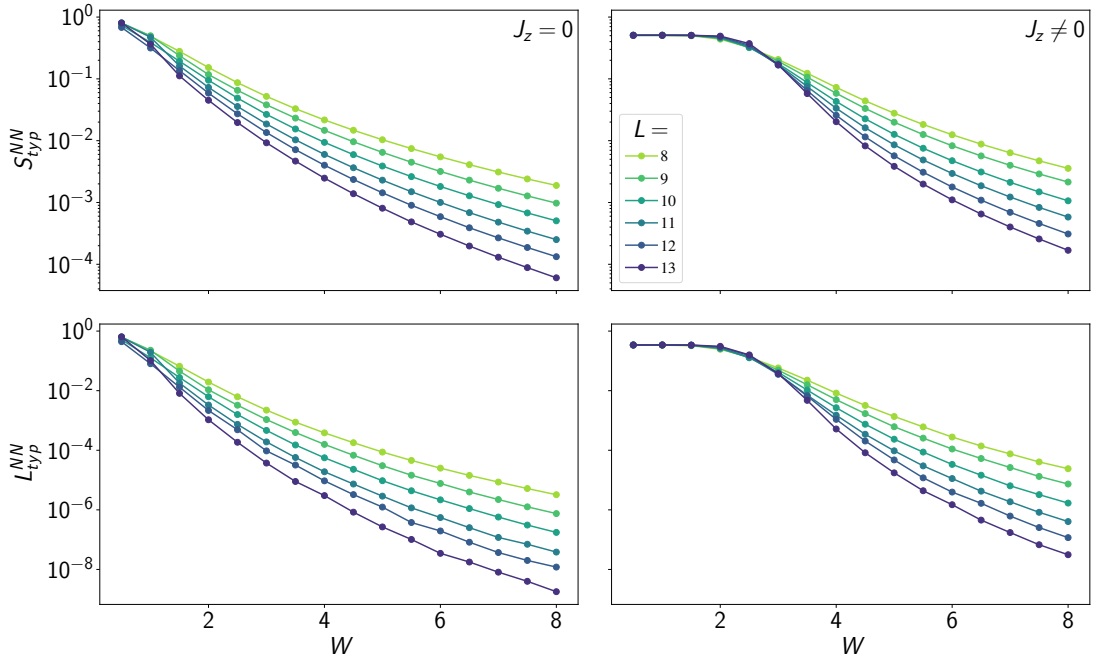


Figure 6.12: L^{NN}_{typ} and S^{NN}_{typ} *vs* W, $L = 8 - 13$, $J_z = 0$ and a uniformly distributed $J_z \in [0.8, 1.2]$ $(J_z \neq 0)$.

Given that $\mathcal{P}_{\tilde{L}^{NN}}(x)$ and $\mathcal{P}_{\tilde{S}^{NN}}(x)$ show qualitatively similar behaviour, with both distributions showing power-law tails at large-x values, for both $J_z = 0$ and $J_z \neq 0$, a natural question to ask is what insight can we gain into this behaviour from the non-interacting problem, MBL_0?

Within MBL_0 in section 6.1.3 we discussed that $L_{nm} \simeq S_{nm} \simeq 1$ when $A^2_{mI} \simeq A^2_{nI}$ for all FS sites $|I\rangle$. For this to occur, for a given pair of eigenstates $|\Psi_m\rangle$ and $|\Psi_n\rangle$, the r_{nm} real-space sites on which the $\tilde{\sigma}^z_l$ spins are different must have 'tiny' fields. The spins on these sites are 'ergodic spins' in the time dynamics initialised from any given FS site $|I\rangle$ (discussed in chapters 3 and 4).

Since the $J_z \neq 0$ problem is perturbatively connected [59] to the $J_z = 0$ problem, a similar mechanism is expected to occur for $J_z \neq 0$, but here the eigenstates would differ by having different orientations of the LIOM (introduced in section 1.8.1) rather than the rotated spins, which is the case in the non-interacting problem. In the interacting problem, many-body resonances between spins have been used to explain many features of the MBL phase [152–156, 158]. Such resonances may lead to L^{NN} and S^{NN} values $\mathcal{O}(1)$. Given the similarity between the $J_z = 0$ and $J_z \neq 0$ distributions, we would however expect many-body resonances to play a relatively minor role, for the probability distributions considered here.

6.4 Summary

In this chapter we have extensively examined two quantities which measure the extent to which nearest neighbour (in energy) eigenstates overlap. Our key results are:

- We have found new order parameters for the MBL transition: L^{NN}_{typ}, L^{NN}_{avg}, S^{NN}_{typ} and S^{NN}_{avg}.

- The behaviour of these quantities on approach to the MBL transition are well

understood from the scaling theory.

- The distributions $\mathcal{P}_{L^{NN}}(x)$ and $\mathcal{P}_{S^{NN}}(x)$ have very different functional forms in the ergodic and the MBL phases. In the ergodic phase, in the thermodynamic limit, $\mathcal{P}_{L^{NN}}(x) = \delta(x - \frac{1}{3})$ and $\mathcal{P}_{S^{NN}}(x) = \delta(x - \frac{1}{2})$ By contrast, in the MBL phase $\mathcal{P}_{L^{NN}}(x)$ and $\mathcal{P}_{S^{NN}}(x)$ have power-law tails at large-x values (i.e. $x \sim \mathcal{O}(1)$), and it is these tails at large-x that cause the average and typical values to differ.

- In the MBL phase, we defined the rescaled distributions, $\mathcal{P}_{\tilde{L}^{NN}}(x)$ and $\mathcal{P}_{\tilde{S}^{NN}}(x)$. This rescaling collapsed the results for different system sizes L onto each other, and we have determined the functional form of their common large-x power law tails. $\mathcal{P}_{L^{NN}}(x)$ and $\mathcal{P}_{S^{NN}}(x)$ have similar power-law tails in both the interacting and non-interacting problems.

- In the non-interacting problem L^{NN} and S^{NN} values of $\mathcal{O}(1)$ can occur due to rare 'ergodic' spins present. Due to perturbative continuity, we expect a similar mechanism to occur in the interacting problem, as indeed appears to be borne out in our numerics.

We have now reached the end of our discussion on our results in this thesis. In the next chapter, we shall summarise our key findings and discuss possible directions for future research.

Chapter 7

Conclusion and Future work

Throughout this thesis we have examined several different aspects of many-body localisation in the TFI model. In this section, we shall summarise the essential results obtained. We will then turn to discuss possible directions for future research.

7.1 Summary

In chapter 2, we introduced the one-dimensional disordered spin-1/2 TFI model. We discussed the usual FS basis considered - the product states of the set of $\{\sigma_l^z\}$ spins - and the properties of the FS lattice that results. We then moved to discuss the two analytical handles, the gaussian random eigenvectors (GRV) model and MBL_0, used to understand our results deep in the ergodic phase and the MBL phase, respectively. We finally discussed the shortest and longest time scales for the dynamics in the TFI model; namely the typical time required to dephase spins, and the Heisenberg time, respectively.

We then went on to discuss (chapters 3 and 4) our work [144] on probability transport on the FS graph. We considered initialising our system in a 'classical' spin configuration or single FS site. We then discussed that the FS graph can be organised such that this initial site sits at the apex of the graph and all sites at a fixed Hamming distance are arranged row-wise. This gave rise to two natural axes along which probability transport can be defined: longitudinal transport and lateral transport.

As a reminder, so called longitudinal transport quantifies how the probability

flows down sites which are an increasing Hamming distance from the initial site. Lateral transport on the other hand measures how probability spreads across sites at the same Hamming distance from the initial site, i.e. on a given row in FS. Longitudinal transport was discussed in chapter 3, while lateral transport was discussed in chapter 4.

In chapter 3 we focused on two quantities. Firstly, a measure of longitudinal transport, the average Hamming distance, $\overline{r}(t) = \sum_{r=0}^{L} \overline{P}(r;t)\ r$, with $\overline{P}(r;t)$ the average probability (taken over FS sites and disorder realisations) of being on any FS site $|J_r\rangle$ a Hamming distance of r away from the initial site $|I\rangle$. Secondly, a real-space quantity, the autocorrelator $C(t) = \frac{1}{L}\sum_{l=1}^{L} C_{ll}(t)$, with the local real-space autocorrelator $C_{ll}(t) = \frac{1}{N_H} Tr(\hat{\sigma}_l^z(t)\hat{\sigma}_l^z)$. The autocorrelator measures the extent to which the system initialised on any FS site $|I\rangle$ retains memory of its initial spin configuration at a given time t.

Through studying longitudinal transport in chapter 3, we uncovered in section 3.2.2 a simple relationship between the average Hamming distance $\overline{r}(t)$ and the average autocorrelator, $\overline{C}(t)$, with

$$\overline{C}(t) = 1 - \frac{2\overline{r}(t)}{L}. \tag{7.1}$$

This relationship provides new insight by connecting between the real-space and Fock-space perspectives, and is not confined to the TFI model considered in this thesis, but equally applies to the XXZ model, and by Jordan Wigner transformation [77] to a related quantity for spinless fermion models.

We then went on to discuss in section 3.2.3, our short time analytical results for the Fock-space length scale $\overline{r}(t)$. Here, we found that at short times ($t << 1$) the system was agnostic to what phase it was in, ergodic or MBL. $\overline{r}(t)$ was found to be $\mathcal{O}(L)$ for finite t however small; which ensured the autocorrrelator is less than unity.

Next, in section 3.2.4 we gave a broad overview of the behaviour of $\overline{P}(r;t)$ in the ergodic and the MBL phases. Section 3.2.5 went on to show that at long times $\overline{r}(t \to \infty)/L \leq \frac{1}{2}$, which means (using eq. 7.1) that $\overline{C}(t \to \infty) \geq 0$.

We then discussed in section 3.2.6 the need to energy resolve $\overline{r}(t)$ and $\overline{C}(t)$ to give $\overline{r}^{[n]}(t)$ and $\overline{C}^{[n]}(t)$, and linked this to the need to energy resolve time-dependent quantities in Anderson (one-body) localisation. Throughout the rest of chapter 3, $\overline{r}^{[n]}(t)$, $\overline{C}^{[n]}(t)$, $\overline{r}(t)$ and $\overline{C}(t)$ were examined extensively.

In the ergodic phase, we found that the band-centre $\overline{C}^{[n]}(t)$ decayed subdiffusively at intermediate times, i.e. $\overline{C}^{[n]}(t) \sim t^{-\alpha}$ with an exponent α that vanished as we approach the transition. Additionally, we saw that $\overline{r}^{[n]}(t \to \infty)/L = 1/2$ which means $\overline{C}^{[n]}(t \to \infty) = 0$. By contrast, in the MBL phase the band-centre $\overline{C}^{[n]}(t)$ was found to reach its long-time finite value at $\Gamma t \simeq 10^2$, with damped oscillations setting in $\Gamma t \simeq 1$. Since $\overline{C}^{[n]}(t \to \infty) > 0$ - reflecting the fact that the system has persistent memory of its initial state for all times - clearly $\overline{r}^{[n]}(t \to \infty)/L < 1/2$. We also saw that in the MBL phase, $\overline{C}^{[n]}(t)$ and $\overline{r}^{[n]}(t)/L$ were well captured by the MBL_0 result.

Finally, in chapter 3 we examined $\overline{C}^{[n]}(t)$ and $\overline{r}^{[n]}(t)/L$ for eigenstates taken from different regions of the band, in order to understand the full $\overline{C}(t)$ and $\overline{r}(t)/L$. We found that in the ergodic phase (for band centre eigenstates), $\overline{C}^{[n]}(t)$ and $\overline{r}^{[n]}(t)/L$ depended on the region of the band the eigenstates were taken from. This reflects the fact that eigenstates from different regions of the band have different propensities for localisation, with the band centre states being the least susceptible to localisation, i.e. in the ergodic phase there are mobility edges present. By contrast, in the MBL phase (for band centre eigenstates), $\overline{C}^{[n]}(t)$ and $\overline{r}^{[n]}(t)/L$ do not depend on the region of the band the eigenstates were taken from, since all eigenstates in the band are localised. This meant $\overline{C}^{[n]}(t) \simeq \overline{C}(t)$ and $\overline{r}^{[n]}(t)/L \simeq \overline{r}(t)/L$, as is the case for our exact MBL_0 ($J_z = 0$) results.

In the first part of chapter 4, we went on to consider lateral transport, through examining how the distribution $P_R(x) = N_H^{-1} \sum_I \langle \delta \left(x - R_I(r;t) \right) \rangle_d$ (with $R_I(r;t) = (\frac{1}{N_r} \sum_{J;r_{IJ}=r} P_{IJ}^2(t))/(\frac{1}{N_r} \sum_{J;r_{IJ}=r} P_{IJ}(t))^2$), its first moment $\langle R \rangle$, and the distribution $P_{\rm rel}(x) = \frac{1}{N_H} \sum_I \frac{1}{N_r} \sum_{J;r_{IJ}=r} \langle \delta(x - (P_{IJ}(t))/(\frac{1}{N_r} \sum_{J;r_{IJ}=r} P_{IJ})) \rangle$, varied with time for different disorder strengths (W). All three measure how homogeneously the set of $\{P_{IJ_r}(t)\}$ are

distributed on a given row r. From examining these quantities in section 4.1 we found that there were three time-regimes for lateral transport.

A short time regime which is agnostic to whether the system is in the ergodic phase or the MBL phase, with the $\{P_{IJ_r}(t)\}$ distributed homogeneously within a given row. This means $P_R(x)$ and $P_{rel}(x)$ are both δ-distributed on $x = 1$, meaning clearly $\langle R \rangle = 1$. Following this is an intermediate time regime, which is again independent of whether the system is in the ergodic phase or the MBL phase, there is strong inhomogeneity in the set of $\{P_{IJ_r}(t)\}$ within a given row r. This is reflected in section 4.1 by the intermediate time $P_R(x)$ having a long-tailed distribution, $\langle R \rangle$ increasing with increasing system size L, and $P_{rel}(x)$ have a broad distribution which becomes broader with increasing L. In the ergodic phase, this inhomogeneity at intermediate times gives way to homogeneity in the $\{P_{IJ_r}(t)\}$ at long times. While in the MBL phase, this inhomogeneity persists for all times.

In section 4.2, we then moved to examine how the time-dependent IPR, $L_2(t) = \frac{1}{N_H}\sum_I \sum_J P_{IJ}^2(t)$, fractal exponent, $\tau_2(t)$ (with the disorder averaged $\overline{L}_2(t) = C_q(t) N_H^{-\tau_2(t)}$) and a similar quantity $a_1(t)$ for the time-dependent first participation entropy, $S_1(t) = \frac{1}{N_H}\sum_I \sum_J P_{IJ}(t) \ln[P_{IJ}(t)]$, (where the disorder averaged $\overline{S}_1(t) = a_1(t) \ln[N_H] + b_1(t) \ln[\ln[N_H]]$), varied with t for different disorder strengths, W. Here, we found that at short times ($\Gamma t < 1$), $\tau_2(t)$ and $a_1(t)$ are both finite and independent of W, where $\tau_2(t)$ is well captured by our short time analytical result (unfortunately no analytical result has been found for $a_1(t)$). This means there is an emergent multi-fractality of the wavefunction at $t \sim \mathcal{O}(1)$. In the ergodic phase, at long times this multifractality is arrested and $\tau_2(t \to \infty) = 1$ and $a_1(t \to \infty) = 1$. By contrast, in the MBL phase this multifractality persists for all times.

Finally in section 4.3, we examined the extent to which the probability of being on row r at time t, $P_I(r;t)$, depends on the initial FS site $|I\rangle$ and/or the disorder realisation, which is probed by $\tilde{P}_{m;rel}(x) = N_H^{-1} \sum_I \langle \delta(x - P_I(r;t)/\overline{P}(r;t)) \rangle_d$. We found that deep in the ergodic phase for all times t $\tilde{P}_{m;rel}(x)$ was a very narrow distribution centred on $x = 1$. This reflects that in the ergodic phase, $P_I(r;t)$ is

independent of the FS site chosen or the disorder realisation. By contrast, in the MBL phase, $\tilde{P}_{m;rel}(x)$ has a broad distribution which broadened with increasing L, reflecting the strong dependence of $P_I(r;t)$ on the initial FS site and/or the disorder realisation.

Having extensively considered probability transport within the TFI model, in chapters 5 and 6 we considered properties of the eigenstates themselves. In chapter 5, we discussed relevant IPR distributions and the origins of multifractality. On the other hand, in chapter 6 we introduced new order parameters for the MBL phase transition.

The essential quantity considered in chapter 5 is the IPR for a given eigenstate and disorder realisation, $L_q = \sum_I |A_{nI}|^{2q}$ (where $A_{nI} = \langle n|I\rangle$ is the probability amplitude of eigenstate $|n\rangle$ on FS site $|I\rangle$), from which we can define a fractal exponent τ_q (with $L_q = C_q N_H^{-\tau_q}$), and $u_q = \ln[L_q]$. Throughout section 5.2 we examined the probability distributions of these quantities taken over band-centre eigenstates and disorder realisations, $P_{L_q}(x) = \langle\delta(x-L_q)\rangle_{n,d}$, $P_{u_q}(x) = \langle\delta(x-u_q)\rangle_{n,d}$ and $P_{\tau_q}(x) = \langle\delta(x-\tau_q)\rangle_{n,d}$, and their first moments $\langle L_q\rangle$, $\langle u_q\rangle$ and $\langle\tau_q\rangle$. We now discuss the essential results obtained from this section.

Firstly, we found that $\langle\tau_q\rangle$ shows very different behaviour in the ergodic phase and the MBL phase. Deep in the ergodic phase, we find that $\langle\tau_q\rangle = q-1$, as expected for extended states. While in the MBL phase, $\langle\tau_q\rangle < q-1$, and is a non-linear function of q, meaning the eigenstates are multifractal. The $J_z \neq 0$ numerical results for $\langle\tau_q\rangle$ are well captured by our exact MBL_0 ($J_z = 0$) results.

Secondly, the distribution $P_{u_q}(x)$ was found to be gaussian in both the ergodic phase and the MBL phase; exactly as predicted by the GRV model and MBL_0. The variance of $P_{u_q}(x)$ was found to differ significantly, with larger inhomogeneity in the distributions in the MBL phase than in the ergodic phase.

Finally, we found that the distributions $P_{L_q}(x)$ have very different functional forms in the ergodic and the MBL phase, with a gaussian distribution found in the ergodic phase and a log-normal distribution in the MBL phase. Again these different

functional forms were predicted by the GRV model and MBL_0.

In section 5.3 we then moved on to discuss generally the origins of multifractality in MBL. In this section - using various mathematical inequalities - we showed that the multifractality arising in the interacting problem can be regarded as having its origins in the non-interacting but many-particle limit.

In the final results chapter of this thesis, we introduced the quantities $L_{nm} = (\sum_I A_{nI}^2 A_{mI}^2)/(\frac{1}{2}\sum_I (A_{nI}^4 + A_{mI}^4))$ and $S_{nm} = \sum_I (A_{nI}^2 A_{mI}^2)/(\frac{1}{2}(A_{nI}^2 + A_{mI}^2))$. Throughout the chapter we focused on L_{nm} and S_{nm} for nearest neighbour eigenstates $|n\rangle$ and $|n+1\rangle$, L_{nn+1} and S_{nn+1}, denoted $L^{NN} = L_{nn+1}$ and $S^{NN} = S_{nn+1}$. In particular, we examined their distributions, $\mathcal{P}_{L^{NN}}(x) = \left\langle \delta(x - L^{NN}) \right\rangle_{n,d}$ and $\mathcal{P}_{S^{NN}}(x) = \left\langle \delta(x - S^{NN}) \right\rangle_{n,d}$, their average values, $L_{avg}^{NN} = \int dx\ x\ \mathcal{P}_{L^{NN}}(x)$ and $S_{avg}^{NN} = \int dx\ x\ \mathcal{P}_{S^{NN}}(x)$, and their typical values, $\ln\left[L_{typ}^{NN}\right] = \int dx\ \ln[x]\ \mathcal{P}_{L^{NN}}(x)$ and $\ln\left[S_{typ}^{NN}\right] = \int dx\ \ln[x]\ \mathcal{P}_{S^{NN}}(x)$. We shall now summarise the results discussed in chapter 6.

Firstly, we found in section 6.2 that L_{typ}^{NN}, L_{avg}^{NN}, S_{typ}^{NN} and S_{avg}^{NN} all act as order parameters for the MBL phase transition. The behaviour of these quantities on approach to the MBL transition are well understood from the scaling theory.

Secondly, we found in section 6.3.1 that the distributions $\mathcal{P}_{L^{NN}}(x)$ and $\mathcal{P}_{S^{NN}}(x)$ have very different functional forms in the ergodic and the MBL phases. In the ergodic phase, in the thermodynamic limit, $\mathcal{P}_{L^{NN}}(x) = \delta(x - \frac{1}{3})$ and $\mathcal{P}_{S^{NN}}(x) = \delta(x - \frac{1}{2})$. By contrast, in the MBL phase $\mathcal{P}_{L^{NN}}(x)$ and $\mathcal{P}_{S^{NN}}(x)$ have power-law tails at large-x values (i.e. $x \sim \mathcal{O}(1)$), and it is these tails at large-x that cause the average and typical values to differ.

Thirdly, in the MBL phase, we defined the rescaled distributions, $\mathcal{P}_{\tilde{L}^{NN}}(x) = \int dy\ \mathcal{P}_{L^{NN}}(y)\ \delta(x - y/L_{typ}^{NN})$ and $\mathcal{P}_{\tilde{S}^{NN}}(x) = \int dy\ \mathcal{P}_{S^{NN}}(y)\ \delta(x - y/S_{typ}^{NN})$. In section 6.3.2 we found that this rescaling collapsed the results for different system sizes L onto each other, and we have determined the functional form of their common large-x power law tails.

Finally, in section 6.3.3 we found that $\mathcal{P}_{L^{NN}}(x)$ and $\mathcal{P}_{S^{NN}}(x)$ have similar power-

law tails in both the interacting and non-interacting problems. In the non-interacting problem L^{NN} and S^{NN} values of $\mathcal{O}(1)$ can occur due to rare 'ergodic' spins present. Due to perturbative continuity, we expect a similar mechanism to occur in the interacting problem. This indeed appears to be borne out in our numerics.

In this thesis, it is clear from the above discussion that we have provided new insight into three separate areas of the MBL transition in Fock-space in the TFI model; namely on probability transport, the origins of multifractality - and related distributions - and defined new order parameters for the transition. There is, however, much more work to be done to fully understand the MBL transition. In the next section, we shall briefly discuss some possible avenues for future research.

7.2 Possible directions for future work

In chapters 3 and 4 of this thesis, we have discussed extensively probability transport in the TFI model. Here, we saw that on approach to the transition we observed subdiffusive transport for e.g. the autocorrelation function. This is believed to occur when the dynamics is constrained by a conservation law, e.g. conversation of spin in the XXZ model [82–87] and conservation of energy in the TFI model (discussed in section 3.2.7). Clearly, it would be of interest to examine probability transport in models with no conservation laws e.g. Floquet models [208–212].

Additionally, in chapters 3 and 4, we saw the persistence of dynamical inhomogeneities in the MBL phase, through the time evolution of e.g. $P_R(x)$, $P_{rel}(x)$, $\langle R(t) \rangle$ and $\overline{r}(t)$, which can provide us with a starting point for understanding and theorising about the role of resonances in the MBL phase from a FS point of view. Speculating that these resonances are caused by rare disorder fluctuations in real space, it is also of interest to ask about probability transport in MBL problems with quasiperiodic potentials (e.g. the Aubry Andre model [20]), which are devoid of such rare regions [109, 180, 213] .

In chapters 3 and 4, we also saw that our results for probability transport in the MBL phase were well captured by our MBL_0 results. At large W we know our

results for the MBL phase are perturbative connected to the $J_z = 0$ (MBL_0) results [59]. It is therefore clearly of interest to examine probability transport starting from an initial quench which is an eigenstate of the non-interacting problem, $|\Psi_n\rangle = \bigotimes_{l=1}^{N} |\tilde{\sigma}_l^z\rangle$ and to then consider 'turning on' interactions and examining probability transport in the product states of the set of rotated spins, $|\{\tilde{\sigma}_l^z\}\rangle$, FS basis.

As well as considering probability transport in the $|\{\tilde{\sigma}_l^z\}\rangle$ FS basis, we could also consider the behaviour of the set of eigenstate amplitudes and the IPRs in this basis. The IPRs in the non-interacting basis was considered in [95, 96] for spinless fermions. The relationship we derived between $\overline{r}(t)$ and $\overline{C}(t)$ does leave some questions about the conclusions drawn in [95, 96].

Finally, given our new order parameters L_{typ}^{NN}, L_{avg}^{NN}, S_{typ}^{NN} and S_{avg}^{NN} for the TFI model, we could consider their behaviour in other commonly studied MBL problems; namely the XXZ model and the MBL problem with a quasiperiodic potentials. The latter would be of interest, as L_{nm} and S_{nm} values $\mathcal{O}(1)$ in the MBL phase occur due to rare low-field regions. Quasiperiodic potentials are devoid of such regions [109, 180, 213] and so the behaviour of $\mathcal{P}_{L^{NN}}(x)$ and $\mathcal{P}_{S^{NN}}(x)$ in these models is clearly of interest.

Bibliography

[1] P. W. Anderson. "Absence of Diffusion in Certain Random Lattices". In: *Phys. Rev.* 109 (1958), p. 1492.

[2] E. Abrahams. *50 Years of Anderson Localization*. World Scientific, 2010.

[3] F. Evers and A. D. Mirlin. "Anderson transitions". In: *Rev. Mod. Phys.* 80 (2008), p. 1355.

[4] P. Phillips. "Anderson Localization and the Exceptions". In: *Annual Review of Physical Chemistry* 44 (1993), p. 115.

[5] D. Thouless. "Electrons in disordered systems and the theory of localization". In: *Physics Reports* 13 (1974), p. 93.

[6] L. D'Alessio et al. "From quantum chaos and eigenstate thermalization to statistical mechanics and thermodynamics". In: *Advances in Physics* 65 (2016), p. 239.

[7] D. A. Abanin et al. "Colloquium: Many-body localization, thermalization, and entanglement". In: *Rev. Mod. Phys.* 91 (2019), p. 021001.

[8] F. Alet and N. Laflorencie. "Many-body localization: an introduction and selected topics". In: *Comptes Rendus Physique* 19 (2018), p. 498.

[9] D. A. Abanin and Z. Papić. "Recent progress in many-body localization". In: *Annalen der Physik* 529 (2017), p. 1700169.

[10] E. Altman and R. Vosk. "Universal dynamics and renormalization in many-body-localized systems". In: *Annual Review of Condensed Matter Physics* 6 (2015), p. 383.

[11] T. J. Sturges et al. “Anderson localisation in steady states of microcavity polaritons”. In: *Sci Rep* 9 (2019), p. 19396.

[12] A. Houghton and H. Won. “Sound attenuation in metals and Anderson localisation”. In: *J. Phys. C: Solid State Phy* 18 (1985), p. L507.

[13] C. M. Aegerter, M. Störzer, and G. Maret. “Experimental determination of critical exponents in Anderson localisation of light”. In: *Europhys. Lett.* 75 (2006), p. 562.

[14] T. Schwartz, S. Fishman, and M. Segev. “Localisation of light in disordered lattices”. In: *Electronics Letters* 44 (2008), p. 165.

[15] M. Van Albada, M. Van Der Mark, and A. Lagendijk. “Polarisation effects in weak localisation of light”. In: *J. Phys. D: Appl. Phys.* 21 (1988), p. 28.

[16] D. H. White et al. “Observation of two-dimensional Anderson localisation of ultracold atoms”. In: *Nat Commun* 11 (2020), p. 4942.

[17] A. Aspect and M. Inguscio. “Anderson localization of ultracold atoms”. In: *Phys. Today* 62 (2009), p. 30.

[18] S. Kondov et al. “Three-dimensional Anderson localization of ultracold matter”. In: *Science* 334 (2011), p. 66.

[19] G. Kucsko et al. “Critical thermalization of a disordered dipolar spin system in diamond”. In: *Phys. Rev. Lett* 121 (2018), p. 023601.

[20] S. Aubry and G. André. “Analyticity breaking and Anderson localization in incommensurate lattices”. In: *Ann. Israel Phys. Soc* 3 (1980), p. 18.

[21] R. E. Prange, D. R. Grempel, and S. Fishman. “Wave functions at a mobility edge: An example of a singular continuous spectrum”. In: *Phys. Rev. B* 28 (1983), p. 7370.

[22] S. D. Sarma, S. He, and X. Xie. “Localization, mobility edges, and metal-insulator transition in a class of one-dimensional slowly varying deterministic potentials”. In: *Phys. Rev. B* 41 (1990), p. 5544.

[23] Y. Wang et al. “One-dimensional quasiperiodic mosaic lattice with exact mobility edges”. In: *Phys. Rev. Lett* 125 (2020), p. 196604.

[24] A. Duthie, S. Roy, and D. E. Logan. “Localization in quasiperiodic chains: A theory based on convergence of local propagators”. In: *Phys. Rev. B* 104 (2021), p. 064201.

[25] C. Castellani, C. Di Castro, and L. Peliti. “On the upper critical dimension in Anderson localisation”. In: *J. Phys. A: Math. Gen.* 19 (1986), p. L1099.

[26] E. Abrahams et al. “Scaling Theory of Localization: Absence of Quantum Diffusion in Two Dimensions”. In: *Phys. Rev. Lett.* 42 (1979), p. 673.

[27] P. W. Anderson et al. “New method for a scaling theory of localization”. In: *Phys. Rev. B* 22 (1980), p. 3519.

[28] J. L. Pichard and G. Sarma. “Finite-size scaling approach to Anderson localisation. II. Quantitative analysis and new results”. In: *J. Phys. C: Solid State Phy* 14 (1981), p. L617.

[29] N. F. Mott and W. Twose. “The theory of impurity conduction”. In: *Advances in Physics* 10 (1961), p. 107.

[30] A. Alvermann et al. “Characterisation of Anderson localisation using distributions”. In: *Physica B: Condensed Matter* 359 (2005), p. 789.

[31] D. Weaire and V. Srivastava. “The Anderson localisation problem II. Some detailed numerical results”. In: *J. Phys. C: Solid State Phy* 10 (1977), p. 4309.

[32] J. T. Chalker and S. Siak. “Anderson localisation on a Cayley tree: a new model with a simple solution”. In: *J. Phys.: Cond. Matt.* 2 (1990), p. 2671.

[33] G. Semeghini et al. “Measurement of the mobility edge for 3D Anderson localization”. In: *Nature Phys* 11 (2015), p. 554.

[34] F. Bloch. “Uber die quantenmechanik der elektronen in kristallgittern”. In: *Zeitschrift fur physik* 52 (1929), p. 555.

[35] E. N. Economou. *Green's Functions in Quantum Physics*. Berlin: Springer, 2006.

[36] E. N. Economou and M. H. Cohen. "Existence of Mobility Edges in Anderson's Model for Random Lattices". In: *Phys. Rev. B* 5 (1972), p. 2931.

[37] R. Abou-Chacra, D. J. Thouless, and P. W. Anderson. "A self-consistent theory of localization". In: *J. Phys. C: Solid State Phy* 6 (1973), p. 1734.

[38] D. C. Licciardello and E. N. Economou. "Study of localization in Anderson's model for random lattices". In: *Phys. Rev. B* 11 (1975), p. 3697.

[39] J. Heinrichs. "Self-consistent theory of localization in random binary alloys and related systems". In: *Phys. Rev. B* 16 (1977), p. 4365.

[40] L. Fleishman and D. Stein. "Localisation in impurity bands". In: *J. Phys. C: Solid State Phy* 12 (1979), p. 4817.

[41] D. E. Logan and P. G. Wolynes. "Localizability and dephasing of dipolar excitons in topologically disordered systems". In: *J. Chem. Phys.* 87 (1987), p. 7199.

[42] D. E. Logan and P. G. Wolynes. "Anderson localization in topologically disordered systems: The effects of band structure". In: *J. Chem. Phys.* 85 (1986), p. 937.

[43] T. Devakul and D. A. Huse. "Anderson localization transitions with and without random potentials". In: *Phys. Rev. B* 96 (2017), p. 214201.

[44] K. S. Tikhonov, A. D. Mirlin, and M. A. Skvortsov. "Anderson localization and ergodicity on random regular graphs". In: *Phys. Rev. B* 94 (2016), p. 220203.

[45] M. Schreiber and H. Grussbach. "Multifractal wave functions at the Anderson transition". In: *Phys. Rev. Lett* 67 (1991), p. 607.

[46] A. Rodriguez et al. "Multifractal finite-size scaling and universality at the Anderson transition". In: *Phys. Rev. B* 84 (2011), p. 134209.

[47] I. M. Khaymovich et al. “Multifractality of random eigenfunctions and generalization of Jarzynski equality”. In: *Nat Commun* 6 (2015), p. 7010.

[48] A. Mirlin and F. Evers. “Multifractality and critical fluctuations at the Anderson transition”. In: *Phys. Rev. B* 62 (2000), p. 7920.

[49] I. A. Gruzberg et al. “Symmetries of Multifractal Spectra and Field Theories of Anderson Localization”. In: *Phys. Rev. Lett.* 107 (2011), p. 086403.

[50] F. Wegner. “Inverse participation ratio in 2+ ε dimensions”. In: *Zeitschrift für Physik B Condensed Matter* 36 (1980), p. 209.

[51] C. Castellani and L. Peliti. “Multifractal wavefunction at the localisation threshold”. In: *J. Phys. A: Math. Gen.* 19 (1986), p. L429.

[52] B. B. Mandelbrot. “Intermittent turbulence in self-similar cascades: divergence of high moments and dimension of the carrier”. In: *Journal of Fluid Mechanics* 62 (1974), p. 331.

[53] R. Bell and P. Dean. “Atomic vibrations in vitreous silica”. In: *Discussions of the Faraday Society* 50 (1970), p. 55.

[54] L. Fleishman and P. W. Anderson. “Interactions and the Anderson transition”. In: *Phys. Rev. B* 21 (1980), p. 2366.

[55] B. L. Altshuler and A. G. Aronov. “Electron–electron interaction in disordered conductors”. In: *Modern Problems in Condensed Matter Sciences*, p. 1.

[56] T. Giamarchi and H. Schulz. “Anderson localization and interactions in one-dimensional metals”. In: *Phys. Rev. B* 37 (1988), p. 325.

[57] A. Finkelshtein. “Effect of Coulomb Interaction on the Properties of Disordered Metals”. In: *Zh. Eksp. Teor. Fiz.* 84 (1983), p. 168.

[58] D. M. Basko, I. L. Aleiner, and B. L. Altshuler. “Metal–insulator transition in a weakly interacting many-electron system with localized single-particle states”. In: *Annals of Physics* 321 (2006), p. 1126.

[59] J. Z. Imbrie. "Diagonalization and Many-Body Localization for a Disordered Quantum Spin Chain". In: *Phys. Rev. Lett.* 117 (2016), p. 027201.

[60] J. A. Kjäll, J. H. Bardarson, and F. Pollmann. "Many-Body Localization in a Disordered Quantum Ising Chain". In: *Phys. Rev. Lett.* 113 (2014), p. 107204.

[61] S. Roy and D. E. Logan. "Fock-space anatomy of eigenstates across the many-body localization transition". In: *Phys. Rev. B* 104 (2021), p. 174201.

[62] D. Abanin et al. "Distinguishing localization from chaos: Challenges in finite-size systems". In: *Annals of Physics* 427 (2021), p. 168415.

[63] S. Roy, J. T. Chalker, and D. E. Logan. "Percolation in Fock space as a proxy for many-body localization". In: *Phys. Rev. B* 99 (2019), p. 104206.

[64] S. Roy, D. E. Logan, and J. T. Chalker. "Exact solution of a percolation analog for the many-body localization transition". In: *Phys. Rev. B* 99 (2019), p. 220201.

[65] V. Oganesyan and D. A. Huse. "Localization of interacting fermions at high temperature". In: *Phys. Rev. B* 75 (2007), p. 155111.

[66] D. E. Logan and S. Welsh. "Many-body localization in Fock space: A local perspective". In: *Phys. Rev. B* 99 (2019), p. 045131.

[67] Y. Bar Lev, G. Cohen, and D. R. Reichman. "Absence of Diffusion in an Interacting System of Spinless Fermions on a One-Dimensional Disordered Lattice". In: *Phys. Rev. Lett.* 114 (2015), p. 100601.

[68] P. Prelovsek et al. "Many-body localization as a percolation phenomenon". In: *Phys. Rev. B* 103 (2021), p. 045139.

[69] L. Rademaker and M. Ortuño. "Explicit Local Integrals of Motion for the Many-Body Localized State". In: *Phys. Rev. Lett.* 116 (2016), p. 010404.

[70] M. Znidaric, T. Prosen, and P. Prelovsek. "Many-body localization in the Heisenberg XXZ magnet in a random field". In: *Phys. Rev. B* 77 (2008), p. 064426.

[71] M. Serbyn and J. E. Moore. “Spectral statistics across the many-body localization transition”. In: *Phys. Rev. B* 93 (2016), p. 041424.

[72] M. Serbyn, Z. Papic, and D. A. Abanin. “Criterion for Many-Body Localization-Delocalization Phase Transition”. In: *Phys. Rev. X* 5 (2015), p. 041047.

[73] P. Sierant, D. Delande, and J. Zakrzewski. “Thouless Time Analysis of Anderson and Many-Body Localization Transitions”. In: *Phys. Rev. Lett.* 124 (2020), p. 186601.

[74] S. Roy and D. E. Logan. “Fock-space correlations and the origins of many-body localization”. In: *Phys. Rev. B* 101 (2020), p. 134202.

[75] C. L. Baldwin et al. “Clustering of Nonergodic Eigenstates in Quantum Spin Glasses”. In: *Phys. Rev. Lett.* 118 (2017), p. 127201.

[76] A. Elben et al. “Rényi Entropies from Random Quenches in Atomic Hubbard and Spin Models”. In: *Phys. Rev. Lett.* 120 (2018), p. 050406.

[77] C. D. Batista and G. Ortiz. “Generalized Jordan-Wigner Transformations”. In: *Phys. Rev. Lett.* 86 (2001), p. 1082.

[78] R. Yousefjani and A. Bayat. “Mobility edge in long-range interacting many-body localized systems”. In: *Phys. Rev. B* 107 (2023), p. 045108.

[79] D. J. Luitz, N. Laflorencie, and F. Alet. “Many-body localization edge in the random-field Heisenberg chain”. In: *Phys. Rev. B* 91 (2015), p. 081103.

[80] T. Kohlert et al. “Observation of Many-Body Localization in a One-Dimensional System with a Single-Particle Mobility Edge”. In: *Phys. Rev. Lett.* 122 (2019), p. 170403.

[81] T. Chanda, P. Sierant, and J. Zakrzewski. “Many-body localization transition in large quantum spin chains: The mobility edge”. In: *Phys. Rev. Res.* 2 (2020), p. 032045.

[82] K. Agarwal et al. “Anomalous Diffusion and Griffiths Effects Near the Many-Body Localization Transition”. In: *Phys. Rev. Lett.* 114 (2015), p. 160401.

[83] E. J. Torres-Herrera and L. F. Santos. “Dynamics at the many-body localization transition”. In: *Phys. Rev. B* 92 (2015), p. 014208.

[84] D. J. Luitz. “Long tail distributions near the many-body localization transition”. In: *Phys. Rev. B* 93 (2016), p. 134201.

[85] D. J. Luitz and Y. Bar Lev. “Anomalous Thermalization in Ergodic Systems”. In: *Phys. Rev. Lett.* 117 (2016), p. 170404.

[86] D. J. Luitz and Y. Bar Lev. “The ergodic side of the many-body localization transition”. In: *Annalen der Physik* 529 (2017), p. 1600350.

[87] S. Roy, Y. Bar Lev, and D. J. Luitz. “Anomalous thermalization and transport in disordered interacting Floquet systems”. In: *Phys. Rev. B* 98 (2018), p. 060201.

[88] Y. Prasad and A. Garg. “Many-body localization and enhanced nonergodic subdiffusive regime in the presence of random long-range interactions”. In: *Phys. Rev. B* 103 (2021), p. 064203.

[89] R. Yao and J. Zakrzewski. “Many-body localization of bosons in an optical lattice: Dynamics in disorder-free potentials”. In: *Phys. Rev. B* 102 (2020), p. 104203.

[90] Y. Wang et al. “Many-Body Critical Phase: Extended and Nonthermal”. In: *Phys. Rev. Lett.* 126 (2021), p. 080602.

[91] A. Solórzano, L. F. Santos, and E. J. Torres-Herrera. “Multifractality and self-averaging at the many-body localization transition”. In: *Phys. Rev. Res.* 3 (2021), p. L032030.

[92] D. J. Luitz, I. M. Khaymovich, and Y. B. Lev. “Multifractality and its role in anomalous transport in the disordered XXZ spin-chain”. In: *SciPost Phys. Core* 2 (2020), p. 006.

[93] K. S. Tikhonov and A. D. Mirlin. “Many-body localization transition with power-law interactions: Statistics of eigenstates”. In: *Phys. Rev. B* 97 (2018), p. 214205.

[94] N. Mace, F. Alet, and N. Laflorencie. “Multifractal Scalings Across the Many-Body Localization Transition”. In: *Phys. Rev. Lett.* 123 (2019), p. 180601.

[95] S. Bera et al. “Many-Body Localization Characterized from a One-Particle Perspective”. In: *Phys. Rev. Lett.* 115 (2015), p. 046603.

[96] T. Orito and K. Imura. “Multifractality and Fock-space localization in many-body localized states: One-particle density matrix perspective”. In: *Phys. Rev. B* 103 (2021), p. 214206.

[97] G. De Tomasi et al. “Rare thermal bubbles at the many-body localization transition from the Fock space point of view”. In: *Phys. Rev. B* 104 (2021), p. 024202.

[98] G. De Tomasi and I. M. Khaymovich. “Multifractality Meets Entanglement: Relation for Nonergodic Extended States”. In: *Phys. Rev. Lett.* 124 (2020), p. 200602.

[99] M. Serbyn, Z. Papic, and D. A. Abanin. “Thouless energy and multifractality across the many-body localization transition”. In: *Phys. Rev. B* 96 (2017), p. 104201.

[100] S. Roy. “Hilbert-space correlations beyond multifractality and bipartite entanglement in many-body localized systems”. In: *Phys. Rev. B* 106 (2022), p. L140204.

[101] S. Roy and D. E. Logan. “Self-consistent theory of many-body localisation in a quantum spin chain with long-range interactions”. In: *SciPost Phys.* 7 (2019), p. 42.

[102] D. J. Luitz, F. Alet, and N. Laflorencie. “Universal Behavior beyond Multifractality in Quantum Many-Body Systems”. In: *Phys. Rev. Lett.* 112 (2014), p. 057203.

[103] D. J. Luitz, N. Laflorencie, and F. Alet. “Participation spectroscopy and entanglement Hamiltonian of quantum spin models”. In: *J. Stat. Mech.* 2014 (2014), p. 08007.

[104] A. Pal and D. A. Huse. “Many-body localization phase transition”. In: *Phys. Rev. B* 82 (2010), p. 174411.

[105] A. C. Potter, R. Vasseur, and S. A. Parameswaran. “Universal Properties of Many-Body Delocalization Transitions”. In: *Phys. Rev. X* 5 (2015), p. 031033.

[106] M. Serbyn, Z. Papic, and D. A. Abanin. “Local Conservation Laws and the Structure of the Many-Body Localized States”. In: *Phys. Rev. Lett.* 111 (2013), p. 127201.

[107] B. Bauer and C. Nayak. “Area laws in a many-body localized state and its implications for topological order”. In: *J. Stat. Mech.* 2013 (2013), p. 09005.

[108] D. A. Huse, R. Nandkishore, and V. Oganesyan. “Phenomenology of fully many-body-localized systems”. In: *Phys. Rev. B* 90 (2014), p. 174202.

[109] V. Khemani et al. “Critical Properties of the Many-Body Localization Transition”. In: *Phys. Rev. X* 7 (2017), p. 021013.

[110] M. Serbyn, Z. Papic, and D. A. Abanin. “Quantum quenches in the many-body localized phase”. In: *Phys. Rev. B* 90 (2014), p. 174302.

[111] D. J. Luitz, N. Laflorencie, and F. Alet. “Extended slow dynamical regime close to the many-body localization transition”. In: *Phys. Rev. B* 93 (2016), p. 060201.

[112] Y. Zhao et al. “Entanglement dynamics in the three-dimensional Anderson model”. In: *Phys. Rev. B* 102 (2020), p. 195132.

[113] M. McGinley, A. Nunnenkamp, and J. Knolle. “Slow growth of out-of-time-order correlators and entanglement entropy in integrable disordered systems”. In: *Phys. Rev. Lett.* 122 (2019), p. 020603.

[114] M. Serbyn, Z. Papic, and D. A. Abanin. “Universal Slow Growth of Entanglement in Interacting Strongly Disordered Systems”. In: *Phys. Rev. Lett.* 110 (2013), p. 260601.

[115] T. L. M. Lezama and D. J. Luitz. “Power-law entanglement growth from typical product states”. In: *Phys. Rev. Res.* 1 (2019), p. 033067.

[116] A. Lerose and S. Pappalardi. “Origin of the slow growth of entanglement entropy in long-range interacting spin systems”. In: *Phys. Rev. Res.* 2 (2020), p. 012041.

[117] T. Zhou and D. J. Luitz. “Operator entanglement entropy of the time evolution operator in chaotic systems”. In: *Phys. Rev. B* 95 (2017), p. 094206.

[118] J. H. Bardarson, F. Pollmann, and J. E. Moore. “Unbounded Growth of Entanglement in Models of Many-Body Localization”. In: *Phys. Rev. Lett.* 109 (2012), p. 017202.

[119] T. L. Hill. *Statistical mechanics: principles and selected applications*. Courier Corporation, 2013.

[120] G. Biroli and M. Tarzia. “Delocalization and ergodicity of the Anderson model on Bethe lattices”. In: *arXiv* (2018).

[121] I. García-Mata et al. “Scaling Theory of the Anderson Transition in Random Graphs: Ergodicity and Universality”. In: *Phys. Rev. Lett.* 118 (2017), p. 166801.

[122] M. Dupont, N. Mace, and N. Laflorencie. “From eigenstate to Hamiltonian: Prospects for ergodicity and localization”. In: *Phys. Rev. B* 100 (2019), p. 134201.

[123] S. Roy and A. Lazarides. “Strong ergodicity breaking due to local constraints in a quantum system”. In: *Phys. Rev. Res.* 2 (2020), p. 023159.

[124] A. De Luca and A. Scardicchio. “Ergodicity breaking in a model showing many-body localization”. In: *Europhys. Lett.* 101 (2013), p. 37003.

[125] J. M. Deutsch. “Quantum statistical mechanics in a closed system”. In: *Phys. Rev. A* 43 (1991), p. 2046.

[126] M. Srednicki. “Chaos and quantum thermalization”. In: *Phys. Rev. E* 50 (1994), p. 888.

[127] W. Beugeling, R. Moessner, and M. Haque. “Finite-size scaling of eigenstate thermalization”. In: *Phys. Rev. E* 89 (2014), p. 042112.

[128] M. Rigol, V. Dunjko, and M. Olshanii. “Thermalization and its mechanism for generic isolated quantum systems”. In: *Nature* 452 (2008), p. 854.

[129] R. Nandkishore and D. A. Huse. “Many-body localization and thermalization in quantum statistical mechanics”. In: *Annual Review of Condensed Matter Physics* 6 (2015), p. 15.

[130] F. Borgonovi et al. “Quantum chaos and thermalization in isolated systems of interacting particles”. In: *Physics Reports* 626 (2016), p. 1.

[131] B. L. Altshuler et al. “Quasiparticle Lifetime in a Finite System: A Nonperturbative Approach”. In: *Phys. Rev. Lett.* 78 (1997), p. 2803.

[132] C. Monthus and T. Garel. “Many-body localization transition in a lattice model of interacting fermions: Statistics of renormalized hoppings in configuration space”. In: *Phys. Rev. B* 81 (2010), p. 134202.

[133] F. Pietracaprina, V. Ros, and A. Scardicchio. “Forward approximation as a mean-field approximation for the Anderson and many-body localization transitions”. In: *Phys. Rev. B* 93 (2016), p. 054201.

[134] C. L. Baldwin et al. “The many-body localized phase of the quantum random energy model”. In: *Phys. Rev. B* 93 (2016), p. 024202.

[135] F. Pietracaprina and N. Laflorencie. “Hilbert-space fragmentation, multifractality, and many-body localization”. In: *Annals of Physics* (2021), p. 168502.

[136] G. De Tomasi et al. “Dynamics of strongly interacting systems: From Fock-space fragmentation to many-body localization”. In: *Phys. Rev. B* 100 (2019), p. 214313.

[137] S. Ghosh et al. “Many-body localization due to correlated disorder in Fock space”. In: *Phys. Rev. B* 99 (2019), p. 165131.

[138] S. Nag and A. Garg. “Many-body localization in the presence of long-range interactions and long-range hopping”. In: *Phys. Rev. B* 99 (2019), p. 224203.

[139] G. Biroli and M. Tarzia. “Anomalous dynamics on the ergodic side of the many-body localization transition and the glassy phase of directed polymers in random media”. In: *Phys. Rev. B* 102 (2020), p. 064211.

[140] M. Tarzia. “Many-body localization transition in Hilbert space”. In: *Phys. Rev. B* 102 (2020), p. 014208.

[141] M. Hopjan and F. Heidrich-Meisner. “Many-body localization from a one-particle perspective in the disordered one-dimensional Bose-Hubbard model”. In: *Phys. Rev. A* 101 (2020), p. 063617.

[142] K. S. Tikhonov and A. D. Mirlin. “Eigenstate correlations around the many-body localization transition”. In: *Phys. Rev. B* 103 (2021), p. 064204.

[143] J. Sutradhar et al. “Scaling of the Fock-space propagator and multifractality across the many-body localization transition”. In: *Phys. Rev. B* 106 (2022), p. 054203.

[144] I. Creed, D. E. Logan, and S. Roy. “Probability transport on the Fock space of a disordered quantum spin chain”. In: *Phys. Rev. B* 107 (2023), p. 094206.

[145] Y. Y. Atas et al. “Distribution of the Ratio of Consecutive Level Spacings in Random Matrix Ensembles”. In: *Phys. Rev. Lett.* 110 (2013), p. 084101.

[146] E. Feenberg. “A note on perturbation theory”. In: *Phys. Rev.* 74 (1948), p. 206.

[147] A. Duthie, S. Roy, and D. E. Logan. “Self-consistent theory of mobility edges in quasiperiodic chains”. In: *Phys. Rev. B* 103 (2021), p. L060201.

[148] E. J. Torres-Herrera, A. M. García-García, and L. F. Santos. "Generic dynamical features of quenched interacting quantum systems: Survival probability, density imbalance, and out-of-time-ordered correlator". In: *Phys. Rev. B* 97 (2018), p. 060303.

[149] M. Schiulaz, E. J. Torres-Herrera, and L. F. Santos. "Thouless and relaxation time scales in many-body quantum systems". In: *Phys. Rev. B* 99 (2019), p. 174313.

[150] L. F. Santos and E. J. Torres-Herrera. "Analytical expressions for the evolution of many-body quantum systems quenched far from equilibrium". In: *AIP Conference Proceedings* 1912 (2017), p. 020015.

[151] E. J. Torres-Herrera et al. "Self-averaging in many-body quantum systems out of equilibrium: Approach to the localized phase". In: *Phys. Rev. B* 102 (2020), p. 094310.

[152] A. Morningstar et al. "Avalanches and many-body resonances in many-body localized systems". In: *Phys. Rev. B* 105 (2022), p. 174205.

[153] R. Ghosh and M. Znidaric. "Resonance-induced growth of number entropy in strongly disordered systems". In: *Phys. Rev. B* 105 (2022), p. 144203.

[154] S. J. Garratt and S. Roy. "Resonant energy scales and local observables in the many-body localized phase". In: *Phys. Rev. B* 106 (2022), p. 054309.

[155] P. J. D. Crowley and A. Chandran. "A constructive theory of the numerically accessible many-body localized to thermal crossover". In: *SciPost Phys.* 12 (2022), p. 201.

[156] D. M. Long et al. "Phenomenology of the Prethermal Many-Body Localized Regime". In: *arXiv* (2022).

[157] V. Ros, M. Müller, and A. Scardicchio. "Integrals of motion in the many-body localized phase". In: *Nucl. Phys. B* 891 (2015), p. 420.

[158] S. J. Garratt, S. Roy, and J. T. Chalker. “Local resonances and parametric level dynamics in the many-body localized phase”. In: *Phys. Rev. B* 104 (2021), p. 184203.

[159] Z. Lan et al. “Quantum Slow Relaxation and Metastability due to Dynamical Constraints”. In: *Phys. Rev. Lett.* 121 (2018), p. 040603.

[160] R. B. Griffiths. “Nonanalytic Behavior Above the Critical Point in a Random Ising Ferromagnet”. In: *Phys. Rev. Lett.* 23 (1969), p. 17.

[161] B. M. McCoy. “Incompleteness of the Critical Exponent Description for Ferromagnetic Systems Containing Random Impurities”. In: *Phys. Rev. Lett.* 23 (1969), p. 383.

[162] T. L. M. Lezama, S. Bera, and J. H. Bardarson. “Apparent slow dynamics in the ergodic phase of a driven many-body localized system without extensive conserved quantities”. In: *Phys. Rev. B* 99 (2019), p. 161106.

[163] J. Suntajs et al. “Quantum chaos challenges many-body localization”. In: *Phys. Rev. E* 102 (2020), p. 062144.

[164] J. Suntajs et al. “Ergodicity breaking transition in finite disordered spin chains”. In: *Phys. Rev. B* 102 (2020), p. 064207.

[165] P. Sierant, M. Lewenstein, and J. Zakrzewski. “Polynomially Filtered Exact Diagonalization Approach to Many-Body Localization”. In: *Phys. Rev. Lett.* 125 (2020), p. 156601.

[166] M. Kiefer-Emmanouilidis et al. “Evidence for Unbounded Growth of the Number Entropy in Many-Body Localized Phases”. In: *Phys. Rev. Lett.* 124 (2020), p. 243601.

[167] D. Sels and A. Polkovnikov. “Dynamical obstruction to localization in a disordered spin chain”. In: *Phys. Rev. E* 104 (2021), p. 054105.

[168] M. Kiefer-Emmanouilidis et al. “Slow delocalization of particles in many-body localized phases”. In: *Phys. Rev. B* 103 (2021), p. 024203.

[169] D. Sels. “Bath-induced delocalization in interacting disordered spin chains”. In: *Phys. Rev. B* 106 (2022), p. L020202.

[170] W. Buijsman, V. Cheianov, and V. Gritsev. “Random Matrix Ensemble for the Level Statistics of Many-Body Localization”. In: *Phys. Rev. Lett.* 122 (2019), p. 180601.

[171] M. Szyniszewski and H. Schomerus. “Random-matrix perspective on many-body entanglement with a finite localization length”. In: *Phys. Rev. Res.* 2 (2020), p. 032010.

[172] P. Kos, M. Ljubotina, and T. Prosen. “Many-Body Quantum Chaos: Analytic Connection to Random Matrix Theory”. In: *Phys. Rev. X* 8 (2018), p. 021062.

[173] S. Welsh and D. E. Logan. “Simple probability distributions on a Fock-space lattice”. In: *J. Phys.: Condens. Matter* 30 (2018), p. 405601.

[174] W. H. Press. *Numerical recipes 3rd edition: The art of scientific computing*. Cambridge University Press, 2007.

[175] A. Weiße and H. Fehske. “Chebyshev expansion techniques”. In: *Computational Many-Particle Physics*. Springer, 2008, p. 545.

[176] F. Pietracaprina et al. “Shift-invert diagonalization of large many-body localizing spin chains”. In: *SciPost Phys* 5 (2018), p. 045.

[177] M. Ostilli. “Cayley Trees and Bethe Lattices: A concise analysis for mathematicians and physicists”. In: *Physica A: Statistical Mechanics and its Applications* 391 (2012), p. 3417.

[178] “Central Limit Theorem”. In: *The Concise Encyclopedia of Statistics*. New York, NY: Springer New York, 2008, p. 66.

[179] I. M. Khaymovich, M. Haque, and P. A. McClarty. “Eigenstate Thermalization, Random Matrix Theory, and Behemoths”. In: *Phys. Rev. Lett.* 122 (2019), p. 070601.

[180] N. Roy, J. Sutradhar, and S. Banerjee. “Diagnostics of nonergodic extended states and many body localization proximity effect through real-space and Fock-space excitations”. In: *Phys. Rev. B* 107 (2023), p. 115155.

[181] C. Tsallis. “Lévy distributions”. In: *Physics World* 10 (1997), p. 42.

[182] F. C. Leone, L. S. Nelson, and R. B. Nottingham. “The Folded Normal Distribution”. In: *Technometrics* 3 (1961), p. 543.

[183] P. T. Dumitrescu, R. Vasseur, and A. C. Potter. “Scaling Theory of Entanglement at the Many-Body Localization Transition”. In: *Phys. Rev. Lett.* 119 (2017), p. 110604.

[184] H. F. Song et al. “Bipartite fluctuations as a probe of many-body entanglement”. In: *Phys. Rev. B* 85 (2012), p. 035409.

[185] S. P. Lim and D. N. Sheng. “Many-body localization and transition by density matrix renormalization group and exact diagonalization studies”. In: *Phys. Rev. B* 94 (2016), p. 045111.

[186] D. J. Luitz, F. Huveneers, and W. De Roeck. “How a Small Quantum Bath Can Thermalize Long Localized Chains”. In: *Phys. Rev. Lett.* 119 (2017), p. 150602.

[187] P. Sierant and J. Zakrzewski. “Challenges to observation of many-body localization”. In: *Phys. Rev. B* 105 (2022), p. 224203.

[188] G. D. Bergland. “A guided tour of the fast Fourier transform”. In: *IEEE Spectrum* 6 (1969), p. 41.

[189] E. Artin. *The gamma function*. Courier Dover Publications, 2015.

[190] F. Weiner, F. Evers, and S. Bera. “Slow dynamics and strong finite-size effects in many-body localization with random and quasiperiodic potentials”. In: *Phys. Rev. B* 100 (2019), p. 104204.

[191] K. Kudo and T. Deguchi. “Finite-size scaling with respect to interaction and disorder strength at the many-body localization transition”. In: *Phys. Rev. B* 97 (2018), p. 220201.

[192] A. S. Aramthottil et al. “Finite-size scaling analysis of the many-body localization transition in quasiperiodic spin chains”. In: *Phys. Rev. B* 104 (2021), p. 214201.

[193] J. F. Karcher et al. “Generalized multifractality at spin quantum Hall transition”. In: *Annals of Physics* 435 (2021), p. 168584.

[194] M. Sonner, K. S. Tikhonov, and A. D. Mirlin. “Multifractality of wave functions on a Cayley tree: From root to leaves”. In: *Phys. Rev. B* 96 (2017), p. 214204.

[195] S. Lin et al. “Many-body localization of spinless fermions with attractive interactions in one dimension”. In: *SciPost Phys* 4 (2018), p. 002.

[196] J. Hadamard. *Essai sur l’étude des fonctions, données par leur développement de Taylor*. Gauthier-Villars, 1892.

[197] E. F. Beckenbach et al. “The fundamental inequalities and related matters”. In: *Inequalities* (1961), p. 1.

[198] Y. V. Fyodorov and A. D. Mirlin. “Strong eigenfunction correlations near the Anderson-localization transition”. In: *Phys. Rev. B* 55 (1997), p. 16001.

[199] E. Tarquini, G. Biroli, and M. Tarzia. “Critical properties of the Anderson localization transition and the high-dimensional limit”. In: *Phys. Rev. B* 95 (2017), p. 094204.

[200] “Special Issue “Localisation 2020”: Editorial Summary”. In: *Annals of Physics* 435 (2021). Special Issue on Localisation 2020, p. 168664.

[201] I. García-Mata et al. “Scaling Theory of the Anderson Transition in Random Graphs: Ergodicity and Universality”. In: *Phys. Rev. Lett.* 118 (2017), p. 166801.

[202] A. Morningstar and D. A. Huse. “Renormalization-group study of the many-body localization transition in one dimension”. In: *Phys. Rev. B* 99 (2019), p. 224205.

[203] A. Morningstar, D. A. Huse, and J. Z. Imbrie. “Many-body localization near the critical point”. In: *Phys. Rev. B* 102 (2020), p. 125134.

[204] A. Goremykina, R. Vasseur, and M. Serbyn. “Analytically solvable renormalization group for the many-body localization transition”. In: *Phys. Rev. Lett* 122 (2019), p. 040601.

[205] N. Laflorencie, G. Lemarié, and N. Macé. “Chain breaking and kosterlitz-thouless scaling at the many-body localization transition in the random-field heisenberg spin chain”. In: *Phys. Rev. Res.* 2 (2020), p. 042033.

[206] P. T. Dumitrescu et al. “Kosterlitz-Thouless scaling at many-body localization phase transitions”. In: *Phys. Rev. B* 99 (2019), p. 094205.

[207] J. M. Kosterlitz and D. J. Thouless. “Ordering, metastability and phase transitions in two-dimensional systems”. In: *J. Phys. C: Solid State Phy* 6 (1973), p. 1181.

[208] W. Berdanier et al. “Floquet quantum criticality”. In: *Proc. Natl. Acad. Sci. U.S.A.* (2018).

[209] G. Floquet. “Sur les équations différentielles linéaires à coefficients périodiques”. In: *Annales scientifiques de l’École normale supérieure*. 1883, p. 47.

[210] S. Roy et al. “Multifractality without fine-tuning in a Floquet quasiperiodic chain”. In: *SciPost Phys.* 4 (2018), p. 25.

[211] C. W. von Keyserlingk and S. L. Sondhi. “Phase structure of one-dimensional interacting Floquet systems. II. Symmetry-broken phases”. In: *Phys. Rev. B* 93 (2016), p. 245146.

[212] D. V. Else, B. Bauer, and C. Nayak. “Floquet Time Crystals”. In: *Phys. Rev. Lett.* 117 (2016), p. 090402.

[213] V. Khemani, D. N. Sheng, and D. A. Huse. “Two Universality Classes for the Many-Body Localization Transition”. In: *Phys. Rev. Lett.* 119 (2017), p. 075702.

[214] G. Strang. *Linear algebra and its applications.* Belmont, CA: Thomson, Brooks/Cole, 2006.

[215] M. I. Lourakis et al. “A brief description of the Levenberg-Marquardt algorithm implemented by levmar”. In: *Foundation of Research and Technology* 4 (2005), p. 1.

Appendix A

Numerical Methods

A.0.1 Probability transport

The basic underlying quantities that are considered in chapters 3 and 4 are

$$P_{IJ}(t) = |G_{IJ}(t)|^2, \tag{A.1}$$

where as usual $G_{IJ}(t) = \langle J|\exp[-i\mathcal{H}t]|I\rangle$ is the propagator between FS sites $|I\rangle$ and $|J\rangle$. It therefore follows that

$$P_{IJ}(t) = |\langle J|\Psi(t)\rangle|^2 = |\langle J|\exp[-i\mathcal{H}t]|I\rangle|^2\,, \tag{A.2}$$

with $|\Psi(t)\rangle$ the time dependent wavefunction following initiation on $|I\rangle$ at $t = 0$. Physically $P_{IJ}(t)$ gives the probability that the system is found on $|J\rangle$ at time t given its initiation on $|I\rangle$ at $t = 0$.

In the TFI model, the set of amplitudes, $\{A_{nI}\}$, of $\{|I\rangle\}$ on eigenstates $\{|n\rangle\}$, $A_{nI} = \langle n|I\rangle$, can be taken to be real. From eq. A.2 it is easy to show (by simply inserting several unit operators) that $P_{IJ}(t)$ can be expressed in terms of the

eigenstate amplitudes, with

$$P_{IJ}(t) = \sum_{n,m} \exp\left[-i(E_n - E_m)t\right] \; A_{nI}A_{nJ}A_{mI}A_{mJ}. \tag{A.3}$$

Eq. A.3 is the key equation we use to calculate for a given initial FS site I, $\{P_{IJ}(t)\}$.

In order to use eq. A.3 to calculate $P_{IJ}(t)$ for a given disorder strength W, system size L, disorder realisation and FS site $|I\rangle$, for all eigenstates $\{|n\rangle\}$ in the band we need to calculate their set of amplitude $\{A_{nJ}\}$ on the set of FS sites $\{J\}$, alongside the eigenstates $\{|n\rangle\}$ set of eigenenergies $\{E_n\}$. These are simply obtained by a standard matrix diagonalisation procedure [214].

In chapter 3 the essential quantity we examine is $\overline{P}(r;t)$ to calculate this, for a given initial site $|I\rangle$ and disorder realisation we can calculate the probability of being on row r, $P_I(r;t) = \sum_{J;r_{IJ}=r} P_{IJ}(t)$. We can then average $P_I(r;t)$ over all initial FS sites I to give $P(r;t) = \frac{1}{N_H}\sum_I P_I(r;t)$. This quantity can then be averaged over disorder realisations to calculate $\overline{P}(r;t)$. From $\overline{P}(r;t)$ we can calculate $\overline{r}(t) = \sum_{r=0}^{L} r \;\overline{P}(r;t)$ and $\overline{C}(t) = 1 - \frac{2\overline{r}(t)}{L}$; two further quantities examined in detail in chapter 3.

In chapter 3, we also examined the eigenstate resolved versions of $\overline{r}(t)$ and $\overline{C}(t)$, $\overline{r}^{[n]}(t)$ and $\overline{C}^{[n]}(t)$. In this case, the same procedure as described above is used but instead of the calculations using the full probabilities the eigenstate resolved probabilities

$$N_H^{-1} P_{IJ}^{[n]}(t) = \sum_m \cos[(E_n - E_m)t] A_{nI}A_{nJ}A_{mI}A_{mJ}, \tag{A.4}$$

for a chosen eigenstate $|n\rangle$ in the particular region of the band that is of interest are used.

In chapter 4, we examined various quantities which probed how the $\{P_{IJ}(t)\}$

are distributed across a given row; so called lateral transport. In order to calculate these quantities the $\{P_{IJ}(t)\}$ for a given initial FS site $|I\rangle$ are calculated; and then separated into the set of $P_{IJ}(t)$ for each row r, $\{P_{IJ}(t)\}_{r_{IJ}=r}$. These values are then stored in an array. For a given disorder strength W, this procedure is then repeated for 50 initial FS sites $|I\rangle$ that have energies $\mathcal{E}_I$ around zero and for different disorder realisations. From this data, $\langle R\rangle$, $P_R(x)$, $P_{rel}(x)$ and $P_{m;rel}(x)$ can be calculated.

All our numerical results calculated in chapters 3 and 4 are obtained using at least 1000 disorder realisations.

A.0.2 Multifractality

In order to calculate the fractal exponents and related distributions the essential quantity considered in chapter 5 is the generalised IPR

$$L_q = \sum_I |A_{nI}|^{2q}, \tag{A.5}$$

with $A_{nI} = \langle n|I\rangle$ the probability amplitude of eigenstate $|n\rangle$ on FS site $|I\rangle$. For a given disorder strength W and system size L, in order to calculate the distributions in chapter 5 we want to calculate L_q and $u_q = \ln[L_q]$. This means we need to calculate $\{|A_{nI}\}$ for band centre eigenstates. As only a small number of eigenstates are required a sparse matrix diagonalisation algorithm known as the shift inverse method [176] can be used which enables us to access larger system sizes.

We can then calculate for a given W and L value, L_q and $u_q = \ln[L_q]$ for a small number of band centre eigenstates (typically 50) and disorder realisations (at least 1000) and store them in an array. These arrays can then be used to calculate the probability distributions $P_{L_q}(x)$, $P_{u_q}(x)$ and $P_{\tau_q}(x)$, and their moments examined in chapter 5.

A.0.3 New order parameter

In chapter 6, we examine two quantities which measure the wavefunction overlap between two eigenstates $|n\rangle$ and $|m\rangle$:

$$L_{nm} = \frac{\sum_I A_{nI}^2 A_{mI}^2}{\frac{1}{2}\sum_I A_{nI}^4 + A_{mI}^4}, \tag{A.6}$$

and

$$S_{nm} = \sum_I \frac{A_{nI}^2 A_{mI}^2}{\frac{1}{2}\left(A_{nI}^2 + A_{mI}^2\right)}. \tag{A.7}$$

In order to determine L_{nm} and S_{nm} we need to determine the set of amplitudes on all FS sites $\{A_{nI}\}$ and $\{A_{mI}\}$ for two eigenstates $|m\rangle$ and $|n\rangle$.

In chapter 6, we are only interested in examining L_{nm} and S_{nm} for nearest neighbour eigenstates around the band centre, denoted L^{NN} and S^{NN}. In this case, as only a small number of eigenstates are required a sparse matrix diagonalisation algorithm known as the shift inverse method [176] can be used which enables us to more easily access larger system sizes.

We can then for a chosen W and L value calculate L^{NN} and S^{NN} for band centre eigenstates (typically 50) and a number of disorder realisations (at least 1000). This enables us to calculate $P_{L^{NN}}(x)$ and $P_{S^{NN}}(x)$ and their moments of interest: L_{avg}^{NN}, L_{typ}^{NN}, S_{typ}^{NN} and S_{avg}^{NN}.

Appendix B

Examining $\overline{P}^{[n]}(r;t)$

In this appendix we examine

$$\tilde{P}_y^{[n]}(y;t) = \int dr\ \delta\left(y - \frac{r}{L}\right)\ \overline{P}^{[n]}(r;t), \tag{B.1}$$

where

$$\overline{P}^{[n]}(r;t) = \left\langle \sum_{J, r_{IJ}=r} P_{IJ}^{[n]}(t) \right\rangle_{nd,I}, \tag{B.2}$$

with

$$N_H^{-1} P_{IJ}^{[n]}(t) = \sum_m \cos[(E_n - E_m)t] A_{nI} A_{nJ} A_{mI} A_{mJ} \tag{B.3}$$

and $\langle\rangle_{nd,I}$ representing an average over disorder realisations and initial FS sites I. The energy resolved quantities $P_{IJ}^{[n]}(t)$ are not bonafide probabilities as $\{P_{IJ}^{[n]}(t)\}$ are not guaranteed to positive for all t and W values. In this section we show that despite this, the energy resolved $\tilde{P}_y(y;t)$, $\tilde{P}_y^{[n]}(y;t)$ behaves similarly to the full $\tilde{P}_y(y;t)$ examined in section 3.2.4.

To this end, figure B.1 shows $\tilde{P}_y^{[n]}(y;t)$ for different t and L values (indicated in plot) and $W = 1, 7$.

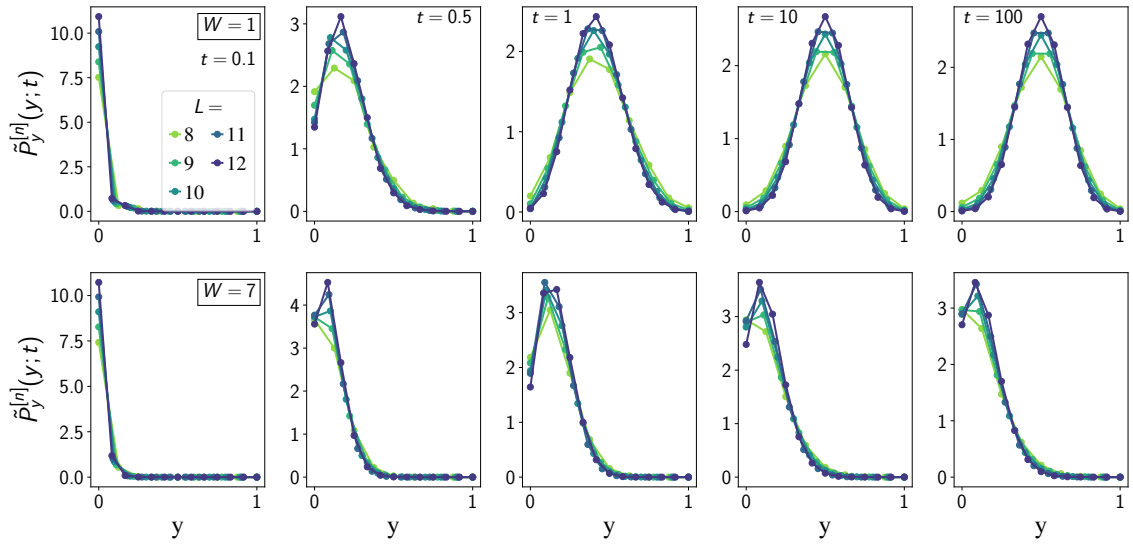


Figure B.1: Top panels: $W = 1$, $\tilde{P}_y^{[n]}(y;t)$ for different t and L values (indicated in plot). Bottom panels: $W = 7$, $\tilde{P}_y^{[n]}(y;t)$ for different t and L values.

B.1 Behemoth operators

In section 3.2.6 we discussed that $P_{IJ}^{[n]}(t)$ can be thought of as being written in terms of expectation values of Behemoth operators [179]. In this section of the appendix we shall further elaborate on this comment.

Considering

$$P_{IJ}(t) = \mathrm{Re}[\langle I \,|\, \exp[i\mathcal{H}t] \,|\, J\rangle \langle J \,|\, \exp[-i\mathcal{H}t] \,|\, I\rangle], \tag{B.4}$$

and inserting the identity operator $\hat{1} = \sum_n |n\rangle \langle n|$ gives

$$P_{IJ}(t) = N_H^{-1} \sum_n P_{IJ}^{[n]}(t): \quad P_{IJ}^{[n]} = N_H \sum_m \cos[(E_n - E_m)t] A_{nI} A_{nJ} A_{mI} A_{mJ}. \tag{B.5}$$

This can be written equally as

$$N_H^{-1} P_{IJ}^{(n)}(t) = \mathrm{Re}[\left\langle n \right| \hat{O}_J(t) \hat{O}_I \left| n \right\rangle]: \quad \hat{O}_J = |J\rangle \langle J|, \tag{B.6}$$

or equivalently as

$$N_H^{-1} P_{IJ}^{(n)}(t) = \frac{1}{2}\left(\left\langle n \,\middle|\, \hat{O}_J(t)\hat{O}_I + \hat{O}_I\hat{O}_J(t) \,\middle|\, n \right\rangle\right), \tag{B.7}$$

with $\hat{O}_J = |J\rangle\langle J|$ a behemoth operator [179].

Appendix C

Analytical results for $\overline{C}(t)$ and $\overline{r}(t)$ MBL_0

When $J_z = 0$, the Hamiltonian

$$\mathcal{H}_{TFI} = \sum_{l=1}^{L} (h_l \hat{\sigma}_l^z + \Gamma \hat{\sigma}_l^x) = \sum_{l=1}^{L} \mathcal{H}_l, \tag{C.1}$$

is site separable. The problem can be solved exactly by defining a rotated spin operator

$$\hat{\tilde{\sigma}}_l^z = \frac{h_l \hat{\sigma}_l^z + \Gamma \hat{\sigma}_l^x}{\sqrt{h_l^2 + \Gamma^2}}, \tag{C.2}$$

where the factor $\sqrt{h_1^2 + \Gamma^2}$ in the denominator ensures that $\hat{\tilde{\sigma}}_l^z$ is a bonafide spin operator with $[\hat{\tilde{\sigma}}_l^z]^2 = 1$ using the usual spin commutation relations, and has eigenvalues of ± 1. The $|\tilde{\sigma}_l^z\rangle$ are the rotated spins, with $\hat{\tilde{\sigma}}_l^z |\tilde{\sigma}_l^z\rangle = \tilde{\sigma}_l^z |\tilde{\sigma}_l^z\rangle$, and $\tilde{\sigma}_l^z = \pm 1$, i.e. each rotated spin can point either up or down.

From eqs. C.2, C.1 clearly

$$\mathcal{H}_{TFI} = \sum_{l=1}^{L} \phi_l \hat{\tilde{\sigma}}_l^z : \quad \phi_l = \sqrt{h_1^2 + \Gamma^2}. \tag{C.3}$$

The probability of being on FS site $|J\rangle$ at time t given its initiation on $|I\rangle$ at

$t = 0$ can be determined from the off-diagonal Green function [35]

$$G_{IJ}(t) = \langle J \,|\, \exp[-i\mathcal{H}t] \,|\, I \rangle \tag{C.4}$$

where

$$P_{IJ}(t) = |G_{IJ}(t)|^2. \tag{C.5}$$

Since in MBL_0 the Hamiltonian is site separable, (i.e. $\mathcal{H} = \sum_l \mathcal{H}_l$ in eq. C.1) it follows that the propagator

$$G_{IJ}(t) = \langle J \,|\, \exp[-i\mathcal{H}t] \,|\, I \rangle = \prod_{l=1}^{L} \left\langle \sigma_l^{(J} \,\middle|\, \exp[-i\mathcal{H}_l t] \,\middle|\, \sigma_l^{(I)} \right\rangle. \tag{C.6}$$

From eq. C.3 it follows that

$$\mathcal{H}_l = \phi_l \tilde{\sigma}_l^z : \quad \phi_l = \sqrt{h_l^2 + \Gamma^2}. \tag{C.7}$$

By expanding $\exp[-i\mathcal{H}_l t]$ as a Taylor series and noting $[\hat{\tilde{\sigma}}_l^z]^2 = 1$ it follows from eq. C.7 that

$$\exp[-i\mathcal{H}_l t] = \cos[\phi_l t] - i\tilde{\sigma}_l^z \sin[\phi_l t]. \tag{C.8}$$

This means that

$$\left\langle \sigma_l^{(J} \,\middle|\, \exp[-i\mathcal{H}_l t] \,\middle|\, \sigma_l^{(I)} \right\rangle = \delta_{\sigma_l^{(J)},\sigma_l^{(I)}} \cos[\phi_l t] - i\frac{\sin[\phi_l t]}{\sqrt{h_l^2+1}} \left\langle \sigma_l^{(J)} \,\middle|\, h_l \hat{\sigma}_l^z + \Gamma \hat{\sigma}_l^x \,\middle|\, \sigma_l^{(I)} \right\rangle, \tag{C.9}$$

with δ_{ij} the usual Kronecker-delta function. Eq. C.9 leads to

$$\left\langle \sigma_l^{(J} \,\middle|\, \exp[-i\mathcal{H}_l t] \,\middle|\, \sigma_l^{(I)} \right\rangle = \begin{cases} \cos[\phi_l t] - i\frac{h_l}{\sqrt{h_l^2+\Gamma^2}} \sigma_l^{(I)} \sin[\phi_l t] & : \sigma_l^{(J)} = \sigma_l^{(I)} \\ -i\frac{\Gamma}{\sqrt{h_l^2+\Gamma^2}} \sin[\phi_l t] & : \sigma_l^{(J)} = -\sigma_l^{(I)}. \end{cases} \tag{C.10}$$

Let J and I be such that the Hamming distance between them $r_{IJ} = r$. Then $L-r$ real-space sites have $\sigma_l^{(J)} = \sigma_l^{(I)}$ and r real-space sites have $\sigma_l^{(I)} = -\sigma_l^{(J)}$. From eqs. C.6, C.10 it follows

$$G_{IJ}(t) = \prod_{l\in r}\left[-i\frac{\Gamma}{\sqrt{h_l^2+\Gamma^2}}\sin[\phi_l t]\right] \times \prod_{l\in L-r}\left[\cos[\phi_l t] - i\frac{h_l}{\sqrt{h_l^2+\Gamma^2}}\sigma_l^{(I)}\sin[\phi_l t]\right]. \tag{C.11}$$

Using $[\sigma_l^{(I)}]^2 = 1$ and $\sin[\phi_l t]^2 + \cos[\phi_l t]^2 = 1$ leads to

$$P_{IJ}(t) = |G_{IJ}(t)|^2 = \prod_{l\in r}\left[\frac{\Gamma^2}{h_l^2+\Gamma^2}\sin^2[\phi_l t]\right] \times \prod_{l\in L-r}\left[1 - \frac{\Gamma^2}{h_l^2+\Gamma^2}\sin^2[\phi_l t]\right]. \tag{C.12}$$

The probabilities $P_{IJ}(t)$ can then be averaged over disorder realisations to give

$$\overline{P}_{IJ}(t) = \left\langle\frac{\Gamma^2}{h_l^2+\Gamma^2}\sin^2[\phi_l t]\right\rangle^r \times \left\langle 1 - \frac{\Gamma^2}{h_l^2+\Gamma^2}\sin^2[\phi_l t]\right\rangle^{L-r} : \quad r_{IJ} = r, \tag{C.13}$$

with $\langle\rangle$ indicating an average over disorder realisations. The disorder averaged $\overline{P}_{IJ}(t)$ is independent of the initial FS site $|I\rangle$ and final FS site J and only depends on the Hamming distance r. It therefore follows that disorder averaged probability of being found on row r, $\overline{P}(r;t) = \binom{L}{r}\overline{P}_{IJ}(t)$, where $N_r = \binom{L}{r}$ is the number of FS sites on row r. This means

$$\overline{P}(r;t) = \binom{L}{r}[1-z_0(t)]^{L-r} z_0(t)^r, \tag{C.14}$$

with

$$z_0(t) = \left\langle\frac{\Gamma^2}{\Gamma^2+h_l^2}\sin^2[\phi_l t]\right\rangle. \tag{C.15}$$

Given the binomial form of $\overline{P}(r;t)$ it follows that the average Hamming distance

$$\overline{r}(t) = \sum_{r=0}^{L} r\overline{P}(r;t) = Lz_0(t); \quad \frac{\overline{r}(t)}{L} = z_0(t). \tag{C.16}$$

using the relationship $\overline{C}(t) = 1 - \frac{2\overline{r}(t)}{L}$ (eq. 3.17, pg. 38),

$$\overline{C}(t) = 1 - 2z_0(t). \tag{C.17}$$

These results are clearly L independent for all t.

MBL_0 is therefore fully determined by $z_0(t)$ (eq. C.15). Using the double angle formula for $\sin^2(\theta)$ (and setting $\Gamma = 1$ as usual), we can rewrite eq. C.15 for $z_0(t)$ as

$$z_0(t) = p - \frac{1}{2}K(t), \quad p = \frac{\tan^{-1}(W)}{2W}, \tag{C.18}$$

with $K(t) = \langle (h^2+1)^{-1} \cos\Big(2\sqrt{h^2+1}t\Big)\rangle_d$. We shall see below that $K(t)$ vanishes as $t \to \infty$. It thus follows that the long-time limits are $\frac{\overline{r}(t)}{L} = p$ and $\overline{C}(t) = 1 - 2p$, with $p < \frac{1}{2}$. This means $\overline{C}(\infty) > 0$ and subsequently $\frac{\overline{r}(t)}{L} < \frac{1}{2}$, which indicates the presence of frozen spins, or equivalently that in MBL_0 the system retains memory of the initial spin configuration for all times.

In order to determine the assymptotic form of $K(t)$, it can be written as

$$K(t) = \frac{1}{W}\int_0^W dh_l \frac{1}{h_l^2+1} \cos[(1 + (\sqrt{h_l^2+1} - 1))2t]. \tag{C.19}$$

Using the relationship $\cos(a+b) = \cos(a)\cos(b) - \sin(a)\sin(b)$, clearly

$$K(t) = \frac{\cos(2t)}{W}\int_0^W dh_l \frac{1}{h_l^2+1} \cos[(\sqrt{h_l^2+1} - 1)2t] - \frac{\sin(2t)}{W}\int_0^W dh_l \frac{1}{h_l^2+1} \sin[(\sqrt{h_l^2-1} - 1)2t], \tag{C.20}$$

or equivalently

$$K(t) = K_A(t) - K_B(t), \tag{C.21}$$

with

$$K_A(t) = \frac{\cos(2t)}{W}\int_0^W dh_l \frac{1}{h_l^2+1} \cos[(\sqrt{h_l^2+1} - 1)2t] \tag{C.22}$$

and

$$K_B(t) = \frac{\sin(2t)}{W} \int_0^W dh_l \frac{1}{h_l^2 + 1} \sin[(\sqrt{h_l^2 - 1} - 1)2t]. \tag{C.23}$$

For use later note that

$$\int_0^\infty \frac{dx}{\sqrt{x}} \cos(x) = \int_0^\infty \frac{dx}{\sqrt{x}} \sin(x) = \sqrt{\frac{\pi}{2}}. \tag{C.24}$$

We shall first consider $K_A(t)$ by defining $x = h^2 t$ and taking a Taylor expansion of the sqrt in eq. C.22 gives

$$K_A(t) = \frac{\cos(2t)}{W} \frac{1}{2\sqrt{t}} \int_0^{W^2 t} \frac{dx}{\sqrt{x}} \frac{1}{1 + \frac{x}{t}} \cos\left[x - \frac{1}{4}\frac{x^2}{t} + \mathcal{O}(\frac{x^3}{t^2})\right]. \tag{C.25}$$

At large t ($t \to \infty$) this clearly reduces to

$$K_A(t) = \frac{\cos(2t)}{W} \frac{1}{2\sqrt{t}} \int_0^\infty dx \frac{\cos[x]}{\sqrt{x}} = \frac{\cos(2t)}{W} \frac{1}{2} \sqrt{\frac{\pi}{2}}. \tag{C.26}$$

Similarly, we shall consider $K_B(t)$ by defining $x = h^2 t$ and taking a Taylor expansion of the sqrt in eq. C.23 leads to

$$K_B(t) = \frac{\sin(2t)}{W} \frac{1}{2\sqrt{t}} \int_0^{W^2 t} \frac{dx}{\sqrt{x}} \frac{1}{1 + \frac{x}{t}} \sin\left[x - \frac{1}{4}\frac{x^2}{t} + \mathcal{O}(\frac{x^3}{t^2})\right]. \tag{C.27}$$

At large t ($t \to \infty$) this clearly reduces to

$$K_B(t) = \frac{\sin(2t)}{W} \frac{1}{2\sqrt{t}} \int_0^\infty dx \frac{\sin[x]}{\sqrt{x}} = \frac{\sin(2t)}{W} \frac{1}{2} \sqrt{\frac{\pi}{2}}. \tag{C.28}$$

It therefore follows that

$$K(t) = K_A(t) - K_B(t) = \frac{\cos(2t) - \sin(2t)}{2W} \sqrt{\frac{\pi}{2}}. \tag{C.29}$$

From eq. C.29 $K(t)$ clearly vanishes as a power-law superimposed on oscillatory behaviour. It thus follows that from eqs. C.17 and C.18 that

$$\overline{C}(t) \sim \left(1 - \frac{\tan^{-1}(W)}{W}\right) + \frac{\sqrt{\pi}}{2W}\frac{1}{\sqrt{t}}. \tag{C.30}$$

In MBL_0 the oscillations in $\overline{C}(t)$ about its long-time value therefore decays as $\frac{1}{\sqrt{t}}$.

Appendix D

Further validating lateral transport results

D.1 Validating the partial sum over FS sites

In this section of the appendix we validate our use of only a small number of FS sites $|I\rangle$ around zero in our calculations in chapter 4.

To this end, we define the distribution

$$\tilde{P}(x) = \frac{1}{N_s} \sum_{I} \frac{1}{N_r} \sum_{J_r\, r} \langle x - P_{IJ_r} \rangle \tag{D.1}$$

which is simply the distribution of probabilities of being on a FS site $|J_r\rangle$ a Hamming distance of r away from the initial FS site $|I\rangle$.

Figure D.1 shows $\tilde{P}(x)$ calculated using all possible initial FS sites $|I\rangle$ (top panel) and only those around zero (bottom panel) for different W and t values (indicated in plot).

The $\tilde{P}(x)$ calculated using only a small number of FS sites $|I\rangle$ shows essentially the same behaviour as $\tilde{P}(x)$ calculated using all FS sites $|I\rangle$, with the latter being marginally broader. Throughout chapter 4 we therefore calculated all lateral transport distributions using a small number of FS sites $|I\rangle$ in the interest of numerical efficiency; a standard practise within MBL.

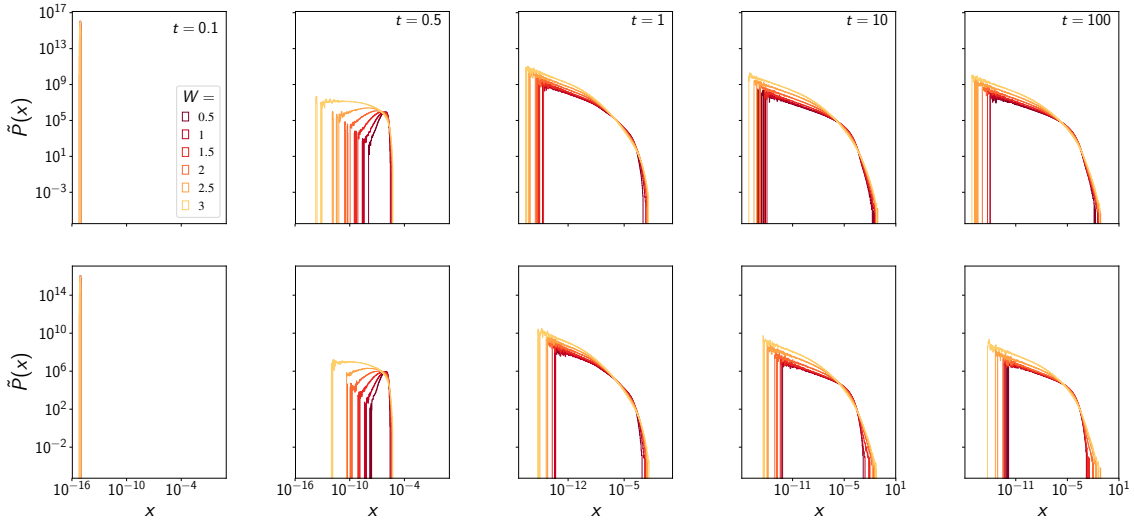


Figure D.1: Top panels: $\tilde{P}(x)$ for different t and W values (indicated in plot), $N = 10$, $r = \frac{L}{2}$ calculated using all possible initial FS sites $|I\rangle$. Bottom panel: $\tilde{P}(x)$ for different t and W values (indicated in plot), $N = 10$, $r = \frac{L}{2}$ calculated using 50 initial FS sites around zero .

D.2 Results for other r values

In this section we shall shows the results for $\langle R \rangle$, $P_R(x)$ and $P_{rel}(x)$ for another r value to show the results we obtained in section 4.1 are not dependent on the particular value of r chosen.

To this end, figure D.2 shows $\langle R \rangle$ *vs* t for different W values (indicated in plot), $r = 3$. Figure D.3 shows $P_R(x)$ for $W = 1$ and $W = 7$ and different t and L values (indicated in plot), $r = 3$. Figures D.4 and D.5 show $W = 1$ and $W = 7$ $P_{rel}(x)$ for different t and L values (indicated in plot). Finally, figure D.6 shows the long-time $P_{rel}(x)$ and $F_c(x)$ for different L values, $r = 3$.

These figures show that $\langle R \rangle$, $P_R(x)$ and $P_{rel}(x)$ for $r = 3$ show essentially the same behaviour as our results for $r = \frac{L}{2}$ shown in chapter 4.

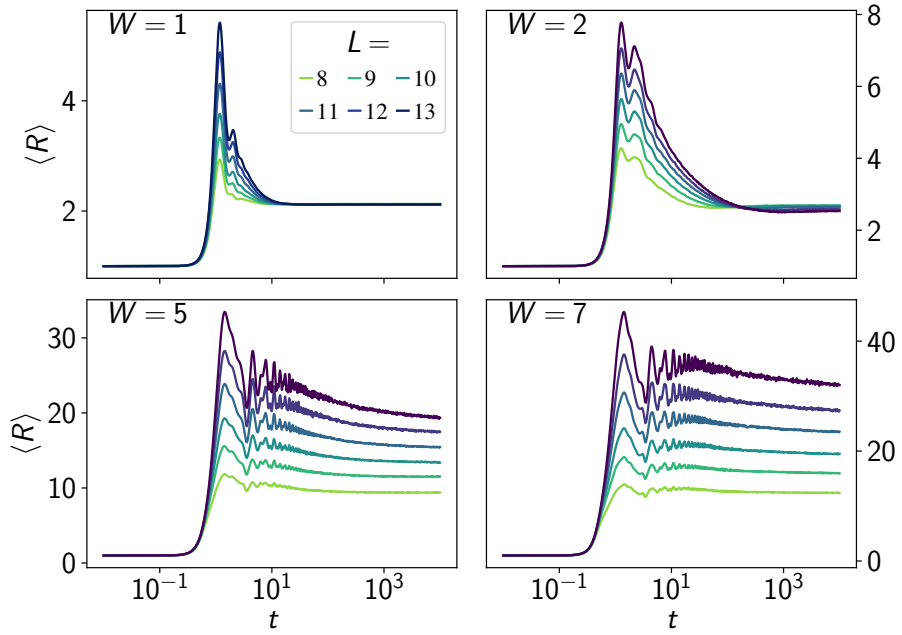


Figure D.2: t-dependence of the average $\langle R \rangle$ ($= N_r \langle \mathcal{I}_2 \rangle$ from eq. 4.18). Shown for $r = 3$ with $W = 1, 2, 5, 7$ for system sizes $L = 8 - 13$.

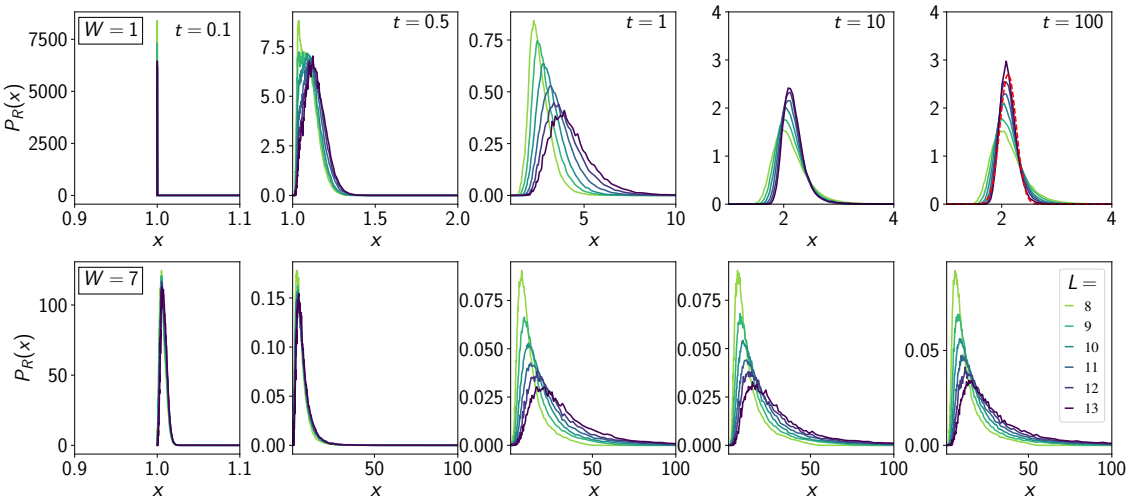


Figure D.3: Probability distribution $P_R(x)$ of x for $W = 1$ (top row) and $W = 7$ (bottom row) at a sequence of t's specified and for different system sizes $L = 8 - 13$, $r = 3$. Dashed red line shows the fit of the $W = 1$, $L = 13$, $t = 100$, $P_R(x)$ to a normal distribution.

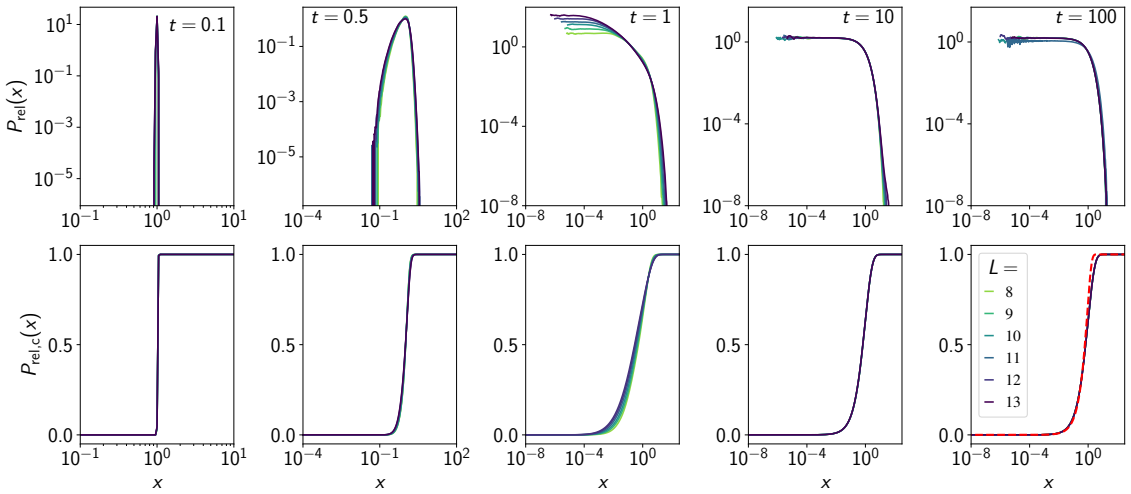


Figure D.4: For $W = 1$. The top panel shows the distribution of $P_{\mathrm{rel}}(x)$ of x (eq. 4.25), at the t's specified, and for system sizes $L = 8 - 13$, $r = 3$. The bottom panel shows the cumulative distribution $P_{\mathrm{rel},c}(x)$ (eq. 4.27). Red dashed line in final panel shows the half-Gaussian fit to the data.

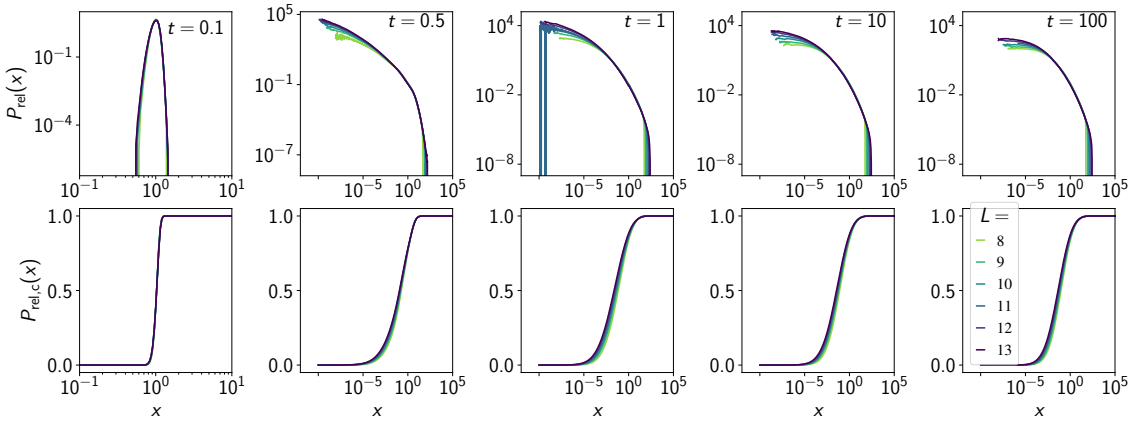


Figure D.5: For $W = 7$. The top panel shows the distribution of $P_{\mathrm{rel}}(x)$ of x (eq. 4.25), at the t's specified, and for system sizes $L = 8 - 13$, $r = 3$. The bottom panel shows the cumulative distribution $P_{\mathrm{rel},c}(x)$ (eq. 4.27).

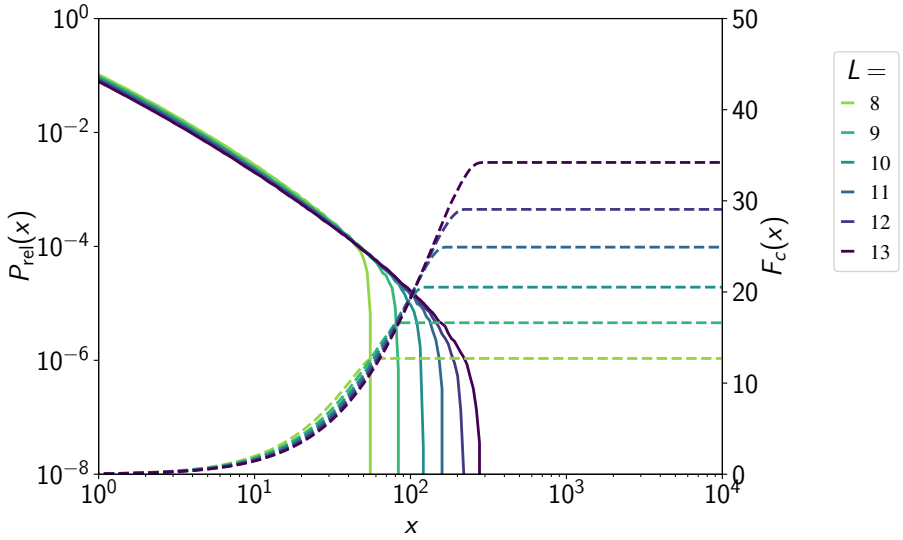


Figure D.6: For $W = 7$, with $t = 100$. $F_c(x)$ *vs* x (dashed lines, right hand scale), shown for $x > 1$ and $L = 8 - 13$, $r = 3$; and $P_{\mathrm{rel}}(x)$ (solid line, left scale).

Appendix E

Fitting of $\overline{L}_2(t)$ and $\overline{S}_1(t)$

In this appendix we show that $\overline{L}_2(t)$ and $\overline{S}_1(t)$ are well described by the equations in section 4.2.3.

To this end, figure E.1 shows the fit of $\overline{L}_2(t)$ to the form

$$\overline{L}_2(t) = -\tau_2(t)\ln[N_H] + \ln[C_2(t)], \tag{E.1}$$

where $\tau_2(t)$ and $C_2(t)$ are fitting parameters for a chosen W and t. Figure E.1 shows that for all t and W values, $\overline{L}_2(t)$ is well captured by eq. E.1.

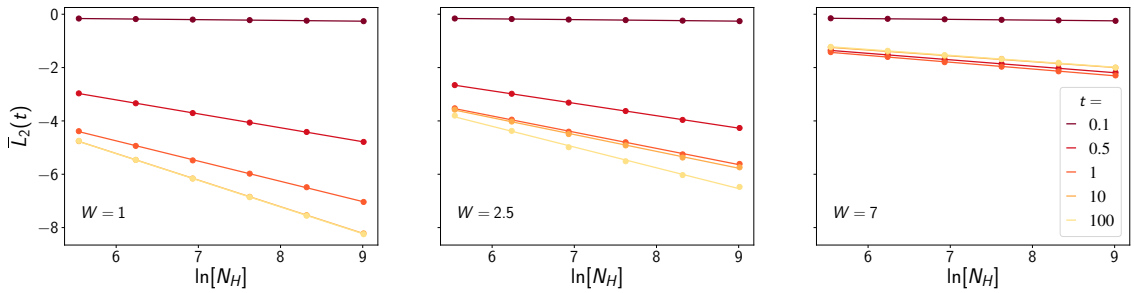


Figure E.1: Fitting of $\overline{L}_2(t)$ to eq. E.1 for different W values (indicated in plot) and $t = 0.1 - 10^3$.

On the other hand, figure E.2 shows the fitting of $\overline{S}_1(t)$ to the functional form

$$\overline{S}_1(t) = a_1(t)\ln[N_H] + b_1(t)\ln[\ln[N_H]], \tag{E.2}$$

where $a_1(t)$ and $b_1(t)$ are fitting parameters for a given W and t. Figure E.2 shows that for all t and W values $\overline{S}_1(t)$ is well captured by eq. E.2.

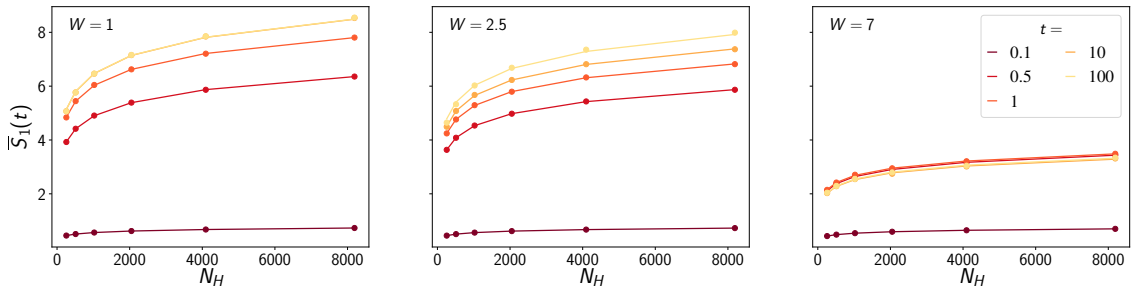


Figure E.2: Fitting of $\overline{S}_1(t)$ to eq. E.2 for different W values (indicated in plot) and $t = 0.1 - 10^3$.

Appendix F

$\tilde{P}_{m;rel}(x)$ results for other r values

In this appendix we show that the essential results we obtained for $\tilde{P}_{m;rel}(x)$ for $r \simeq \frac{L}{2}$ in section 4.3 are not dependent on this particular choice of r value.

To this end, figures F.1 and F.2 show the time evolution of $\tilde{P}_{m;rel}(x)$ for $r \simeq \frac{L}{4}$, where $r = 2$ for $L = 8, 9, 10$ and $r = 3$ for $L = 11, 12, 13$.

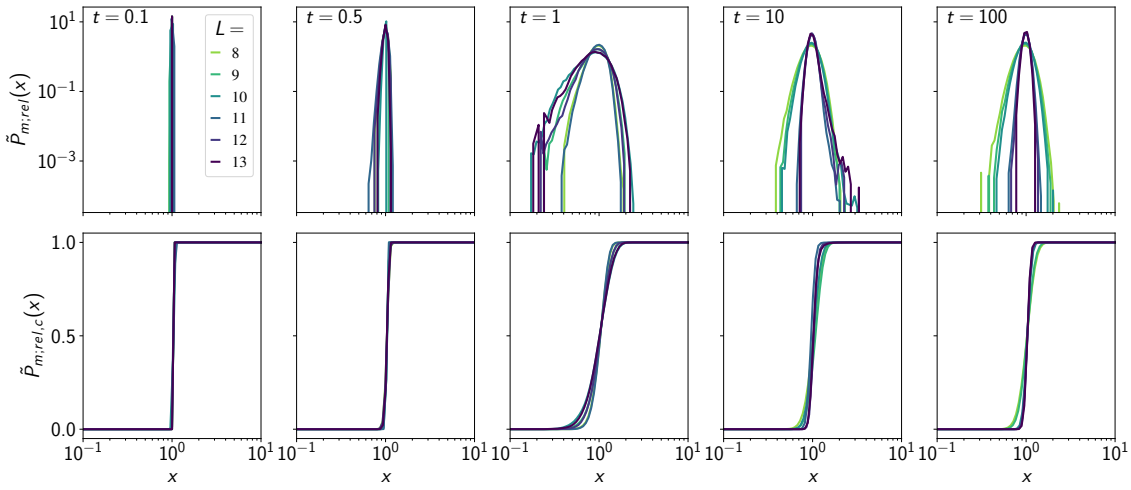


Figure F.1: For $W = 1$. Top panel shows the distribution of $\tilde{P}_{rel;m}(x)$ of x (eq. 4.53, pg. 104), at the t's specified, and $L = 8 - 13$. The bottom panel shows the cumulative distribution $\tilde{P}_{rel;m,c}(x)$ (eq. 4.54, pg. 105). $r \simeq \frac{L}{4}$.

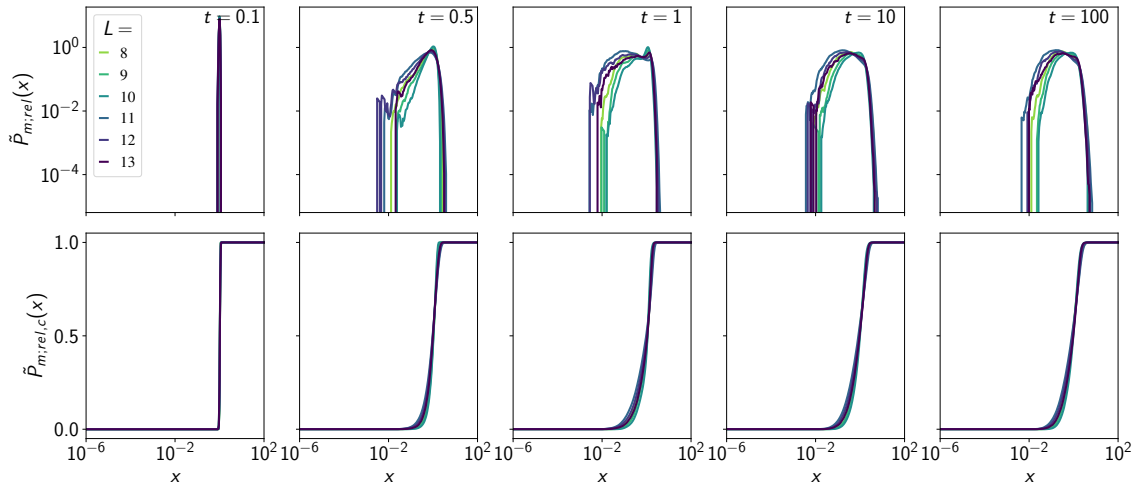


Figure F.2: For $W = 7$. The top panel shows the distribution of $\tilde{P}_{rel;m}(x)$ of x (eq. 4.53, pg. 104), at the t's specified, and for system sizes $L = 8 - 13$. The bottom panel shows the cumulative distribution $\tilde{P}_{rel;m,c}(x)$ (eq. 4.54, pg. 105). $r \simeq \frac{L}{4}$.

Figures F.1 and F.2 show that $\tilde{P}_{rel;m}(x)$ for $r \simeq \frac{L}{4}$ shows essentially the same behaviour as $\tilde{P}_{rel;m}(x)$ for $r \simeq \frac{L}{2}$ in section 4.3, with the $r \simeq \frac{L}{4}$ distributions shown in this appendix being less broad than the $r \simeq \frac{L}{2}$ distributions shown in chapter 4.

In particular, figures F.1 and F.2 show that for $t \lesssim 0.1$, $\tilde{P}_{rel;m}(x)$ is δ-distributed on $x = 1$, as expected from our short-time analytical results (pgs. 39-42). Physically, this occur as at short times $\{P_{IJ_r}(t)\}$ are independent of the initial FS site $|I\rangle$ or disorder realisation, and depend only on the Hamming distance between a pair of sites $|I\rangle$ and $|J_r\rangle$.

Figure F.1 shows that in the ergodic phase for $t \gtrsim 10$, $\tilde{P}_{rel;m}(x)$ rapidly narrows with increasing L, and is thus δ-distributed on $x = 1$ in the thermodynamic limit. This means at long times in the ergodic phase $P_I(r;t)$ is independent of the disorder realisation or the initial FS site. This occurs as deep in the ergodic phase, at long times there is homogeneity in the set $\{P_{IJ}(t)\}$ across the FS graph. The difference in $P_I(r;t)$ for different rows solely occurs due to each row having a different number of FS sites, $N_r = \binom{N}{r}$, which is an inherent property of the FS graph, and is independent of the initial FS site I at the apex of the graph (discussed in chapter 2). For $t \simeq 1$, figure 4.10 shows that $\tilde{P}_{rel;m}(x)$ appear converged with system size.

It, however, remains a very narrow distribution. It therefore follows that there are only small fluctuations in the intermediate time, $t \simeq 1$, $P_I(r;t)$, depending on the initial FS site or disorder realisation. This means for all times in the ergodic phase $\{P_I(r;t)\}$ all are well-captured by the average $\overline{P}(r;t)$.

By contrast, figure F.2 shows that in the MBL phase ($W = 7$) that for all but the smallest t values - for which our short-time analytical results apply - $\tilde{P}_{rel;m}(x)$ is a broad distribution, which broadens with increasing L. The cumulative distribution, $\tilde{P}_{rel;m,c}(x)$, confirms this, as $\tilde{P}_{rel;m}(x)$ has significant weight over several orders of magnitude. This means that $P_I(r;t)$ in the MBL phase depend strongly on the initial FS site and/or disorder realisation. Physically, this reflect the strong inhomogeneity of the $\{P_{IJ}(t)\}$ in the MBL, which changes depending on the FS site $|I\rangle$ or the disorder realisation considered.

Appendix G

Fluctuations in $C_j^{[n]}(t)$

In this appendix we shall examine the quantity

$$\delta^2_{C_j}(t) = \langle \frac{1}{N}\sum_{j=1}^{N} \mathrm{Re}[C_j^{[n]}(t)]^2 \rangle - \langle \frac{1}{N}\sum_{j=1}^{N} \mathrm{Re}[C_j^{[n]}] \rangle^2, \tag{G.1}$$

with

$$C_j^{[n]}(t) = \left\langle n \middle| \hat{\sigma}_j^z(t)\hat{\sigma}_j^z \middle| n \right\rangle. \tag{G.2}$$

This quantity measures the variation in the time evolution of the spin autocorrelation function for spins on different real space sites $\{j\}$.

Figures G.1 and G.2 show how $\delta_{C_j}(t)$ and $\overline{C}^{[n]}(t)$ vary with t in the ergodic and the MBL phases respectively.

From our discussions in section 3.2.3 on the universal short time behaviour we expect that at time scales that our short time analytical results are valid ($t \lesssim 0.1$) $\delta_{C_j}(t) = 0$ as all spins are rotated away from the z axis by the same amount. We expect this result independent of whether the system at long times is ergodic or MBL. Figures G.1 and G.2 shows that this exactly what we observe in our numerics.

In MBL_0 from our discussion in section 2.2.2 we know that at long-times spins on different real space sites j are tilted at different angles from the z axis depending on the strength of the field h_l compared to the hopping strength Γ. It follows that

in MBL_0 at long times $\delta_{C_j}(t)$ remains finite. Since at strong disorder the $J_z \neq 0$ problem is known [59] to be perturbatively connected to the $J_z = 0$ problem we expect that in the MBL phase for a uniformly distributed $J_z \in [0.8, 1.2]$ $\delta_{C_j}(t)$ will remain finite also. Figure G.2 shows this is exactly what is observed in our numerics, with $\delta_{C_j}(t)$ results for $J_z \neq 0$ being well captured by the MBL_0 results.

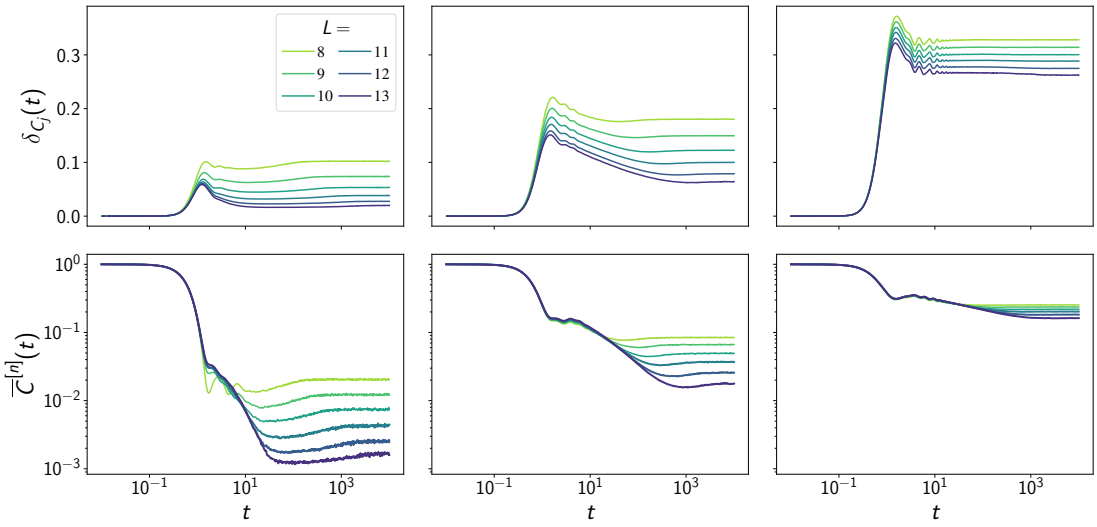


Figure G.1: Top panels: $\delta_{C_j}(t)$ *vs* t for different W values (indicated in plot) and $L = 8 - 13$. Bottom panels: $\overline{C}^{[n]}(t)$ *vs* t for different W values (indicated in plot) and $L = 8 - 13$.

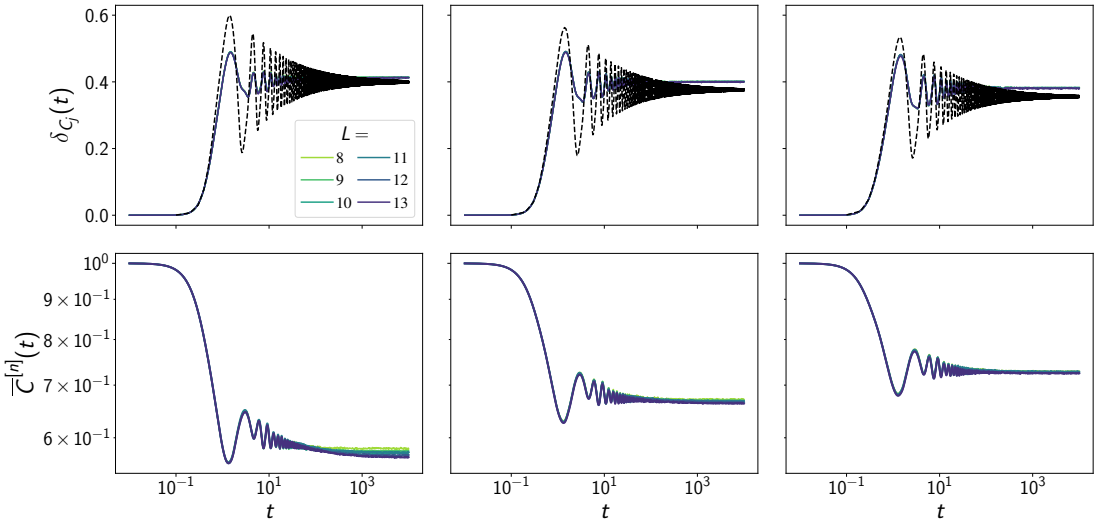


Figure G.2: Top panels: $\delta_{C_j}(t)$ *vs* t for different W values (indicated in plot) and $L = 8 - 13$. Bottom panels: $\overline{C}^{[n]}(t)$ *vs* t for different W values (indicated in plot) and $L = 8 - 13$. The black dotted line shows the MBL_0 results for the same W values.

Finally, figure G.1 shows that at intermediate times when the power-law decay in $\overline{C}^{[n]}(t)$ starts to occur, $\delta_{C_j}(t)$ has a maximum. This maximum still decreases with increasing system size L. This maximum may be due to rare slow spins in the system, and it may be these spins that are responsible for the power-law decay at intermediate times.

Appendix H

IPR distributions MBL_0

When $J_z = 0$, the Hamiltonian

$$\mathcal{H}_{TFI} = \sum_{l=1}^{L} \left(h_l \hat{\sigma}_l^z + \Gamma \hat{\sigma}_l^x \right), \tag{H.1}$$

is site separable. The problem can be solved exactly by defining a rotated spin operator

$$\hat{\tilde{\sigma}}_l^z = \frac{h_l \hat{\sigma}_l^z + \Gamma \hat{\sigma}_l^x}{\sqrt{h_l^2 + \Gamma^2}}, \tag{H.2}$$

where the factor $\sqrt{h_1^2 + \Gamma^2}$ in the denominator ensures that $\hat{\tilde{\sigma}}_l^z$ is a bonafide spin operator with $[\hat{\tilde{\sigma}}_l^z]^2 = 1$ using the usual spin commutation relations, and has eigenvalues of ± 1. The $|\tilde{\sigma}_l^z\rangle$ are the rotated spins, with $\hat{\tilde{\sigma}}_l^z |\tilde{\sigma}_l^z\rangle = \tilde{\sigma}_l^z |\tilde{\sigma}_l^z\rangle$, and $\tilde{\sigma}_l^z = \pm 1$, i.e. each rotated spin can point either up or down.

From eqs. H.2, H.1 clearly

$$\mathcal{H}_{TFI} = \sum_{l=1}^{L} \tilde{h}_l \hat{\tilde{\sigma}}_l^z : \quad \tilde{h}_l = \sqrt{h_1^2 + \Gamma^2}. \tag{H.3}$$

It follows from eq. H.3 that the eigenvectors of $\mathcal{H}_{TFI}$, $\{|n\rangle\}$, are simply product states of the $\tilde{\sigma}_l^z$ spins

$$|n\rangle = \bigotimes_{l=1}^{L} |\tilde{\sigma}_l^z\rangle \,, = |\{\tilde{\sigma}_l^z\}\rangle \,, \tag{H.4}$$

where $\{\tilde{\sigma}_l^z\}$ is a specified configuration of the rotated spins for the different real space sites l. Clearly, $|n\rangle$ eigenvalue, $E_n = \sum_{l=1}^{L} \tilde{h}_l \tilde{\sigma}_l^z$.

In order to work out the distributions of L_q and u_q, we need to work out

$$|A_{nI}|^2 = |\langle I|n\rangle|^2. \tag{H.5}$$

The $|I\rangle$ themselves are eigenstates of the original $\hat{\sigma}_l^z$ operators, i.e.

$$|I\rangle = \bigotimes_{l=1}^{L} |\sigma_l^z\rangle = |\{\sigma_l^z\}\rangle\,, \tag{H.6}$$

where $\{\sigma_l^z\}$ is a specified configuration of the original σ_l^z spins. It thus follows that

$$|A_{nI}|^2 = |\langle I|n\rangle|^2 = \prod_{l=1}^{L} |\langle \sigma_l^z|\tilde{\sigma}_l^z\rangle|^2 = \prod_{l=1}^{L} p_{l,I}. \tag{H.7}$$

In order to determine $p_{l,I}$ we need to consider the form of $\tilde{\sigma}_l^z$ spins, $\left|\tilde{\uparrow}_l\right\rangle$ and $\left|\tilde{\downarrow}_l\right\rangle$, which are eigenstates of

$$\mathcal{H}_l = h_l \sigma_l^z + \Gamma \sigma_l^x, \tag{H.8}$$

in the σ_l^z basis $|\uparrow_l\rangle$ and $|\downarrow_l\rangle$. These eigenstates are obtained by simply diagonalising the 2×2 matrix H_l. The result is

$$\left|\tilde{\uparrow}_l\right\rangle = \frac{|\uparrow\rangle + \lambda_l |\downarrow\rangle}{\sqrt{1+\lambda_l^2}}, \quad \left|\tilde{\downarrow}_l\right\rangle = \frac{|\downarrow\rangle - \lambda_l |\uparrow\rangle}{\sqrt{1+\lambda_l^2}}, \tag{H.9}$$

with

$$\lambda_l^2 = \frac{E_+ - h_l}{E_+ + h_l}, \tag{H.10}$$

and

$$E_\pm = \pm\sqrt{h_l^2 + \Gamma^2}. \tag{H.11}$$

To calculate $p_{l,I}$ we simply consider the projections of the $\tilde{\sigma}_l^z$ spins on the σ_l^z spins, where

$$|\left\langle \uparrow_l \middle| \tilde{\uparrow}_l \right\rangle|^2 = |\left\langle \downarrow_l \middle| \tilde{\downarrow}_l \right\rangle|^2 = \frac{1}{\lambda_l^2+1} = p_{l+} \tag{H.12}$$

and

$$|\left\langle \uparrow_l \middle| \tilde{\downarrow}_l \right\rangle|^2 = |\left\langle \downarrow_l \middle| \tilde{\uparrow}_l \right\rangle|^2 = \frac{\lambda^2}{\lambda_l^2+1} = p_{l-}. \tag{H.13}$$

This can be equivalently written as

$$p_{l,I} = p_{l+}\delta_{s_l^I,+\tilde{\sigma}_l^z} + p_{l-}\delta_{s_l^I,-\tilde{\sigma}_l^z}; \quad p_{l\pm} = \frac{1}{2}\left[1 \pm \frac{h_l}{\sqrt{h_l^2+1}},\right], \tag{H.14}$$

where $s_{l,I} = \langle I \,|\, \sigma_l^z \,|\, I \rangle$ and δ_{ij} is the usual Kronecker-delta function.

Since $A_{nI}^2 = \prod_{l=1}^{L} p_{l,I}$, L_q (eq. 5.6, pg. 113) is clearly given by:

$$L_q = \sum_I \prod_{l=1}^{L} [p_{l,I}]^q. \tag{H.15}$$

Summing over all I in eq. H.15 is equivalent to allowing for each real space site l both $p_{l,+}^q$ and $p_{l,-}^q$. This means eq. H.15 reduces to

$$L_q = \prod_{l=1}^{L} \left[(p_{l,+})^q + (p_{l,-})^q\right]. \tag{H.16}$$

Since $u_q = \ln[L_q]$ it follows

$$u_q = \sum_{l=1}^{L} x_l; \quad x_l = \ln[(p_{l,+})^q + (p_{l,-})^q]. \tag{H.17}$$

From eq. H.17, u_q is seen to be a sum of L independent random variables x_l, each with a finite variance. It thus follows from central limit theorem [178] that in the thermodynamic limit $L \to \infty$, the distribution $P_{u_q}(x)$ (eq. 5.9, pg. 114) of

$u_q = \ln[L_q]$ will be a normal distribution, with

$$P_{u_q}(x) = \frac{1}{\sqrt{2\pi\sigma_{u_q}^2}} \exp\left(\frac{-[x - \langle u_q \rangle]^2}{2\sigma_{u_q}^2}\right). \tag{H.18}$$

Given this, it follows directly that in the thermodynamic limit $P_{L_q}(x)$ (eq. 5.9, pg. 114) will be a log-normal distribution,

$$P_{L_q}(x) = \frac{1}{\sqrt{2\pi\sigma_{u_q}^2}} \frac{1}{x} \exp\left(\frac{-[\ln[x] - \langle u_q \rangle]^2}{2\sigma_{u_q}^2}\right). \tag{H.19}$$

Appendix I

IPR distributions GRV

Assuming that the eigenstates are gaussian random eigenvectors is known to explain many of their properties deep in the ergodic phase [163, 170–172]. In this appendix, we shall outline the full derivation of the results arising for the IPR distributions.

As a reminder to the reader, the sets of amplitudes $A_{nI} = \langle n|I\rangle$, refer to amplitude of eigenstate $|n\rangle$ on FS site $|I\rangle$.

Within the gaussian random vectors (GRV) model, for any given eigenstate $|n\rangle$, $\{A_{nI}\}$ across the set of FS sites, $\{|I\rangle\}$, are independent random variables. Likewise, for any given FS site $|I\rangle$, the set of $\{A_{nI}\}$ across the set of eigenstates, $\{|n\rangle\}$, are independent random variables. In both cases they are gaussian distributed, with

$$P_{A_{nI}}(x) = \frac{1}{\sqrt{2\pi\sigma^2_{A_{nI}}}} \exp\left[\frac{-x^2}{2\sigma^2_{A_{nI}}}\right], \tag{I.1}$$

with a mean of zero - as the set of amplitudes, $\{A_{nI}\}$, are equally likely to be positive or negative - and a variance $\sigma^2_{A_{nI}} = \frac{1}{N_H}$, which simply occurs as the average A^2_{nI}, $\langle A^2_{nI}\rangle = \frac{1}{N_H}$ in order for the wavefunction to be normalised, $N_H\langle A^2_{nI}\rangle = 1$.

From $P_{A_{nI}}(x)$ the distribution of $|A_{nI}|^{2q}$,

$$P_{|A_{nI}|^{2q}}(x) = \int dy\ P_{A_{nI}}(y)\ \delta\left(x - |y|^{2q}\right) \tag{I.2}$$

can be calculated. Using eq. I.1 and a simple change of variables, it follows that

$$P_{|A_{nI}|^{2q}}(x) = \frac{1}{q}\frac{1}{\sqrt{2\pi\sigma^2_{A_{nI}}}} x^{\frac{-(2q-1)}{2q}} \exp\left[\frac{-x^{\frac{1}{q}}}{2\sigma^2_{A_{nI}}}\right]\theta(x), \tag{I.3}$$

with $\theta(x)$ the usual step function. For all $q > 0$ these distributions clearly have a non-infinite mean and variance, since $|A_{nI}|^{2q} \leq 1$.

Within the GRV model, the generalised IPR,

$$L_q = \sum_{I=1}^{N_H} |A_{nI}|^{2q}, \tag{I.4}$$

is clearly given by a sum of N_H terms, each of which are independent random variables, with a non-infinite variance, whose distribution is given by eq. I.3. This means from central limit theorem [178] that in the thermodynamic limit $P_{L_q}(x)$ (eq. 5.9, pg. 114) is a gaussian distribution,

$$P_{L_q}(x) = \frac{1}{\sqrt{2\pi\sigma^2_{L_q}}} \exp\left(\frac{-[x - \langle L_q\rangle]^2}{2\sigma^2_{L_q}}\right). \tag{I.5}$$

Since the $\{A_{nI}\}$ are assumed to be independent random variables both $\sigma^2_{L_q}$ and $\langle L_q\rangle$ can be calculated using $P_{|A_{nI}|^{2q}}(x)$ (eq. I.3), where

$$\langle L_q\rangle = N_H\langle|A_{nI}|^{2q}\rangle; \quad \langle|A_{nI}|^{2q}\rangle = \int dx\; x\; P_{|A_{nI}|^{2q}}(x), \tag{I.6}$$

and

$$\sigma^2_{L_q} = \langle L_q^2\rangle - \langle L_q\rangle^2; \quad \langle L_q^2\rangle = N_H\langle|A_{nI}|^{4q}\rangle + N_H(N_H-1)\langle|A_{nI}|^{2q}\rangle^2. \tag{I.7}$$

This gives

$$\langle L_q \rangle = \frac{2^q \, \Gamma\left(\frac{1}{2}+q\right)}{\sqrt{\pi}} N_H^{1-q}; \quad \sigma_{L_q}^2 = N_H^{1-2q} \frac{2^{2q}}{\sqrt{\pi}} \left(\Gamma\left(2q+\frac{1}{2}\right) + \frac{\Gamma(q+\frac{1}{2})^2}{\sqrt{\pi}} \right). \quad \text{(I.8)}$$

Given the distribution of $P_{L_q}(x)$ we can calculate the distribution of $y_q = \frac{x}{\langle L_q \rangle}$, where clearly $P_{y_q}(y) = \int dx \; P_{L_q}(x) \; \delta(y - \frac{x}{\langle L_q \rangle})$. From eq. I.5 it follows

$$P_{y_q}(y) = \frac{1}{\sqrt{2\pi\tilde{\sigma}^2}} \exp\left[\frac{-(y-1)^2}{2\tilde{\sigma}^2}\right]; \quad \tilde{\sigma}^2 = \frac{\sigma_{L_q}^2}{\langle L_q \rangle^2} \propto N_H^{-1}. \quad \text{(I.9)}$$

The other distribution that is of central interest in chapter 5 is the distribution of $u_q = \ln[L_q]$, $P_{u_q}(x)$. In order to determine this, we shall first consider the distribution of $\tilde{u}_q = \ln[y_q] = \ln[L_q] - \ln[\langle L_q \rangle]$, $P_{\tilde{u}_q}(x)$. This is clearly calculated using $P_{\tilde{u_q}}(x) = \int dy \; P_{y_q}(y) \; \delta(x - \ln[y])$, which gives

$$P_{\tilde{u}_q}(x) = \frac{1}{\sqrt{2\pi\tilde{\sigma}^2}} \exp\left[x - \frac{(e^x-1)^2}{2\tilde{\sigma}^2}\right] = A \exp[g(x)]. \quad \text{(I.10)}$$

Since $\tilde{\sigma}^2 \propto N_H^{-1}$ is exponentially small it is obvious that $P_{\tilde{u}_q}(x)$ x-dependence is controlled by the behaviour of $g(x)$ arounds it minimum, $x = 0$. A steepest descents (SD) calculation can therefore be done on eq. I.10 expanding $g(x)$ to quadratic order to determine $P_{\tilde{u}_q}(x)$. In the SD calculation,

$$g(x) = g(x_0) + \frac{1}{2}(x - x_0)^2 g''(x_0) \quad \text{(I.11)}$$

with

$$P_{\tilde{u}_q}(x) = N e^{g(x_0)} \exp\left[\frac{1}{2}(x - x_0)^2 g''(x_0)\right], \quad \text{(I.12)}$$

where N is simply a normalisation constant.

To proceed forwards we need to determine when $g'(x_0) = 1 - \frac{e^{x_0}(1-e^{x_0})}{\tilde{\sigma}^2} = 0$. This

gives $\delta(1+\delta) = \tilde{\sigma}^2$, where $x_0 = \ln[1+\delta] = \tilde{\sigma}^2 + \mathcal{O}(\tilde{\sigma}^4)$. Given $g''(x_0) = \frac{2\exp[2x_0]-\exp[x_0]}{\tilde{\sigma}^2}$, clearly $g''(x_0) \sim \frac{-1}{\tilde{\sigma}^2}$ to leading order.

Putting the above results into eq. I.12 leads to the SD results for

$$P_{\tilde{u}_q}(x) \simeq \frac{1}{\sqrt{2\pi\tilde{\sigma}^2}} \exp\left[\frac{-(x-x_0)^2}{2\tilde{\sigma}^2}\right]. \tag{I.13}$$

Since $x_0 \simeq \tilde{\sigma}^2 \sim N_H^{-1}$, in thermodynamic limit it follows that

$$P_{\tilde{u}_q}(x) \simeq \frac{1}{\sqrt{2\pi\tilde{\sigma}^2}} \exp\left[\frac{-x^2}{2\tilde{\sigma}^2}\right]. \tag{I.14}$$

The distribution of $u_q = \tilde{u}_q + \ln[\langle L_q \rangle]$, $P_{u_q}(x)$ is then given by:

$$P_{u_q}(x) = \frac{1}{\sqrt{2\pi\tilde{\sigma}^2}} \exp\left[\frac{-(x-\ln[\langle L_q \rangle])^2}{2\tilde{\sigma}^2}\right]. \tag{I.15}$$

Appendix J

IPR distributions for other q values

In this appendix, we show results for the IPR distributions for different q values to show that the key results for the functional forms of $P_{u_q}(x)$ and $P_{L_q}(x)$ are independent of the q value chosen.

To this end, figure J.1 shows plots of $P_{\tilde{u}_q}(x)$ (eq. 5.11, pg. 115) for $q = 2, 3$ and $W = 1$ and $W = 7$. This figure shows that for all q and W values $P_{\tilde{u}_q}(x)$ are very similar, and expected to be gaussian distributions in the thermodynamic limit $L \to \infty$.

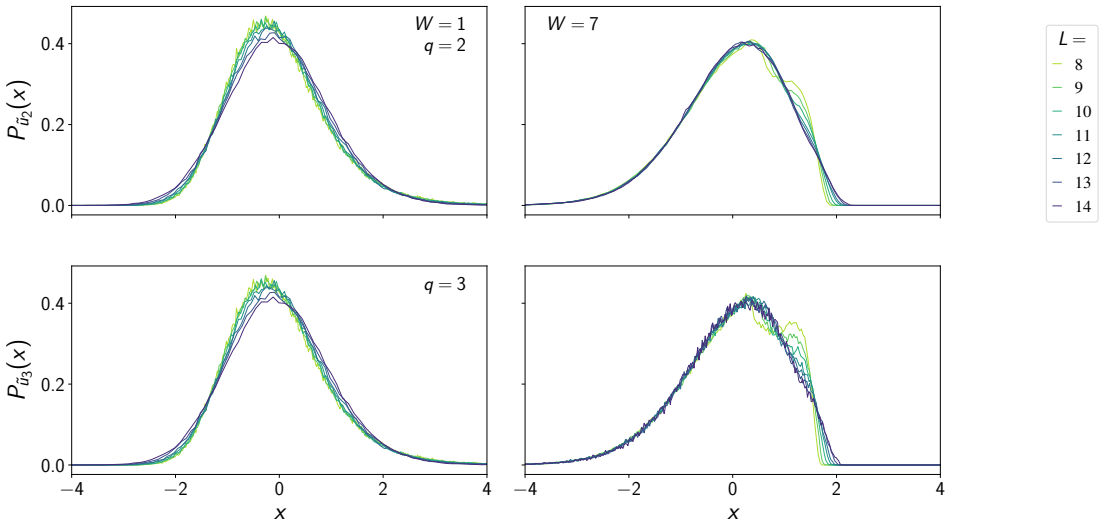


Figure J.1: $P_{\tilde{u}_q}(x)$ for $q = 2, 3$ and $W = 1, 7$ indicated in plot, $L = 8 - 14$.

Figure J.2 shows $P_{L_q}(x)$ (eq. 5.9, pg. 114) for $W = 1, 7$ and $q = 2$ and $q = 3$.

This figure shows that for both $q = 2$ and $q = 3$ $P_{L_q}(x)$ has very different functional forms in the ergodic phase ($W = 1$) and the MBL phase ($W = 7$). In the ergodic phase, for both q values $P_{L_q}(x)$ is a very narrow distribution which narrows with increasing L. The red dotted lines in the $W = 1$ plots show that the largest system size ($L = 14$) $P_{L_q}(x)$ plot are well captured by a gaussian distribution for both q values.

On the other hand, figure J.2 shows that for both q values the $W = 7$ $P_{L_q}(x)$ is a very broad distribution which broadens with increasing L. For both q values, the red dotted lines in figure J.2 show that the largest system size ($L = 14$) $P_{L_q}(x)$ are well captured by log-normal distributions.

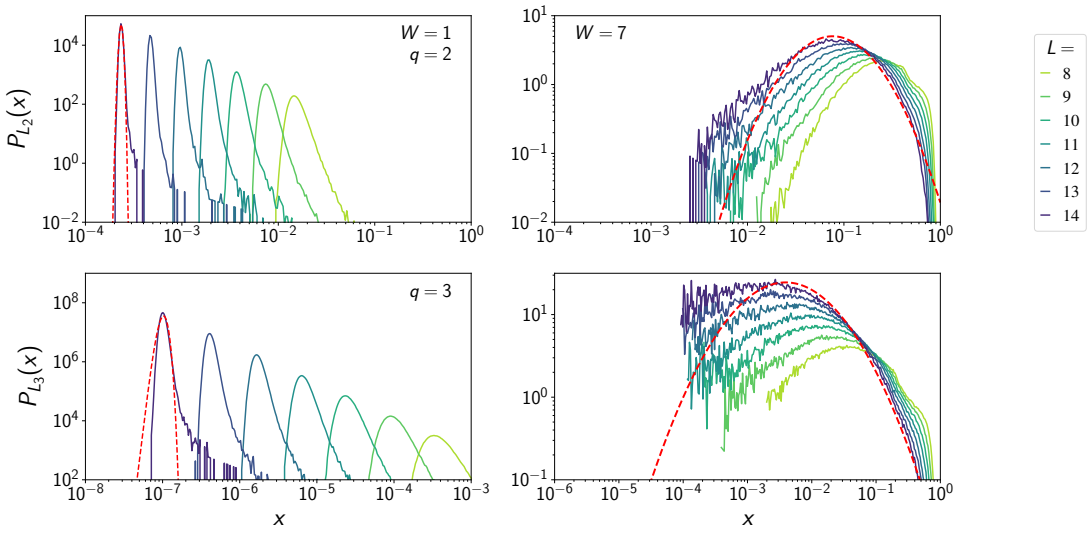


Figure J.2: $P_{L_q}(x)$ for $q = 2, 3$ and $W = 1, 7$ indicated in plot, $L = 8 - 14$. The red dotted lines in the ergodic phase ($W = 1$) show the fitting of the $L = 14$ $P_{L_q}(x)$ to a gaussian distribution. The red dotted lines in the MBL phase ($W = 7$) show the fitting of the $L = 14$ $P_{L_q}(x)$ to a log-normal distribution.

Appendix K

Scaling of $\langle L_2 \rangle$ and $\sigma^2_{L_2}$ with N_H

In this appendix we consider the scaling of $\langle L_2 \rangle$ and $\sigma^2_{L_2}$ with N_H.

To this end, figure K.1 shows plots of $\langle L_2 \rangle$ and $\sigma^2_{L_2}$ *vs* N_H. On the left-hand side of figure K.1 the blue plot shows the fitting of the $W = 1$ $\langle L_2 \rangle$ to $\frac{4}{N_H}$, while on the right-hand side of figure K.1 the blue line shows the fitting of the $W = 1$ $\sigma^2_{L_2}$ to $N_H^{-2.9}$, which within numerical errors means $\sigma^2_{L_2}$ to N_H^{-3}. This is exactly as predicted by the GRV model in section 5.2.2.

By contrast, in the MBL phase ($W = 7$), figure K.1 shows that $\langle L_2 \rangle \sim N_H^{-0.17}$ and $\sigma^2_{L_2} \sim N_H^{-0.2}$.

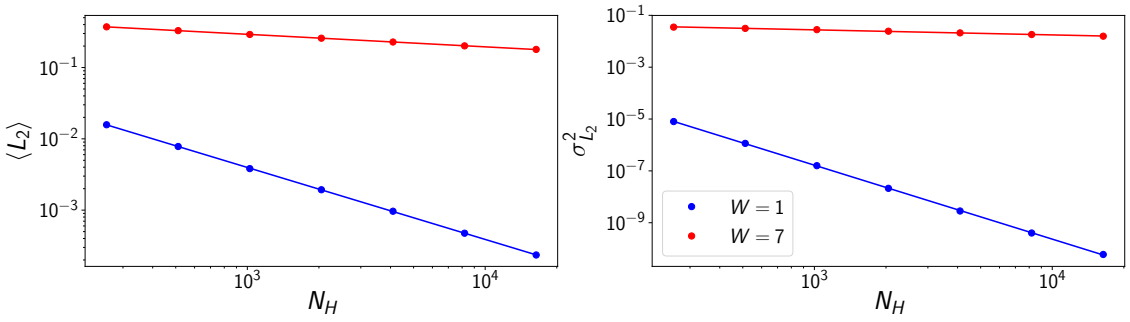


Figure K.1: Left hand panel: $\langle L_2 \rangle$ *vs* N_H. Right panel: $\sigma^2_{L_2}$ *vs* N_H. Both plots shown on a log-log scale, $L = 8 - 14$, $W = 1, 7$.

Appendix L

Scaling theory results S_{avg}^{NN} and L_{avg}^{NN}

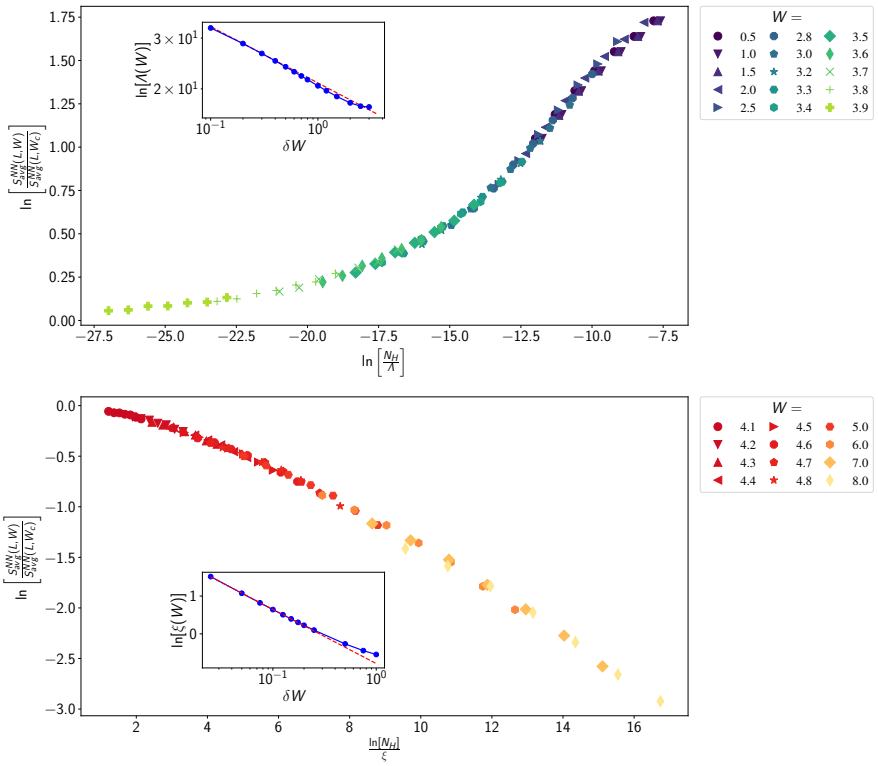


Figure L.1: Top panel: Ergodic phase scaling analysis $\ln\left[\frac{S_{avg}^{NN}(L,W)}{S_{avg}^{NN}(L,W_c)}\right]$ *vs* $x = N_H/\Lambda(W)$. Bottom panel: MBL scaling analysis $\ln\left[\frac{S_{avg}^{NN}(L,W)}{S_{avg}^{NN}(L,W_c)}\right]$ *vs* $x = \ln[N_H]/\xi(W)$. $\Lambda(W)$ and $\xi(W)$ are determined by a fitting procedure discussed in appendix M. Top inset: $\ln[\Lambda(W)]$ *vs* $\delta W = W_c - W$ in the ergodic phase. Bottom inset: $\ln[\xi(W)]$ *vs* $\delta W = W - W_c$ in the MBL phase.

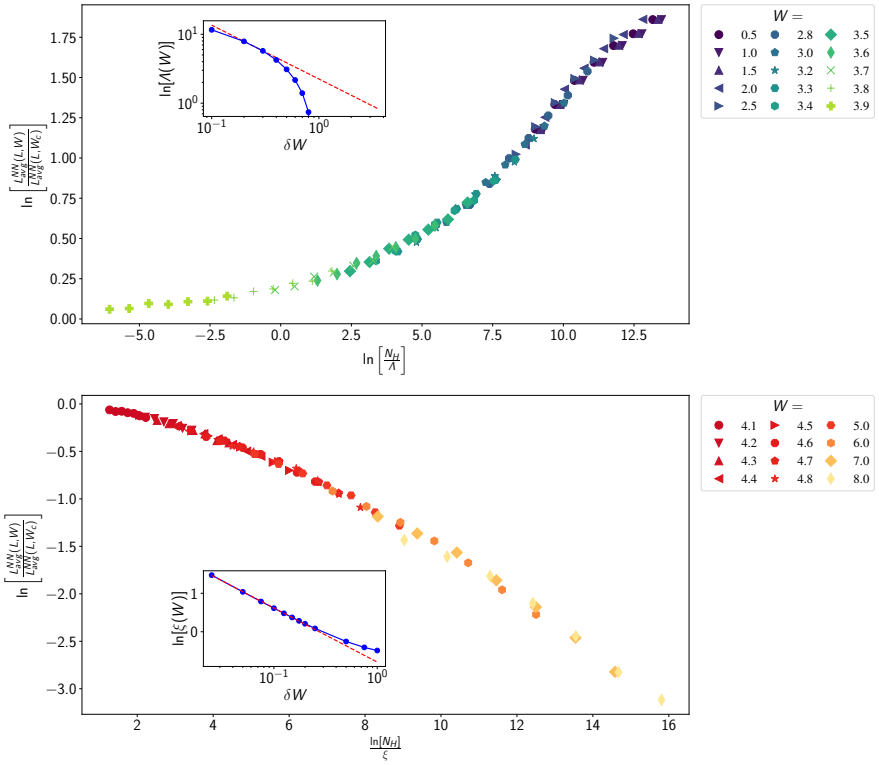


Figure L.2: Top panel: Ergodic phase scaling analysis $\ln\left[\frac{L_{avg}^{NN}(L,W)}{L_{avg}^{NN}(L,W_c)}\right]$ *vs* $x = N_H/\Lambda(W)$. Bottom panel: MBL scaling analysis $\ln\left[\frac{L_{avg}^{NN}(L,W)}{L_{avg}^{NN}(L,W_c)}\right]$ *vs* $x = \ln[N_H]/\xi(W)$. $\Lambda(W)$ and $\xi(W)$ are determined by a fitting procedure discussed in appendix M. Top inset: $\ln[\Lambda(W)]$ *vs* $\delta W = W_c - W$ in the ergodic phase. Bottom inset: $\ln[\xi(W)]$ *vs* $\delta W = W - W_c$ in the MBL phase.

For completeness in this appendix we show our results for the scaling collapse of S_{avg}^{NN} and L_{avg}^{NN} using the scaling theory introduced in sections 6.2.3-6.2.4.

Figure L.1 shows the scaling collapse obtained for S_{avg}^{NN}, while figure L.2 shows the scaling collapse obtained for L_{avg}^{NN}. These figures show that while a reasonable scaling collapse is obtained for S_{avg}^{NN} and L_{avg}^{NN} these are clearly not as good collapses as obtained for the typical values, S_{typ}^{NN} and L_{typ}^{NN}, figures 6.3 and 6.4 (pgs. 166-167) in the main body of the text. In chapter 6 we discussed that this is due to long tails in the distributions in the MBL phase.

Appendix M

Further details of the scaling analysis

In this appendix we discuss the scaling procedure used to obtain our numerical results in section 6.2.3. We also show the results obtained for the scaling collapse using different W_c values to validate our choice of W_c in the main body of the thesis.

M.1 Procedure for scaling analysis

Our scaling ansatz (eq. 6.17, pg. 163) assumed that in the ergodic phase $\ln\left[\frac{L_{typ}^{NN}(L,W)}{L_{typ}^{NN}(L,W_c)}\right]$ is fully described by a function $\mathcal{G}_{vol}(x)$ with $x = N_H/\Lambda(W)$, while in the MBL phase $\ln\left[\frac{L_{typ}^{NN}(L,W)}{L_{typ}^{NN}(L,W_c)}\right]$ is fully described by a function $\mathcal{G}_{lin}(x)$ with $x = \ln[N_H]/\xi(W)$ in this case. In order to do our scaling analysis, we need to find the $\Lambda(W)$ and $\xi(W)$ which best describe our numerical data.

To this end, we can assume that our scaling function $\mathcal{G}_{vol}(x)/\mathcal{G}_{lin}(x) = \mathcal{G}(L,W)$ can be expanded as a Taylor series, i.e.

$$\mathcal{G}(L,W) = \mathcal{G}(wX^{\frac{1}{\nu}}) = \sum_{k=0}^{n_f} c_k w^k X^{\frac{k}{\nu}}, \tag{M.1}$$

where

$$w = W - W_c + \sum_{k=1}^{n_w} d_k (W - W_c)^k, \tag{M.2}$$

and $X = N_H$ in the ergodic phase and $X = \ln[N_H]$ in the MBL phase. The $\{c_k\}$,

$\{d_k\}$ and ν are the fitting parameters (discussed below). n_f and n_w are the number of terms we choose to keep in the Taylor expansion in our analysis (in this thesis we chose $n_f = 4$, $n_w = 3$).

Since in our scaling analysis we assume $\ln\left[\frac{L_{typ}^{NN}(L,W)}{L_{typ}^{NN}(L,W_c)}\right] = \mathcal{G}_{vol}(x)$ in the ergodic phase and $\ln\left[\frac{L_{typ}^{NN}(L,W)}{L_{typ}^{NN}(L,W_c)}\right] = \mathcal{G}_{lin}(x)$ in the MBL phase, we clearly want to find the $\mathcal{G}(L,W)$ which best describes our numerical data for $\ln\left[\frac{L_{typ}^{NN}(L,W)}{L_{typ}^{NN}(L,W_c)}\right]$.

To this end, we use a standard curve fitting algorithm [215] to determine the values of $\{c_k\}$, $\{d_k\}$ and ν which leads to the function $\mathcal{G}(L,W)$ which closest fits our data for $\ln\left[\frac{L_{typ}^{NN}(L,W)}{L_{typ}^{NN}(L,W_c)}\right]$.

Once the value of $\{c_k\}$, $\{d_k\}$ and ν has been determined, since in our scaling ansatz (eq. 6.17, pg. 163) in both phases we assume

$$\mathcal{G}(L,W) \equiv f(x), \tag{M.3}$$

then it follows from eq. M.1 that

$$x^{\frac{k}{\nu}} = X^{\frac{k}{\nu}} w^k, \tag{M.4}$$

where $x = \frac{N_H}{\Lambda(W)}$ in the ergodic phase and $x = \frac{\ln[N_H]}{\xi(W)}$ in the MBL phase, which by comparing to eq. M.4 means $\Lambda(W) = cw^{-\nu}$ and $\xi = cw^{-\nu}$, with c a chosen scaling constant. It therefore follows that from this procedure we can determine $\Lambda(W)$ and $\xi(W)$, to within a constant c which we are free to choose.

Once $\Lambda(W)$ and $\xi(W)$ have been determined, we can simply plot our numerical data for $\ln\left[\frac{L_{typ}^{NN}(L,W)}{L_{typ}^{NN}(L,W_c)}\right]$ *vs* $N_H/\Lambda(W)$ in the ergodic phase, and $\ln\left[\frac{L_{typ}^{NN}(L,W)}{L_{typ}^{NN}(L,W_c)}\right]$ *vs* $\ln[N_H]/\xi(W)$ to generate scaling collapse seen in figure 6.3 (pg. 166) in the main body of the thesis.

An identical procedure is used to determine the values of $\Lambda(W)$ and $\xi(W)$ needed

to obtain the scaling collapse of $\ln\left[\frac{S^{NN}_{typ}(L,W)}{S^{NN}_{typ}(L,W_c)}\right]$ *vs* $N_H/\Lambda(W)$ in the ergodic phase, and $\ln\left[\frac{S^{NN}_{typ}(L,W)}{S^{NN}_{typ}(L,W_c)}\right]$ *vs* $\ln[N_H]/\xi(W)$ in figure 6.4 (pg. 167).

M.2 Scaling analysis

In this section, we show the scaling collapse obtained for S^{NN}_{typ} using different choices of W_c values either side of the $W_c = 4$ value shown in section 6.2.3.

To this end, figures M.1 and M.2 show the scaling collapse obtained for S^{NN}_{typ} using $W_c = 3.9$ and $W_c = 4.1$. These figures show that a better scaling collapse is obtained using $W_c = 4$, shown in figure 6.4 (pg. 167) than for the values either side of it, validating our choice of W_c in the main body of the thesis.

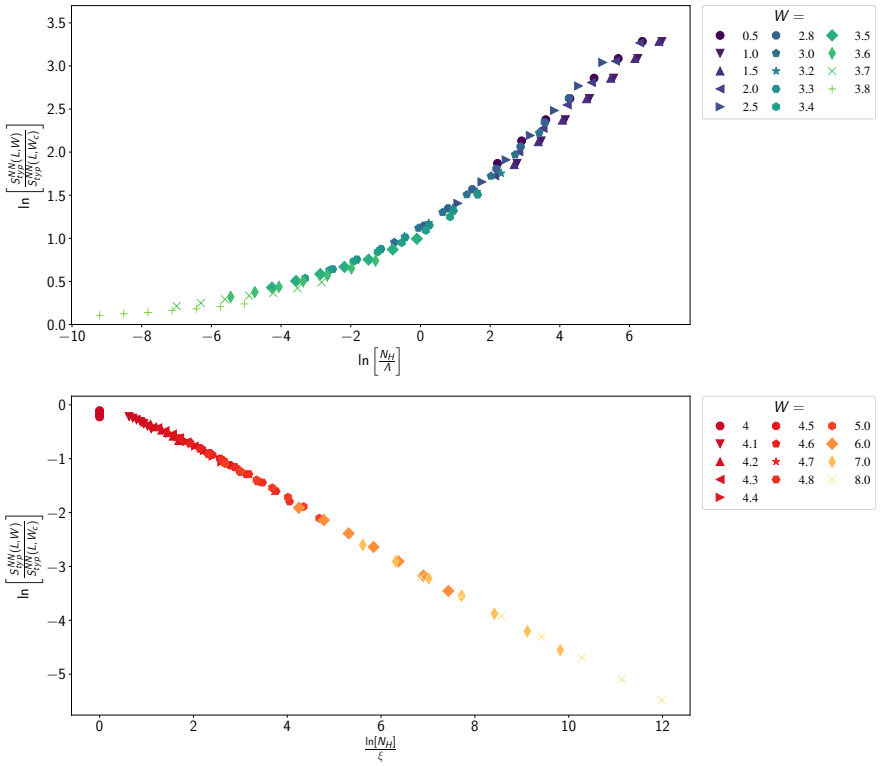


Figure M.1: Top panel: Ergodic phase scaling analysis $\ln\left[\frac{S^{NN}_{typ}(L,W)}{S^{NN}_{typ}(L,W_c)}\right]$ *vs* $x = N_H/\Lambda(W)$. Bottom panel: MBL scaling analysis $\ln\left[\frac{S^{NN}_{typ}(L,W)}{S^{NN}_{typ}(L,W_c)}\right]$ *vs* $x = \ln[N_H]/\xi(W)$. $W_c = 3.9$ chosen.

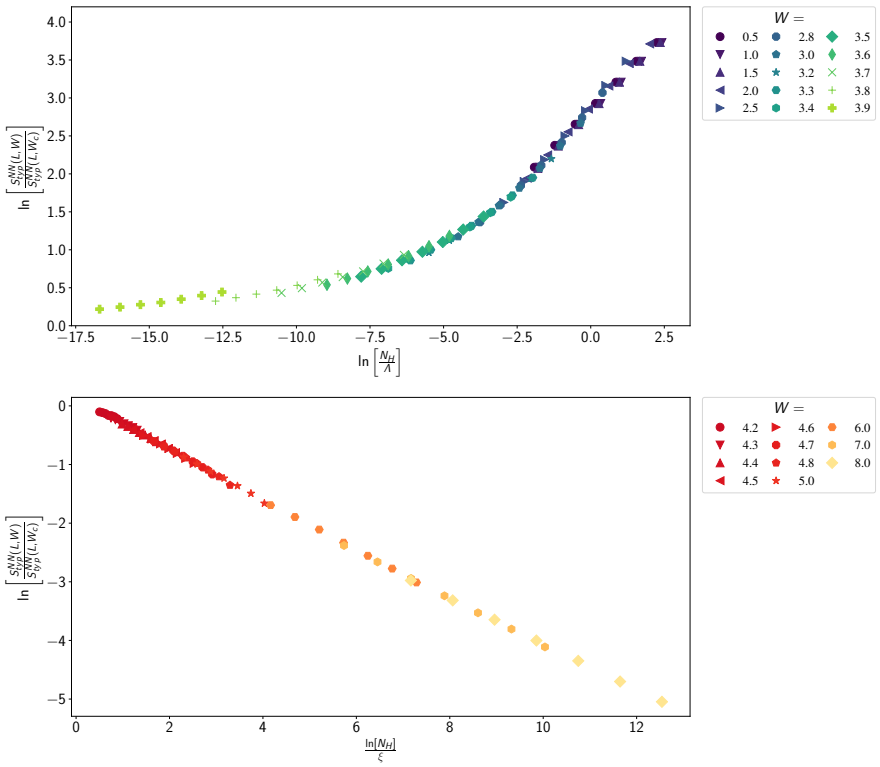


Figure M.2: Top panel: Ergodic phase scaling analysis $\ln\left[\frac{S_{typ}^{NN}(L,W)}{S_{typ}^{NN}(L,W_c)}\right]$ *vs* $x = N_H/\Lambda(W)$. Bottom panel: MBL scaling analysis $\ln\left[\frac{S_{typ}^{NN}(L,W)}{S_{typ}^{NN}(L,W_c)}\right]$ *vs* $x = \ln[N_H]/\xi(W)$. $W_c = 4.1$ chosen.